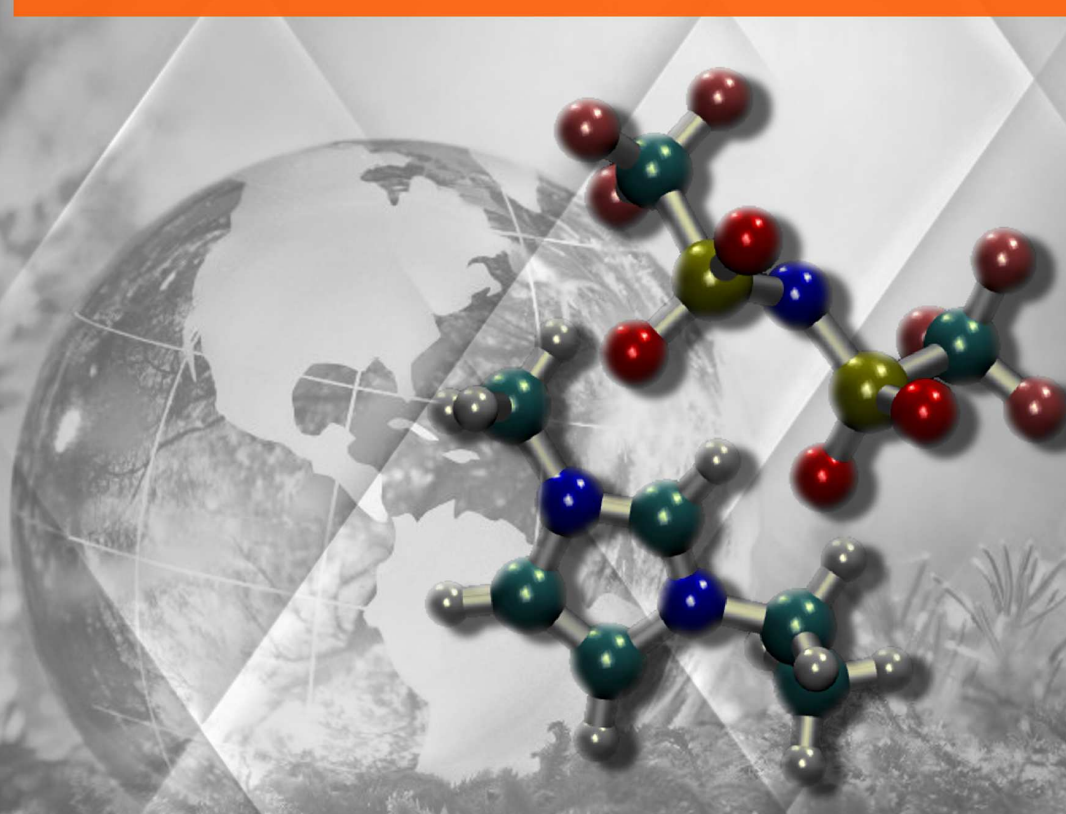# Molecular Simulation of Ionic Liquids-Based Systems for Energy Applications

José Manuel Vicent Luna

Molecular Simulation of Ionic Liquids-Based Systems For Energy Applications

By

JOSÉ MANUEL VICENT LUNA

Licenciado en Física

Department of Physical, Chemical, and Natural Systems

UNIVERSITY PABLO DE OLAVIDE

SUPERVISORS

Sofía Calero

Prof. University Pablo de Olavide

Juan Antonio Anta

Prof. University Pablo de Olavide

Dissertation submitted to obtain the degree of Doctor with international mention.

SEVILLE, JANUARY 2018

0000-0001-8712-5591

- **Doctoral Supervisors**

    Prof. Sofía Calero

    Prof. Juan A. Anta

- **Examination Committe**

    Chair: Prof. José B. Parra Soto

    Secretary: Dr. Ariana Torres Knoop

    Member: Prof. Benito Garzón Sánchez

- **External Committe**

    Dr. David Dubbeldam

    Dr. Juan José Gutiérrez Sevillano

Table of Contents

Introduction

I onic liquids as a new class of eco-friendly compounds have been widely studied. Their unique properties make them very attractive materials and offers opportunities in a wide range of applications. The combination of a high number of cations and anions is possible, which gives rise to numerous ionic liquids. In this context, molecular simulations are useful to investigate and understand their physicochemical properties at a molecular level. Molecular simulation plays an important role in the investigation of the microscopic foundation of a process and complements and even substitutes experimental studies. In this work we study, via molecular simulation techniques (Monte Carlo and molecular dynamics), the role of ionic liquids as potential candidates for energy and environmental applications. The applications investigated in this thesis are organized in three blocks: i) combination of ionic liquids with porous materials to obtain a new class of hybrid systems for gas capture and separation; ii) use of ionic liquid-based electrolytes for dye-sensitized solar cells and metal-ion batteries; iii) interaction of ionic liquids with water as alternative surfactants.

MATERIALS AND SYSTEMS

Room-Temperature Ionic Liquids

The study of species in solution is of great interest in chemistry.[1, 2] Although any liquid may be used as a solvent, relatively few are of general use. In addition, solvents are usually considered as damaging chemicals since they are employed in huge amounts and as a rule, they are volatile compounds. Actually the search for alternatives has become a priority. In this context, ionic liquids have attracted the attention of many researchers and they have gained the nickname of "green solvents". It has been proposed that these ionic liquids provide a useful extension to the range of solvents that are available for synthetic chemistry.

Room-temperature ionic liquid, non-aqueous ionic liquid, molten salt, liquid organic salt, and fused salt have all been used to describe salts in the liquid phase.[3–6] Since they are very well known, we refer to them simply as ionic liquids (ILs). ILs are salts that remain in the liquid state in a wide range of temperatures, usually below 373 K. They are formed by a combination of organic cations and organic or inorganic anions (Figure 1). The combination of a high number of cations and anions is possible, giving rise to an extremely large number of compounds with different physicochemical properties.[7] These properties make them advantageous over other options in many applications.[8, 9] First of all, they

exhibit low vapor pressure and excellent thermal, chemical, and electrochemical stability. ILs are nonflamable and they have relatively high ionic conductivity, heat capacity, and viscosity. In addition, they manifest a great environmental compatibility, being selected as good candidates to replace the so-called volatile organic compounds.[10, 11] Thanks to these appealing properties, ILs are widely used, for example as heat transfer fluids, lubricants, and in membrane science. Many reports have explored their possibilities as advantageous electrolytes in electrochemical double-layer capacitors [12–15] or batteries,[16–30] electrodeposition, [31–37] and thin film solar cells. [38–41] ILs has been proved good solvents for extraction and separation process of gases,
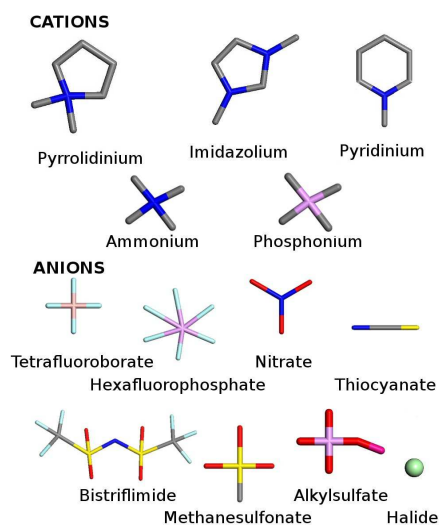
Figure 1. Example of common anionic and cationic constituents of ILs. Hydrogen atoms are omitted for clarity.

such as carbon dioxide capture or natural gas purification.[42–49] They have also been employed in liquid phase separation processes, as for example alcohol/water separation to produce bioethanol fuel.[50, 51] There are other applications in which ILs are combined with other materials to improve their properties. For instance, they are used in conjunction with biopolymers to develop ion jelly.[52–54] This makes possible to have flexible solid materials with the properties of ionic liquids. Ion jelly can be used as flexible electrolytes, biosensors,[55] or even as drug delivery devices.[56] Moreover ILs are constituents of ionic liquid cristals, materials that exhibit an intermediate phase between solid and liquid.[57] The most common use of ionic liquids cristals is the production of computer monitors, televisions, instrument panels, or displays for small gadgets.

Among the large number of cations and anions which can be mixed to obtain ILs, we focus on the well-known cations of the family of imidazolium and pyrrolidinium combined with different anions. These anions include bis[(trifluoromethyl)sulfonyl]imide, thiocyanate, nitrate, tetrafluoroborate, hexafluorophosphate, and halide anions. 1-alkyl-3-methylimidazolium cations result from the protonation of the imidazole compound attached to a methyl group and an alkyl group. This is an assymetric organic cation, bulky, and chain-like constituted by carbon, hydrogen, and nitrogen

atoms. Very similar to this, N-methyl-N-alkyl-pyrrolidinium cations are the result of the protonation of the pyrrolidine formed by the same elements. The nomenclature of the cations is $[C_n MIM]^+$ and $[C_n PYR]^+$ respectively. Concerning to the anions, bis[(trifluoromethyl)sulfonyl]imide or bistriflimide is a non-coordinating anion with chemical formula $(CF_3 SO_2)_2 N^-$. This anion, commonly known by the formula $[Tf_2 N]^-$ is widely used in ionic liquids, since it is less toxic and more stable than more traditional counterions. Thiocyanate $[SCN]^-$ (also known as rhodanide) is the conjugate base of thiocyanic acid. Organic compounds containing the functional group SCN are called thiocyanates. It is produced by the reaction of elemental sulfur or thiosulfate with cyanide. The nitrate anion $[NO_3]^-$ is the conjugate base of nitric acid, consisting of one central nitrogen atom surrounded by three identically bonded oxygen atoms in a trigonal planar arrangement. Nitrates are mainly produced for use as fertilizers in agriculture because of their high solubi- lity and biodegradability. The second major application of nitrates is as oxidizing agents, most notably in explosives where the rapid oxidation of carbon compounds liberates large volumes of gases. Hexafluorophosphate $[PF_6]^-$ is a non-coordinating anion and generally very stable in solution. The practical uses of the hexafluorophosphate ion typically exploit one or more of the following properties: hexafluorophosphate compounds are soluble in organic solvents,

particularly polar solvents, but have low solubility in aqueous solution. It has a high degree of stability, including resistance to both acidic and basic hydrolysis. Tetrafluoroborate $[BF_4]^-$ is an anion composed by a central boron and four fluorine atoms forming a tetrahedral structure. The utility of this compound arises because its salts are often more soluble in organic solvents than the related nitrate or halide salts. Finally, halide anions are halogen atoms bearing a negative charge. As an example we use chloride Cl^-, bromide Br^-, and iodide I^-.

Porous Materials

We study the combination of ionic liquids with metal-organic frameworks (MOFs) and covalent organic frameworks (COFs). The idea is to improve adsorption and separation capabilities of these porous materials.[58–60] Metal-organic frameworks, or MOFs,[61–63] have emerged as an extensive class of cristalline materials that result from the combination of metallic centers connected by organics linkers. These assemblies generate an organized three dimensional network of channels and cages. Covalent organic frameworks, or COFs, are crystalline porous polymers constructed by linking light elements such as boron, nitrogen, carbon, silicon, oxygen, and hydrogen through strong covalent bonds.[64–67] This forms rigid and highly porous and chemically stable two and three dimensional materials. These

materials are well known by their high surface area, pore volume, remarkable storage capacity, and low density. A high variety of structures can be synthetized connecting metallic centers (MOFs) or light elements with (COFs) organic linkers. The resulting structures exhibit many topologies and properties. The opportunity of designing new MOFs and COFs for specific applications, varying the appropiate constituents, make these compounds desirable for industrial applications. However, the election of the right combination of elements is not trivial. With the aim of explore new possibilities we highlight the advantages of adding low amounts ionic liquids into the pores of these adsorbents (Figure 2).
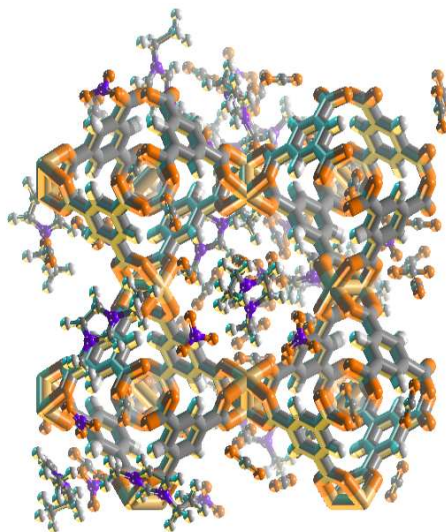
Figure 2. Representative snapshot of the adsorbent (Cu-BTC metal-organic framework) loaded with IL ion pairs for carbon dioxide capture.

Dye-Sensitized Solar Cells

A Dye-sensitized solar cell (DSC) is a photovoltaic cell originally invented by O'Reagan and Grätzel in 1991.[68] This electrochemical device for energy conversion is based on a mesoporous metal oxide film (tipically TiO_2) sensitized with an organic dye and embedded by a liquid electrolyte.[69] On the one hand, the TiO_2 semiconductor is a highly porous structure with a very large surface area. The organic dye (also called molecular sensitizer) absorbs in the visible part of the electromagnetic spectrum. On the other hand, the liquid electrolyte is composed by a organic solvent that dissolves a redox mediator, tipically the iodide/triiodide couple. The mechanism of a DSC is the following (see Figure 3):

1. The photosensitive dye is excited by the absorption of an incident photon. This results in the oxidation of the dye.

2. The excited electron is injected to the conduction band of the TiO_2 semiconductor.

3. The semiconductor transports the electron from the electrode to the external contact.

4. To close the circuit, the oxidized dye accepts an electron from the redox mediator, thus allowing its regeneration. This results in the oxidation of the redox mediator.

5. The oxidized redox mediator diffuses towards the counter electrode to be reduced thanks to the elctrochemical reduction reaction:

$$I_3^- + 2e^- = 3I^- \qquad (1.1)$$
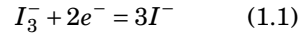
In DSCs, unlike conventional solar cells, light absorption and charge separation occurs in separate molecular layers. The semiconductor is used solely for the charge transport, while the photoelectron is provided by the photosensitive dye. The charge separation takes places at the surface between the dye, semiconductor, and the electrolyte. The electrolyte is one of the most crucial components in DSCs, it is responsible for the ionic charge carrier transport between electrodes and continuously regenerates the dye and itself during DSC operation. The electrolyte has great influence on the conversion efficiency and long-term stability of the devices. This efficiency/stability strongly depends on the nature of the electrolyte components. Due to their unique features, ionic liquids-based electrolytes has been proposed as excellent candidates for this kind of solar cells. The main advantage of the use of ILs is their extremely high stability due to their low vapour pressure, thus reducing the evaporation losses. In contrast to this, the drawback of these compounds is their high viscosity, that hinders the motion of the ions. This results in a slower regeneration of the dye and a decrease of the efficiency of the device. We study the ionic

transport in ILs-based electrolytes with the aim of examine a balance between efficiency and stability of DSCs.[**?**]
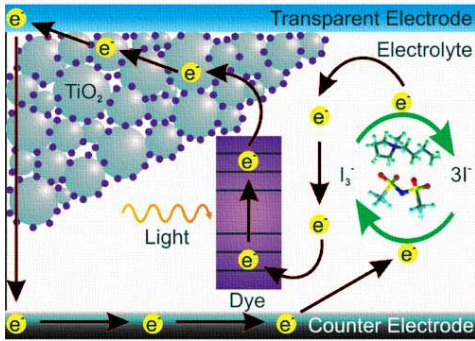
Figure 3. Schematic representation of the mechanism of a DSC.

Ion Batteries

One of the most common and useful devices used to store energy are rechargeable batteries.[70] These are collective arrangements of electrical cells that store and produce electricity by chemical reactions. Among them, metal-ion batteries [71] are the most used in home electronic gadgets (commonly Li-ion batteries). An ion battery consists of three main components, a positive and a negative electrode separated by an electrolyte, normally embedded in another material. The negative electrode (anode) is normally an electron donor group and the positive electrode (cathode) is an electron acceptor. The anode is electrochemically oxidized and releases an electrons. This electron moves through the outer circuit to the cathode which accepts the electrons.[72] In Li-ion

batteries, lithium ions are dissolved in a liquid electrolyte, this allows the movement of ions from one electrode to the other during the charge and discharge process (Figure 4). The nature of the liquid electrolyte limits the efficiency, stability, and consequently the duration of the battery.

ILs has been widely studied as electrolytes for ion batteries for the same reasons that for DSCs. In these batteries, the electrolyte consists in a IL solvent with a low amount of a salt dissolved in it. Here, we analyze the dynamical properties as well as the microscopic organization of ILs-based electrolytes for ion batteries.
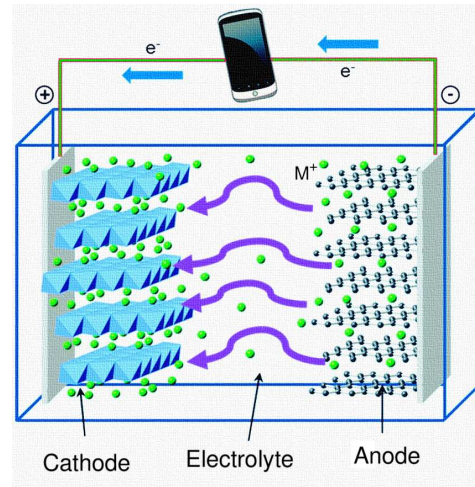
Figure 4. Schematic representation of a M^+-ion battery and the processes taking place during discharge.

Surfactants

Surfactants are compounds which reduce the surface tension between two

liquids.[73] They are used as detergents, wetting agents, emulsifiers, foaming agents, dispersants, among other applications. Surfactants are usually amphiphilic organic compounds containing hydrophobic groups (tails) and hydrophilic groups (heads). Due to this composition, when they are mixed with water, they form aggregates, such as micelles (Figure 5). Here, the hydrophobic tails gather together in the middle of a sphere and the hydrophilic heads are in contact with the surrounding water. This arrangement depends on the concentration and nature of surfactant, giving rise to different aggregates, such as spherical or cylindrical micelles, bilayers, etc. In this context, ionic liquids as 1-alkyl-3-methylimidazolium based ILs with long alkyl chains have been proposed as an alternative to traditional ionic surfactants,[74–78] due to their ability to self-aggregate in presence of water. We study the microscopic behavior of ionic liquids in water media and their effect in the microscopic structure of water.
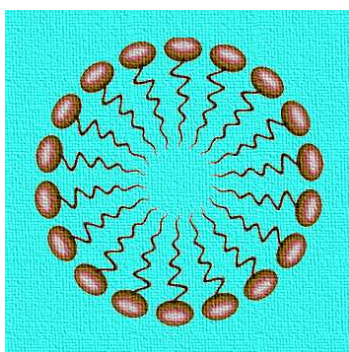
Figure 5. Schematic representation of a 2D-spherical micelle.

METHODS AND MODELS

Molecular simulation is an extense field. In this section we summarize the most important concepts involved in the simulations performed in this work. Specific details are given in each chapter of the thesis.

Molecular Simulations

Molecular simulation is nowadays an important tool to study microscopic and macroscopic processes.[79, 80] Computer simulations can predict thermodynamic properties and complement experimental methods, very often providing great advantages over them. They offer a microscopic point of view of the system, which is difficult, if not impossible, to obtain experimentally. At the same time, molecular simulation gives the possibility to create hypothetical scenarios and to test theories and the suitability of molecular models.

To connect molecular simulation with real systems it is crucial to compare the microscopic properties of individual atoms and molecules to the macroscopic properties of materials. These properties such as temperature, pressure, energies, amount of adsorbed compounds, conductivity, etc. can be measured experimentally. The relation between the microscopic and macroscopic view of the system can be accomplished using Statistical Mechanics.[81–83] Statistical Mechanics is a branch of physics that applies probability theory to

the study of the thermodynamic behavior of systems composed of a large number of particles.

Considering an isolated system in thermodynamic equilibrium, each accesible microscopic state or microstate of the system, corresponding to the same total energy can be found with equal probability. The density probability function is then

$$\aleph(\Gamma) = \delta(H(\Gamma) - E) \qquad (1.2)$$

where H is the Hamiltonian function, corresponding to the total energy of the system. Γ denotes the phase space ($3N$ spatial coordinates and $3N$ velocity or linear momentum coordinates, where N is the total number of particles in the system), and $\delta(x)$ is the Dirac delta function.

In order to calculate a macroscopic property of a non isolated system, it is necessary to average the value of this property over all the possible microstates. The probability function of a non isolated system with a fixed number of particles N in a given volume V at a temperature T, is proportional to the Boltzmann factor: $e^{-\beta H(\Gamma)}$, where $\beta = 1/(k_B T)$, with k_B the Boltzmann constant. Knowing this probability function, the thermodynamic average is

$$\langle A \rangle = \frac{\int e^{-\beta H(\Gamma)} A(\Gamma) d\Gamma}{\int e^{-\beta H(\Gamma)} d\Gamma} \qquad (1.3)$$

The denominator of this equation is the partition function defined as Z

$$Z = \int e^{-\beta H(\Gamma)} d\Gamma \qquad (1.4)$$

The ratio $e^{\beta H(\Gamma)}/Z$ is the probability density of finding the system in a configuration around Γ. Usually, the partition function cannot be computed. Instead, we can compute averages corresponding to a certain *statistical ensemble*.[81] This concept refers to a collection of systems that share common macroscopic properties. Averages performed over an ensemble yield the thermodynamic quantities of a system as well as other equilibrium and dynamic properties.

In the following lines a basic summary of the statistical ensembles from a molecular simulation point of view is given.[79, 84] Among a variety of ensembles, we focus on these employed in this thesis, i.e. canonical, isobaric-isothermal, and grand-canonical ensembles.[81]

Canonical ensemble (NVT)

In the canonical ensemble, the number of particles N, the temperature T, and the volume V are constant. This is a closed system which can exchange heat but not particles with the surroundings. As a consequence, the equilibrium temperature T defines the state of the system.

The partition function of the canonical ensemble is Eq. (1.4). This can be reduced by integrating the velocity coordinates.[79,

84] The result is

$$Z_{NVT} = \frac{1}{\Lambda^{3N} N!} \int e^{-\beta U(\vec{r}^N)} d\vec{r}^N \quad (1.5)$$

where $\Lambda = \sqrt{h^2/2\pi m k_B T}$ is the thermal de Broglie wavelength and $U(\vec{r}^N)$ is the total potential energy of the system. The probability of finding the system in configuration $\vec{r}^N$ is

$$\aleph_{NVT}(\vec{r}^N) \propto e^{-\beta U(\vec{r}^N)} \quad (1.6)$$

where $\vec{r}^N$ represents 3N-dimensional vector containing the positions of the N particles of the system.

The average of the variable $A(\vec{r}^N)$ in the NVT ensemble is given by

$$\langle A(\vec{r}^N) \rangle = \frac{\int A(\vec{r}^N) e^{-\beta U(\vec{r}^N)} d\vec{r}^N}{\int e^{-\beta U(\vec{r}^N)} d\vec{r}^N} \quad (1.7)$$

Isobaric-isothermal ensemble (NPT)

The NPT ensemble represents a closed system with fixed pressure, temperature, and number of particles. The volume can be considered a dynamic variable that changes during the simulation. To allow volume change, the coordinates are rescaled with the box dimensions as[79, 84]:

$$\vec{r}_i = L\vec{s}_i \quad \text{for} \quad i = 1, 2, ...N \quad (1.8)$$

where L is the length of a cubic box (for simplicity), $L = V^{1/3}$. The partition function of this ensemble is given by

$$Z_{NPT} = \frac{\beta P}{\Lambda^{3N} N!} \int V^N e^{-\beta PV} \times$$
$$\times \left(\int e^{-\beta U(\vec{s}^N)} d\vec{s}^N \right) dV \quad (1.9)$$

and the corresponding average of the variable $A(\vec{s}^N)$ is

$$\langle A(\vec{s}^N) \rangle = \frac{1}{Z_{NPT}} \int_0^\infty e^{-\beta PV} V^N$$
$$\left(\int_0^1 A(\vec{s}^N) e^{-\beta U(\vec{s}^N)} d\vec{s}^N \right) dV \quad (1.10)$$

The probability density of finding the system in a particular configuration of scaled coordinates $\vec{s}^N$ at a given volume V is given by

$$\aleph_{NPT}(V; \vec{s}^N) \propto V^N e^{-\beta PV} e^{-\beta U(\vec{s}^N)} \quad (1.11)$$

Grand-Canonical ensemble ($\mu V T$)

To study adsorption processes, one can perform simulations in the grand-canonical ensemble. In this ensemble, temperature T, volume V, and chemical potential μ are fixed. The Grand-canonical ensemble represents an open system that can exchange both heat and mass with the surroundings. Consecuently the equilibrium temperature and the chemical potential should be specified to define the state of the system.

The partition function of this ensemble is given by [79, 84]

$$Z_{\mu VT} = \sum_{N=0}^{\infty} \frac{e^{\beta\mu N}V^N}{\Lambda^{3N}N!} \int e^{-\beta U(\vec{s}^N)}d\vec{s}^N$$

$$(1.12)$$

with a density probability given by

$$\aleph_{\mu VT}(N;\vec{s}^N) \propto \frac{e^{\beta\mu N}V^N}{\Lambda^{3N}N!}e^{-\beta U(\vec{s}^N)} \quad (1.13)$$

Monte Carlo Method

Monte Carlo (MC) is a numerical stochastic method which uses random numbers and probability theory to solve problems having a probabilistic interpretation.[85] In particular, we use this method to get an approximate value of the thermodynamic properties of a system. For example, to measure a property in the canonical ensemble, one needs to calculate its average value given by Eq. (1.7). The main problem arises when the number of microstates is too large to be computed. This can be solved by generating configurations with a probability proportional to the Boltzmann weigth $\left(e^{-\beta U(\vec{r}^N)}\right)$. For this purpose, we use the Markov Chain Monte Carlo (MCMC) method based in the Metropolis algorithm.[86] This algorithm generates random trial moves from the current microscopic state (o) to a new state (n). The acceptation or rejection of the new state depends on the energy difference and the additional generation of a random number. If $P_B(o)$ and $P_B(n)$ denote the probability of finding the system in the microscopic state (o) and (n), respectively, and $\alpha(o \rightarrow n)$ denotes the conditional probability to per-

form a trial move from $o \rightarrow n$, the application of the detailed balance [79] condition gives the following relation

$$P_B(o)\alpha(o \rightarrow n)P_{acc}(o \rightarrow n) =$$
$$= P_B(n)\alpha(n \rightarrow o)P_{acc}(n \rightarrow o)$$

$$(1.14)$$

where P_{acc} is the acceptance probability. Metropolis *et al.* assumed that

$$\alpha(o \rightarrow n) = \alpha(n \rightarrow o) \qquad (1.15)$$

and fixed the acceptance probability using

$$P_{acc}(o \rightarrow n) = min\left(1, \frac{P_B(n)}{P_B(0)}\right) \qquad (1.16)$$

Configurational-bias Monte Carlo (CBMC)

Usually it is neccesary to improve the statistics of the MC sampling.[87] The typical case is the simulation of long chain molecules, where a molecule is grown segment by segment. In this case the CBMC technique can be applied. For each segment a set of k trial orientations is generated according to the internal energy. Then, the external energy of each trial position j of segment i is computed. The probability is

$$P_i(j) = \frac{e^{-\beta U_i^{ext}(j)}}{\sum_{i=1}^{k} e^{-\beta U_i^{ext}(j)}} = \frac{e^{-\beta U_i^{ext}(j)}}{w_i} \quad (1.17)$$

The selected trial orientation is added to the chain and the procedure is repeated until the entire molecule is grown. For this

newly grown molecule the so-called Rosembluth factor [88] is computed by

$$W^{new} = \prod_i w_i \qquad (1.18)$$

To compute the Rosembluth factor W^{old} of an already existing chain, $k-1$ trial orientations are generated for each segment. These orientations, together with the already existing bond, form the set of k trial orientations. Every new configuration is accepted or rejected using an acceptance/rejection rule. There are two ways to satisfy detailed balance:

• The system is coupled to a heat bath and an infinite reservoir considered as an infinite ideal gas with which it can exchange particles. Every time a transfer attempt to and from the reservoir, the Rosembluth factor W^{IG} (Rosembluth weight of the reference state of the ideal gas) is evaluated. Because the particle reservoir is an ideal gas, only intramolecular interactions are acting in the system.

• Detailed balance is also obeyed when W^{IG} is replaced by $\langle W^{IG} \rangle$, the average Rosembluth weight of a chain in the reservoir. This implies that $\langle W^{IG} \rangle$ has to be computed only once for a given molecule and temperature.

MONTE CARLO MOVES FOR THE CBMC SCHEME

The following types of molecular moves or actions can be ejecuted in a MC simulation.[84]

• Displacement move

The selected molecule is given a random displacement. The maximum displacement is set in such a way that a reasonable amount of moves are accepted (tipically around 50 %). The acceptance rule is

$$acc(o \rightarrow n) =$$
$$= min\left(1, e^{-\beta(U^{new} - U^{old})}\right) \qquad (1.19)$$

• Rotation move

The selected molecule is given a random rotation around the center of mass. The maximum rotation angle is set in such a way that the acceptance probability is 50 % of the moves. The acceptance rule is also given by Eq. (1.19) with the *new* and *old* energies determined by the rotation of the molecule.

• Regrow move

The selected molecule is totally or partially regrown at a random position. The acceptance rule is given by

$$acc(o \rightarrow n) = min\left(1, \frac{W^{new}}{W^{old}}\right) \qquad (1.20)$$

• Identity change move

A molecule of one of the components is selected randomly and a change of its identity is attempted

$$acc(A \rightarrow B) =$$
$$= min\left(1, \frac{W^{new} f_B \langle W_A^{IG} \rangle N_A}{W^{old} f_B \langle W_B^{IG} \rangle (N_B + 1)}\right) \quad (1.21)$$

where f_i are the fugacities and N_i the number of particles.

- Insertion move

A molecule is inserted at a random position with the acceptance rule

$$acc(N \rightarrow N + 1) =$$
$$= min\left(1, \frac{W^{new} \beta V}{N + 1} \frac{f}{\langle W^{IG} \rangle}\right) \quad (1.22)$$

where W^{new} and W^{IG} are the Rosembluth factors of the new state and the reference state of the ideal gas.

- Deletion move

The selected molecule is deleted.

$$acc(N \rightarrow N - 1) =$$
$$= min\left(1, \frac{N}{W^{old} \beta V} \frac{\langle W^{IG} \rangle}{f}\right) \quad (1.23)$$

where W^{old} and W^{IG} are the Rosembluth factors of the new state and the reference state of the ideal gas.

Molecular Dynamics Method

The idea behind Molecular dynamics simulations (MD) is to generate a representative trajectory of the system over time.[89] To do so, the forces between the atoms and how the system evolves in time is calculated using Newton's equations of motion. At each time step, the forces on the atoms are calculated and combined with their current positions and velocities to create new positions and velocities. The atoms are moved to their new positions, the forces updated and a new cycle begins. These dynamically generated states are averaged in time to determine the system properties. The Verlet algorithm is the most widely used method for integrating the equations of motion.[79] This is implemented according to the following equations:

$$\vec{r}(t + \Delta t) = \vec{r}(t) + \vec{v}(t)\Delta t + \frac{\vec{f}(t)}{2m}\Delta t^2 \quad (1.24)$$

$$\vec{v}(t + \Delta t) = \vec{v}(t) + \frac{\vec{f}(t) + \vec{f}(t + \Delta t)}{2m}\Delta t \quad (1.25)$$

where $\vec{r}(t)$ y $\vec{v}(t)$ are the positions and velocity vectors, respectively, $\vec{f}(t)$ is the force acting at time t, m is the mass of the particles, and Δt is the time step of the MD simulation.

An unphysical drift in the energy of the system could appear after long integration time since the equations of motion are numerically integrated. To test this energy drift ΔE of the numerical integration

algorithm for a given time step after M integration steps, the following condition is applied:

$$\Delta E(\Delta t) = \frac{1}{M} \sum_{i=1}^{M} \left| \frac{E(0) - E(i\Delta t)}{E(0)} \right| < 10^{-3}$$
$$(1.26)$$

After equilibration, one measures the average values of properties from the trajectories of the particles. The ergodic hypothesys states that ensemble averages can be obtained from time averages. This indicates that one can follow the time evolution of the systems instead of sampling the phase space by generating microstates with a given probability. According to this, the time average value of a property can be obtained by the following expression

$$\langle A \rangle = \lim_{t \to \infty} \frac{1}{t} \int A(\vec{r}^N, t) dt \qquad (1.27)$$

which should equal the thermodynamic average of the Eq. (1.3) if the system is *ergodic*.[79]

Simulation Box and Boundary Conditions

During a simulation, the position and velocity coordinates of all the particles are stored in the memory of the computer. For this reason, computer simulations are limited to a certain number of particles. Currently, simulations of thousands of atoms have been reported. However, this number is still far from the thermodynamic limit. To obtain values, from a molecular simulation that extrapolate for a macroscopic

finite system and to overcome problems of surface effects, one employs *periodic boundary conditions*.[84] With this, the simulation box is replicated though the space in every direction creating images of each particle of the system at equivalent positions. The distances computed between two particles correspond with the minimum distances of their periodic images (Figure 6).

Usually the unit cell of a system is defined by the cell lengths a, b, and c and cell angles α, β, and γ. The cell lenght a is aligned with the $x-axis$ and b in the $xy-plane$. It is common to work with fractional coordinates of the atoms within the unit cell. These coordinates, which form an orthonormal dimensionless space, are related with the cartesian coordinates through the transformation matrix:

$$\begin{pmatrix} a & b\cos(\gamma) & c\cos(\beta) \\ 0 & b\sin(\gamma) & c\chi \\ 0 & 0 & c\sqrt{1-\cos^{(}\beta)-\chi^2} \end{pmatrix}$$
$$(1.28)$$

with

$$\chi = \frac{\cos(\alpha - \cos(\gamma)\cos(\beta))}{\sin(\gamma)} \qquad (1.29)$$

This matrix is also used to create the images corresponding to the periodic boundary conditions.[84]
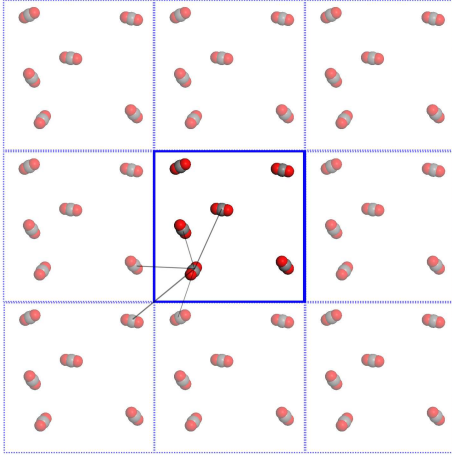
Figure 6. Schematic representation of the periodic boundary conditions.

Molecular Interactions

In order to describe the interactions of the systems it is necessary the use of force fields.[90–95] These are sets of equations that define specific interactions with energy dimensions. They can be parameterized in a variety of analytical forms to give the correct energies and consecuently the forces of a given process.

The total potential energy of the system can be divided in two parts, corresponding to intramolecular (bonded) and intermolecular (non-bonded) interactions

$$U^{Total} = U^{Bonded} + U^{Non-Bonded} \quad (1.30)$$

Intramolecular Interactions

The contributions to the energy for intramolecular interactions are given by the following terms (Figure 7):

$$U^{Bonded} = U^{Bond} + U^{Bend} + U^{Torsion} \quad (1.31)$$

where:

• U^{Bond} corresponds to bond stretching that describes the change of energy when a bond between atoms is enlarged or reduced in length. This interaction is usually defined by a harmonic potential given by the following equation:

$$U^{Bond}(r_{ij}) = \frac{1}{2} k_{ij} \left(r_{ij} - r_{ij}^0 \right)^2 \quad (1.32)$$

where k_{ij} is the bond constant, and r_{ij} and r_{ij}^0 represent the distance and the equilibrium distance between the atoms, respectively. Note that one can also define fixed bonds, with fixed distances.

• U^{Bend} describes in a similar manner the bending interaction. This interaction is also defined by a harmonic potential given by

$$U^{Bend}(\theta_{ijk}) = \frac{1}{2} k_{ijk} \left(\theta_{ijk} - \theta_{ijk}^0 \right)^2 \quad (1.33)$$

where k_{ijk} is the bend constant for the atoms ijk that form the angle θ_{ijk}, and θ_{ikj}^0 is the equilibrium angle. A similiar explanation than for bonds can be done here. It is also possible to give the angle a

fixed value.

• $U^{Torsion}$. In a chain of atoms $ijkl$ the dihedral angle is defined as the angle between the plane containing the first three atoms (ijk) and the plane containing the last three atoms (jkl) of the chain. This interaction is described by different dihedral potentials depending on the origin of the force field. An example of torsion potential is:

$$U^{Torsion}(\phi_{ijkl}) = k_{ijkl}\left[1 + cos\left(n\phi_{ijkl} - \delta\right)\right]$$
(1.34)

where k_{ijkl} is the torsion barrier, n is the number of minima occuring in the function (periodicity), ϕ_{ijkl} is the torsion angle formed by the atoms $ijkl$ and δ is a phase factor.
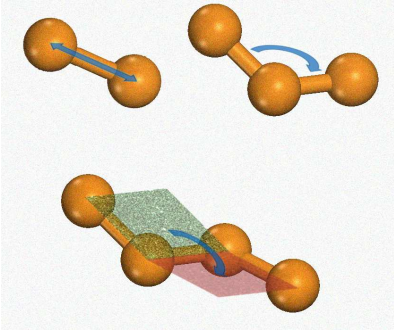
Figure 7. Schematic representation of the interatomic relations that establish the intramolecular interactions.

Intermolecular Interactions

Intermolecular interactions correspond to these interactions that are not due to chemical bonds. In this thesis, we consider of two types, van der Waals forces and electrostatics interactions.

$$U^{Non-Bonded} = U^{vdW} + U^{elec}$$
(1.35)

• van der Waals interactions are due to the fluctuating densities of electrons surrounding atoms. When two atoms approach each other, the fluctuations become correlated. This correlation causes them to be attracted. This interaction is referred to London dispersion or van der Waals dispersion and is very often modeled by the popular Lennard-Jones potential [96] (Figure 8).

$$U^{vdW}(r_{ij}) = 4\varepsilon_{ij}\left[\left(\frac{\sigma_{ij}}{r_{ij}}\right)^{12} - \left(\frac{\sigma_{ij}}{r_{ij}}\right)^{6}\right]$$
(1.36)

where the parameter σ_{ij} represents the distance between atoms at which attraction and repulsion are balanced. The parameter ε_{ij} corresponds to the depth of the minimum energy and r_{ij} is the distance between particles i and j. The interaction between like atoms, ε_{ii} and σ_{ii} are fixed using an effective potential, and the cross-terms are estimated by the Lorentz-Berthelot mixing rules,[97] calculated by an arithmetic and geometry means, respectively.

$$\sigma_{ij} = \frac{\sigma_{ii} + \sigma_{jj}}{2}$$
(1.37)

$$\varepsilon_{ij} = \sqrt{\varepsilon_{ii}\varepsilon_{jj}}$$
(1.38)
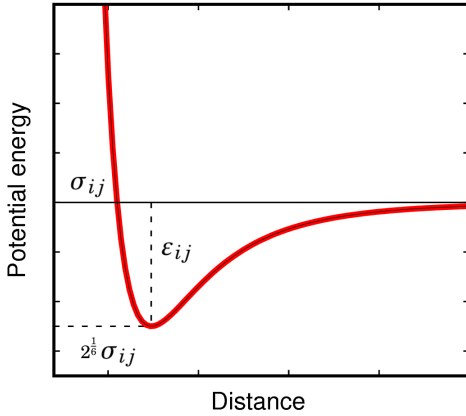
Figure 8. Graphical representation of the functional form of the Lennard-Jones potential.

• The electrostatics interactions are described by the classical Coulombic potential.

$$U^{elec}(r_{ij}) = \frac{1}{4\pi\varepsilon_0\varepsilon_r}\frac{q_i q_j}{r_i r_j} \qquad (1.39)$$

where ε_r is the electric constant of the medium where the charges are placed, ε_0 is the permittivity in the vacuum, q_i and q_j are the charges of the interacting atoms and r_{ij} the distance between the atoms i and j.

Coulombic forces are very long-ranged forces and special methods are required to calculate then in finite boxes combined with periodic boundary conditions. In this thesis we compute the electrostatic forces making use of the well-known Ewald sums method.[98, 99]

Molecular Properties

There are many thermodynamic, structural and dynamical properties, that can be obtained by Monte Carlo or Molecular dynamics simulation. We focus on the properties calculated in the context of this thesis.

Adsorption Properties

Adsorption isotherms can be obtained by Monte Carlo simulations in the grand-canonical ensemble (GCMC).[79] Molecules can be added or removed from the system. These molecules are exchanged with a reservoir at the same temperature and chemical potential. It is possible to compute the average number of adsorbed molecules as the number of molecules fluctuates during the simulation.

In the simulations the pressure p is fixed and related with the fugacity f as:

$$f = \phi p \qquad (1.40)$$

where ϕ is the fugacity coefficient obtained from the equation of state of the vapor in the reservoir. Besides, the chemical potential is computed using the fugacity

$$\mu(T,p) = \mu^0 + RT ln f \qquad (1.41)$$

where μ^0 is the reference chemical potential and R the ideal gas constant.

Adsorption Selectivities

To get an idea of the separation of a mixture of two components, adsorption selectivities can be computed from the molar fractions:

$$S_{ads} = \frac{x_A/y_A}{x_B/y_B} \qquad (1.42)$$

where x_i is the molar fraction in the adsorbed phase (loading) for the i component and y_i the molar fraction in the bulk phase. We focus on equimolar mixtures, so $y_i = 0.5$ and the adsorption selectivity will be $S = x_A/x_B$.

Thermodynamic Potentials (Energies) and Entropy of Adsorption

1) Internal energy (ΔU). The internal energy of a system involved in adsorption process is given by

$$\Delta U = \langle U_{hg} \rangle - \langle U_h \rangle - \langle U_g \rangle \qquad (1.43)$$

where $\langle U_{hg} \rangle$ is the average potential energy of the host-guest system, $\langle U_h \rangle$ is the average host energy, and $\langle U_g \rangle$ the energy of the isolated chain molecule in the ideal gas.

2) Enthalpy of adsorption (ΔH). The enthalpy of adsorption or isosteric heat of adsorption is obtained from a Monte Carlo simulation in the NVT ensemble using the energies of the system.[100]

$$\Delta H = -Q_{st}^0 = \Delta U - RT \qquad (1.44)$$

where R is the gas constant and T the temperature.

3) Helmholtz free energy (ΔF). The Helmholtz free energy gives an idea of the work exchange in a process. This energy can be computed using MC simulations via,

$$\Delta F = -RT ln(W_{hg} - W_g) \qquad (1.45)$$

where W_i is the calculated Rosembluth factor of host-guest and guest, respectively.

4) Gibbs free energy (ΔG). The Gibbs free energy is the minimun energy at constant temperature and pressure of a sytem which is in chemical equilibrium. This can be calculated from the Helmholtz free energy:

$$\Delta G = \Delta F - RT \qquad (1.46)$$

5) Entropy of adsorption (ΔS). The entropy of adsorption is the entropy change caused by the adsorption of guest molecules. It can be computed from the energies of adsorption:

$$\Delta S = \frac{\Delta U - \Delta F}{T} = \frac{\Delta H - \Delta G}{T} \qquad (1.47)$$

Density

The equilibrium density of a liquid or gas system is calculated averaging the volume fluctuations of a simulation in the isobaric-isothermal ensemble (NPT), once the vol-

ume and the energy of the system are fluctuating around a mean value over time.

Structural Properties

The key magnitude computed to analyze the structural properties of a system is the radial distribution function (RDF or $g(r)$). RDF from a statistical point of view is the normalized probability of finding particles at a certain distance between distances r and $r + dr$ from other reference particle.[79, 101]

The RDF of particles of types A and B is computed via:

$$g_{AB}(r) = \frac{1}{\langle \rho_b \rangle} \frac{1}{N_A} \sum_{i=1}^{N_A} \sum_{j=1}^{N_B} \frac{\delta(r_{ij} - r)}{4\pi r^2} \quad (1.48)$$

where $\langle \rho_b \rangle$ is the B type averaged particle density and N_A is the number of particles of type A.

Dynamical Properties

The computed dynamical properties are the diffusion coefficients and the ionic conductivity.

1) <u>Diffusion coefficients</u>. (D_s) Diffusion coefficients or self-diffusion coefficients gives an idea about the net movement of atoms or molecules from a reference state. The diffusion coefficient in a three dimensional system can be extracted from the slope of the mean squared displacement (MSD) in the diffusive regime (see Figure 9) using the Einstein equation:

$$D_s = \lim_{t \leftarrow \infty} \frac{\langle \sum_i^n ||r(t) - r(0)||^2 \rangle}{6t} \quad (1.49)$$

The MSD versus time of liquid systems exhibits different regimes depending on the time scale of the simulation. At very short times scales, the system is in the ballistic regime where the MSD is proportional to t^2. Afterwards, the regime is controlled by the collisions between particles until they finally reach the diffusive regime, in which the MSD scales linearly with time. In the diffusive regime, the MSD gives an idea of the translational mobility of the individual species of the systems, allowing to calculate the self-diffusion coefficient.

2) <u>Ionic conductivity</u>. (σ) Ionic conductivity is an important property which measures the ability of an electrolyte to conduct electricity. It is a macroscopic property that can be estimated from microscopic properties. The ionic conductivity is computed as the sum of the partial ionic conductivities of the individual species of the system using the Nernst-Einstein equation[102]:

$$\sigma_i = D_{s_i} \frac{N_i}{V} \frac{(q_i e)^2}{k_B T} \quad (1.50)$$

where D_{s_i} is the self-diffusion coefficient of the particle i, N_i is the number of charge carrier, V is the volume of the simulation box, $q_i e$ is the net charge of the ion, and k_B is the Boltzmann constant. For this calculation, two different simulations are

needed. One in the NPT ensemble to establish the system in an equilibrated volume V and other in the NVT ensemble to obtain the diffusion coefficients.
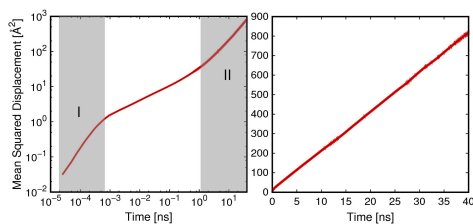
Figure 9. Example of mean squared displacement of a liquid system. Log-log scale (left) and linear scale (right). Regions highlighted correspond to the ballistic (I) and diffusive (II) regime, respectively.

OUTLINE OF THE THESIS

In this thesis we have investigated by molecular simulation the behavior of ionic liquid-based materials for energy applications. From an energetic and environmental point of view ionic liquids are attractive materials due to their unique features. This thesis is divided into three blocks covering the use of ionic liquids combined with porous materials, as electrolytes for solar cells and batteries, and mixed with water to study its colloidal behavior.

• **Ionic liquids embedded into porous materials for carbon dioxide storage and separation. (Chapters 2, 3, and 4)**

In chapter 2 we study the effect exerted by ILs loaded within the pores of the Cu-BTC MOF in gas adsorption. We used ILs composed by 1-ethyl-3-methylimidazolium cations and six anions. We investigate the effect of using different anions and different amount of loaded ILs in the adsorption of carbon dioxide, methane, and nitrogen, as well as their mixtures. We computed adsorption energies, isotherms, and selectivities. We also study the distribution of guest molecules in the hybrid structures and the location of ILs inside the pores of Cu-BTC.

Based on the results obtained in chapter 3 we add ILs to four bi- and tri-dimensional COFs to improve their behavior in the adsorption and separation of carbon dioxide and methane. Additionally we compared the effect exerted by ILs and water in the gas adsoprtion using COFs. To this aim, we introduced in each structure different amounts of ILs and water and computed the adsorption properties in hydrated and bare COFs.

In chapter 4 we investigate the MOF/IL composites for gas adsorption and separation using four MOFs with different topologies. We study the separation of carbon dioxide from methane or nitrogen and additionally the separation of the components of a mixture containing nitrogen and methane. We also study the diffusion of guest molecules in these hybrid materials.

- **Ionic liquids-based electrolytes for dye sensitized solar cells and metal-ion batteries. (Chapters 5, 6, and 7)**

In chapter 5 we study the ionic transport of IL-based electrolytes for DSCs. We compared two ILs composed by imidazolium and pyrrolidinium cations and bis-trifluoromethane-sulfonylimide anion. Firstly, we fit the force field parameters to reproduce experimental density and diffusion of pure ILs. We validated the results by increasing the hydrocarbon tail of the cations. Once the models are developed, we analyzed the transport of redox mediators in electrolytes composed by a mixture of ILs and a common solvent, such as acetonitrile. To do this, we vary the composition of the electrolyte as well as the working temperature of the systems.

Using the validated models of the previous work, in chapter 6 we studied the use of pyrrolidinium-based ILs as electrolites for sodium- and lithium-ion batteries. We investigated the decrease in the conductivity with the addition of a salt to the electrolyte. For this, we monitored the structural changes at microscopic level and their consecuences in the mobility of the constituents.

Once we set the relation between structure and transport properties of IL-based electrolytes for metal-ion batteries, in

chapter 7 we study in deep the interaction of metallic cations with the anionic constituent of ILs. We compared the use of monovalent (Na, and Li), divalent (Ni, Zn, Co, and Cd), and trivalent (Al) metallic cations. These metals has different charge, but also different size. We analyze the effect of these magnitudes in the local structure of aggregates formed by the metallic cations and the surrounding anions. Looking for connections between the microscopic behavior of the aggregates with the microscopic and macroscopic charge transport of the electrolyte.

- **Water solutions of ionic liquids. (Chapters 8, and 9)**

In chapter 8 we investigate the effect of ILs on the hydrogen-bond network of water in dilute aqueous solutions of ionic liquids with various combinations of cations and anions. On the one hand, we use 1-alkyl-3-methylimidazolium cations increasing the hydrocarbon chain length combined with six anions. On the other hand, we varied the concentration of IL in the water-IL mixtures. The structure of water and the water-ionic liquid interactions involved in the formation of a heterogeneous network are analyzed by using radial distribution functions and hydrogen-bond statistics.

In chapter 9 we study IL/water systems varying the concentration of ILs but keeping water as the majority com-

ponent. We computed structural properties, i. e., radial distribution functions (RDF) and transport parameters such as diffusion coefficients and conductivities as a function of the IL/water mole fraction. We analyzed the structural phase transitions such as micelle formation, of systems with increasing IL concentration and alkyl chain length of imidazolium cations and discussed the behavior of homogeneous and heterogeneous IL/water mixtures.

Bibliography

[1] Fawcett, W. *Liquids, Solutions, and Interfaces: From Classical Macroscopic Descriptions to Modern Microscopic Details*; Topics in Analytical Chemistry; Oxford University Press, USA, 2004.

[2] Murrell, J.; Jenkins, A. *Properties of Liquids and Solutions, 2nd Edition*; Wiley, 1994.

[3] Welton, T. *Chem. Rev.* **1999**, *99*, 2071–2083.

[4] Welton, T. *Coord. Chem. Rev.* **2004**, *248*, 2459.

[5] Wasserscheid, P.; Welton, T. *Ionic liquids in Synthesis*; 2008; Vol. 1.

[6] Hallett, J. P.; Welton, T. *Chem. Rev.* **2011**, *111*, 3508–3576.

[7] Mun, J.; Sim, H. *Handbook of Ionic Liquids: Properties, applications, and hazards*; Nova Science Publishers, 2012.

[8] Plechkova, N. V.; Seddon, K. R. *Chem. Soc. Rev.* **2008**, *37*, 123–150.

[9] Seddon, K. R. *J. Chem. Technol. Biotechnol.* **1997**, *68*, 351–356.

[10] Adams, D. J.; Dyson, P. J.; Tavener, S. J. *Chemistry in Alternative Reaction Media*; John Wiley and Sons, Ltd, 2005; pp 75–93.

[11] Kerton, F.; Marriott, R. *Alternative Solvents for Green Chemistry*; Green Chemistry Series; The Royal Society of Chemistry, 2013; pp FP001–350.

[12] Palm, R.; Kurig, H.; Tonurist, K.; Jaenes, A.; Lust, E. *Electrochim. Acta* **2012**, *85*, 139–144.

[13] Palm, R.; Kurig, H.; Tonurist, K.; Jaenes, A.; Lust, E. *Electrochem. commun.* **2012**, *22*, 203–206.

[14] Tonurist, K.; Thomberg, T.; Jaenes, A.; Kink, I.; Lust, E. *Electrochem. commun.* **2012**, *22*, 77–80.

[15] Ju, Y.-J.; Lien, C.-H.; Chang, K.-H.; Hu, C.-C.; Wong, D. S.-H. *J. Chinese Chem. Soc.* **2012**, *59*, 1280–1287.

[16] Fujii, K.; Hamano, H.; Doi, H.; Song, X.; Tsuzuki, S.; Hayamizu, K.; Seki, S.; Kameda, Y.; Dokko, K.; Watan-

abe, M.; Umebayashi, Y. *J. Phys. Chem. C* **2013**, *117*, 19314–19324.

[17] Solano, C. J. F.; Jeremias, S.; Paillard, E.; Beljonne, D.; Lazzaroni, R. *J. Chem. Phys.* **2013**, *139*, 34502.

[18] Haskins, J. B.; Bennett, W. R.; Wu, J. J.; Hernández, D. M.; Borodin, O.; Monk, J. D.; Bauschlicher, C. W.; Lawson, J. W. *J. Phys. Chem. B* **2014**, *118*, 11295–11309.

[19] Kunze, M.; Jeong, S.; Paillard, E.; Schönhoff, M.; Winter, M.; Passerini, S. *Adv. Energy Mater.* **2011**, *1*, 274–281.

[20] Lassègues, J.-C.; Grondin, J.; Talaga, D.; Lassegues, J. C.; Grondin, J.; Talaga, D. *Phys. Chem. Chem. Phys.* **2006**, *8*, 5629–5632.

[21] Castiglione, F.; Ragg, E.; Mele, A.; Appetecchi, G. B.; Montanino, M.; Passerini, S. *J. Phys. Chem. Lett.* **2011**, *2*, 153–157.

[22] Wilken, S.; Xiong, S.; Scheers, J.; Jacobsson, P.; Johansson, P. *J. Power Sources* **2015**, *275*, 935–942.

[23] Diddens, D.; Heuer, A. *J. Phys. Chem. B* **2013**, *c*, 1–20.

[24] Borodin, O.; Smith, G. D.; Henderson, W. *J. Phys. Chem. B* **2006**, *110*, 16879–16886.

[25] Li, Z.; Borodin, O.; Smith, G. D.; Bedrov, D. *J. Phys. Chem. B* **2015**, *119*, 3085–3096.

[26] Li, S.; Banuelos, J. L.; Guo, J.; Anovitz, L.; Rother, G.; Shaw, R. W.; Hillesheim, P. C.; Dai, S.; Baker, G. A.; Cummings, P. T. *J. Phys. Chem. Lett.* **2012**, *3*, 125–130.

[27] Lassègues, J.-C.; Grondin, J.; Aupetit, C.; Johansson, P. *J. Phys. Chem. A* **2009**, *113*, 305–314.

[28] Castiglione, F.; Famulari, A.; Raos, G.; Meille, S. V.; Mele, A.; Appetecchi, G. B.; Passerini, S. *J. Phys. Chem. B* **2014**, *118*, 13679–13688.

[29] Lesch, V.; Li, Z.; Bedrov, D.; Borodin, O.; Heuer, A. *Phys. Chem. Chem. Phys.* **2016**, *18*, 382–392.

[30] Menne, S.; Vogl, T.; Balducci, A. *Phys. Chem. Chem. Phys.* **2014**, *16*, 5485–5489.

[31] Tułodziecki, M.; Tarascon, J.-M.; Taberna, P.; Guery, C. *Electrochimica Acta* **2014**, *134*, 55 – 66.

[32] Endres, F.; Bukowski, M.; Hempelmann, R.; Natter, H. *Angew. Chemie Int. Ed.* **2003**, *42*, 3428–3430.

[33] Endres, F.; MacFarlane, D.; Abbott, A. *Electrodeposition from Ionic Liquids*; 2008.

[34] Azaceta, E.; Chavhan, S.; Rossi, P.; Paderi, M.; Fantini, S.; Ungureanu, M.; Miguel, O.; Grande, H.-J.; Tena-Zaera, R. *Electrochim. Acta* **2012**, *71*, 39–43.

[35] Azaceta, E.; Tena-Zaera, R.; Marcilla, R.; Fantini, S.; Echeberria, J.; Pomposo, J. A.; Grande, H.; Mecerreyes, D. *Electrochem. commun.* **2009**, *11*, 2184–2186.

[36] Tulodziecki, M.; Tarascon, J. M.; Taberna, P. L.; Guery, C. *J. Electrochem. Soc.* **2012**, *159*, D691–D698.

[37] Lair, V.; Sirieix-Plenet, J.; Gaillon, L.; Rizzi, C.; Ringuedé, A. *Electrochim. Acta* **2010**, *56*, 784–789.

[38] Pinilla, C.; Del Popolo, M. G.; Lynden-Bell, R. M.; Kohanoff, J. *J. Phys. Chem. B* **2005**, *109*, 17922–17927.

[39] Pinilla, C.; Del Popolo, M. G.; Kohanoff, J.; Lynden-

Bell, R. M. *J. Phys. Chem. B* **2007**, *111*, 4877–4884.

[40]   Hao, F.; Lin, H. *Rsc Adv.* **2013**, *3*, 23521–23532.

[41]   Yu, Z.; Vlachopoulos, N.; Hagfeldt, A.; Kloo, L. *Rsc Adv.* **2013**, *3*, 1896–1901.

[42]   Lei, Z.; Dai, C.; Chen, B. **2012**,

[43]   Tome, L. C.; Florindo, C.; Freire, C. S. R.; Rebelo, L. P. N.; Marrucho, I. M. *Phys. Chem. Chem. Phys.* **2014**, *16*, 17172–17182.

[44]   Ramdin, M.; de Loos, T. W.; Vlugt, T. J. H. *Ind. Eng. Chem. Res.* **2012**, *51*, 8149–8177.

[45]   Babarao, R.; Dai, S.; Jiang, D.-e. *J. Phys. Chem. B* **2011**, *115*, 9789–9794.

[46]   Ramdin, M.; Chen, Q.; Balaji, S. P.; Manuel Vicent-Luna, J.; Torres-Knoop, A.; Dubbeldam, D.; Calero, S.; de Loos, T. W.; Vlugt, T. J. H. *J. Comput. Sci.* **2016**, *15*, 74–80.

[47]   Ramdin, M.; Balaji, S. P.; Vicent-Luna, J. M.; Gutiérrez-Sevillano, J. J.; Calero, S.; de Loos, T. W.; Vlugt, T. J. H. *J. Phys. Chem. C* **2014**, *118*, 23599–23604.

[48]   Cadena, C.; Anthony, J. L.; Shah, J. K.; Morrow, T. I.; Brennecke, J. F.; Maginn, E. J. *J. Am. Chem. Soc.* **2004**, *126*, 5300–5308.

[49]   Lourenço, T. C.; Coelho, M. F. C.; Ramalho, T. C.; Van Der Spoel, D.; Costa, L. T. *Environ. Sci. Technol.* **2013**, *47*, 7421–7429.

[50]   Chapeaux, A.; Simoni, L. D.; Ronan, T. S.; Stadtherr, M. a.; Brennecke, J. F. *Green Chem.* **2008**, *10*, 1301.

[51]   Neves, C. M. S. S.; Granjo, J. F. O.; Freire, M. G.; Robertson, A.; Oliveira, N. M. C.; Coutinho, J. A. P. *Green Chem.* **2011**, *13*, 1517–1526.

[52]   Rana, S.; Carvalho, T.; Fangueiro, R.; Vidinha, P. *Polym. Adv. Technol.* **2013**, *24*, 191–196.

[53]   Carvalho, T.; Augusto, V.; Bras, A. R.; Lourenco, N. M. T.; Afonso, C. A. M.; Barreiros, S.; Correia, N. T.; Vidinha, P.; Cabrita, E. J.; Dias, C. J.; Dionisio, M.; Roling, B. *J. Phys. Chem. B* **2012**, *116*, 2664–2676.

[54]   Vidinha, P.; Lourenco, N. M. T.; Pinheiro, C.; Bras, A. R.; Carvalho, T.; Santos-Silva, T.; Mukhopadhyay, A.; Romao, M. J.; Parola, J.; Dionisio, M.; Cabral, J. M. S.; Afonso, C. A. M.; Barreiros, S. *Chem. Commun.* **2008**, 5842–5844.

[55]   Liu, Y.; Shi, L.; Wang, M.; Li, Z.; Liu, H.; Li, J. *Green Chem.* **2005**, *7*, 655–658.

[56]   Bica, K.; Rodriguez, H.; Gurau, G.; Andreea Cojocaru, O.; Riisager, A.; Fehrmann, R.; Rogers, R. D. *Chem. Commun.* **2012**, *48*, 5422–5424.

[57]   Trilla, M.; Pleixats, R.; Parella, T.; Blanc, C.; Dieudonne, P.; Guari, Y.; Man, M. W. C. *Langmuir* **2008**, *24*, 259–265.

[58]   Kinik, F. P.; Uzun, A.; Keskin, S. *ChemSusChem* **2017**, *10*, 2842–2863.

[59]   Zhang, S.; Zhang, J.; Zhang, Y.; Deng, Y. *Chem. Rev.* **2017**, *117*, 6755–6833.

[60]   Wang, J.; Luo, J.; Feng, S.; Li, H.; Wan, Y.; Zhang, X. *Green Energy Environ.* **2016**, *1*, 43–61.

[61]   Li, H.; Eddaoudi, M.; O'Keeffe, M.; Yaghi, O. M. *Nature* **1999**, *402*, 276.

[62]   Keskin, S.; Liu, J.; Rankin, R. B.; Johnson, J. K.; Sholl, D. S. *Industrial & Engineering Chemistry Research* **2009**, *48*, 2355–2371.

[63]   Meek, S. T.; Greathouse, J. A.; Allendorf, M. D. *Advanced Materials* **2011**, *23*, 141–141.

[64]   Feng, X.; Ding, X.; Jiang, D. *Chem. Soc. Rev.* **2012**, *41*, 6010–6022.

[65]   Ding, S.-Y.; Wang, W. *Chem. Soc. Rev.* **2013**, *42*, 548–568.

[66]   Jackson, K. T.; Reich, T. E.; El-Kaderi, H. M. *Chem. Commun.* **2012**, *48*, 8823–8825.

[67]   Tilford, R. W.; Mugavero III, S. J.; Pellechia, P. J.; Lavigne, J. J. *Adv. Mater.* **2008**, *20*, 2741–+.

[68]   Oregan, B.; Gratzel, M. *Nature* **1991**, *353*, 737–740.

[69]   Wu, J.; Lan, Z.; Lin, J.; Huang, M.; Huang, Y.; Fan, L.; Luo, G. *Chemical Reviews* **2015**, *115*, 2136–2173.

[70]   Armand, M.; Endres, F.; MacFarlane, D. R.; Ohno, H.; Scrosati, B. *Nat. Mater.* **2009**, *8*, 621–9.

[71]   Whittingham, M. S. *Science (80-.).* **1976**, *192*, 1126.

[72]   Dell, R.; Rand, D.; of Chemistry (Great Britain), R. S. *Understanding Batteries*; RSC paperbacks; Royal Society of Chemistry, 2001.

[73]   Myers, D. *Surfactant science and technology*; John Wiley & Sons, 2005.

[74]   Figueira-González, M.; Francisco, V.; García-Río, L.; Marques, E. F.; Parajó, M.; Rodríguez-Dafonte, P. *J. Phys. Chem. B* **2013**, *117*, 2926–2937.

[75]   Javadian, S.; Ruhi, V.; Heydari, A.; Shahir, A. A.; Yousefi, A.; Akbari, J. *Ind. Eng. Chem. Res.* **2013**, *52*, 4517–4526.

[76]   He, Y.; Shang, Y.; Liu, Z.; Shao, S.; Liu, H.; Hu, Y. *Colloids Surfaces B Biointerfaces* **2013**, *101*, 398–404.

[77]   Liu, Y.; Yang, L.; Guo, R. *Soft Matter* **2013**, *9*, 3671.

[78]   Tourne-Peteilh, C.; Coasne, B.; In, M.; Brevet, D.; Devoisselle, J. M.; Vioux, A.; Viau, L. *Langmuir* **2014**, *30*, 1229–1238.

[79]   Frenkel, D.; Smit, B. *Understanding Molecular Simulations: from Algorithms to Applications*; Academic Press: San Diego, 2002.

[80]   Allen, M.; Tildesley, D. *Computer simulation of liquids*; Oxford science publications; Clarendon Press, 1987.

[81]   Tuckerman, M. *Statistical mechanics: theory and molecular simulation*; Oxford University Press, 2010.

[82]   Chandler, D. *Introduction to Modern Statistical Mechanics*; Oxford university Press: New York, 1987.

[83]   Pathria, R., Ed. *Statistical Mechanics (Second Edition)*, second edition ed.; Butterworth-Heinemann: Oxford, 1996; pp 523 – 529.

[84]   Dubbeldam, D.; Torres-Knoop, A.; Walton, K. S. *Mol. Simul.* **2013**, *39*, 1253–1292.

[85]   Robert, C. P. *Monte carlo methods*; Wiley Online Library, 2004.

[86] Metropolis, N.; Rosenbluth, A. W.; Rosenbluth, M. N.; Teller, A. H.; Teller, E. *The Journal of Chemical Physics* **1953**, *21*, 1087–1092.

[87] Smit, B.; Siepmann, J. I. *The Journal of Physical Chemistry* **1994**, *98*, 8442–8452.

[88] Rosenbluth, M. N.; Rosenbluth, A. W. *The Journal of Chemical Physics* **1955**, *23*, 356–359.

[89] others,, et al. *Computers in Physics* **1996**, *10*, 456–456.

[90] Mayo, S. L.; Olafson, B. D.; Goddard, W. A. *J. Phys. Chem.* **1990**, *94*, 8897–8909.

[91] Rappe, A. K.; Casewit, C. J.; Colwell, K. S.; Goddard, W. A.; Skiff, W. M. *J. Am. Chem. Soc.* **1992**, *114*, 10024–10035.

[92] Jorgensen, W. L.; Maxwell, D. S.; Tirado-Rives, J. *J. Am. Chem. Soc.* **1996**, *118*, 11225–11236.

[93] Jorgensen, W. L.; McDonald, N. A. *J. Mol. Struct. THEOCHEM* **1998**, *424*, 145–155.

[94] McDonald, N. A.; Jorgensen, W. L. *J. Phys. Chem. B* **1998**, *102*, 8049–8059.

[95] Rizzo, R. C.; Jorgensen, W. L. *J. Am. Chem. Soc.* **1999**, *121*, 4827–4836.

[96] Jones, J. E. *Proceedings of the Royal Society of London Series A* **1924**, *106*, 463–477.

[97] Lorentz, H. A. *Annalen der Physik* **1881**, *248*, 127–136.

[98] Darden, T.; York, D.; Pedersen, L. *J. Chem. Phys.* **1993**, *98*, 10089–10092.

[99] Essmann, U.; Perera, L.; Berkowitz, M. L.; Darden, T.; Lee, H.; Pedersen, L. G. *J. Chem. Phys.* **1995**, *103*, 8577–8593.

[100] Vlugt, T. J. H.; Krishna, R.; Smit, B. *The Journal of Physical Chemistry B* **1999**, *103*, 1102–1118.

[101] Hansen, J.-P.; McDonald, I. R. *Theory Simple Liq. (Fourth Ed.*; Academic Press: Oxford, 2013; pp 1–11.

[102] Every, H. a.; Bishop, A. G.; MacFarlane, D. R.; Orädd, G.; Forsyth, M. *J. Mater. Chem.* **2001**, *11*, 3031–3036.

Effect of Room Temperature Ionic Liquids on CO$_2$ Separation by Cu-BTC Metal-Organic Framework

José Manuel Vicent-Luna, Juan José Gutierrez-Sevillano, Juan Antonio Anta, and Sofía Calero

We report a molecular simulation study aimed to ascertain the effect exerted in gas adsorption when room temperature ionic liquids (RTILs) are added into the pores of the Cu-BTC metal-organic framework. Carbon dioxide, methane, nitrogen, and their mixtures are studied. We take into account the influence of the type of anion and the relative amount of RTILs used. It is observed that the presence of RTILs in the MOF pores enhances significantly CO$_2$ adsorption at low pressures whereas methane and nitrogen adsorption is unaffected.
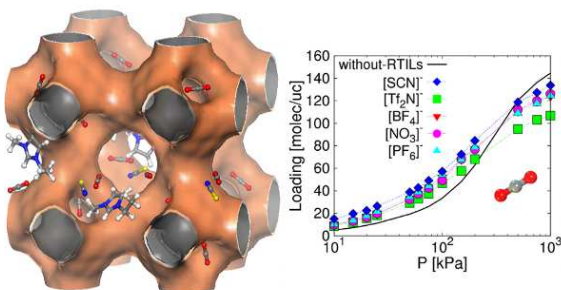
INTRODUCTION

Separation of gas mixtures, involving carbon dioxide (CO$_2$), is not only of scientific interest but also a social issue for environmental protection, due to its implications on global warming.[1] Carbon dioxide is constantly being exchanged among the atmosphere, ocean, and land surface as it is produced and absorbed by many microorganisms, plants, and animals. Room Temperature Ionic Liquids (RTILs) have been proposed as potentially good solvents for CO$_2$ capture and separation.[2–5] RTILs

are salts in the liquid state whose melting points are below some arbitrary temperature (usually 373 K). They are formed by a combination of organic cations and organic or inorganic anions. RTILs have attracted extensive attention in recent years due to their appealing properties:[6] excellent thermal and electrochemical stability, very low vapor pressure, relatively high ionic conductivity, among others. Many reports have explored the possibilities of RTILs as advantageous electrolytes in electrochemical double-layer capacitors (EDLCs),[7–10] electrodeposition,[11] and in dye-sensitized solar cells (DSSCs).[12, 13] Furthermore various applications have arisen from the concomitant use of RTILs with other materials such as biopolymers to develop ion jelly,[14–16] or liquid crystals to develop ionic liquid crystals.[17] In this work we focus in the use of RTILs in separation processes.[18–20]

Metal-organic frameworks (MOFs) are relatively novel materials known for their high surface area, large pore volume, and remarkable storage capacity. MOFs exhibit a high variety of topologies, which can be used to improve the storage or the separation of CO_2 [21] from other gases such as methane or nitrogen.

In this work we have studied the separation capability of Cu-BTC, a MOF that has attracted a great deal of attention since its first synthesis by Chui et al.[22] This structure consists of a metal coordination polymer based on Cu as the metal center and benzene-1,3,5-tricarboxylate

(BTC) as the organic linker. Cu-BTC is formed by two big central cages (commonly referred to as L_2 and L_3) of 9 Å in diameter and by small cages (T_1) of 5 Å in diameter.[23] The large cavities are connected by small windows (L_w) whereas L_3 and T_1 are connected by triangular windows of 3.5 Å in diameter. Cu-BTC has been studied thoroughly both theoretically [24–30] and experimentally.[31–35] It has been proposed as a promising material for technological applications, [36–40] like CO_2 /CH_4 separation.[41]

In the past few years, the use of RTILs in conjunction with MOFs has given rise to various applications, such as ionic liquid-based synthesis of MOFs.[42–46] The combination of RTILs and MOFs has also been studied by molecular simulations. In previous publications Chen et al.[47, 48] investigated the RTIL/MOF composite for CO_2 capture. In this case the ionic liquid is supported on the structure by confinement effects. They found that CO_2 /N_2 selectivity was enhanced if IRMOF-1 supported ionic liquids membranes were used. In our previous study [23] we investigated the RTIL/Cu-BTC composite with the aim to enhance the adsorption selectivity of a given mixture and the water resistance of the Cu-BTC structure.

Although it is already well-known that RTILs alone act as good CO_2 solvents,[2–5] most RTILs are expensive compared to the MOFs. This is currently one important limitation for their use in indus-

trial processes and it makes the combina-
tion RTIL/MOF an attractive material for
the CO_2 separation. The main idea of this
study is to find a suitable composite for
this purpose using a low amount of RTILs.
This work explores the RTIL/Cu-BTC com-
posite as a suitable candidate for purifica-
tion and separation of carbon dioxide from
methane and nitrogen. To do so we have
carried out molecular simulations of the
RTIL/Cu-BTC system aimed to establish
its adsorption capacity for carbon dioxide
and its preferential adsorption over nitro-
gen and methane. We have also analyzed
the role played by the RTILs moieties in
the enhancement of the carbon dioxide sep-
aration selectivity by the hybrid system.

This paper is organized as follows. In
section 2 we describe the methods and
models used. The results and discussion
are detailed in section 3. Finally, in section
4 the main conclusions that can be drawn
for this work are presented.

SIMULATION DETAILS

Molecular Dynamics (MD) and Monte
Carlo (MC) simulations in the NVT en-
semble and in the Grand Canonical en-
semble (GCMC) have been performed. The
gas systems studied were composed by car-
bon dioxide, methane, nitrogen, and their
mixtures. Adsorption isotherms and ad-
sorptions energies and entropies were com-
puted for each component at room temper-
ature. In all cases ionic liquids were added
to the cages of Cu-BTC by performing MC

simulations in the NVT ensemble. This
allows the RTILs to relax to their pref-
erential sites inside the structure. Subse-
quently, adsorption isotherms were evalu-
ated using MC simulations in the Grand
Canonical ensemble.

We identify five preferential sites of ad-
sorption in Cu-BTC:[23] Two large cages
that we define as spheres of 12 Å in diam-
eter. One of these cages is located at the
pores with the copper atoms of BTC point-
ing to the center of the pore (L_3) and the
other is centered at the pore with inner
surface conformed by the aromatic rings
(L_2). The third preferential site of adsorp-
tion is the small tetrahedral cage that we
define with one sphere of 9.5 Å in diameter
(T_1). The other two sites are the windows
that communicate cages L_3 and L_2 (L_w)
and L_3 and T_1 (T_w).

In a first set of calculations, the pref-
erential distribution of RTILs into Cu-
BTC was investigated by performing MD
and MC simulations. RTILs are not ad-
sorbed in the structure but introduced *ad
hoc* within the pores. Radial distribution
functions providing information about the
cation-anion pairs when they are confined
in the structure are shown in Figure A1.1-
1.3 in the Appendix 1. We found that these
molecules tend to be located evenly in L_3
and L_2 cages and occasionally in the win-
dows. The studied RTILs were unable to
enter the T_1 cages.

We use a united atom model with a sin-
gle interaction center as effective potential
for methane.[49, 50] For nitrogen and car-

bon dioxide we use full atom models. The quadrupole moment of nitrogen was reproduced by placing negative point charges on the atoms and a positive point charge in the center of mass of the molecules.[51, 52] To reproduce the quadrupole moment of carbon dioxide adequate charges were placed on each atom.[53, 54]

The molecular models of the ionic liquids studied in this work are shown in Figure 1. A common cation was considered in all cases: 1-ethyl-3-methylimidazolium [EMIM]$^+$. This cation is combined with the following anions: bis[(trifluoromethyl)sulfonyl]imide [Tf$_2$N]$^-$, thiocyanate [SCN]$^-$, nitrate [NO$_3$]$^-$, tetrafluoroborate [BF$_4$]$^-$, and hexafluorophosphate [PF$_6$]$^-$. We use full atom models for the RTILs. The cation is constituted by flexible ethyl and methyl groups attached to an aromatic moiety which is modeled by a rigid ring. The [Tf$_2$N]$^-$ anion is fully flexible whereas the others anions are defined as rigid molecules. For all flexible components we use the potential:

$$\Phi_{int} = \sum_{bonds} k_b(r - r_0)^2 + \sum_{angles} k_\theta(\theta - \theta_0)^2 + \sum_{dihedrals} k_\chi[1 + \cos(n\chi - \delta)]$$

(1)

The point charges and the Lennard-Jones and intramolecular forcefield parameters for the RTILs are taken from Kelkar and Maggin.[55] ([EMIM]$^+$ and [Tf$_2$N]$^-$), Liu et al.[56] ([BF$_4$]$^-$), Yan et al.[57] ([NO$_3$]$^-$), Cadena et al.[58] ([PF$_6$]$^-$), and

Chaumont and Wipff.[59] ([SCN]$^-$).
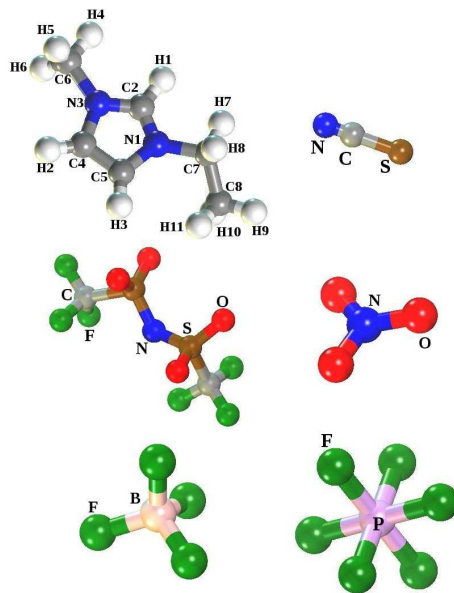
Figure 1. Schematic representation of the RTILs used in this work. [EMIM]$^+$ (top left), [SCN]$^-$ (top right), [Tf$_2$N]$^-$ (middle left), [NO$_3$]$^-$ (middle right), [BF$_4$]$^-$ (bottom left), and [PF$_6$]$^-$ (bottom right), respectively.

RESULTS AND DISCUSSION

Figure 2 shows the computed isosteric heats of adsorption of carbon dioxide in Cu-BTC containing different anions and for different RTIL concentrations inside the pores. It is observed that the
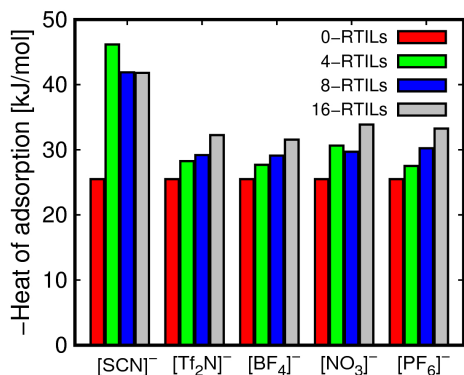
Figure 2. Computed isosteric heats of adsorption (absolute values) for carbon dioxide in Cu-BTC. Results are shown for the bare Cu-BTC (red) and for the structures containing 4 (green), 8 (blue), and 16 (gray) molecules of RTILs per unit cell.

absolute value of the heat of adsorption increases with the presence of RTILs inside the pores. The structures containing the different anions exhibit similar behavior except for the one containing [SCN]$^-$. For this structure the computed heats of adsorption have a particularly large value. The rest of the energies and the entropies of adsorption computed for carbon dioxide in the different Cu-BTC structures show similar trends than the observed for the heats of adsorption (Figure A1.4 in the Appendix 1). We also performed the analysis for methane and nitrogen (Figure A1.5-1.7 in the Appendix 1), obtaining similar results as for carbon dioxide but at a different scale. The largest values in energies and entropies of adsorption were obtained for carbon dioxide, followed by methane and nitrogen.

The computed energies of adsorption for the three molecules increase in the framework/RTIL composite with respect to the MOF without RTILs. This can be interpreted as a combination of the size and shape of the adsorbates -that preferentially adsorb in the small cages-,[23] and the polar nature of the ionic liquids located inside the largest pores. Hence, due to its size and polarizability, carbon dioxide tends to get "dissolved" in the RTILs media more easily than methane and nitrogen. Furthermore, the increase of RTILs units in the framework favors the adsorption of the gas molecules. This explains the monotonous trend observed when increasing the concentration of RTILs inside the pores. In addition, the very similar results obtained for all anions (leaving aside [SCN]$^-$) confirm that the adsorption energies are affected by the ionic character and the amount of the RTILs. The peculiar behavior found for [SCN]$^-$ can be attributed to its size since this anion is small enough to allow additional adsorption sites for carbon dioxide inside the big cages.

In order to analyze the effect of the type of anion in a fully interacting system we have computed the adsorption isotherms for carbon dioxide, methane, and nitrogen as pure components and as equimolar mixtures. As shown in Figure 3 the presence of RTILs in the structure increases the adsorption of carbon dioxide up to 300 kPa, independently of the type of anion studied. In the entire pressure range the highest loadings were obtained
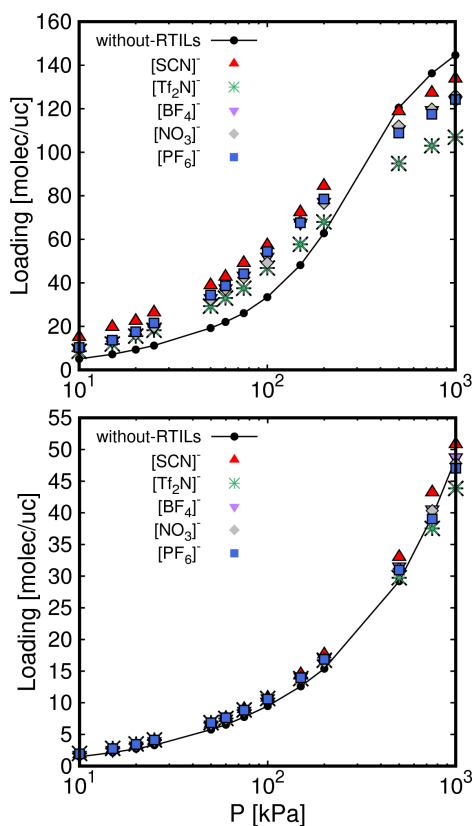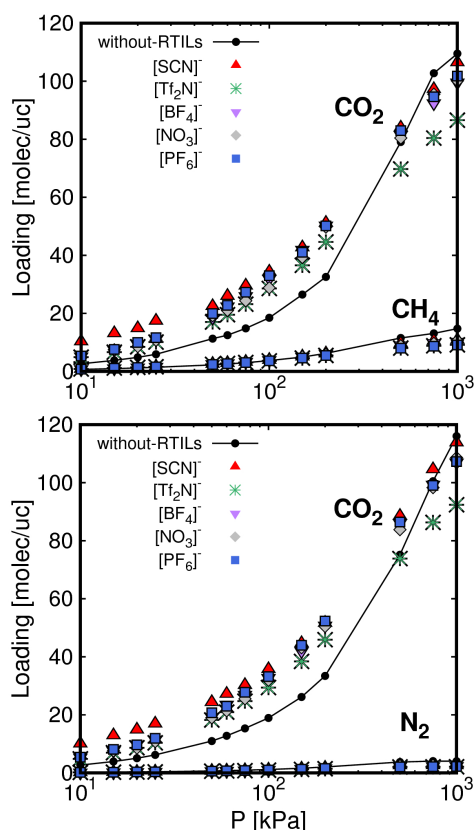
Figure 3. Adsorption isotherms obtained for carbon dioxide (top) and methane (bottom) in the bare Cu-BTC and in the structure with eight molecules of RTILs per unit cell.

for [SCN]⁻ and the lowest loadings for [Tf$_2$N]⁻ . These are the smallest and the bulkiest anions studied in this work. At high pressure the presence of RTILs in the structure reduces accessible pore volume leading to lower saturation values for carbon dioxide; the bulkier the anion, the lower the saturation value.

The adsorption of methane (Figure 3) and nitrogen (Figure A1.8 in the Appendix 1) is not sensitive to the presence of RTILs

in the structure. On the one hand for the pressure range studied, the adsorption of methane and nitrogen takes place in the small cages and in the windows. On the other hand, the lack of polarizability prevents the interaction of these molecules with the ionic liquids. Figure 4 shows the adsorption isotherms of the CO_2 /CH_4 and CO_2 /N_2 mixtures, for all anions considered in Figure 1.


Figure 4. Adsorption isotherms computed for CO_2 /CH_4 (top) and CO_2 /N_2 (bottom) equimolar mixtures in the bare Cu-BTC and in the structure with eight molecules of RTILs per unit cell.

The adsorption of methane and nitrogen is almost negligible for the full range of pressure. However, the adsorption of carbon dioxide increases when the structure is loaded with RTILs up to 300 kPa and decreases at high values of pressure. This proves that carbon dioxide interacts strongly with the molecules of RTILs. This interaction is not observed for the other two gases. The obtained results are in line with the behavior derived from the computed heats of adsorption.

To further understand the effect of the amount of RTILs in the adsorption capabilities of Cu-BTC we performed additional simulations increasing the amount of RTILs moieties in the structure from 0 to 20 molecules of $[EMIM]^+$ $[SCN]^-$ per unit cell. Simulations were carried out for the equimolar mixture CO_2/CH_4 at 100 kPa. The obtained loading as a function of the number of molecules of RTILs is depicted in Figure 5. At this pressure the adsorption of carbon dioxide increases with the amount of RTILs in the structure while the adsorption of methane remains constant. Similar results were obtained with the other anions. To rationalize previous results it is important to investigate the location of the adsorbates in the bare Cu-BTC and in the structure with RTILs. Figure 6 shows the average occupation profiles of carbon dioxide and methane as a function of the concentration of RTILs. In absence of RTILs our results indicate that carbon dioxide and methane molecules are located preferentially in the small cavities.
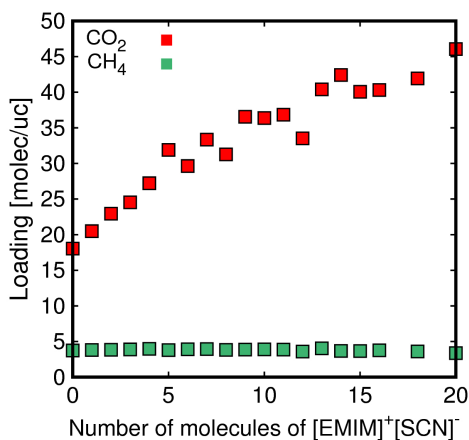
Figure 5. Adsorption of the equimolar mixture CO_2/CH_4 obtained as a function of the number of molecules of $[EMIM]^+$ $[SCN]^-$ at room temperature and 100 kPa.

As RTILs moieties are introduced into the structure, the molecules of carbon dioxide move to the big cages forming small clusters around the molecules of RTILs. This increases the amount of adsorbed carbon dioxide. These effects can be interpreted as a consequence of the aforementioned affinity between RTILs and carbon dioxide due to polar interactions. On the basis of this interpretation, the location of methane should not be affected by the presence of RTILs. This prediction is confirmed by the simulation results. Further increase of the amount of RTILs leads to a wider distribution of carbon dioxide in the structure, whereas methane location is unaffected.

In summary, the presence of RTILs generates new centers of adsorption for carbon dioxide, increasing the amount of gas adsorbed.
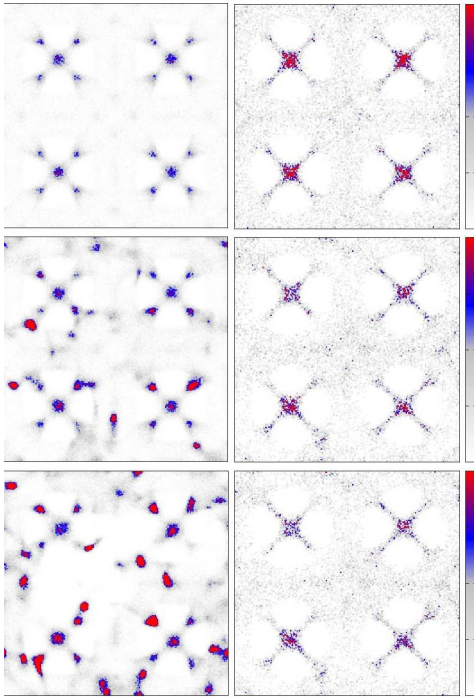
Figure 6. Average occupation profiles for CO_2 (left) and CH_4 (right) in Cu-BTC, without RTILs (top), with 10 ion pairs of [EMIM]$^+$ [SCN]$^-$ (center), and with 20 ion pairs of [EMIM]$^+$ [SCN]$^-$ (bottom).

To understand the cluster formed by carbon dioxide molecules around the RTILs, we computed the radial distribution function between CO_2 and RTILs moieties (Figure A1.9 in the Appendix 1). It is observed that carbon dioxide molecules are located nearest the anion than the cation independently of the ionic liquid concentration. This evidences specific interactions between carbon dioxide and the negative part of RTILs.

The adsorption selectivity is defined as $S = \frac{(x_A/y_A)}{(x_B/y_B)}$, where x_i is the molar frac-

tion in the adsorbed phase for the i component and y_i the molar fraction in the bulk phase. To analyze the effect exerted by the different nature of the ions, the selectivity was computed for equimolar mixtures ($y_i = 0.5$). A large value of selectivity indicates preferential adsorption for one the components of the mixture (component A) over the other (component B).

Figure 7 shows the adsorption selectivity obtained for carbon dioxide over methane and nitrogen. This was obtained for the bare Cu-BTC and for the structure with several concentrations of RTILs with the thiocyanate anion. The adsorption selectivity is always in favor of carbon dioxide. The presence of RTILs in the structure leads to an increase of the adsorption selectivity in favor of carbon dioxide. We observe similar trends for the mixture CO_2/CH_4 than for the mixture CO_2/N_2, but at different scale, the carbon dioxide adsorption selectivity being larger for the mixture containing nitrogen than for the mixture containing methane. It is also observed that the adsorption selectivity is enhanced in the structures containing RTILs. This behavior is observed for the entire range of pressures. The adsorption selectivity in the Cu-BTC structures containing the other anions were also obtained (Figure A1.10-1.11 in the Appendix 1). For all anions, the adsorption selectivity follows a similar trend in the intermediate and high-pressure regime. However, in the low-pressure regime the increase in the adsorption selectivity observed for the
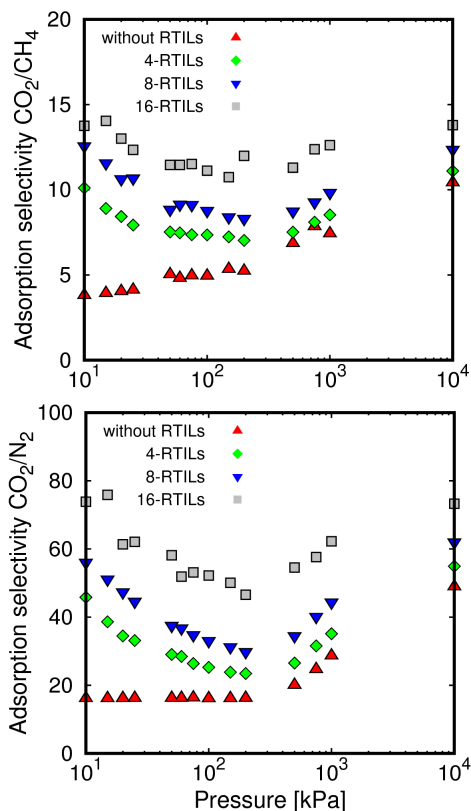
Figure 7. Adsorption selectivity obtained for the equimolar mixtures CO_2/CH_4 (top) and CO_2/N_2 (bottom) in the bare Cu-BTC (red) and in Cu-BTC with 4 (green), 8 (blue), and 16 (gray) molecules of $[EMIM]^+[SCN]^-$ per unit cell, respectively.

cess we analyse the adsorption selectivity of the mixture of carbon dioxide/methane as a function of the adsorption selectivity of the mixture of carbon dioxide and nitrogen. The study was performed at room temperature showing a relatively linear trend where the best performance is obtained for the thiocyanate and the hexafluorophosphate anion (see Figure A1.12 in the Appendix 1).

CONCLUSIONS

Room temperature ionic liquids embedded in Cu-BTC have been investigated to study carbon dioxide separation from mixtures containing methane or nitrogen. Molecular simulations with validated force fields show that the presence of RTILs in the pores of the structure enhances carbon dioxide adsorption at low pressure whereas methane and nitrogen adsorption is unaffected. This leads to higher values of adsorption selectivity in favor of carbon dioxide. The isosteric heats of adsorption of these three gases are larger in the structures that contain RTILs. We also provide evidence that the type of anion influences the adsorption of carbon dioxide in Cu-BTC. The preferential adsorption for carbon dioxide over methane and nitrogen is due to the affinity of the former molecule for the RTILs moieties within the framework. This can be attributed to the polar character of both, carbon dioxide and RTILs. On the basis of our results, the composite RTIL/Cu-BTC

thiocyanate anion does not occur. The particular behavior of the adsorption selectivity of carbon dioxide over nitrogen and over methane observed in the structures containing thiocyanate anion is due to the small size of this ion. These results are in accordance with the computed heats of adsorption shown in Figure 2.

To provide additional insight on the optimal RTIL for a given separation pro-

proves to be a promising system for separation of carbon dioxide from mixtures CO_2/CH_4 and CO_2/N_2 in the entire pressure range considered in this work.

Bibliography

[1] Cox, P. M.; Betts, R. A.; Jones, C. D.; Spall, S. A.; Totterdell, I. J. *Nature* **2000**, *408*, 750.

[2] Babarao, R.; Dai, S.; Jiang, D.-e. *J. Phys. Chem. B* **2011**, *115*, 9789–9794.

[3] Yan, F.; Lartey, M.; Damodaran, K.; Albenze, E.; Thompson, R. L.; Kim, J.; Haranczyk, M.; Nulwala, H. B.; Luebke, D. R.; Smit, B. *Phys. Chem. Chem. Phys.* **2013**, *15*, 3264–3272.

[4] Kolding, H.; Fehrmann, R.; Riisager, A. *Sci. China-Chemistry* **2012**, *55*, 1648–1656.

[5] Ramdin, M.; de Loos, T. W.; Vlugt, T. J. H. *Ind. Eng. Chem. Res.* **2012**, *51*, 8149–8177.

[6] Plechkova, N. V.; Seddon, K. R. *Chem. Soc. Rev.* **2008**, *37*, 123–150.

[7] Palm, R.; Kurig, H.; Tonurist, K.; Jaenes, A.; Lust, E. *Electrochim. Acta* **2012**, *85*, 139–144.

[8] Palm, R.; Kurig, H.; Tonurist, K.; Jaenes, A.; Lust, E. *Electrochem. commun.* **2012**, *22*, 203–206.

[9] Tonurist, K.; Thomberg, T.; Jaenes, A.; Kink, I.; Lust, E. *Electrochem. commun.* **2012**, *22*, 77–80.

[10] Ju, Y.-J.; Lien, C.-H.; Chang, K.-H.; Hu, C.-C.; Wong, D. S.-H. *J. Chinese Chem. Soc.* **2012**, *59*, 1280–1287.

[11] Azaceta, E.; Chavhan, S.; Rossi, P.; Paderi, M.; Fantini, S.; Ungureanu, M.; Miguel, O.; Grande, H.-J.; Tena-Zaera, R. *Electrochim. Acta* **2012**, *71*, 39–43.

[12] Kuang, D.; Klein, C.; Zhang, Z.; Ito, S.; Moser, J.-E.; Zakeeruddin, S. M.; Graetzel, M. *Small* **2007**, *3*, 2094–2102.

[13] Guillén, E.; Fernández-Lorenzo, C.; Alcántara, R.; Martín-Calleja, J.; Anta, J. A. *Sol. Energy Mater. Sol. Cells* **2009**, *93*, 1846–1852.

[14] Rana, S.; Carvalho, T.; Fangueiro, R.; Vidinha, P. *Polym. Adv. Technol.* **2013**, *24*, 191–196.

[15] Carvalho, T.; Augusto, V.; Bras, A. R.; Lourenco, N. M. T.; Afonso, C. A. M.; Barreiros, S.; Correia, N. T.; Vidinha, P.; Cabrita, E. J.; Dias, C. J.; Dionisio, M.; Roling, B. *J. Phys. Chem. B* **2012**, *116*, 2664–2676.

[16] Vidinha, P.; Lourenco, N. M. T.; Pinheiro, C.; Bras, A. R.; Carvalho, T.; Santos-Silva, T.; Mukhopadhyay, A.; Romao, M. J.; Parola, J.; Dionisio, M.; Cabral, J. M. S.; Afonso, C. A. M.; Barreiros, S. *Chem. Commun.* **2008**, 5842–5844.

[17] Trilla, M.; Pleixats, R.; Parella, T.; Blanc, C.; Dieudonne, P.; Guari, Y.; Man, M. W. C. *Langmuir* **2008**, *24*, 259–265.

[18] Kim, J.; Maiti, A.; Lin, L.-C.; Stolaroff, J. K.; Smit, B.; Aines, R. D. *Nat. Commun.* **2013**, *4*, 1694.

[19] Neves, C. M. S. S.; Granjo, J. F. O.; Freire, M. G.; Robertson, A.; Oliveira, N. M. C.; Coutinho, J. A. P. *Green Chem.* **2011**, *13*, 1517–1526.

[20] Iarikov, D. D.; Hacarlioglu, P.; Oyama, S. T. *Chem. Eng. J.* **2011**, *166*, 401–406.

[21] Britt, D.; Furukawa, H.; Wang, B.; Glover, T. G.; Yaghi, O. M. *Proc. Natl. Acad. Sci. U. S. A.* **2009**, *106*, 20637–20640.

[22] Chui, S. S. Y.; Lo, S. M. F.; Charmant, J. P. H.; Orpen, A. G.; Williams, I. D. *Science (80-.).* **1999**, *283*, 1148–1150.

[23] Gutiérrez-Sevillano, J. J.; Vicent-Luna, J. M.; Dubbeldam, D.; Calero, S. *J. Phys. Chem. C* **2013**, *117*, 11357–11366.

[24] Krishna, R.; van Baten, J. M. *Phys. Chem. Chem. Phys.* **2011**, *13*, 10593–10616.

[25] Amirjalayer, S.; Tafipolsky, M.; Schmid, R. *J. Phys. Chem. C* **2011**, *115*, 15133–15139.

[26] Grajciar, L.; Bludsky, O.; Nachtigall, P. *J. Phys. Chem. Lett.* **2010**, *1*, 3354–3359.

[27] Fischer, M.; Hoffmann, F.; Froeba, M. *Chemphyschem* **2010**, *11*, 2220–2229.

[28] Wang, S. Y.; Yang, Q. Y.; Zhong, C. L. *Sep. Purif. Technol.* **2008**, *60*, 30–35.

[29] Zhou, C.; Cao, L.; Wei, S.; Zhang, Q.; Chen, L. *Comput. Theor. Chem.* **2011**, *976*, 153–160.

[30] Greathouse, J. A.; Ockwig, N. W.; Criscenti, L. J.; Guilinger, T. R.; Pohl, P.; Allendorf, M. D. *Phys. Chem. Chem. Phys.* **2010**, *12*, 12621–12629.

[31] Bordiga, S.; Regli, L.; Bonino, F.; Groppo, E.; Lamberti, C.; Xiao, B.; Wheatley, P. S.; Morris, R. E.; Zecchina, A. *Phys. Chem. Chem. Phys.* **2007**, *9*, 2676–2685.

[32] Li, Y. W.; Yang, R. T. *J. Am. Chem. Soc.* **2006**, *128*, 8136–8137.

[33] Prestipino, C.; Regli, L.; Vitillo, J. G.; Bonino, F.; Damin, A.; Lamberti, C.; Zecchina, A.; Solari, P. L.; Kongshaug, K. O.; Bordiga, S. *Chem. Mater.* **2006**, *18*, 1337–1346.

[34] Kusgens, P.; Rose, M.; Senkovska, I.; Frode, H.; Henschel, A.; Siegle, S.; Kaskel, S. *Microporous Mesoporous Mater.* **2009**, *120*, 325–330.

[35] Liang, Z. J.; Marshall, M.; Chaffee, A. L. *Greenh. Gas Control Technol. 9* **2009**, *1*, 1265–1271.

[36] Keskin, S.; van Heest, T. M.; Sholl, D. S. *ChemSusChem* **2010**, *3*, 879–891.

[37] Dueren, T.; Bae, Y.-S.; Snurr, R. Q. *Chem. Soc. Rev.* **2009**, *38*, 1237–1247.

[38] Calero, S.; Martin-Calvo, A.; Hamad, S.; Garcia-Perez, E. *Chem. Commun.* **2011**, *47*, 508–510.

[39] Castillo, J. M.; Vlugt, T. J. H.; Calero, S. *J. Phys. Chem. C* **2008**, *112*, 15934–15939.

[40] Martin-Calvo, A.; Garcia-Perez, E.; Manuel Castillo, J.; Calero, S. *Phys. Chem. Chem. Phys.* **2008**, *10*, 7085–7091.
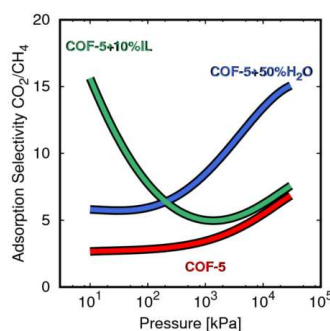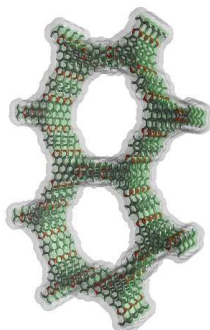
[41] Jose Gutierrez-Sevillano, J.; Caro-Perez, A.; Dubbeldam, D.; Calero, S. *Phys. Chem. Chem. Phys.* **2011**, *13*, 20453–20460.

[42] Siddiqui, K. A.; Bolte, M.; Mehrotra, G. K. *Inorganica Chim. Acta* **2010**, *363*, 457–463.

[43] Yan, N.; Fei, Z.; Scopelliti, R.; Laurenczy, G.; Kou, Y.; Dyson, P. J. *Inorganica Chim. Acta* **2010**, *363*, 504–508.

[44] Xu, L.; Yan, S.; Choi, E.-Y.; Lee, J. Y.; Kwon, Y.-U. *Chem. Commun.* **2009**, 3431–3433.

[45] Xie, Z.-L.; Feng, M.-L.; Tan, B.; Huang, X.-Y. *Crystengcomm* **2012**, *14*, 4894–4901.

[46] Xu, L.; Choi, E.-Y.; Kwon, Y.-U. *Inorg. Chem.* **2007**, *46*, 10670–10680.

[47] Chen, Y.; Hu, Z.; Gupta, K. M.; Jiang, J. *J. Phys. Chem. C* **2011**, *115*, 21736–21742.

[48] Gupta, K. M.; Chen, Y.; Hu, Z.; Jiang, J. *Phys. Chem. Chem. Phys.* **2012**, *14*, 5785–5794.

[49] Dubbeldam, D.; Calero, S.; Vlugt, T. J. H.; Krishna, R.; Maesen, T. L. M.; Smit, B. *J. Phys. Chem. B* **2004**, *108*, 12301–12313.

[50] Ryckaert, J. P.; Bellemans, A. *Faraday Discuss.* **1978**, 95–106.

[51] Stogryn, D. E.; Stogryn, A. P. *Mol. Phys.* **1966**, *11*, 371.

[52] Murthy, C. S.; Singer, K.; Klein, M. L.; McDonald, I. R. *Mol. Phys.* **1980**, *41*, 1387–1399.

[53] Garcia-Sanchez, A.; Ania, C. O.; Parra, J. B.; Dubbeldam, D.; Vlugt, T. J. H.; Krishna, R.; Calero, S. *J. Phys. Chem. C* **2009**, *113*, 8814–8820.

[54] Harris, J. G.; Yung, K. H. *J. Phys. Chem.* **1995**, *99*, 12021–12024.

[55] Kelkar, M. S.; Maginn, E. J. *J. Phys. Chem. B* **2007**, *111*, 4867–4876.

[56] Liu, Z. P.; Huang, S. P.; Wang, W. C. *J. Phys. Chem. B* **2004**, *108*, 12978–12989.

[57] Yan, T. Y.; Burnham, C. J.; Del Popolo, M. G.; Voth, G. A. *J. Phys. Chem. B* **2004**, *108*, 11877–11881.

[58] Cadena, C.; Anthony, J. L.; Shah, J. K.; Morrow, T. I.; Brennecke, J. F.; Maginn, E. J. *J. Am. Chem. Soc.* **2004**, *126*, 5300–5308.

[59] Chaumont, A.; Wipff, G. *Inorg. Chem.* **2009**, *48*, 4277–4289.

Storage and Separation of Carbon Dioxide and Methane in Hydrated Covalent Organic Frameworks

José Manuel Vicent-Luna, Azahara Luna-Triguero, and Sofía Calero

Storage and separation of carbon dioxide and methane and their mixtures are important processes for environmental and energetic reasons. We study these processes using hydrated nanoporous materials and explore the use of solvents as alternative to improve the performance of these materials. We used boronate ester Covalent Organic Frameworks (COF-5,-6,-10, and -102) because their stability upon water. The best separation for hydrated structure is obtained with COF-102. However, the improvement on the separation performance requires a high percentage of hydration, reducing the capacity of the structure. To overcome this limitation, we suggest to introduce room-temperature ionic liquid as a solvent. Our simulations show that the use of small amounts of ionic liquids in the structure leads to higher values of adsorption selectivity than the use of hydrated structures.

INTRODUCTION

The development of new adsorbents for gas separation is receiving increasing attention over the past years. In particular, adsorption of methane (CH_4) and carbon dioxide (CO_2) and their mixtures is a challenging research topic for energetic and environmental reasons. Carbon dioxide emissions resulting from the burning of fossil fuels in automobiles and power plants contribute to global warming.[1, 2] Moreover, natural gas is one of the cleanest carbon fuels and its global demand is expected to grow in the next years. The natural gas reserves are usually contaminated with gases like carbon dioxide that reduce the energy content of natural gas. Therefore, to utilize and to transport methane gas it is desirable to first remove and capture carbon dioxide.

The amine-based adsorption and stripping process has been used for a long time for CO_2/CH_4 separation, but the solvents used, e.g. aqueous alkanoamines, usually require high energy.[3] Adsorption-based separation methods such as pressure swing adsorption are commonly accepted to be some of the most efficient processes, but the development of adsorbents with high carbon dioxide capacity and good CO_2/CH_4 separation is key factor for this separation. Traditional adsorbents such as activated carbons,[4, 5] zeolites,[6, 7] metal organic frameworks,[8–10] and silica gel [11, 12] have been widely studied. In recent years Covalent Organic Frame-

works (COFs)[13–16] have also attracted a great deal of attention. COFs are crystalline porous polymers constructed by linking light elements such as boron, carbon, silicon, and oxygen through strong covalent bonds. This forms rigid and highly porous and chemically stable materials. COF structures are being used in diverse applications as catalysis,[17–19] gas storage,[20, 21] and energy storage and conversion devices.[22, 23]

Previous works have shown that COFs are also useful for gas storage. For example, the studies of Furukawa [24] demonstrated that COFs exhibit high adsorption capacities for hydrogen, methane, and carbon dioxide comparing with the most common carbon materials, and M. Tong et al.[25] collected a database of COFs and evaluated the separation performance of gas mixtures such as CH_4/H_2, CO_2/H_2, and CO_2/CH_4. Despite these efforts, the reported selectivity for CO_2/CH_4 mixture is lower than 10 for high pressure range in these COFs. Therefore, the aim of our work is to provide strategies to improve the separation capabilities of these materials. To this aim we have selected four COFs, developing specific set of point charges for them. In particular we focused on the boronate ester COF-5,-6,-10, and -102 with pore sizes of 27, 9, 32, and 12 Å, respectively. We selected these COFs, which structures are depicted in Figure 1, for their high thermal stability (temperatures up to 400-600 °C) and their extremely low framework densities, i.e. 0.58

g/cm^3 (COF-5), 1.08 g/cm^3 (COF-6), 0.47 g/cm^3 (COF-10), and 0.42 g/cm^3 (COF-102). Another important property of boronate ester COFs is their stability upon water.[26]

Motivated by previous works which proposed COFs as excellent materials for gas adsorption, we analyze the separation capability of these structures for CO_2/CH_4 mixtures. We also examine the influence that two solvents (water and ionic liquids) have on the adsorption of carbon dioxide and methane, and on the selectivity in favor of carbon dioxide. The adsorption of mixtures of carbon dioxide and methane was analyzed using COFs with various degrees of hydration, and also COFs loaded with room-temperature ionic liquids (RTILs or simply ILs). The election of these candidates as solvents is mainly due to practical applications. On the one hand, COFs have demonstrated excellent water stability and the cost and availability of water make of this solvent an interesting option to investigate. On the other hand, ILs have been proven to be excellent solvents for carbon dioxide capture showing high carbon dioxide solubility.[27–32] The use of ILs and porous materials in conjunction has been investigated both theoretically [33–36] and experimentally [37–39] exhibiting good performance for the separation of this mixture of gases. ILs are highly dense systems; the absorption capacity of small gases can be compared with the adsorption capacity of zeolites. One of the limitations of zeolites is that most of them lack of pores of high size. On the con-

trary, MOFs and COFs have larger pore size, pore volume and surface area than most zeolites. This, in addition to the fact that ILs are more expensive than porous structures make these materials interesting adsorbents for gas capture. One of the aims of our work is the use in conjunction of ILs and COFs to combine the properties of each one and improve the adsorption capabilities that would have in their own, while simultaneously reducing expenses.

Room-temperature ionic liquids are salts in the liquid state with melting point below some arbitrary temperature, commonly below 100 °C. They are formed by a combination of organic cations and organic or inorganic anions leading to a larger number of compounds with different physical and chemical properties. We use the IL composed by the 1-ethyl-3-methylimidazolium cation and thiocyanate anion. This commonly used solvent has high ionic conductivity and low viscosity compared with other ILs [40, 41] and it has been tested for the high carbon dioxide solubility.[42, 43] Moreover, in a previous work [34] we found an exceptional increase in the CO_2/CH_4 selectivity when adding the mentioned IL to metal-organic frameworks. We attributed the improvement of selectivity to the strong interaction of the IL with the molecules of carbon dioxide. The small size of the anion is also an important factor since it generates additional adsorption sites for carbon dioxide while allows the structure to keep most of the available pore volume.
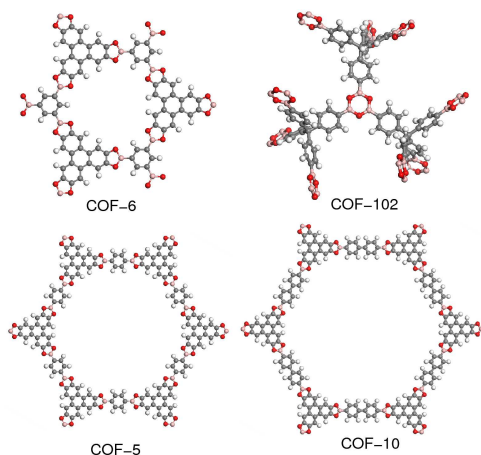
Figure 1. Schematic representation of atomic connectivity for COFs used in this work. Hydrogen atoms in white, carbon atoms in gray, boron atoms in pink, and oxygen atoms in red.

SIMULATION DETAILS

Adsorption isotherms were computed using Monte Carlo simulations in the grand canonical ensemble (GCMC), where chemical potential, volume, and temperature are fixed. Pressure was obtained from fugacity using the Peng-Robinson equation of state. The Monte Carlo moves used are translation, rotation, regrowth at random position, insertion, and identity change for multi-component systems. We have run $2 \cdot 10^5$ MC cycles after $2 \cdot 10^4$ cycles of initialization to ensure an equilibrium fluctuation around a mean value of loading of adsorbates. The heat of adsorption was calculated using MC simulations with the Widom particle-insertion method.[44]

We obtained the surface area (S_A) of the COFs by rolling a helium molecule over the surface of the framework. Hence, we have access to the amount of overlap with other framework atoms. The fraction of the overlap is multiplied by the area of the sphere, and the summation over all framework atoms gives the geometric surface area. The pore volume (V_p) is the void fraction times the unit cell volume, being the void fraction the empty space of the structure divided by the total volume. Such as in experiment procedures we also measure this fraction using helium at room temperature that it is easily computed from Widom particle insertion. Simulations were performed using the RASPA code.[45, 46]

Molecular simulations were performed for methane, carbon dioxide, and their equimolar mixtures in hydrated COFs and with various percentages of IL. The structures used here were taken from previous works for 2D-COFs [47, 48] (COF-5,-6, and -10), and 3D-COF [49] (COF-102). We considered the COFs frameworks rigid. The interaction of the framework with methane is by Lennard-Jones potentials and with carbon dioxide and water by Lennard-Jones and Coulombic potentials. Because of the lack of theoretical studies about COFs, we have developed a set of point charges, which we validated with reported experimental adsorption of carbon dioxide in these structures. The charges of COFs were obtained using EQeq [50] method based on Ewald sums. The obtained sets of charges are listed in Table 1, and the atom labels used for each COF can

be found in Figure A2.1 in the Appendix 2. Lennard-Jones parameters were taken from DREIDING generic force field. [51]

Table 1. Atomic Charges Obtained for the Studied COFs.

Atom	COF-102	COF-10	COF-6	COF-5
B1	0.48530	0.97060	0.48476	2.42070
O1	-0.32852	-0.37212	-0.17748	-0.89950
C1	0.08748	-0.50092	-0.30788	-1.06030
C2	-0.23128	0.14108	0.19502	0.19400
C3	-0.06710	-0.05852	0.00208	0.05990
C4	0.05218	0.04096	0.01362	-0.06280
C5	0.08754	0.02924	-0.01388	0.00800
C6	-0.06612	0.00568		
C7	-0.05584	-0.00068		
H1	-0.02344	-0.06008	-0.00686	-0.05660
H2	0.02086	-0.02962		0.07680
H3	-0.02380	-0.03046		
H4	0.02086			

We used Tip5pEw for the molecules of water. [**?**] This model has been successfully applied in previous works, providing results in good agreement with experimental data. [52] TraPPE united-atom model with a single interaction center was used for CH_4 .[53] For carbon dioxide we used a full atom model and to reproduce the quadrupole moment of carbon dioxide adequate charges were placed on top of each atom.[54]

The full atom model used for the IL is composed by cation-anion pairs (1-ethyl-3-methylimidazolium cation and thiocyanate anion). The cation consists on flexible ethyl and methyl groups bonded to an aromatic moiety which is modeled by rigid rings. The point charges and the Lennard-Jones and inter-molecular force fields parameters were taken from Kelkar and Maggin [55] ([EMIM]$^+$) and Chaumont and Wipff [56] ([SCN]$^-$).

The ILs and water molecules were added to the pores of the COFs using MC simulations in NVT ensemble. This allows the molecules to relax in their preferential sites within the structures. The estimation of the loaded percentages of water and ILs is done attending to the available pore volume of each structure and the liquid density of the solvents at room conditions. The maximum amount of solvent (100 %) is obtained from the available pore volume times the liquid density of the solvents. The accessible pore volume is obtained using the Widom particle-insertion method. [44] The adsorption isotherms for the gas mixtures were computed after equilibration of the ILs inside the COF cavities.

RESULTS AND DISCUSSION

To validate the force fields and charges that we are using for the COFs, the computed adsorption isotherms were compared with experimental data reported by Furukawa and Yaghi.[24] Figure 2 shows the adsorption isotherms of methane and carbon dioxide at 298 K. The agreement between experiments and simulation is excellent for COF-5, COF-10, and COF-6. There is also agreement between experiments and simulations for COF-102,
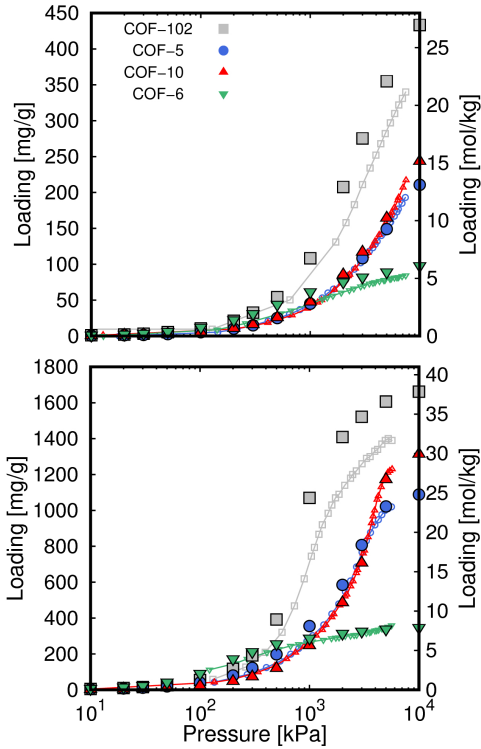
Figure 2. Adsorption isotherms comparing experimental [24] (empty symbols) and simulation (full symbols) data for methane (a) and carbon dioxide (b) in COF-5, COF-6, COF-10, and COF-102.

though simulation data overestimate experimental data. The maxima relative errors obtained for methane in COF-102 are 11.8 % and for carbon dioxide 12.1 %. As reflected in Table 2, differences in pore volume due to the presence of impurities in the structures could explain these differences.

In addition to S_A and V_p, the heat of adsorption is one of the most important properties to evaluate the adsorption and separation performance of the COFs. Fig-

ure 3 compares the calculated heats of adsorption of methane and carbon dioxide upon loading with previous experimental values.[24]

Table 2. Surface Area (S_A) and Pore Volume (V_p) for the Studied COFs.

COF	S_A (m^2/g)			V_p (cm^3/g)		
	exp^a	sim^a	this work	exp^a	sim^a	this work
COF-5	1670	1520	1856	1.07	1.17	1.17
COF-6	750	1050	1119	1.32	0.55	0.42
COF-10	1760	1830	1998	1.44	1.65	1.50
COF-102	3260	4940	5319	1.55	1.81	1.89

^{a} Values used for comparison are taken from refs [24] and [57], respectively.
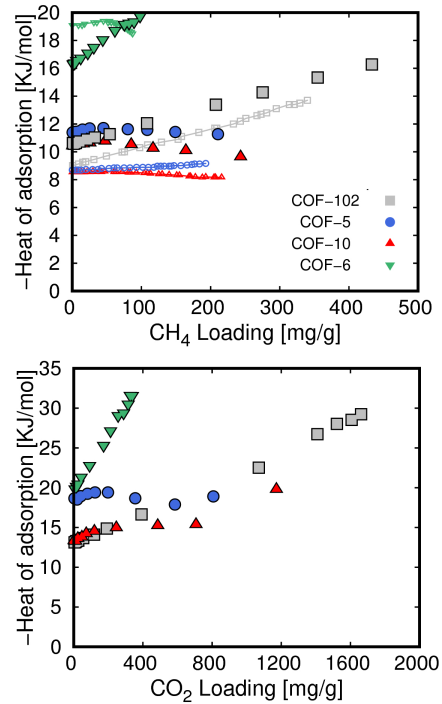

Figure 3. Heats of adsorption of methane (a) and carbon dioxide (b) as a function of loading in the different structures comparing experimental [24] (empty symbols) and simulation (full symbols) data in COF-5, COF-6, COF-10, and COF-102.

Except for COF-6, the heats of adsorption obtained from our simulations exhibit similar trends than the experimental values, though overestimate them by about 3 kJ/mol. Discrepancies in COF-6 could be explained by the fact that this is the structure with the smallest pore size, and therefore, the presence of impurities there strongly affects the interaction of the adsorbate with the structure. Unfortunately, we lack of reported experimental values of heat of adsorption for carbon dioxide in the structures, but as can be observed in Figure A2.2 in the Appendix 2 the trends of the heat of adsorption as a function of loading obtained for carbon dioxide are similar than the obtained for methane. Differences in the magnitudes are due to the strongest affinity of carbon dioxide for the structures. The heats of adsorption of carbon dioxide and methane at zero loading were also calculated and compared with experimental values, which in the case of carbon dioxide have been estimated from the experimental adsorption isotherms. The calculated heats of adsorption for methane in COF-5, -6, -10, and -102 are 10.88, 15.77, 10.47, and 10.07 kJ/mol respectively, and the values estimated from the experimental adsorption isotherms are 8.6, 18.5, 8.8, and 9.1 kJ/mol in the same order. For carbon dioxide, the heats of adsorption calculated at zero coverage are 18.03 kJ/mol (COF-5), 18.30 kJ/mol (COF-6), 13.50 kJ/mol (COF-10), and 12.60 kJ/mol (COF-102). The high values of the heats of adsorption at low

coverage observed for COF-6 reflect that the molecules of methane and carbon dioxide commensurate better in the smallest pores. COF-5 and -10 exhibit analogous adsorbate-adsorbent interactions due to their structural resemblance. Differences are only due to the pore diameter. The values calculated for COF-102 indicate low host-guest interaction at zero coverage, and it is for that reason that the heat of adsorption increases with loading.
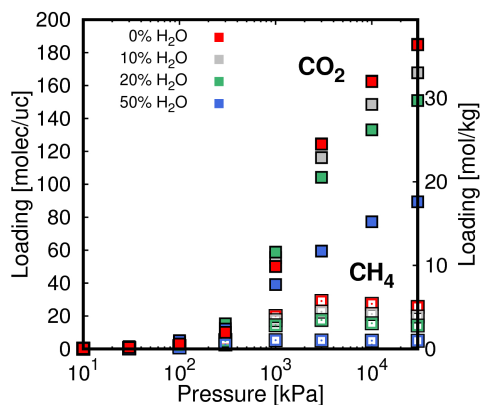
To analyze the separation capabilities of the proposed COFs, we calculated the adsorption isotherms of equimolar mixtures of carbon dioxide and methane. The adsorption isotherms are shown in Figure A2.3 in the Appendix 2 and here we only report the selectivity values (Figure 4) that indicate the large preference of all COFs for the molecule of carbon dioxide, being the molecule of methane almost excluded from some of the structures. Hence, at saturation pressures the number of molecules of methane per unit cell obtained from the equimolar adsorption isotherms is 1 for COF-6, 4 for COF-5 and 6 molec/uc for COF-10. Larger methane uptake is observed for COF-102 (29 molec/uc) at saturation pressure.

The adsorption selectivity is defined as $S = \frac{(x_A/y_A)}{(x_B/y_B)}$, were x_i is the molar fraction in the adsorbed phase for the i component and y_i the molar fraction in the bulk phase. As shown in Figure 4, the selectivity of the COFs in favour of carbon dioxide increases with pressure up to saturation pressure. The lowest values of selectivity
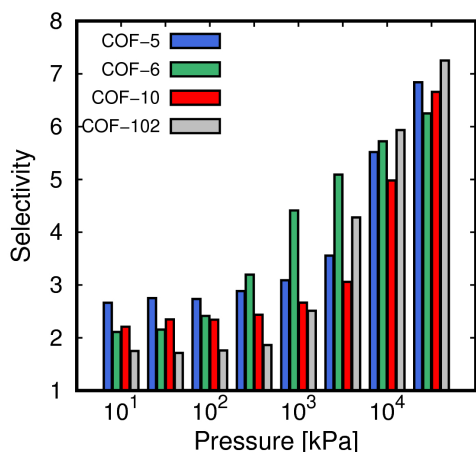
Figure 4. CO_2/CH_4 adsorption selectivity obtained from the adsorption isotherms of the equimolar mixture for COF-5, COF-6, COF-10, and COF-102 at 298 K.

Figure 5. Adsorption isotherms calculated for the CO_2/CH_4 mixture in the dehydrated and the hydrated COF-102 at 298 K. CO_2 (full symbols) and CH_4 (empty symbols). In order to compare with the different systems, the weight of the solvents is not taken into account in the isotherms.

are obtained at 10 kPa, and these are 2.6, 2.1, 2.2, and 1.8 for COF-5, -6, -10, and -102, respectively. To explore if the presence of water or any other solvent could improve the separation capability of these COFs, we generate hydrated structures and also structures loaded with ILs. Figure 5 shows the adsorption isotherms of the equimolar mixture in the dehydrated and the hydrated COF-102 (10 %, 20 %, and 50 %). The effect of hydration in adsorption is similar for the other COFs (Figures A2.4-2.6 at Appendix 2). As shown in the figure, the adsorption of carbon dioxide decreases with the degree of hydration of the structure. On the other hand, the adsorption of methane also decreases in the hydrated structures, and this component is completely excluded from the structures with 50 % of hydration.

In other words, it is possible to increase selectivity in favor of carbon dioxide via structural hydration. However, this requires high degree of hydration reducing by half the adsorption capacity of the structure in return (see Figures A2.4-2.6 of the Appendix 2). In an attempt to solve this drawback, we added ionic liquids to the dehydrated structure. As for water, the concentration of ionic liquid in the structure was defined using the accessible volume for each COF. As shown in Figure 6, the presence of IL within COF-102 (loaded with 10 % and 30 %) increases adsorption selectivity in favour of carbon dioxide without drastic reduction of the adsorption capacity of the structure. This effect is similar for the other COFs (Figures A2.11-2.13 in Appendix 2).
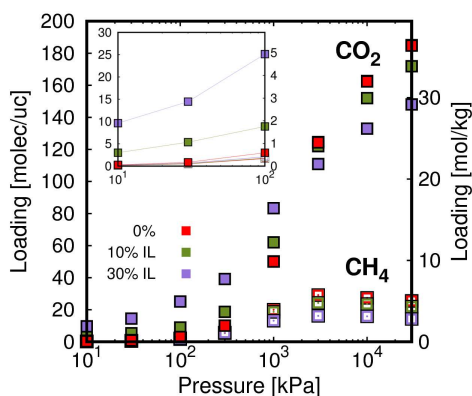
Figure 6. Adsorption isotherms calculated for the CO_2/CH_4 mixture at 298 K in COF-102 containing 10% of IL, 30% of IL, and without IL. CO_2 (full symbols) and CH_4 (empty symbols). In order to compare with the different systems, the weight of the solvents is not taken into account in the isotherms.

Figure A2.14 shows the effect of the weight of the solvent in the adsorption isotherm of carbon dioxide in each COF when the graph is given in moles of adsorbate per kilogram of structure. The decrease observed in the isotherm due to the mass of added ILs to the structure does not influence the final values of adsorption selectivity, because the factor is the same for both components of the mixture. In addition, to show the potential for the carbon dioxide adsorption in these systems with respect the ionic liquid itself, the figure includes the experimental adsorption isotherm of carbon dioxide in pure $[EMIM]^+$ $[SCN]^-$ ionic liquid.[43] The CO_2 uptake capacity of the COFs with larger pore volume is larger than the corre-

sponding to the pure ionic liquid. In addition, the adsorption in the selected porous materials takes place at values of pressure that are almost two orders of magnitude lower than in the ionic liquid.

The performance of each COF in adsorption selectivity as a function of pressure is analyzed in detail using the dehydrated structure and the structures with 10 %, 20 %, and 50 % hydration (see Figure 7 and Figures A2.7-2.10 in Appendix 2). In both, hydrated and dehydrated structures selectivity in favour of carbon dioxide incresases with presssure with a maximum at $3 \cdot 10^4$ kPa. However, as can be seen in Figure 7a selectivity is more than twice larger in the structures hydrated by 50 % than in the other structures. In contrast, the adsorption selectivity obtained for the structures with ILs is better at low pressure (Figures A2.15-2.18). In particular, at 10 kPa the selectivity for the structure containing 10 % IL is more than 8 times larger than the selectivity obtained for the dehydrated structure. It is also noteworthy that the selectivity obtained for the structure contining 30 % IL shows abrupt increase and is more than 20 times larger than the selectivity obtained for dehydrated COF-10 and -102 (Figure 7b), whereas the selectivity obtained for the hydrated structure is only twice the obtained for the dehydrated structure. Figures 7c and 7d show the same results than 7a and 7b but taking into account the capacity of each structure.
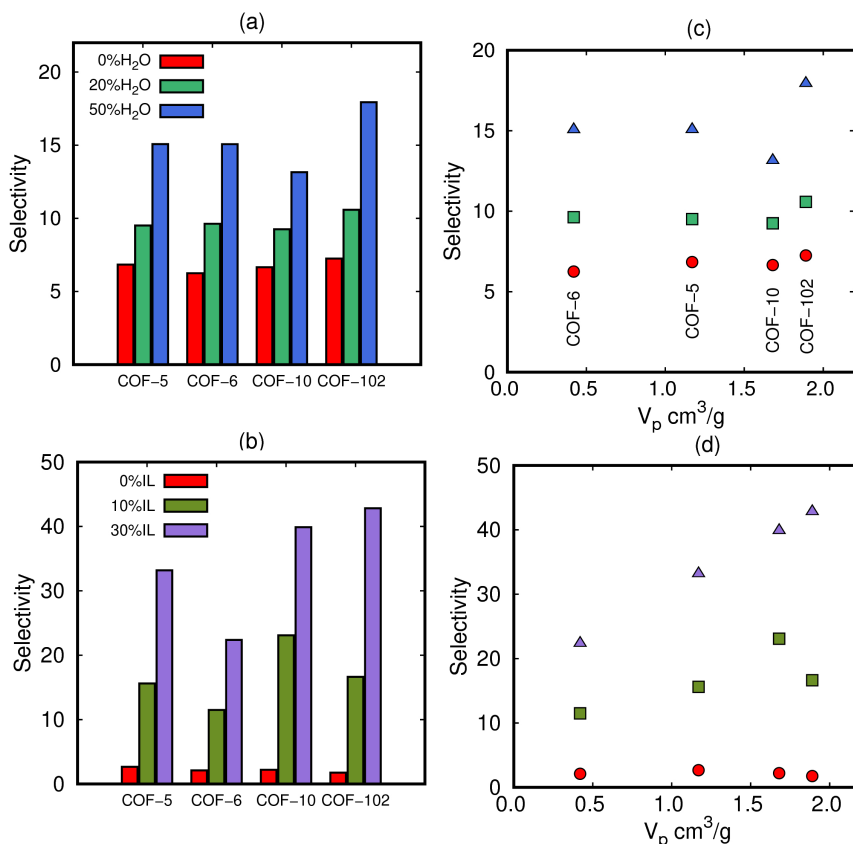
Figure 7. CO_2/CH_4 adsorption selectivity obtained from the adsorption isotherms of the mixture at 298 K in (a) the dehydrated and the hydrated structure at $3\cdot10^4$ kPa and (b) the structure without IL and with IL at 10 kPa. Adsorption selectivity as a function of the COF capacity in (c) the dehydrated and the hydrated structure at $3\cdot10^4$ kPa and (d) the structure without IL and with IL at 10 kPa.

CONCLUSIONS

We pursued the differences between the selectivities obtained from the adsorption of equimolar mixtures of carbon dioxide and methane in dehydrated and hydrated Covalent Organic Frameworks. We demonstrated that the presence of water can be used to increase the adsorption selectivity in favor of carbon dioxide when the adsorption is achieved at high pressure (above $3\cdot10^4$ kPa). The highest values of adsorption selectivity in favour of carbon dioxide were obtained for the hydrated COF-102 (3D COF) followed by the hydrated COF-5 (2D COF). It is also possible to improve the adsorption selectivity at low pressure by adding ionic liquids to the structure,

where the synergy ILs-COFs and the polarity of the IL make the difference. Therefore, the choice of the optimal pressure range to exploit the separation capabilities of these structures depends on the type of solvent used within the pores and the amount of available pore volume once the pores have been filled with the solvent. Taking into account both selectivity and adsorption capacity, the best candidates to separate carbon dioxide from methane at low pressure are COF-102 and COF-10 loaded with 30 % of IL, whereas at high pressure the best candidate will be COF-102 hydrated by 50 %.

Bibliography

[1] Cox, P. M.; Betts, R. A.; Jones, C. D.; Spall, S. A.; Totterdell, I. J. *Nature* **2000**, *408*, 750.

[2] Leaf, D.; Verolme, H. J. H.; Hunt, W. F. *Environ. Int.* **2003**, *29*, 303–310.

[3] Yang, H.; Xu, Z.; Fan, M.; Gupta, R.; Slimane, R. B.; Bland, A. E.; Wright, I. *J. Environ. Sci.* **2008**, *20*, 14–27.

[4] Peng, X.; Wang, W. C.; Xue, R. S.; Shen, Z. M. *Aiche J.* **2006**, *52*, 994–1003.

[5] Bai, B. C.; Cho, S.; Yu, H.-R.; Yi, K. B.; Kim, K.-D.; Lee, Y.-S. *J. Ind. Eng. Chem.* **2013**, *19*, 776–783.

[6] Huang, Z.; Xu, L.; Li, J.-H.; Guo, G.-M.; Wang, Y. *J. Chem. Eng. Data* **2010**, *55*, 2123–2127.

[7] Heymans, N.; Alban, B.; Moreau, S.; De Weireld, G. *Chem. Eng. Sci.* **2011**, *66*, 3850–3858.

[8] Garcia, E. J.; Mowat, J. P. S.; Wright, P. A.; Perez-Pellitero, J.; Jallut, C.; Pirngruber, G. D. *J. Phys. Chem. C* **2012**, *116*, 26636–26648.

[9] Krishna, R. *Microporous Mesoporous Mater.* **2012**, *156*, 217–223.

[10] Abid, H. R.; Pham, G. H.; Ang, H.-M.; Tade, M. O.; Wang, S. *J. Colloid Interface Sci.* **2012**, *366*, 120–124.

[11] Morishige, K. *J. Phys. Chem. C* **2011**, *115*, 9713–9718.

[12] Hao, S.; Zhang, J.; Zhong, Y.; Zhu, W. *Adsorpt. Int. Adsorpt. Soc.* **2012**, *18*, 423–430.

[13] Feng, X.; Ding, X.; Jiang, D. *Chem. Soc. Rev.* **2012**, *41*, 6010–6022.

[14] Ding, S.-Y.; Wang, W. *Chem. Soc. Rev.* **2013**, *42*, 548–568.

[15] Jackson, K. T.; Reich, T. E.; El-Kaderi, H. M. *Chem. Commun.* **2012**, *48*, 8823–8825.

[16] Tilford, R. W.; Mugavero III, S. J.; Pellechia, P. J.; Lavigne, J. J. *Adv. Mater.* **2008**, *20*, 2741–+.

[17] Xu, H.; Chen, X.; Gao, J.; Lin, J.; Addicoat, M.; Irle, S.; Jiang, D. *Chem. Commun.* **2014**, *50*, 1292–1294.

[18] Fang, Q.; Zhuang, Z.; Gu, S.; Kaspar, R. B.; Zheng, J.; Wang, J.; Qiu, S.; Yan, Y. *Nat. Commun.* **2014**, *5*.

[19] Shinde, D. B.; Kandambeth, S.; Pachfule, P.; Kumar, R. R.; Banerjee, R. *Chem. Commun.* **2015**, *51*, 310–313.

[20] Rabbani, M. G.; Sekizkardes, A. K.; Kahveci, Z.; Reich, T. E.; Ding, R.; El-Kaderi, H. M. *Chem. Eur. J.* **2013**, *19*, 3324–3328.

[21] Doonan, C. J.; Tranchemontagne, D. J.; Glover, T. G.; Hunt, J. R.; Yaghi, O. M. *Nat. Chem.* **2010**, *2*, 235–238.

[22] DeBlase, C. R.; Silberstein, K. E.; Thanh-Tam, T.; Abruna, H. D.; Dichtel, W. R. *J. Am. Chem. Soc.* **2013**, *135*, 16821–16824.

[23] Guo, J.; Xu, Y.; Jin, S.; Chen, L.; Kaji, T.; Honsho, Y.; Addicoat, M. A.; Kim, J.; Saeki, A.; Ihee, H.; Seki, S.; Irle, S.; Hiramoto, M.; Gao, J.; Jiang, D. *Nat. Commun.* **2013**, *4*.

[24] Furukawa, H.; Yaghi, O. M. *J. Am. Chem. Soc.* **2009**, *131*, 8875–8883.

[25] Tong, M.; Yang, Q.; Zhong, C. *Microporous Mesoporous Mater.* **2015**, *210*, 142–148.

[26] Smith, B. J.; Hwang, N.; Chavez, A. D.; Novotney, J. L.; Dichtel, W. R. *Chem. Commun.* **2015**, *51*, 7532–7535.

[27] Yan, F.; Lartey, M.; Damodaran, K.; Albenze, E.; Thompson, R. L.; Kim, J.; Haranczyk, M.; Nulwala, H. B.; Luebke, D. R.; Smit, B. *Phys. Chem. Chem. Phys.* **2013**, *15*, 3264–3272.

[28] Kumar, S.; Cho, J. H.; Moon, I. *Int. J. Greenh. Gas Control* **2014**, *20*, 87–116.

[29] Kolding, H.; Fehrmann, R.; Riisager, A. *Sci. China-Chemistry* **2012**, *55*, 1648–1656.

[30] Ramdin, M.; Balaji, S. P.; Vicent-Luna, J. M.; Gutiérrez-Sevillano, J. J.; Calero, S.; de Loos, T. W.; Vlugt, T. J. H. *J. Phys. Chem. C* **2014**, *118*, 23599–23604.

[31] Ramdin, M.; Balaji, S. P.; Manuel Vicent-Luna, J.; Torres-Knoop, A.; Chen, Q.; Dubbeldam, D.; Calero, S.; de Loos, T. W.; Vlugt, T. J. H. *Fluid Phase Equilib.* **2016**, *418*, 100–107.

[32] Corvo, M. C.; Sardinha, J.; Casimiro, T.; Marin, G.; Seferin, M.; Einloft, S.; Menezes, S. C.; Dupont, J.; Cabrita, E. J. *ChemSusChem* **2015**, *8*, 1935–1946.

[33] Gutiérrez-Sevillano, J. J.; Vicent-Luna, J. M.; Dubbeldam, D.; Calero, S. *J. Phys. Chem. C* **2013**, *117*, 11357–11366.

[34] Vicent-Luna, J. M.; Gutiérrez-Sevillano, J. J.; Anta, J. A.; Calero, S. *J. Phys. Chem. C* **2013**, *117*, 20762–20768.

[35] Chen, Y.; Hu, Z.; Gupta, K. M.; Jiang, J. *J. Phys. Chem. C* **2011**, *115*, 21736–21742.

[36] Gupta, K. M.; Chen, Y.; Hu, Z.; Jiang, J. *Phys. Chem. Chem. Phys.* **2012**, *14*, 5785–5794.

[37] Fujie, K.; Kitagawa, H. *Coord. Chem. Rev.* **2016**, *307*, 382–390.

[38] da Silva, F. W. M.; Magalhaes, G. M.; Jardim, E. O.; Silvestre-Albero, J.; Sepulveda-Escribano, A.; de Azevedo, D. C. S.; de Lucena, S. M. P. *Adsorpt. Sci. Technol.* **2015**, *33*, 223–242.

[39] Casado-Coterillo, C.; Fernandez-Barquin, A.; Zornoza, B.; Tellez, C.; Coronas, J.; Irabien, A. *Rsc Adv.* **2015**, *5*, 102350–102361.

[40] Lan, G.-Y.; Yang, Z.; Lin, Y.-W.; Lin, Z.-H.; Liao, H.-Y.; Chang, H.-T. *J. Mater. Chem.* **2009**, *19*, 2349–2355.

[41] Sun, G.-h.; Li, K.-x.; Sun, C.-g. *J. Power Sources* **2006**, *162*, 1444–1450.

[42] Revelli, A. L.; Mutelet, F.; Jaubert, J. N. *Ind. Eng. Chem. Res.* **2010**, *49*, 3883.

[43] Kim, J. E.; Kim, H. J.; Lim, J. S. *Fluid Phase Equilib.* **2014**, *367*, 151–158.

[44] Widom, B. *J. Chem. Phys.* **1963**, *39*, 2808–2812.

[45] Dubbeldam, D.; Calero, S.; Ellis, D. E.; Snurr, R. Q. *Mol. Simul.* **2016**, *42*, 81–101.

[46] Dubbeldam, D.; Torres-Knoop, A.; Walton, K. S. *Mol. Simul.* **2013**, *39*, 1253–1292.

[47] Cote, A. P.; Benin, A. I.; Ockwig, N. W.; O'Keeffe, M.; Matzger, A. J.; Yaghi, O. M. *Science (80-.).* **2005**, *310*, 1166–1170.

[48] Cote, A. P.; El-Kaderi, H. M.; Furukawa, H.; Hunt, J. R.; Yaghi, O. M. *J. Am. Chem. Soc.* **2007**, *129*, 12914–12915.

[49] El-Kaderi, H. M.; Hunt, J. R.; Mendoza-Cortes, J. L.; Cote, A. P.; Taylor, R. E.; O'Keeffe, M.; Yaghi, O. M. *Science (80-.).* **2007**, *316*, 268–272.

[50] Wilmer, C. E.; Kim, K. C.; Snurr, R. Q. *J. Phys. Chem. Lett.* **2012**, *3*, 2506–2511.

[51] Mayo, S. L.; Olafson, B. D.; Goddard, W. A. *J. Phys. Chem.* **1990**, *94*, 8897–8909.

[52] Rick, S. W. *J. Chem. Phys.* **2004**, *120*, 6085–6093.

[53] Potoff, J. J.; Siepmann, J. I. *Aiche J.* **2001**, *47*, 1676–1682.

[54] Harris, J. G.; Yung, K. H. *J. Phys. Chem.* **1995**, *99*, 12021–12024.

[55] Kelkar, M. S.; Maginn, E. J. *J. Phys. Chem. B* **2007**, *111*, 4867–4876.

[56] Chaumont, A.; Wipff, G. *Inorg. Chem.* **2009**, *48*, 4277–4289.

[57] Mendoza-Cortes, J. L.; Han, S. S.; Furukawa, H.; Yaghi, O. M.; Goddard III, W. A. *J. Phys. Chem. A* **2010**, *114*, 10824–10833.

CHAPTER
4

Role of Ionic Liquid [EMIM]$^+$[SCN]$^-$ in the Adsorption and Diffusion of Gasses in Metal-Organic Frameworks

José Manuel Vicent-Luna, Juan José Gutierrez-Sevillano, Juan Antonio Anta, and Sofía Calero

We study the adsorption performance of metal-organic frameworks (MOFs) impregnated of ionic liquids (ILs). To this aim we calculated adsorption and diffusion of light gases (CO_2, CH_4, N_2) and their mixtures in hybrid composites using molecular simulations. The hybrid composites consist of 1-ethyl-3-methylimidazolium thiocyanate impregnated in IRMOF-1, HMOF-1, MIL-47, and MOF-1. We found that the increase of the amount of IL enhances the adsorption selectivity in favour of carbon dioxide for the mixtures CO_2/CH_4 and CO_2/N_2 and in favour of methane in the mixture CH_4/N_2. We also provide detailed analysis of the microscopic organization of ILs and adsorbates via radial distribution functions and average occupation profiles and study the impact of the ILs in the diffusion of the adsorbates inside the pores of the MOFs. Based on our findings, we discuss the advantages of using IL/MOFs composites for gas adsorption to increase the adsorption of gases and to control the pore sizes of the structures to foster selective adsorption.
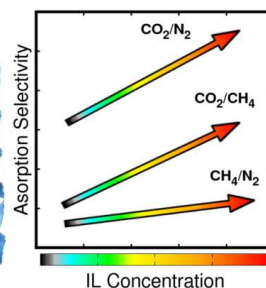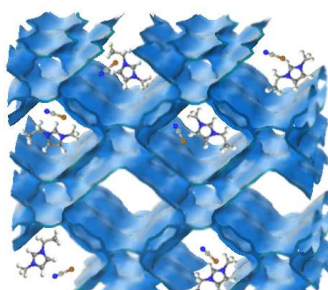
Introduction

Carbon dioxide capture and natural gas purification are processes of environmental interest.[1–3] For instance, the separation and purification of natural gas from mixtures containing nitrogen or carbon dioxide are still demanding processes since these two gases reduce the heat content of the fossil fuel. Efficient separation of carbon dioxide from nitrogen is also challenging.[4] Adsorption is an efficient process to achieve gas capture or separation at reducing cost. In particular, many studies proposed zeolites and metal-organic frameworks (MOFs) as excellent candidates for separation of gas mixtures involving CH_4, CO_2, and N_2.[5, 6] Metal-organic frameworks (MOFs) are a class of nanoporous materials characterized by high surface area, pore volume, and storage capacity. They are composed by metallic centers linked by organic ligands. A large variety of MOFs topologies can be synthesized using different metals and organic linkers. They can be designed for specific purposes focusing in the size or shape of cavities and chemical composition. Other compounds such as room-temperature ionic liquids (ILs) are an alternative to MOFs for gas capture. ILs are salts with melting points usually below the boiling temperature of water.[7] They are commonly used in a wide range of applications due to their nonflammable and nonvolatile nature as well as their high thermal stability, ionic conductivity

and very low vapor pressure. They are used as electrolytes in batteries,[8, 9] dye-sensitized solar cells (DSCs)[10–12] and ionic liquid crystals.[13] They are also good candidates to dissolve CO_2 as reported in experimental [14–17] and theoretical studies.[18–21] Since ILs are expensive compared to MOFs we are investigating an alternative combining these materials in IL/MOFs composites [22] generally known as nanoconfined ionic liquids systems [23] or supported ionic liquid membranes (SILM).[24] The aim is to improve the adsorption capabilities of MOFs with low amount of ILs. These composites were investigated previously by Jiang et al.[25–27] and computationally by ourselves.[28–30] Nowadays, this issue is still challenging.[22] Recent experimental studies [31–35] have corroborated our findings, making IL/MOFs composites realistic alternatives to conventional solvents. Even though many experimental efforts have been developed in the field, it is difficult to gain a molecular description of the fundamental understanding of the effect of confining ILs in nanopores. This is due to the complexity of the systems and the difficulties of analyzing individual effects (based on variables such as pore size, shape, and connectivity) on the properties of nanoconfined ILs systems. Molecular simulation is an optimal tool to complement experimental observations gaining insight into these questions. In our previous work, we investigated the IL/Cu-BTC composite for gas adsorption.

We explored adsorption capabilities of Cu-BTC for the adsorption of carbon dioxide, methane, and nitrogen when ILs are added into the MOF pores.[29] We analyzed the effect exerted by different anion types and varying the amount of ILs inside the composite, finding a strong interaction between ILs and carbon dioxide. This leads to an enhancement of the separation of carbon dioxide from methane and nitrogen in the Cu-BTC hybrid. Moreover, we compared the use of ILs with a common solvent like water in the separation of CO_2/CH_4 mixtures showing the advantages of the ILs.[28] In this work, we have extended previous studies to other MOFs and the IL composed by 1-ethyl-3-methylimidazolium [EMIM]$^+$ cation and thiocyanate [SCN]$^-$ anion. This IL is highly conductive and is less viscous than other ionic liquids.[36, 37] It has also been tested for the high carbon dioxide solubility.[38, 39] In our previous works [28, 29] we found that the addition of IL to a nanoporous structures results in an enhancement of the CO_2 adsorption with respect to the bare structure, and that this positive effect was attributed to the partially dipolar nature of this molecule. In this work we have included in our study IRMOF-1, HMOF-1, MIL-47, and MOF-1 so that a significant wide variety of topologies, chemical compositions, and pore volumes are covered. For these structures, we investigate the role of IL in the adsorption of CO_2/CH_4 and CO_2/N_2 mixtures, and discuss the separation of methane from

nitrogen as part of the process of natural gas purification. ILs are especially suited to capture compounds with which they strongly interact, as it is the case of carbon dioxide or acidic gases containing sulfur.[16, 40, 41] However, as we will show here, they can also improve MOFs capabilities for the separation of less interacting gases. In addition to adsorption properties, we also performed dynamical analysis focusing on diffusion coefficients. Calculation of diffusion coefficients is aimed at discarding mobility limitations of adsorbates produced by the ILs. Moreover radial distribution functions and average occupation profiles help to clarify the structural organization of ILs and adsorbates inside the MOFs. These properties allow for the understanding of the molecular mechanisms involved in the capture and separation molecular processes that take place in IL/MOFs composites.

SIMULATION DETAILS

We performed Monte Carlo (MC) simulations in the NVT ensemble and in the Grand Canonical ensemble (GCMC) and molecular dynamics (MD) in the NVT ensemble to study adsorption and dynamics of carbon dioxide, methane and nitrogen in the four selected MOFs. The simulation boxes are unit cells with side lengths of at least of 24 Å. The cavities of the structures are loaded with ILs. The IL ion pairs are added into the pores of MOFs using MC simulations in the NVT ensemble to relax

to their preferential sites inside the structures. Then we performed GCMC simulations to evaluate adsorption isotherms. Simulations require $2x10^5$ MC cycles after initialization to adequately average adsorption properties. To compare the effect of adding different amounts of IL to the structures, the adsorption isotherms do not take into account the weight of the added solvent. However, this effect is almost negligible as showed in our previous work.[28] In addition we performed MD simulations in the NVT ensemble to obtain transport properties of the adsorbates. These simulations consist of 10^7 cycles of production run with a time step of 0.5 fs (total simulation time, 5 ns). The initial configuration of these simulations is taken from the results of the adsorption of mixtures at room conditions. The temperature was set at 298 K and controlled using the Nose-Hoover thermostat.[42, 43] Lennard-Jones and Coulombic contributions to the potential were truncated with a cutoff of 12 Å. Coulombic interactions were evaluated using the particle-mesh Ewald method [44, 45] and Lennard-Jones parameters between different atoms were calculated using Lorentz-Berthelot mixing rules. Simulations were carried out using RASPA molecular simulation software.[46, 47] The IL is modeled using a full atom model with specific interactions in each atom. The cation is constituted by flexible ethyl and methyl groups attached to an imidazolium group which is modeled by a rigid ring, whereas the

anion is considered totally rigid. The potential parameters and point charges of the cation $[EMIM]^+$ were adopted from Kelkar and Maginn [48] and those of the anion $[SCN]^-$ were taken from Chaumont and Wipff.[49] An atomistic representation of this IL is depicted in Figure 1. We study systems containing carbon dioxide, methane, nitrogen, and their mixtures at room temperature. For carbon dioxide and nitrogen we used full atom models. To reproduce their quadrupole moments, we placed point charges in each atom for carbon dioxide [50, 51] and nitrogen, using for the latter an extra point charge in the center of mass of the molecule.[52, 53] For methane we used a united atom model with a single effective potential.[54, 55] MOFs were considered rigid structures and Lennard-Jones parameters are taken from DREIDING [56] force field except these for metallic atoms that were taken from UFF force field.[57] The complete set of charges for MOFs are taken from Bueno-Perez et al.[58] (MIL-47 and HMOF-1), Dubbeldam et al.[59] (MOF-1), and Frost et al.[60] and Dubbeldam et al.[61] (IRMOF-1).

As shown in Figure 1, MOF-1 and IRMOF-1 are formed by small (ϕ = 8.5 Å) and large (ϕ = 15 Å) cavities connected by small cages or windows, respectively. On the other hand, MIL-47 and HMOF-1 are formed by straight channels in one direction of 7 Å and 11 Å in diameter respectively.
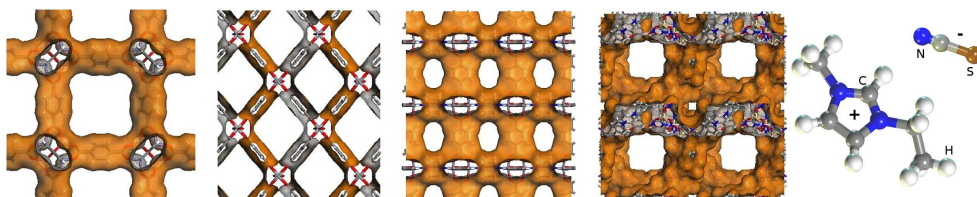
Figure 1. Schematic representation of MOFs and IL used in this work. From left to right: IRMOF-1, MIL-47, MOF-1, HMOF-1, and $[EMIM]^+[SCN]^-$.

Concerning the chemical composition, MOF-1, IRMOF-1, and MIL-47 have the same organic linker, (1,4-benzenedicarboxylate (BDC)) and in the case of HMOF-1 metallic centers are connected with chiral ligand (R)-6,6'-dichloro-2,2'-dihydroxy-1,1'-binaphthyl-4,4'-bipyridine. The coordination metals are zinc (IRMOF-1 and MOF-1), vanadium (MIL-47) and cadmium (HMOF-1). The MOF structures were reported by Eddaoudi et al.[62] (IRMOF-1), Dybtsev et al.[63] (MOF-1), Alaerts et al.[64] (MIL-47), and Wu and Lin [65]

Table 1. IL ion pairs (ILs) and their approximate percentage of volume (% V) occupied within the MOF pores.

MOF	ILs	% V
IRMOF-1	16	30
	24	45
	32	60
MIL-47	16	25
	24	40
	32	55
MOF-1	16	20
	24	35
	32	40
HMOF-1	16	10
	64	35

(HMOF-1). Table 1 shows the number of IL ion pairs per simulation box and the percentage of volume occupied inside the pores for the IL/MOF systems. The simulation box is larger for HMOF-1 than for the other structures, so we added more IL ion pairs to this structure.

RESULTS AND DISCUSSION

Figure 2 reports the pore size distribution of the MOFs, showing decreasing pore size in the order IRMOF-1, HMOF-1, MOF-1, and MIL-47. The structural properties of these MOFs are summarized in Table 2. IRMOF-1 and MIL-47 have similar available pore volume per simulation box, however IRMOF-1 exhibits large interconnected cavities symmetric in all directions and MIL-47 individual narrow straight channels in x direction (Figures 1-2). This fact affects the distribution of IL in the pores. In IRMOF-1 and MOF-1 the ILs are distributed homogenously. However, in MIL-47 and HMOF-1 the IL is divided filling the isolated channels. Figure 3 depicts a snapshot of the distribution of ILs in the cavities of IRMOF-1 and MIL-47 for the highest concentration studied.

Table 2. Large cavity diameter (LCD), pore volume (PV), framework density (FD), volume of the simulation cell (V/sc) and available pore volume per simulation cell (APV/sc) of the MOFs used in this work.

MOF	LCD [Å]	PV [cm^3/g]	FD [kg/m^3]	V/sc [$Å^3$]	APV/sc [$Å^3$]
IRMOF-1	15	1.37	593.3	17237.5	14043.1
MIL-47	7	0.61	1054.9	24546.3	15885.7
MOF-1	8.5	0.77	826.4	30985.5	19809.1
HMOF-1	11	0.65	891.4	81865.7	47312.7
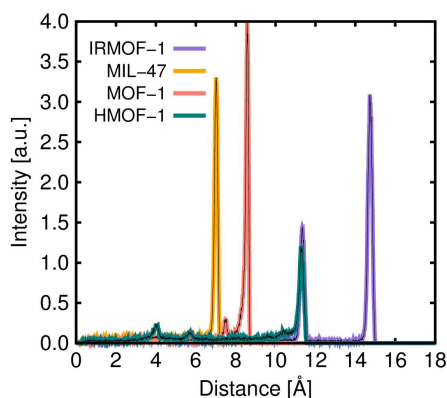
Figure 2. Pore size distribution of the MOFs used in this work.

The effect exerted by the IL in the adsorption of the adsorbates varies with the MOF. Figures 4-6 show adsorption isotherms of the equimolar mixtures CO_2/CH_4, CO_2/N_2, and CH_4/N_2 in the bare and hybrid structures at 298 K. Mixtures involving carbon dioxide exhibit similar behavior in all situations where it is the most adsorbed component. This is also the trend observed for the adsorption isotherms of single carbon dioxide as shown in Figure A3.1 of the Appendix 3. The onset pressures of carbon dioxide adsorption increases with the size of the pores as shown in Figure 2.
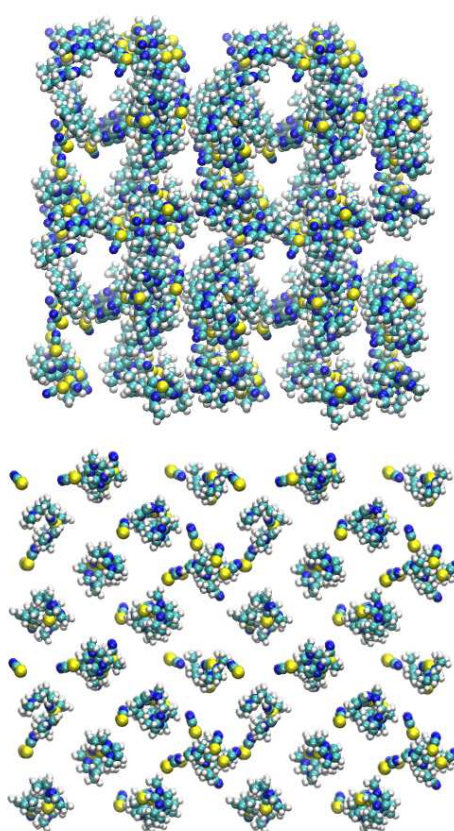
Figure 3. Representative snapshot of IL ion pairs in IRMOF-1 (top) and MIL-47 (bottom). The snapshot is replicated to a 2x2x2 simulation cell so that the IL network is more clearly visualized.
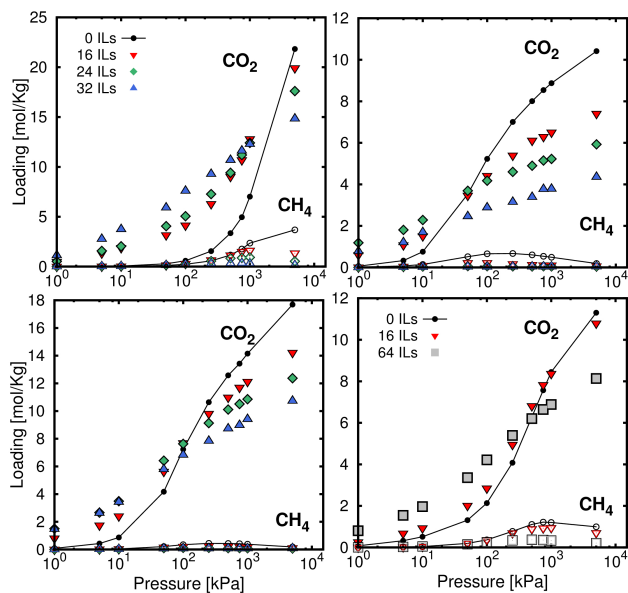
Figure 4. Calculated adsorption isotherm (298 K) of equimolar CO_2/CH_4 mixtures on IRMOF-1 (top-left), MIL-47 (top right), MOF-1 (bottom left), and HMOF-1 (bottom right) with IL loaded within the pores.
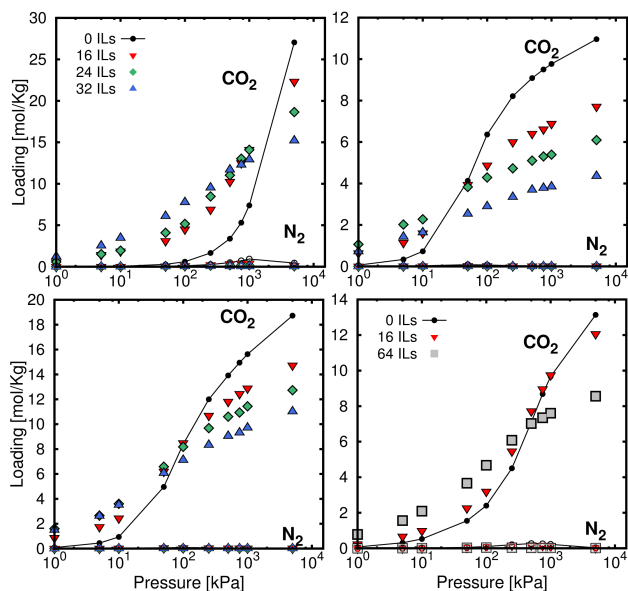
Figure 5. Calculated adsorption isotherm (298 K) of equimolar CO_2/N_2 mixtures on IRMOF-1 (top-left), MIL-47 (top right), MOF-1 (bottom left), and HMOF-1 (bottom right) with ILs loaded within the pores.
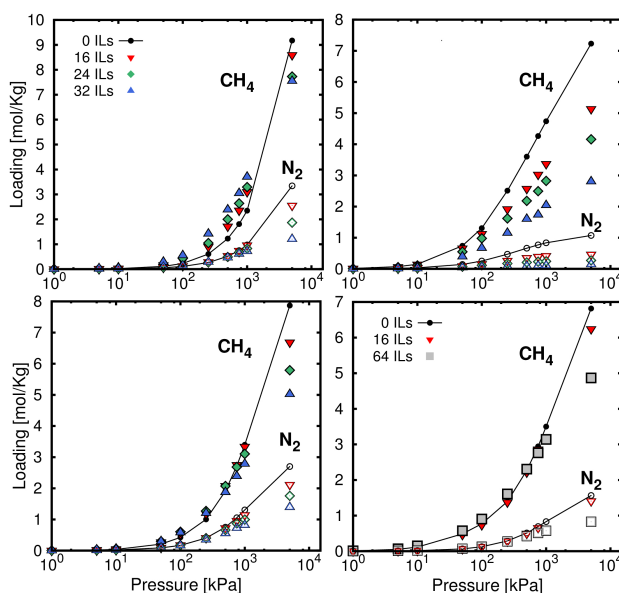
Figure 6. Calculated adsorption isotherm (298 K) of equimolar N_2/CH_4 mixtures in IRMOF-1 (top-left), MIL-47 (top right), MOF-1 (bottom left), and HMOF-1 (bottom right) with ILs loaded within the pores.

The presence of ILs within the MOFs enhances the adsorption of carbon dioxide up to a given value of pressure that depends on the structure. Above this value, the presence of ILs reduces the adsorption of carbon dioxide due to the lack of accessible pore volume of the IL/MOF composites. The increase of carbon dioxide adsorption in the structures with ILs is larger for IRMOF-1, the structure with the highest pore volume and where the ion pairs are allocated in the big cavities, distributed as in the liquid phase (Figure 3). The solubility of carbon dioxide in the IL enhances adsorption in IL/IRMOF-1 composite. The adsorption isotherms calculated for methane and nitrogen (single

components) in the MOFs show that the adsorption in IL/MOF-1 and IL/HMOF-1 is almost unaffected by the IL concentration (Figure A3.2 of the Appendix 3). In IL/IRMOF-1 we found a slight increase in the loading of CH_4 and N_2 that can be attributed to the solubility of these gases in the IL. However, the effect is small since the solubility of these gases is low compared with the solubility of carbon dioxide.[19] IL/MIL-47 exhibits opposite behavior. The increase of the concentration of IL reduces the accessible pore volume and therefore the adsorption of methane and nitrogen. The adsorption isotherms calculated for the CO_2/CH_4 and CO_2/N_2 mixtures show that the presence

of ILs excludes most methane and all nitrogen from the structures. A recent work reported a MOF with extraordinary CO_2/N_2 adsorption selectivity that was synthetized controlling the pore/window size.[4] However, the adsorption capacity of the structure is very much limited by the pore size of about 4 Å. Instead of this strategy that demands precise MOF design, we suggest adding IL into the MOF pores to control the accessible pore volume. With this strategy, the structures become blocking for nitrogen adsorption in the CO_2/N_2 mixture, while keeping a relatively high adsorption capacity (Figure 5).

The use of IL confined within the MOF is mostly used to improve the adsorption of adsorbates that interact strongly with the ILs, i.e. those with high solubility in IL-based solvents. In the case of N_2/CH_4 mixtures (Figure 6) the two components have low solubility in IL. However, the adsorption of methane in IL/IRMOF-1 becomes favored with respect to the less soluble component when the proportion of IL is larger, hence improving the separation. On the other hand, the ILs reduce the adsorption of the two components of the mixture in IL/MIL-47, and almost excludes totally nitrogen. The presence of IL in IL/MOF-1 and IL/HMOF-1 only modifies the adsorption isotherms at very high pressures.

Table 3. Adsorption selectivity in the studied systems (equimolar mixtures at 298 K and 100 kPa). Values in brackets indicate the increment factor of selectivity regarding the selectivity in the bare structures.

MOF	ILs	CO_2/CH_4	CO_2/N_2	CH_4/N_2
IRMOF-1	0	2.5	5.5	2.1
	16	14.3 (5.7)	46.3 (8.4)	2.8 (1.3)
	24	18.9 (7.6)	65.3 (11.9)	3.4 (1.6)
	32	40.8 (16.3)	168.7 (30.7)	4.2 (2.0)
MIL-47	0	7.9	90.4	5.2
	16	20.1 (2.5)	234.8 (2.6)	7.1 (1.4)
	24	73.3 (9.3)	519.8 (5.8)	8.7 (1.7)
	32	105.9 (13.4)	515.8 (5.7)	11.7 (2.3)
MOF-1	0	20.8	95.1	2.5
	16	37.3 (1.8)	193.2 (2.0)	3.0 (1.2)
	24	66.5 (3.2)	349.7 (3.7)	3.3 (1.3)
	32	103.2 (5.0)	507.3 (5.3)	3.6 (1.4)
HMOF-1	0	5.8	24.4	6.1
	16	7.8 (1.3)	35.9 (1.5)	5.9 (0.9)
	64	17.8 (3.1)	126.8 (5.2)	7.1 (1.2)

The adsorption selectivity can be extracted from Figures 4-6 as $S = (x_A/y_A)/(x_B/y_B)$ where x_i and y_i are the molar fraction of the i component in the adsorbed and in the bulk phase, respectively. In the case of equimolar mixtures y_i=0.5, hence $S = x_A/x_B$. The adsorption selectivity increases with the addition of IL to the MOFs (Figures A3.3-3.5 in the Appendix 3). To quantify the improvement Table 3 summarizes the adsorption selectivity for all the studies systems at room conditions. The table contains the variation of the selectivity regarding to the selectivity in the structure without IL. The adsorption selectivity for the CO_2/CH_4 mixture is always in favor of carbon dioxide with enhancement factors of 16.3 (IL/IRMOF-1), 13.4 (IL/MIL-47), 5.0 (IL/MOF-1), and 3.1 (IL/HMOF-1), respectively. For the CO_2/N_2 mixtures in

IL/IRMOF-1 the factor is 30 and around 5 for the other IL/MOFs. IL/IRMOF-1 and IL/MIL-47 are also the best candidates for the separation of CH_4/N_2 mixtures, providing twice the value of the reference (bare) structures.

The results provided by the simulations suggest that for applications involving adsorptive gas separation, the impregnation of structures with a certain amount of ILs inside their pores is an efficient technique. One strategy consists in selecting structures with large cavities so that the IL could act as a fluid dissolving the most adsorbed component. The larger solubility of one of the components of the mixture in IL leads to more adsorption of this component and consequently less adsorption of the other, hence improving the separation. A second strategy is to select structures which pore sizes that can be tuned with the IL concentration. This leads to the removal of the less adsorbed component, hence purifying the most adsorbed component.

Figure 7 depicts the average occupation profiles of carbon dioxide in the bare IRMOF-1 and in IL/IRMOF-1 loaded with the highest concentration (32 IL ion pairs per simulation box). These profiles were calculated at 298 K and 100 kPa. In the bare structure carbon dioxide is adsorbed almost homogenously near the metallic centers. The loading of carbon dioxide increases in the IL/IRMOF-1 where the gas molecules form clusters around the IL ion pairs. This indicates that IL dissolves the

compound generating new centers of adsorption for the molecule inside the MOF. The average occupation profiles obtained for carbon dioxide in the other IL/MOFs structures are similar than for IL/IRMOF-1 as shown in Figures A3.6-3.8 of the Appendix 3.
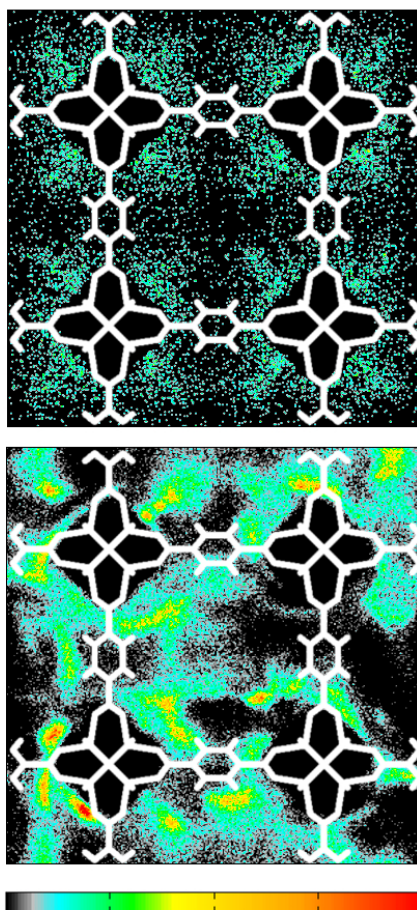
Figure 7. Average occupation profiles of carbon dioxide in the bare IRMOF-1 (top) and in the structure loaded with 32 IL ion pairs (bottom).
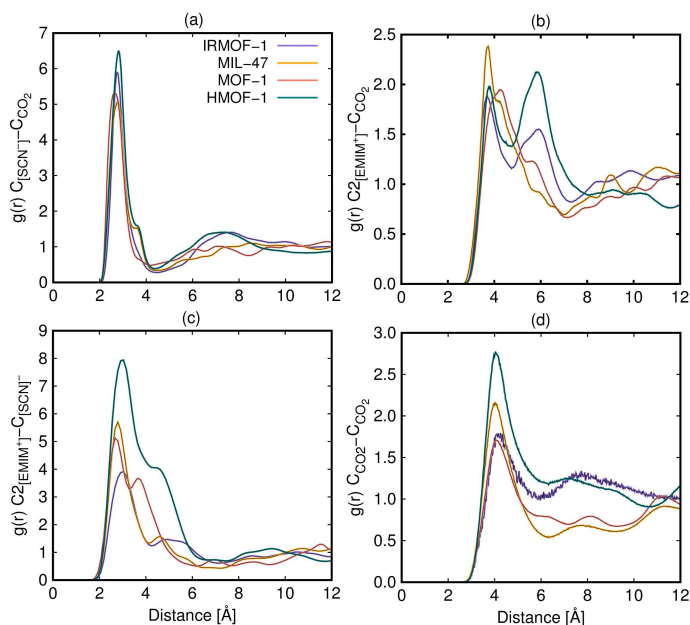
Figure 8. Radial distribution functions between anion-CO_2 (a), cation-CO_2 (b), cation-anion (c), and CO_2-CO_2 (d) for the systems with the highest IL concentration. The reference atoms are the carbon atoms of CO_2 and the anion and the carbon atom of the imidazolium ring of the cation attached to nitrogen atoms.

The radial distribution functions (RDFs) between the adsorbate and IL constituents provide information about the microscopic organization of carbon dioxide around IL moieties (Figure 8). Carbon dioxide interacts more strongly with the anion that with the cation. The central atom of the molecule is located at less than 3 Å of the central atom of the anion in all structures. This proximity together with the intensity of the first peak prove the affinity of the anion for carbon dioxide. On the other hand, carbon dioxide is adsorbed at distances close to 4 Å of the imidazolium ring of the cation with a lower intensity than in the case of the anion. In IRMOF-1 and HMOF-1, the RDFs show a second peak at about 6 Å. This is because they have the largest pore sizes and allow for the formation of a second coordination shell in the same cavity. Moreover, cation and anion are placed together at distances lower than 3 Å, thus preventing a charge balance in the systems. Finally, CO_2-CO_2 RDFs evidence that the interaction of the molecules of carbon dioxide with the anion is stronger than between the carbon dioxide molecules themselves.
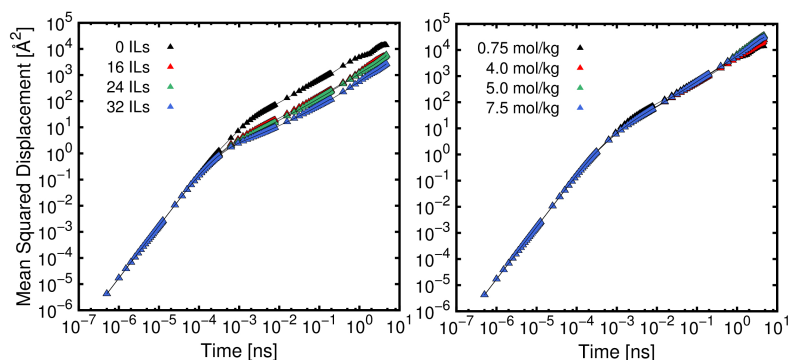
Figure 9. Mean squared displacement of carbon dioxide in IRMOF-1 containing ILs (left) and for several loadings of carbon dioxide in the bare IRMOF-1 (right).

Gas separation in porous materials involves adsorption and diffusion. Hence, we performed MD simulations to calculate diffusion coefficients of carbon dioxide and methane in the IL/MOF composites. The diffusion of nitrogen is excluded from the analysis since the adsorption of this component, as shown above, is almost negligible in most structures. Figure 9 shows the mean squared displacement (MSD) of carbon dioxide in IL/IRMOF-1. Even in the less favorable situation the adsorbate molecules can diffuse through the IL/IRMOF pores within the simulation time scale considered, although the increase of the IL concentration reduces the diffusion of the adsorbate. This could be due to two factors, the presence of IL inside the pores or the increase of the loading of carbon dioxide in the system. To assess what is the main cause, we performed MD simulations for several loadings of carbon dioxide in the bare structure. The chosen loading of carbon dioxide matches the loading of the adsorption isotherm at 100 kPa in the IL/IRMOF-1 composites. As shown in Figure 9 the MSD is almost unaffected by the carbon dioxide loading. This proves that the slowdown in the CO_2 diffusion in the IL/IRMOF-1 composites is mostly due to the interaction of the adsorbates with the IL ion pairs. We found similar behavior of the MSD of carbon dioxide for the other IL/MOFs composites (Figure A3.9 of the Appendix 3).

To study in depth the origin of the lower mobility of the adsorbates with the addition of ILs, we have also calculated self-diffusion coefficients of carbon dioxide and methane. In Figure 10, the self-diffusion coefficients are plotted as a function of the percentage of volume occupied by the IL in the composite (Table I). The self-diffusion coefficients of the adsorbates are slightly lower for carbon dioxide than for methane. This is consistent with the adsorption that is always higher for the former than for the latter.
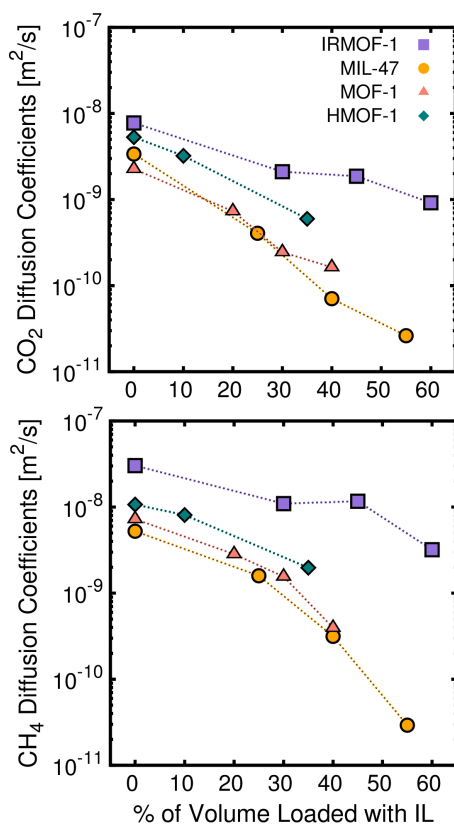
Figure 10. Self-diffusion coefficients of carbon dioxide (top) and methane (bottom) as a function of the percentage of volume occupied by IL within the MOF pores. Dashed lines are guides to the eyes.

Self-diffusion coefficients depend on the pore size of the structure. MOFs with larger pore sizes allow faster diffusion of the adsorbed compounds. On the other hand, the decrease if the self-diffusion coefficients with the IL concentration is more pronounced in MOFs with narrow pores. The self diffusion of the adsorbates decreases up to one order of magnitude in the IL/IRMOF-1 composite with the highest

IL concentration and two orders of magnitude in IL/MIL-47. However, despite this diminution, the diffusion of the adsorbates is guaranteed even for the most unfavorable conditions.

CONCLUSIONS

By means of molecular dynamics simulations, we have investigated the effect exerted by the presence of ionic liquids in the adsorption of carbon dioxide, methane, nitrogen, and their mixtures in MOFs. We found that ILs enhance the CO_2 adsorption selectivity. The selectivity enhacement is especially remarkable for structures with large interconnected cavities. This is attributed to the improved solubility of carbon dioxide in the IL. Another strategy to improve the separation capabilities of the structures with narrow pores is the use of ILs to control the pore size. This can lead to the exclusion of the less adsorbed component of the mixture, thus purifying the mixture in the preferred component. The presence of ILs in the pores reduces the mobility of the adsorbates but still allows diffusion through the cavities even for the highest IL concentration studied.

Bibliography

[1]   Cox, P. M.; Betts, R. A.; Jones, C. D.; Spall, S. A.; Totterdell, I. J. *Nature* **2000**, *408*, 750.

[2]   Lin, H.; White, L. S.; Lokhandwala, K.; Baker, R. W.; Hoek, E. M. V.; Tarabara, V. V. *Encycl. Membr. Sci. Technol.*; John Wiley & Sons, Inc., 2013.

[3] Leaf, D.; Verolme, H. J. H.; Hunt, W. F. *Environ. Int.* **2003**, *29*, 303–310.

[4] Zhang, L.; Jiang, K.; Jiang, M.; Yue, D.; Wan, Y.; Xing, H.; Yang, Y.; Cui, Y.; Chen, B.; Qian, G. *Chem. Commun.* **2016**, *52*, 13568–13571.

[5] Keskin, S.; van Heest, T. M.; Sholl, D. S. *ChemSusChem* **2010**, *3*, 879–891.

[6] Mason, J. A.; McDonald, T. M.; Bae, T.-H.; Bachman, J. E.; Sumida, K.; Dutton, J. J.; Kaye, S. S.; Long, J. R. *J. Am. Chem. Soc.* **2015**, *137*, 4787–4803.

[7] Plechkova, N. V.; Seddon, K. R. *Chem. Soc. Rev.* **2008**, *37*, 123–150.

[8] Vicent-Luna, J. M.; Ortiz-Roldan, J. M.; Hamad, S.; Tena-Zaera, R.; Calero, S.; Anta, J. A. *Chemphyschem* **2016**, *17*, 2473–2481.

[9] Azaceta, E.; Lutz, L.; Grimaud, A.; Vicent-Luna, J. M.; Hamad, S.; Yate, L.; Cabanero, G.; Grande, H. J.; Anta, J. A.; Tarascon, J. M.; Tena-Zaera, R. *ChemSusChem* **2017**, *10*, 1616–1623.

[10] Vicent-Luna, J. M.; Idígoras, J.; Hamad, S.; Calero, S.; Anta, J. A. *J. Phys. Chem. C* **2014**, *118*, 28448–28455.

[11] Guillén, E.; Fernández-Lorenzo, C.; Alcántara, R.; Martín-Calleja, J.; Anta, J. A. *Sol. Energy Mater. Sol. Cells* **2009**, *93*, 1846–1852.

[12] Kuang, D.; Klein, C.; Zhang, Z.; Ito, S.; Moser, J.-E.; Zakeeruddin, S. M.; Graetzel, M. *Small* **2007**, *3*, 2094–2102.

[13] Trilla, M.; Pleixats, R.; Parella, T.; Blanc, C.; Dieudonne, P.; Guari, Y.; Man, M. W. C. *Langmuir* **2008**, *24*, 259–265.

[14] Lei, Z.; Dai, C.; Chen, B. **2012**,

[15] Tome, L. C.; Florindo, C.; Freire, C. S. R.; Rebelo, L. P. N.; Marrucho, I. M. *Phys. Chem. Chem. Phys.* **2014**, *16*, 17172–17182.

[16] Ramdin, M.; de Loos, T. W.; Vlugt, T. J. H. *Ind. Eng. Chem. Res.* **2012**, *51*, 8149–8177.

[17] Babarao, R.; Dai, S.; Jiang, D.-e. *J. Phys. Chem. B* **2011**, *115*, 9789–9794.

[18] Ramdin, M.; Chen, Q.; Balaji, S. P.; Manuel Vicent-Luna, J.; Torres-Knoop, A.; Dubbeldam, D.; Calero, S.; de Loos, T. W.; Vlugt, T. J. H. *J. Comput. Sci.* **2016**, *15*, 74–80.

[19] Ramdin, M.; Balaji, S. P.; Vicent-Luna, J. M.; Gutiérrez-Sevillano, J. J.; Calero, S.; de Loos, T. W.; Vlugt, T. J. H. *J. Phys. Chem. C* **2014**, *118*, 23599–23604.

[20] Cadena, C.; Anthony, J. L.; Shah, J. K.; Morrow, T. I.; Brennecke, J. F.; Maginn, E. J. *J. Am. Chem. Soc.* **2004**, *126*, 5300–5308.

[21] Lourenço, T. C.; Coelho, M. F. C.; Ramalho, T. C.; Van Der Spoel, D.; Costa, L. T. *Environ. Sci. Technol.* **2013**, *47*, 7421–7429.

[22] Kinik, F. P.; Uzun, A.; Keskin, S. *ChemSusChem* **2017**, *10*, 2842–2863.

[23] Zhang, S.; Zhang, J.; Zhang, Y.; Deng, Y. *Chem. Rev.* **2017**, *117*, 6755–6833.

[24] Wang, J.; Luo, J.; Feng, S.; Li, H.; Wan, Y.; Zhang, X.

[25] Gupta, K. M.; Chen, Y.; Jiang, J. *J. Phys. Chem. C* **2013**, *117*, 5792–5799.

[26] Gupta, K. M.; Chen, Y.; Hu, Z.; Jiang, J. *Phys. Chem. Chem. Phys.* **2012**, *14*, 5785–5794.

[27] Chen, Y.; Hu, Z.; Gupta, K. M.; Jiang, J. *J. Phys. Chem. C* **2011**, *115*, 21736–21742.

[28] Vicent-Luna, J. M.; Luna-Triguero, A.; Calero, S. *J. Phys. Chem. C* **2016**, *120*, 23756–23762.

[29] Vicent-Luna, J. M.; Gutiérrez-Sevillano, J. J.; Anta, J. A.; Calero, S. *J. Phys. Chem. C* **2013**, *117*, 20762–20768.

[30] Gutiérrez-Sevillano, J. J.; Vicent-Luna, J. M.; Dubbeldam, D.; Calero, S. *J. Phys. Chem. C* **2013**, *117*, 11357–11366.

[31] Luo, Q. X.; An, B. W.; Ji, M.; Park, S. E.; Hao, C.; Li, Y. Q. *J. Porous Mater.* **2015**, *22*, 247–259.

[32] da Silva, F. W. M.; Magalhaes, G. M.; Jardim, E. O.; Silvestre-Albero, J.; Sepulveda-Escribano, A.; de Azevedo, D. C. S.; de Lucena, S. M. P. *Adsorpt. Sci. Technol.* **2015**, *33*, 223–242.

[33] Koyuturk, B.; Altintas, C.; Kinik, F. P.; Keskin, S.; Uzun, A. *J. Phys. Chem. C* **2017**, *121*, 10370–10381.

[34] Sezginel, K. B.; Keskin, S.; Uzun, A. *Langmuir* **2016**, *32*, 1139–1147.

[35] Althuluth, M.; Overbeek, J. P.; van Wees, H. J.; Zubeir, L. F.; Haije, W. G.; Berrouk, A.; Peters, C. J.; Kroon, M. C. *J. Memb. Sci.* **2015**, *484*, 80–86.

[36] Lan, G.-Y.; Yang, Z.; Lin, Y.-W.; Lin, Z.-H.; Liao, H.-Y.; Chang, H.-T. *J. Mater. Chem.* **2009**, *19*, 2349–2355.

[37] Sun, G.-h.; Li, K.-x.; Sun, C.-g. *J. Power Sources* **2006**, *162*, 1444–1450.

[38] Revelli, A. L.; Mutelet, F.; Jaubert, J. N. *Ind. Eng. Chem. Res.* **2010**, *49*, 3883.

[39] Kim, J. E.; Kim, H. J.; Lim, J. S. *Fluid Phase Equilib.* **2014**, *367*, 151–158.

[40] Khan, N. A.; Hasan, Z.; Hwa, S. **2014**, 376–380.

[41] Jamali, S. H.; Ramdin, M.; Becker, T. M.; Torres-Knoop, A.; Dubbeldam, D.; Buijs, W.; Vlugt, T. J. H. *Fluid Phase Equilib.* **2017**, *433*, 50–55.

[42] Nose, S. *Mol. Phys.* **2002**, *100*, 191–198.

[43] Hoover, W. G. *Phys. Rev. A* **1985**, *31*, 1695–1697.

[44] Essmann, U.; Perera, L.; Berkowitz, M. L.; Darden, T.; Lee, H.; Pedersen, L. G. *J. Chem. Phys.* **1995**, *103*, 8577–8593.

[45] Darden, T.; York, D.; Pedersen, L. *J. Chem. Phys.* **1993**, *98*, 10089–10092.

[46] Dubbeldam, D.; Calero, S.; Ellis, D. E.; Snurr, R. Q. *Mol. Simul.* **2016**, *42*, 81–101.

[47] Dubbeldam, D.; Torres-Knoop, A.; Walton, K. S. *Mol. Simul.* **2013**, *39*, 1253–1292.

[48] Kelkar, M. S.; Maginn, E. J. *J. Phys. Chem. B* **2007**, *111*, 4867–4876.

[49] Chaumont, A.; Wipff, G. *Inorg. Chem.* **2009**, *48*, 4277–4289.

[50] Garcia-Sanchez, A.; Ania, C. O.; Parra, J. B.; Dubbeldam, D.; Vlugt, T. J. H.; Krishna, R.; Calero, S. *J. Phys. Chem. C* **2009**, *113*, 8814–8820.

[51] Harris, J. G.; Yung, K. H. *J. Phys. Chem.* **1995**, *99*, 12021–12024.

[52] Stogryn, D. E.; Stogryn, A. P. *Mol. Phys.* **1966**, *11*, 371.

[53] Murthy, C. S.; Singer, K.; Klein, M. L.; McDonald, I. R. *Mol. Phys.* **1980**, *41*, 1387–1399.

[54] Dubbeldam, D.; Calero, S.; Vlugt, T. J. H.; Krishna, R.; Maesen, T. L. M.; Smit, B. *J. Phys. Chem. B* **2004**, *108*, 12301–12313.

[55] Ryckaert, J. P.; Bellemans, A. *Faraday Discuss.* **1978**, 95–106.

[56] Mayo, S. L.; Olafson, B. D.; Goddard, W. A. *J. Phys. Chem.* **1990**, *94*, 8897–8909.

[57] Rappe, A. K.; Casewit, C. J.; Colwell, K. S.; Goddard, W. A.; Skiff, W. M. *J. Am. Chem. Soc.* **1992**, *114*, 10024–10035.

[58] Bueno-Perez, R.; Martin-Calvo, A.; Gomez-Alvarez, P.; Gutierrez-Sevillano, J. J.; Merkling, P. J.; Vlugt, T. J. H.; van Erp, T. S.; Dubbeldam, D.; Calero, S. *Chem. Commun.* **2014**, *50*, 10849–10852.

[59] Dubbeldam, D.; Galvin, C. J.; Walton, K. S.; Ellis, D. E.; Snurr, R. Q. *J. Am. Chem. Soc.* **2008**, *130*, 10884–10885.

[60] Frost, H.; Düren, T.; Snurr, R. Q. *J. Phys. Chem. B* **2006**, *110*, 9565–9570.

[61] Dubbeldam, D.; Frost, H.; Walton, K. S.; Snurr, R. Q. *Fluid Phase Equilib.* **2007**, *261*, 152.

[62] Eddaoudi, M.; Kim, J.; Rosi, N.; Vodak, D.; Wachter, J.; O'Keefe, M.; Yaghi, O. M. *Science (80-.).* **2002**, *295*, 469.

[63] Dybtsev, D. N.; Chun, H.; Kim, K. *Ang. Chem. Int. Ed.* **2004**, *43*, 5033.

[64] Alaerts, L.; kirschcock, C.; Maes, M.; van der Veen, M.; Finsy, V.; Depla, A.; Martens, J.; Baron, G.; Jacobs, P.; Denayer, J. F.; De Vos, D. *Angew. Chemie Int. Ed.* **2007**, *46*, 4293–4297.

[65] Wu, C.-D.; Lin, W. *Angew. Chemie Int. Ed.* **2007**, *46*, 1075–1078.

Ion Transport in Electrolytes for Dye-Sensitized Solar Cells: A Combined Experimental and Theoretical Study

José Manuel Vicent-Luna, Jesús Idígoras, Said Hamad, Sofía Calero, and Juan Antonio Anta

The ion transport properties of electrolytes based on room temperature ionic liquids (RTILs) used in dye-sensitized solar cells (DSCs) have been studied by electrochemical voltammetry experiments and molecular dynamics (MD) simulations. Fully atomistic models based on the Lennard-Jones potential with atomic point charges have been developed for imidazolium and pyrrolidinium imides ($[Tf_2N]^-$). MD simulations with the proposed force-fields reproduce accurately the density and the self-diffusion coefficient of the anion and cation of the RTIL, as well as their temperature dependence and the effect of the length of the alkyl chain. The diffusion coefficients of iodide/tri-iodide redox mediator in mixture of RTIL and acetonitrile have been studied by voltammetry and MD. Both experiment and simulation show a two orders of magnitude decrease of the diffusion coefficient of the redox mediator between pure acetonitrile and pure RTIL. However, the variation of the diffusion coefficient with the RTIL/acetonitrile mixing ratio shows that a small amount of acetonitrile is sufficient to induce an improvement of the ion transport properties of the electrolyte, which can be very beneficial to design efficient and stable electrolytes for DSCs.
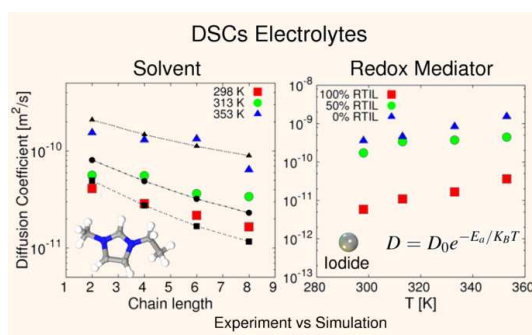
INTRODUCTION

The dye-sensitized solar cell (DSC), discovered by O'Regan and Grätzel in 1991,[1] is one of the most studied concepts in modern photovoltaics. This type of solar cell is based on the combination of a mesoporous metal-oxide, typically TiO_2, an organic dye that acts as light harvester sensitizing the oxide, and a liquid electrolyte that embeds the mesoporous nanostructure. The role of the electrolyte is to drive the electrochemical reactions of dye regeneration and transport of holes to the external contact. DSCs have recently achieved a record efficiency of 13%.[2] Furthermore, they are considered the basis of the promising perovskite solar cell concept,[3] which has already reported efficiencies as high as 19.3%.[4–6]

The main drawback of DSCs is the lack of long term stability due to the liquid nature of the electrolyte. This is the cause of electrolyte leakage and evaporation losses. Although this inconvenience can be surmounted by the use of solid hole conductors, the relatively low electronic conductivity of these materials as well as their high recombination rate and low stability limit their performance. In this context, the use of room-temperature ionic liquids (RTILs),[7] has been recognized as a very interesting alternative, due to their negligible vapor pressure and relatively high ionic conductivities.[8]

In spite of the importance of RTILs as electrolytes in DSCs, there are very few studies discussing the structure and dynamics of RTILs mixtures as working electrolytes for DSCs from the theoretical point of view.[9, 10] Furthermore, very recently the possibility of using mixtures of RTILs and organic solvents as a good compromise between efficiency and stability has been stressed.[11] These studies point to the relevance of transport of electrochemically active species, that is, iodide and tri-iodide ions, in the functioning of DSCs. As ionic transport is directly related to the viscosity of the solvent, it is of paramount importance to develop molecular models of RTILs and their mixtures capable of reproducing their liquid structure and transport properties at conditions of device operation.

In this work we use molecular dynamics simulations to look at the structure and diffusion coefficients of RTILs typically used in state-of-the art DSCs, i.e., imidazolium and pyrrolidinium imides, as well as their mixtures with the common organic solvent acetonitrile. One of the main aims of the present study is to describe the diffusion coefficient of iodide ions in RTIL/acetonitrile mixtures, for different mixing ratios. As these are one of the carriers of charge in a DSC at operation, to have a realistic model for them is of great importance. To obtain this model we have employed the following strategy: (1) first we have obtained adequate force field parameters (Lennard-Jones parameters and atomic point charges) for imidazolium and pyrrolidinium cations by fitting to exper-

imental values of density and diffusion coefficients of RTILs, as a function of temperature. To do so we have used, when available, literature values and ab initio calculations of atomic point charges. (2) Second, we have validated the obtained force fields by reproducing the experimental behavior of iodide diffusion coefficients as a function of the RTIL/acetonitrile mixing ratio. (3) Finally, the fitted and validated force fields have been used to predict the behavior of the pyrrolidinum cations (not available experimentally) and iodide diffusion coefficients at temperatures approaching those of devices at photovoltaic operation.

METHODS

Simulation Details

Molecular Dynamics (MD) simulations in the NVT and NPT ensemble have been performed to study the microscopic behavior of electrolytes based on RTILs. All simulations were carried out using GROMACS molecular simulation package.[12–15] All interactions were evaluated using a van der Waals cutoff of 1.2 nm whereas Coulombic forces were dealt with using the particle-mesh Ewald method.[16, 17] Simulations were performed for a cubic unit cell with periodic boundary conditions.

The molecular models of the RTILs and acetonitrile molecules studied in this work are shown in Figure 1 and in the Figure A4.1 in the Appendix 4. Full atom force fields were considered

in all cases. To reduce computational costs we use a nonpolarizable and systematic model of RTILs, where the intermolecular interactions are evaluated using Lennard-Jones and electrostatic potentials based on atomic point charges. For 1-alkyl-3-methylimidazolium-based RTILs ($[C_n MIM]^+$) the complete set of parameters were taken from the force field developed by Canongia Lopes et al.,[18] except for the torsion potential, which was taken from Kelkar and Maginn.[19] As there was not any nonpolarizable force field available in the reported literature, we have developed a new systematic force field for N-alkyl-N-methylpyrrolidinium ($[C_n PYR]^+$), based on the parameters of $[C_n MIM]^+$. Lennard-Jones parameters and force constants for intramolecular interactions were adopted from Canongia Lopes et al.[18], adapted to cations. Meanwhile charges and optimized geometry (force constants for intramolecular interactions) are obtained using ab initio calculations. The Gaussian09 code [20] has been employed to perform a natural population analysis [21] (NPA) of the electron density obtained from HF/6-31++G** calculations. We first calculated the charges of the representative $[C_4 PYR]^+$ cation in vacuo. This molecule was then placed in close proximity of an anion. The charges of this ionic liquid dimer were then calculated and were found to be similar to those obtained when the cation was isolated. In order to check the convergence with
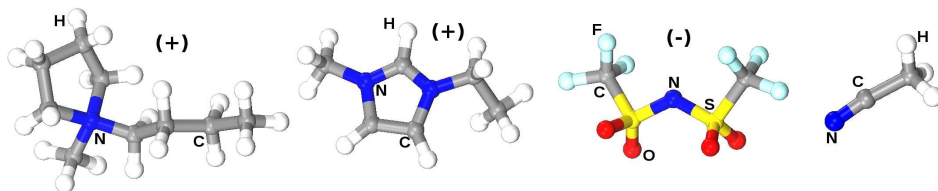
Figure 1. Schematic representation of representative models used in this work. From left to right, $[C_4PYR]^+$, $[C_2MIM]^+$, $[Tf_2N]^-$, and acetonitrile.

the number of molecules that are taken into account, we also calculated the charges of two and four dimers. The atomic charges for each atom did not change significantly, which gives us confidence as to the validity of the charges to model the ionic liquid. In order to obtain the set of charges we calculated the average charge of each atom in the four structures mentioned above. The positive net charge in the cations is provided by the atoms of the pyrrolidinium ring, for this reason we extrapolate the set of partial charges to the rest of $[C_nPYR]^+$ cations.

The initial configurations were generated by randomly placing in the cubic simulation box (side length 35 Å) a number of molecules close to the experimental density of the system considered. In the first set of calculations, we performed energy minimization simulations using a steepest descent algorithm, followed by MD in the NPT ensemble to relax the systems to their equilibrium density. This equilibrium is reached when the cell volume and the system energy fluctuate around a mean value over time.

We employed the Martyna-Tuckerman-Tobias-Klein (MTTK) barostat,[22] with a fixed pressure of 1 atm, while the temperature was controlled by the Nose-Hoover thermostat.[23, 24] These simulations were performed for 1 ns with an integration timestep of 0.1 fs. After that, a 5 ns production run in the NVT ensemble was performed, with an integration timestep of 0.5 fs. Self-diffusion coefficients were obtained from the mean squared displacement (MSD) through the Einstein equation (for more details, see Figure A4.2 in the Appendix 4).

The intramolecular contribution to the potential is given by the following expression:

$$\Phi_{int} = \sum_{bonds} k_b(r - r_0)^2 + \sum_{angles} k_\theta(\theta - \theta_0)^2 + \sum_{dihedrals} k_\chi[1 + \cos(n\chi - \delta)]$$

(1)

The complete set of Lennard-Jones parameters (σ, ε), intramolecular parameters and charges (q) for $[C_4PYR]^+$ are listed in Table A1.1 in the Appendix 1. The force field parameters for $[Tf_2N]^-$ were

adopted from Kelkar and Maginn,[19] for acetonitrile from the general AMBER force field,[25, 26] and for lithium iodide from ref [27].

Unfortunately, the force field used for RTILs has important limitations in reproducing their dynamical properties, as reported by several groups.[28–30] For this reason we have modified the initial set of parameters of the force field to reproduce the experimental density and diffusion coefficients of RTILs. To do so, we have fitted the potential by multiplying the Lennard-Jones parameters and charges for each system by a scaling factor. The scaling relations that we obtained were $\sigma_f = 1.0 \cdot \sigma_i$, $\varepsilon_f = 0.9 \cdot \varepsilon_i$, and $q_f = 0.9 \cdot q_i$ for $[C_n MIM]^+$ cations and $\sigma_f = 0.99 \cdot \sigma_i$, $\varepsilon_f = 0.8 \cdot \varepsilon_i$, and $q_f = 0.8 \cdot q_i$ for $[C_n PYR]^+$ cations, where i and f refer to initial and final values respectively. It is worth to mention that some authors have already proposed models for ionic liquids where the sum of partial charges for the anion and cation are less than unity.[30–32] This phenomenon is due to the polarizable character of the big anions and cations, which leads to a charge transfer between the cation and the anion. In summary, the fitting procedure is described as follows; we adjust the parameters to reproduce the density and self-diffusion coefficients for RTILs containing butyl-methyl-cations at room temperature. Once the optimal parameters are found, we simulate all range of temperatures. If the experimental values are correctly

reproduced, we extrapolate the force field to the rest of cations with varying chain lengths.

Experimental Section

In this work we compare the predicted diffusion coefficients of iodide ions with experimental values for electrolytes of the same composition. Experimental diffusion coefficients were obtained by recording cyclic voltammograms (CV) for different electrolytes sandwiched between two platinized transparent conducting oxides, with a scan rate of $20 \text{ mV} \cdot \text{s}^{-1}$. More details can be found in ref [33] The composition of the electrolytes is indicated in Table 1.

Table 1. Composition of the electrolytes used in this work[a].

electrolyte	solvent (v/v, %)	solutes
Acn	100 % acetonitrile	
Imid25/Pyr25	75 % Acn + 25 % RTIL	0.03 M I_2
Imid50/Pyr50	50 % Acn + 50 % RTIL	+ 0.3 M LiI
Imid75/Pyr75	25 % Acn + 75 % RTIL	
Imid/Pyr	100 % RTIL	

[a] (I_2: Iodine (99.5%, Fluka), LiI: Lithium iodide (99%, Aldrich), Acn: Acetonitrile (99.9%, Panreac), Imid: 1-Ethyl-3-Methylimidazolium bis(trifluoromethanesulfonyl)imide (99.9%, Solvionic), Pyr: 1-Butyl-1-Methylpyrrolidinium bis(trifluoromethanesulfonyl)imide (99.9%, Solvionic).

Once an electrical bias is applied in the sandwich cell, the following electrochemical reaction takes place at the platinized electrodes:

$$I_3^- + 2e^- \leftrightarrow 3I^-$$
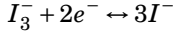
If the voltage is large enough a maximum value of the current is obtained, due to diffusion limitations. The diffusion coefficient of tri-iodide (which is assumed to be equal to that of iodide [34]) can then be obtained from the limiting current as:[35, 36]

$$D_{I_3^-} = \frac{l}{2nFc_{I_3^-}} j_{lim} \qquad (2)$$

where l is the distance between electrodes, n is the number of electrons of the reduction reaction, F is Faraday's constant, $c_{I_3^-} = 0.03$ M is the concentration of tri-iodide, and j_{lim} is the limiting current density. In the present experiments, $n = 2$ and l is assumed to be equal to 20 μm, which is the original thickness of the thermoplastic polymer (Surlyn) utilized as spacer between the electrodes.

RESULTS AND DISCUSSION

Density and Structure

In this section, we first analyze the temperature dependence of the density and the structural properties for RTILs in the bulk phase. The first property we used to refine the force fields is the density of the fluids. Figure 2 shows the predicted density of RTILs for different temperatures and chain lengths, compared with the experimental results obtained by Tokuda et al.[37–39] Experimental densities of $[C_6MIM]^+$ and
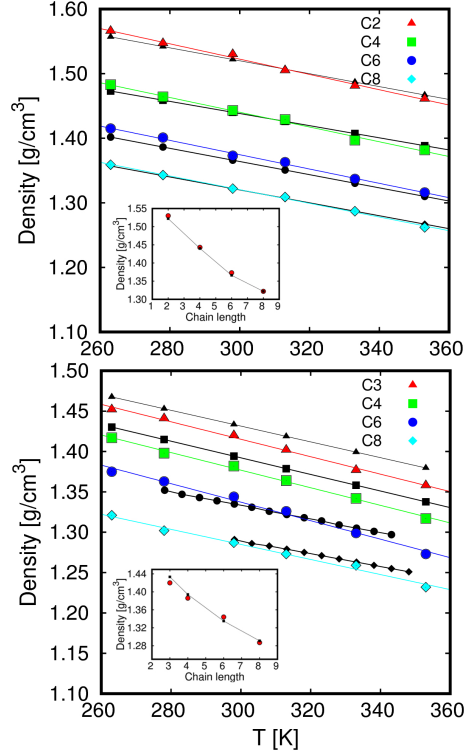
Figure 2. Density of RTILs as a function of the temperature, for different chain lengths. Results are for RTILs containing $[C_nMIM]^+$ (top) and $[C_nPYR]^+$ (bottom). Black symbols and dashed lines correspond to experimental data.[5, 37, 38] Color symbols correspond to data obtained in this work. Solid color lines represent a linear fitting from simulation data. The insets show the density as a function of the chain length of cations at 298 K.

$[C_8MIM]^+$ were provided by the Dortmund Data Bank [5] (private communication). It is observed that the simulated densities are in good agreement with the experiments over the whole range of temperatures, showing a largest deviation of less than 2% with respect to the experiments.

Linear fits of simulated values yield correlation coefficients of 0.99 in all cases. The simulations clearly show that as the temperature increases the density decreases. An increase in the length of the alkyl chain length also results in a decrease of density (see insets in Figure 1).

Cation-anion radial distribution functions (RDF) of both representative RTILs are depicted in the Appendix 4 (Figure A4.3). The typical RDF of a liquid system is observed, with the important feature that increasing the chain length increases slightly the height of the first peak in the RDF, which is in line with previous simulation results.[40, 41] This finding indicates that: a) RTILs containing the bulkiest cations tend to draw near the polar heads of the cations and anions, and b) the interaction between the polar head of the cation and the anion is slightly stronger for cations with large chain lengths than for those with shorter chain lengths. Hence, although with longer chain length the values of density are lower, the centers of mass of the anions are located closer to the cation rings. This aggregation behavior of the molecules hinders their mobility, thus reducing the diffusion, as we will discuss later.

Self-diffusion Coefficients of RTIL

Figures 3 and 4 show how the ionic self-diffusion coefficient varies with temperature. We present a comparison between published experimental data [37–39] and our simulation results, for both representative cations containing four hydrocarbons in the chain length and their respective anions. The temperature dependence of the self-diffusion coefficients can be described by Vogel-Fulcher Tamman's (VFT) equation,[42–46] which is an empirical extension of Arrhenius's equation:

$$D = D_0 e^{\frac{B}{T - T_0}} \tag{3}$$

where D is the self-diffusion coefficient, T the temperature, and D_0, B, and T_0 are adjustable parameters. The results obtained from simulations are in agreement with experiments, reproducing the tendency in most of the range of temperatures studied. The simulated diffusion coefficients show the same trend than the empirical equation, from room temperature onward. However, a systematic deviation is found at low temperatures. This may be explained by the physical state of RTILs at these temperatures. RTILs used here typically undergo a glass transition at temperatures around 100 K below room conditions.[47–50] A glassy state is a nonequilibrium situation, where molecules do not diffuse, they only vibrate around neighbors. When the glass transition is approached RTILs tend to be in a supercooled state, characterized by a subdiffusive regime. This state might be stable for this class of materials, but is not an equilibrium state. On the contrary, MD simulations are ideally performed at thermodynamic equilibrium.
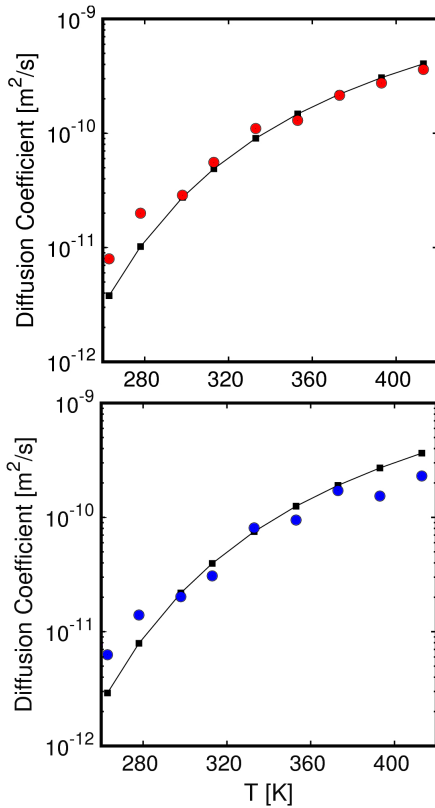
Figure 3. Self-diffusion coefficients of $[C_4MIM]^+$ cation (top) and $[Tf_2N]^-$ anion (bottom) as a function of the temperature. Black symbols with solid lines correspond to experimental data,[38] and color symbols correspond to simulation data.
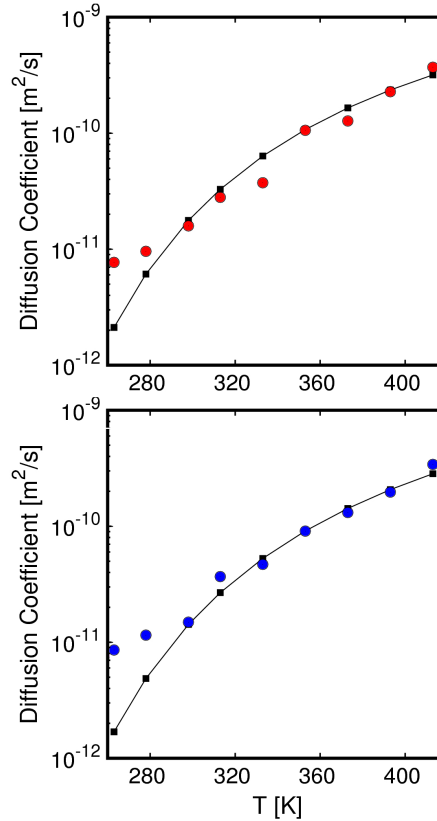
Figure 4. Self-diffusion coefficients of $[C_4PYR]^+$ cation (top) and $[Tf_2N]^-$ anion (bottom) as a function of the temperature. Black symbols with solid lines correspond to experimental data,[38] and color symbols correspond to simulation data.

This feature can well explain the overestimation of the diffusion coefficients at low temperatures. However, as the working regime for DSC devices is over room temperature, this disagreement cannot be considered an inconvenience for the study of ionic diffusion in this kind of solar cells. The computation of diffusion coefficients is extended to different chain lengths in Figures A4.4-4.9, in the Appendix 4.

Imidazolium cations exhibit similar good agreement with the experiments. Due to the lack of available experimental values for pyrrolidinium cations we cannot compare with experiments, but we found a similar trend as in the rest of systems. Therefore, these results can be considered to be *predictions* of the diffusion behavior of the RTILs for different temperatures.

Figure 6. Current as a function of applied voltage for electrochemical sandwich cells containing electrolytes with compositions indicated in Table 1, acetonitrile (green), $[C_2MIM]^+$ (red), and $[C_4PYR]^+$ (blue).

Figure 5. Self-diffusion coefficients of cation $[C_nMIM]^+$ (top) and $[C_nPYR]^+$ (bottom) as a function of the chain length at different temperatures. Black symbols with dashed lines correspond to experimental data,[37, 38] and color symbols correspond to simulation data.

To provide an additional insight into the diffusion of RTILs, we also studied the chain length dependence of the self-diffusion coefficients (see Figure 5). The good agreement between simulation and experiment is confirmed for imidazolium cations. Pyrrolidinium cations exhibit a general trend very similar to the other cations. In both cases, increasing the chain length decreases the self-diffusion coefficient. This result can be correlated with

the features observed in the RDFs described above. Longer chain lengths induce a stronger attraction between the polar head of the cations and the anions. As Coulombic interactions constitute the main contribution to the total cohesive energy, diffusion gets, as a consequence, slowed down. However, steric impediments for the longer chain lengths cannot be ruled out as an additional factor that contributes to this reduction of the self-diffusion coefficient.

Self-diffusion Coefficients of Redox Mediators in RTIL/acetonitrile Mixtures

To analyze the mobility of redox mediators in the solvent mixtures, we performed additional simulations containing lithium iodide and RTILs, acetonitrile, and their mixtures. From these simulations we can calculate the self-diffusion coefficients of I^-, which we compare with experimental

values obtained from voltammetry mea-
surements for the same compositions.

Figure 6 shows the limiting current
density measured for systems containing
acetonitrile and RTILs for different mix-
ing ratios. Due to the larger viscosity of
this material an increase of the amount
of RTILs in the mixture produces a de-
crease of the limiting current density. Con-
sequently the diffusion coefficient is re-
duced, in accordance to eq 2.

Figure 7 shows the experimental diffu-
sion coefficients of tri-iodide and the simu-
lated self-diffusion coefficients of iodide for
varying amounts of RTILs. Three impor-
tant aspects should be taken into account
at this point:

(1) For simplicity, simulations were
performed for solutions of LiI of concen-
tration 0.3 M in a solvent constituted by
RTIL/acetonitrile mixtures. In contrast,
voltammetry measurements were carried
out with electrolytes where 0.3 M of LiI
and 0.03 M of I_2 are dissolved in the same
RTIL/acetonitrile compositions. As iodine
converts quantitatively to tri-iodide, the
voltammetry experiment probes the kinet-
ics of the electrochemical reaction

$$I_3^- + 2e^- \leftrightarrow 3I^-$$
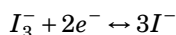
Once the diffusion limit is reached,
the limiting current is determined
by the minority component of the
redox couple, that is, tri-iodide. It
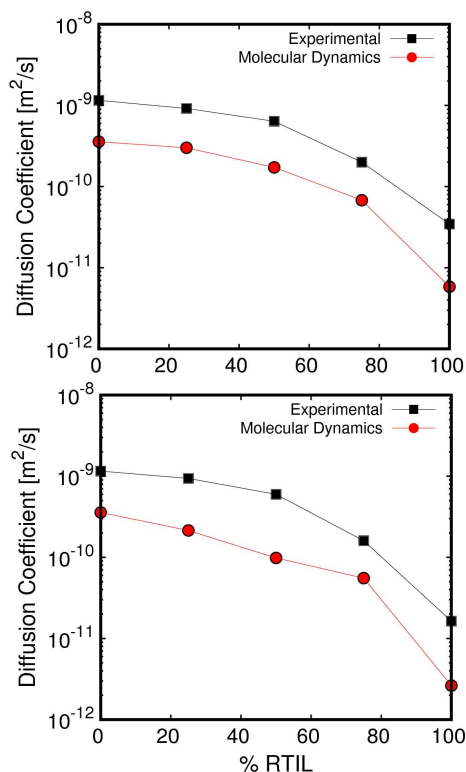
Figure 7. Self-diffusion coefficients of
I^- in acetonitrile and RTIL solutions
containing $[C_2MIM]^+$ cation (top) and
$[C_4PYR]^+$ cation (bottom). Black symbols
correspond to experimental data, and
red symbols correspond to simulated values.

can be argued that it could be more di-
rect to make experiments on an electrolyte
where 0.3 M of iodine is dissolved or run
simulations with 0.03 M of iodide. How-
ever, the saturation concentration of io-
dine in RTIL/acetonitrile mixtures is very
low, which forces one to work with low con-
centrations of iodine (which is in fact the
case in real DSC at working conditions).
On the other hand, to simulate 0.03 M of
iodide is cumbersome; as it requires a very

big simulation box. However, since the diffusion coefficients of I^- and I_3^- are known to be similar [34] and, furthermore, their dependence on concentration is very small (see Appendix 4 Figure A4.10), we argue that is basically correct to compare the iodide diffusion coefficient obtained from the simulations with that of tri-iodide, extracted from the voltammetry measurements.

(2) The diffusion coefficient extracted from the simulations is a self-diffusion quantity, which is obtained, as mentioned above, from the mean square displacement using Einstein's equation:

$$D_s = \lim_{t \to \infty} \frac{\langle \sum_i^n \| r(t) - r(0) \|^2 \rangle}{6t} \qquad (4)$$

In contrast, the diffusion coefficient that is extracted from the limiting current of the voltamogramms is a collective or mass transport quantity, defined by Fick's law, where molecular interactions and non-idealities are taken implicitly into account. Fick's law defines a *chemical diffusion coefficient D* as:

$$J = -D \nabla \rho \qquad (5)$$

where J is the diffusion current density and ρ is the density of diffusing species. Both chemical and self-diffusion coefficients are related by Darken's equation:[51]

$$D = \Gamma D_s \qquad (6)$$

where Γ is a thermodynamic factor given by:

$$\Gamma = \frac{\partial ln \frac{\mu}{k_B T}}{\partial ln \rho} \qquad (7)$$

where μ is the chemical potential. The thermodynamic factor Γ includes the effect of the interactions and hence, for ideal systems (where $\mu \sim k_B T ln \rho$), $\Gamma = 1$.

(3) For electrolytes containing the iodide/tri-iodide a non-diffusional mechanism of charge transport has been proposed. This is the Grotthus exchange mechanism [52]

$$I_3^- + I^- \to I^- + I_3^- \qquad (8)$$
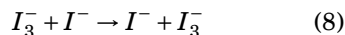
This kind of transport might play a role in the experimental limiting currents, but not in the MD calculations, where only iodide ions are present.

Once it is clarified what is obtained from each method (D_s from MD, and D from voltammetry), we can discuss the results for the diffusion of the iodide/tri-iodide ions. In Figure 7 both simulation and experimental data show that increasing the amount of ionic liquid in solution leads to a dramatic decrease of the diffusion coefficient of the mediators. Furthermore, experiment and simulation have the same trend, with a two orders of magnitude difference between pure acetonitrile and pure RTIL. This result is consistent with a previous study by Fabregat-Santiago et al.[36] Pure acetonitrile results are also similar to the data reported by Hauch and Georg.[53]

In spite of both set of results showing the same trend, there is a systematic un-

derestimation of the simulated diffusion coefficients with respect to the experimental values. As mentioned before, this disagreement can be due to the fact that we are not looking at the same kind of ion (iodide in one case, tri-iodide in the other), or due to the thermodynamic factor in eq 7, or, in addition, to a contribution of the Grotthus exchange mechanism. As regards to the first, reported values for iodide and tri-iodide are very similar.[34] On the other hand, the small dependence of the diffusion coefficient on concentration of iodide suggests that the thermodynamic factor is really very close to one. Hence, we ascribe the mismatch between MD and experiment to limitations of the molecular model used for iodide ions, or/and contributions from a Grotthus mechanism.

Self-diffusion Coefficients of Redox Mediators as a Function of Temperature

To predict the self-diffusion coefficients of mediators we performed MD simulations at different temperatures. Figure 8 depicts the temperature dependence of the self-diffusion coefficient of I^- in pure acetonitrile, pure RTIL, and a 50/50 volume mixture. A progressive increment of the diffusivity of the ions is observed. In fact, all simulation data, in the temperature range studied, fits to the approximate Arrhenius's expression:

$$D = D_0 e^{-\left(\frac{13.0 \pm 0.5 K}{T}\right)} \qquad (9)$$
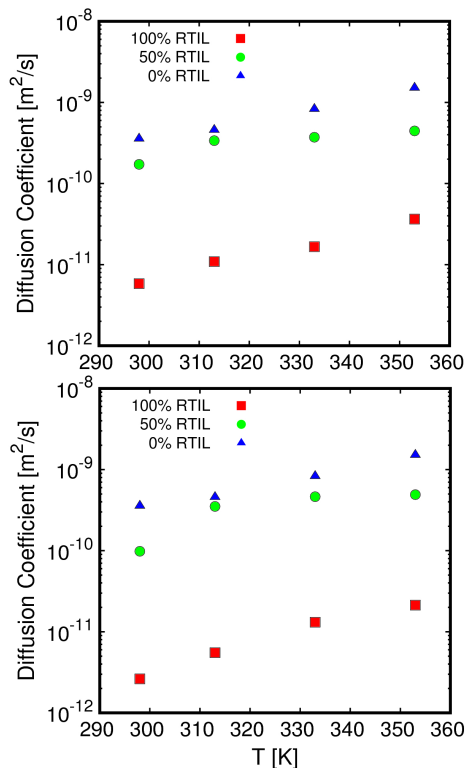
Figure 8. Self-diffusion coefficients of I^- as a function of temperature for different RTIL solutions containing $[C_2MIM]^+$ cation (top) and $[C_4PYR]^+$ cation (bottom).

where D_0 is a prefactor that depends on the nature, i.e. the viscosity, of the solvent mixture.

The activation energy and the temperature dependence of the diffusion of iodide ions are found to be roughly the same for all solvents. As a consequence, the two orders of magnitude difference between the diffusion of I^- in pure acetonitrile and in pure RTIL is preserved in the whole temperature range.

Finally, it is important to stress that

iodide ions have a very similar diffusion coefficient in the 50/50 mixture and in pure acetonitrile. This is a very interesting result, because it suggests that adding small quantities of an organic solvent can improve significantly the transport of charge in the solar cell, while preserving the non-volatile character of the electrolyte by the presence of the RTIL component. Furthermore, the addition of the small amount of organic solvent can also compensate the strong recombination losses and the slower dye regeneration which is characteristic of RTIL, as discussed in a recent work by some of us.[54] In fact, in that work it was observed that by using the right dye and the right RTIL (pyrrolidinium produces slower recombination than imidazolium, for instance), a good compromise between performance and stability can be reached.

CONCLUSIONS

Fully atomistic force fields, based on the Lennard-Jones interatomic potential with atomic point charges, are found to be realistic for room temperature ionic liquids commonly used as electrolytes in dye-sensitized solar cells. Molecular dynamics simulations reproduce accurately the experimental densities and the diffusion coefficients of anions and cations as a function of temperature and length of the hydrocarbon chain for imidazolium and pyrrolidinium imides, as well as their mixtures with acetonitrile.

The diffusion coefficients of iodide and tri-iodide ions, which act as redox mediators in the solar cell, have been studied by voltammetry and by molecular dynamics simulations in the same mixtures. A two orders of magnitude difference between pure acetonitrile and pure ionic liquid is found in both experiments and simulations. However, the variation is not linear, in such a way that a small addition of the organic solvent leads to a large increase of the diffusivity. This is a very appealing property of these mixtures for further progress in the DSC field.

Bibliography

[1]   Oregan, B.; Gratzel, M. *Nature* **1991**, *353*, 737–740.

[2]   Mathew, S.; Yella, A.; Gao, P.; Humphry-Baker, R.; Curchod, B. F. E.; Ashari-Astani, N.; Tavernelli, I.; Rothlisberger, U.; Nazeeruddin, M. K.; Graetzel, M. *Nat. Chem.* **2014**, *6*, 242–247.

[3]   Snaith, H. J. *J. Phys. Chem. Lett.* **2013**, *4*, 3623–3630.

[4]   Jeon, N. J.; Noh, J. H.; Kim, Y. C.; Yang, W. S.; Ryu, S.; Seok, S. I. *Nat Mater* **2014**, *advance on.*

[5]   http://www.ddbst.com/online.html.

[6]   Zhou, H.; Chen, Q.; Li, G.; Luo, S.; Song, T.-b.; Duan, H.-S.; Hong, Z.; You, J.; Liu, Y.; Yang, Y. *Science (80-.).* **2014**, *345*, 542–546.

[7]   Hao, F.; Lin, H. *Rsc Adv.* **2013**, *3*, 23521–23532.

[8]   Plechkova, N. V.; Seddon, K. R. *Chem. Soc. Rev.* **2008**, *37*, 123–150.

[9]   Pinilla, C.; Del Popolo, M. G.; Lynden-Bell, R. M.; Kohanoff, J. *J. Phys. Chem. B* **2005**, *109*, 17922–17927.

[10]   Pinilla, C.; Del Popolo, M. G.; Kohanoff, J.; Lynden-Bell, R. M. *J. Phys. Chem. B* **2007**, *111*, 4877–4884.

[11]   Yu, Z.; Vlachopoulos, N.; Hagfeldt, A.; Kloo, L. *Rsc Adv.* **2013**, *3*, 1896–1901.

[12]   Berendsen, H. J. C.; Vanderspoel, D.; Vandrunen, R. *Comput. Phys. Commun.* **1995**, *91*, 43–56.

[13]   Hess, B.; Kutzner, C.; van der Spoel, D.; Lindahl, E. *J. Chem. Theory Comput.* **2008**, *4*, 435–447.

[14]   Pronk, S.; Pall, S.; Schulz, R.; Larsson, P.; Bjelkmar, P.; Apostolov, R.; Shirts, M. R.; Smith, J. C.; Kasson, P. M.; van der Spoel, D.; Hess, B.; Lindahl, E. *Bioinformatics* **2013**, *29*, 845–854.

[15] Van der Spoel, D.; Lindahl, E.; Hess, B.; Groenhof, G.; Mark, A. E.; Berendsen, H. J. C. *J. Comput. Chem.* **2005**, *26*, 1701–1718.

[16] Darden, T.; York, D.; Pedersen, L. *J. Chem. Phys.* **1993**, *98*, 10089–10092.

[17] Essmann, U.; Perera, L.; Berkowitz, M. L.; Darden, T.; Lee, H.; Pedersen, L. G. *J. Chem. Phys.* **1995**, *103*, 8577–8593.

[18] Lopes, J. N. C.; Deschamps, J.; Padua, A. A. H. *J. Phys. Chem. B* **2004**, *108*, 11250.

[19] Kelkar, M. S.; Maginn, E. J. *J. Phys. Chem. B* **2007**, *111*, 4867–4876.

[20] Frisch, M. J. et al. Gaussian 09, Revision A.01. 2009.

[21] Reed, A. E.; Weinstock, R. B.; Weinhold, F. *J. Chem. Phys.* **1985**, *83*, 735–746.

[22] Martyna, G. J.; Tuckerman, M. E.; Tobias, D. J.; Klein, M. L. *Mol. Phys.* **1996**, *87*, 1117–1157.

[23] Nose, S. *Mol. Phys.* **2002**, *100*, 191–198.

[24] Hoover, W. G. *Phys. Rev. A* **1985**, *31*, 1695–1697.

[25] Wang, J. M.; Wolf, R. M.; Caldwell, J. W.; Kollman, P. A.; Case, D. A. *J. Comput. Chem.* **2005**, *26*, 114.

[26] Caleman, C.; van Maaren, P. J.; Hong, M.; Hub, J. S.; Costa, L. T.; van der Spoel, D. *J. Chem. Theory Comput.* **2012**, *8*, 61–74.

[27] Glosli, J. N.; Philpott, M. R. *J. Chem. Phys.* **1993**, *98*, 9995–10008.

[28] Singh, R.; Monk, J.; Hung, F. R. *J. Phys. Chem. C* **2011**, *115*, 16544–16554.

[29] Dommert, F.; Holm, C. *Phys. Chem. Chem. Phys.* **2013**, *15*, 2037–2049.

[30] Bhargava, B. L.; Balasubramanian, S. *J. Chem. Phys.* **2007**, *127*.

[31] Maginn, E. J. *J. Physics-Condensed Matter* **2009**, *21*.

[32] Ghatee, M. H.; Zolghadr, A. R.; Moosavi, F.; Ansari, Y. *J. Chem. Phys.* **2012**, *136*.

[33] Guillén, E.; Fernández-Lorenzo, C.; Alcántara, R.; Martín-Calleja, J.; Anta, J. A. *Sol. Energy Mater. Sol. Cells* **2009**, *93*, 1846–1852.

[34] Rogers, E. I.; Silvester, D. S.; Aldous, L.; Hardacre, C.; Compton, R. G. *J. Phys. Chem. C* **2008**, *112*, 6551–6557.

[35] Wachter, P.; Zistler, M.; Schreiner, C.; Berginc, M.; Krasovec, U. O.; Gerhard, D.; Wasserscheid, P.; Hinsch, A.; Gores, H. J. *J. Photochem. Photobiol. a-Chemistry* **2008**, *197*, 25–33.

[36] Fabregat-Santiago, F.; Bisquert, J.; Palomares, E.; Otero, L.; Kuang, D.; Zakeeruddin, S. M.; Gratzel, M. *J. Phys. Chem. C* **2007**, *111*, 6550–6560.

[37] Tokuda, H.; Hayamizu, K.; Ishii, K.; Susan, M.; Watanabe, M. *J. Phys. Chem. B* **2005**, *109*, 6103–6110.

[38] Tokuda, H.; Ishii, K.; Susan, M.; Tsuzuki, S.; Hayamizu, K.; Watanabe, M. *J. Phys. Chem. B* **2006**, *110*, 2833–2839.

[39] Tokuda, H.; Hayamizu, K.; Ishii, K.; Abu Bin Hasan Susan, M.; Watanabe, M. *J. Phys. Chem. B* **2004**, *108*, 16593–16600.

[40] Li, S.; Banuelos, J. L.; Guo, J.; Anovitz, L.; Rother, G.; Shaw, R. W.; Hillesheim, P. C.; Dai, S.; Baker, G. A.; Cummings, P. T. *J. Phys. Chem. Lett.* **2012**, *3*, 125–130.

[41] Margulis, C. J. *Mol. Phys.* **2004**, *102*, 829–838.

[42] Harris, K. R.; Kanakubo, M.; Woolf, L. A. *J. Chem. Eng. Data* **2007**, *52*, 2425–2430.

[43] Harris, K. R.; Kanakubo, M.; Woolf, L. A. *J. Chem. Eng. Data* **2007**, *52*, 1080–1085.

[44] Ghatee, M. H.; Zare, M.; Moosavi, F.; Zolghadr, A. R. *J. Chem. Eng. Data* **2010**, *55*, 3084–3088.

[45] Jacquemin, J.; Husson, P.; Padua, A. A. H.; Majer, V. *Green Chem.* **2006**, *8*, 172–180.

[46] Seddon, K. R.; Stark, A.; Torres, M. J. In *Clean Solvents Altern. Media Chem. React. Process.*; Abraham, M. A., Moens, L., Eds.; 2002; Vol. 819; pp 34–49.

[47] Mirkhani, S. A.; Gharagheizi, F.; Ilani-Kashkouli, P.; Farahani, N. *Thermochim. Acta* **2012**, *543*, 88–95.

[48] Mousavisafavi, S. M.; Gharagheizi, F.; Mirkhani, S. A.; Akbari, J. *J. Therm. Anal. Calorim.* **2013**, *111*, 1639–1648.

[49] Lazzus, J. A. *Thermochim. Acta* **2012**, *528*, 38–44.

[50] Jiang, W.; Yan, T.; Wang, Y.; Voth, G. A. *J. Phys. Chem. B* **2008**, *112*, 3121–3131.

[51] Gomer, R. *Diffusion of adsorbates in metal surfaces*; Rep. Prog. Phys., 1950; Vol. 53; Chapter 917-1002.

[52] Soga, T. *Nanostructured Materials for Solar Energy Conversion*; Elsevier: Oxford, 2006.

[53] Hauch, A.; Georg, A. *Electrochim. Acta* **2001**, *46*, 3457–3466.

[54] Idigoras, J.; Tena-Zaera, R.; Anta, J. A. *Phys. Chem. Chem. Phys.* **2014**, *16*, 21513–21523.

RADIAL DISTRIBUTION FUNCTION
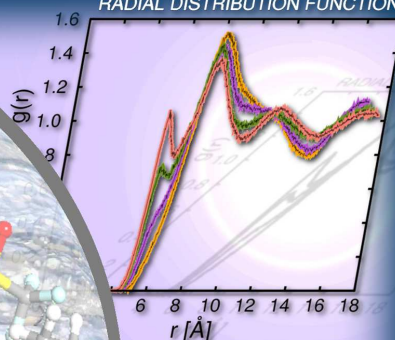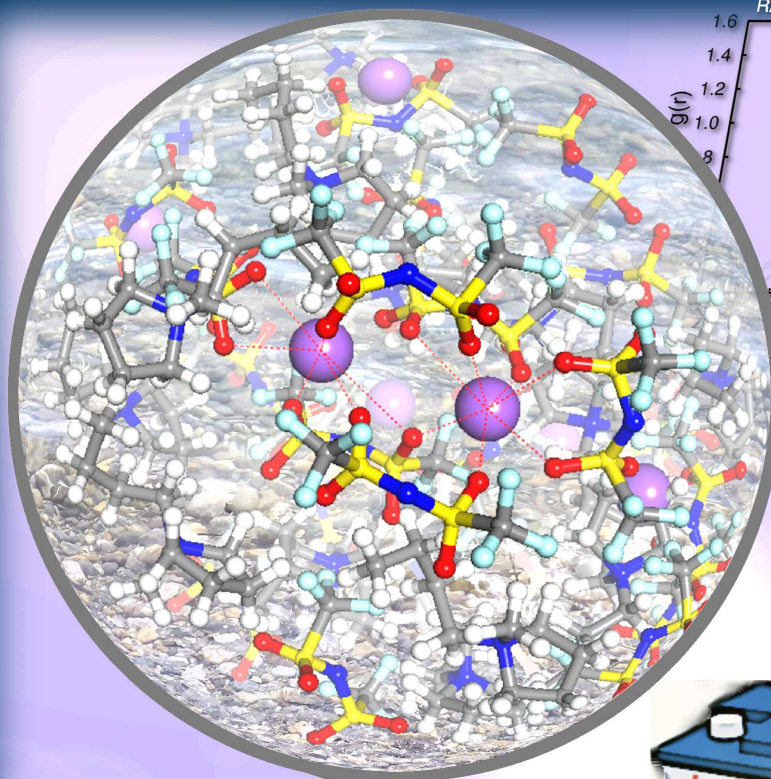
**MOLECULAR INTERACTIONS IN
ELECTROLYTES FOR LITHIUM
AND SODIUM-BASED BATTERIES**

16/2016

WILEY-VCH

**www.chemphyschem.org**

A Journal of

ChemPubSoc
Europe

Quantum and Classical Molecular Dynamics of Ionic Liquids Electrolytes for Na/Li-based Batteries: Molecular Origins of the Conductivity Behavior

José Manuel Vicent-Luna, José Manuel Ortiz-Roldán, Said Hamad, Ramón Tena-Zaera, Sofía Calero, and Juan Antonio Anta

Compositional effects in the charge-transport properties of electrolytes for batteries based on room temperature ionic liquids (ILs) are well-known. However, further understanding is required about the molecular origin of these effects, in particular regarding the replacement of Li by Na. In this work we investigate the use of RTILs in batteries, by means of both classical molecular dynamics (MD), which provides information about structure and molecular transport and ab initio molecular dynamics (AIMD), which provides information about structure. The focus has been placed on the effect of adding either Na^+ or Li^+ to 1-methyl-1-butyl-pyrrolidinium $[C_4PYR]^+$ bis(trifluoromethanesulfonyl)imide $[Tf_2N]^-$. Radial distribution functions show excellent agreement between MD and AIMD, which ensures the validity of the force fields used in the MD. This is corroborated by the MD results for the density, the diffusion coefficients, and the total conductivity of the electrolytes, which reproduce remarkably well the experimental observations for all studied Na/Li concentrations. By extracting partial conductivities, it is demonstrated that the main contribution to the
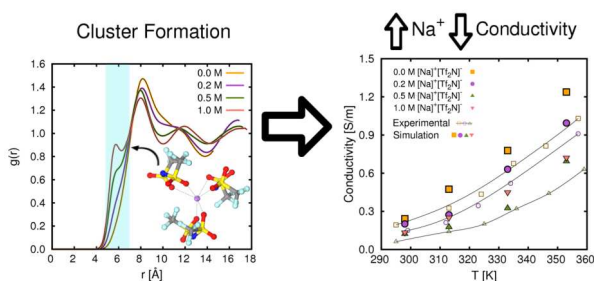
conductivity is that of $[C_4PYR]^+$ and $[Tf_2N]^-$. However, addition of Na^+/Li^+, although not significant on its own, produces a dramatic decrease in the partial conductivities of the RTIL ions. The origin of this indirect effect can be traced down to the modification of the microscopic structure of the liquid as observed in the radial distribution functions, owing to the formation of $[Na(Tf_2N)_n]^{-(n-1)}$ and $[Li(Tf_2N)_n]^{-(n-1)}$ clusters at high concentrations. This formation hinders the motion of the large ions, hence reducing the total conductivity. We demonstrate that this clustering effect is common to both Li and Na, showing that both ions behave in a similar manner at a microscopic level in spite of their distinct ionic radii. This is an interesting finding for extending Li-ion and Li-air technologies to their potentially cheaper Na-based counterparts.

INTRODUCTION

Room-temperature ionic liquids (RTILs or simply ILs) are a new class of salts with melting point below an arbitrary temperature, such as 100 °C. In recent years, they have attracted extensive attention for their appealing chemical and physical properties.[1] In particular they have excellent electrochemical and thermal stability, very low vapor pressure, and relatively high ionic conductivity. These properties make ILs interesting candidates to be used as electrolytes for electrochemical devices such as dye-sensitized solar cells [2–4] (DSCs) and batteries.[5]

In particular, pyrrolidinium bis(trifluoromethanesulfonyl)imide ($[C_4PYR]^+$ $[Tf_2N]^-$)-based electrolytes have been proved as value added electrolytes for Li-ion batteries,[6–8] allowing unique achievements such as high voltage, that is 5 V,[9] owing to their very wide electrochemical window. Furthermore, ILs have been proposed as

promising electrolytes for the emerging Li-air batteries.[10] However, replacing Li with Na can be a suitable choice in terms of battery cost, safety, and raw material abundance. As a result, there is growing interest and research efforts on Na-based batteries, including significant progresses in Na-ion technology [11, 12] but also pioneering studies on Na-air technologies.[13]

Although there are a few studies on the physical properties of the ionic liquids containing Na^+,[12, 14–16] further knowledge into the interactions between the Na^+ and ionic liquid moieties and their influence in the physical properties of the electrolyte is needed to progress beyond of the state of the art in IL-based Na batteries. As an example, a remarkable experimental observation in working electrolytes for Na-based batteries with IL-based electrolytes is the ubiquitous decrease of conductivity as more sodium salt is added to the electrolyte.[14, 15] In this regard, a strong interaction between Na^+

cations and $[Tf_2N]^-$ anions has been reported in several studies.[12, 14, 15] The impact of the equivalent interaction for the case of Li^+ on the total conductivity has already been studied by Borodin and co-workers [17] and Li and co-workers.[18] These authors linked the conductivity compositional effect to the formation of Li clusters, which hinder the motion of the mobile ions. In this connection, it is important to see whether the same effect takes place in the case of Na^+. Na is bulkier and has a lower charge/size ratio than Li, and the formation of clusters or "adducts" is not that obvious, in particular when the concentration of added salt is small. However, Johansson's group [14] detected by Raman spectroscopy the formation of $Na([Tf_2N]^-{}_3)^{2-}$ complexes. Although the effect of progressively adding Na is not easily monitored by the analysis of the spectra, this work suggested that these complexes were responsible of the conductivity decrease at high Na concentration. In this context, a global interpretation, including both Li and Na, of the molecular origins of the conductivity behavior of these electrolytes is still lacking in the literature. The study of the actual role of the $[Na(Tf_2N)_n]^{(n-1)-}$ clusters in the transport properties requires the use of atomistic approaches. The use of polarizable potentials in classical molecular dynamics (MD), such as those used in the case of Li, are costly, especially at low temperatures.[19] This makes it difficult to carry out theoretical studies aimed to study transport properties as a function of Na concentration and temperature.

In this paper, we study the microscopic organization and dynamical properties of ILs by means of molecular simulations based on atomistic models. The aim of the work is twofold. On the one hand, we intend to test the ability of non-polarizable classical force fields to describe correctly the microscopic structure and the transport behavior of IL-based electrolytes for batteries. For this purpose, we have used ab initio molecular dynamics (AIMD) to obtain the radial distribution function of Li and Na-based IL electrolytes and compared the results with those of the classical MD. This is the first time, to the best of our knowledge, that AIMD has been used to study these systems. On the other hand, we have carried extensive classical MD simulations with the AIMD-tested force field. We have analyzed the effect of temperature and concentration of $[Na]^+[Tf_2N]^-$ salts dissolved in $[C_4PYR]^+[Tf_2N]^-$ (Figure 1). The comparison to $[Li]^+[Tf_2N]^-$ salts is discussed in order to emphasize differences and similarities between both cations. In this respect, we focus on partial conductivities and the shape of the relevant radial distribution functions as the concentration of Li^+/Na^+ is increased. A critical local structure change, only detectable by MD, indicates how the partial conductivities of $[C_4PYR]^+$ and $[Tf_2N]^-$ become affected by the addition of salt.
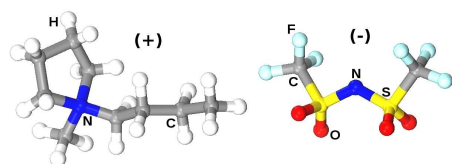
Figure 1. Atomic representation of IL $[C_4PYR]^+$ $[Tf_2N]^-$ used in this work.

SIMULATION DETAILS

Quantum mechanics calculations and classical molecular dynamics simulations in the NVT and NPT ensembles have been carried out to investigate the microscopic behavior of electrolytes based on ILs. In particular, we performed simulations for the IL composed of 1-methyl-1-butyl-pyrrolidinium $[C_4PYR]^+$ cations and bis(trifluoromethanesulfonyl)imide $[Tf_2N]^-$ anions (Figure 1).

Two types of quantum calculations were carried out. First, we employed density functional theory (DFT) calculations, at the B97D/6-311++G** level of theory [20] to obtain the binding energy between a $[C_4PYR]^+$ cation and a $[Tf_2N]^-$ anion, as well as between a Na^+ or Li^+ cation and the $[Tf_2N]^-$ anion. The Gaussian code [21] was used to perform the energy minimizations. Several calculations, with different initial configurations, were carried out for each system to ensure that we reach its minimum configuration.

Secondly, we have made use of ab initio molecular dynamics, as implemented in the VASP code.[22] The Perdew-Burk-

Ernzerhof (PBE) exchange-correlation functional was utilized in this case, with a cut-off energy of 500 eV, and a time step of 1 fs. The Gamma point was used to sample the Brillouin zone. The simulations were 1.5 ps long, which proved to be enough to obtain valuable structural information. The AIMD simulation box contains 15 ion pairs of RTIL $[C_4PYR]^+$ $[Tf_2N]^-$ and three or five ion pairs of $[Na/Li]^+[Tf_2N]^-$ for concentrations of 0.5 M and 1.0 M, respectively, giving rise to a cubic cell of approximately 2.05 nm side-length, which reproduces the equilibrium density. In this respect, the molecular structure of the electrolytes was analyzed by radial distribution functions (RDFs). The spherical integration of the RDF up to a certain distance corresponds with its coordination number, that is, the number of atoms surrounding any specific atom. This is useful to characterize the formation of complexes that govern the behavior of electrolytes and to connect the results with the binding energies provided by the DFT calculations.

In addition to AIMD, classical MD were also performed. In these calculations the molecular models for the ILs were taken from our previous work,[23] where they were fitted to reproduce the structural and dynamical properties of the family of pyrrolidinium cations $[C_nPYR]^+$ (n=2,..,8) and $[Tf_2N]^-$ anion. In this molecular model, interactions were evaluated by using a classical force field including Lennard-Jones and Coulombic potentials with point charges as well as intramolec-

ular contributions described by harmonic bonds, bending angles and dihedral angles. For lithium and sodium cations we used the OPLS force field [24–27] with Aqvist potential.[28] All molecules were described by using full atomistic models with effective Lennard-Jones parameters and point charges placed on each atom. Non-bonded interactions were truncated by using a cutoff of 1.2 nm and electrostatic interactions were dealt with employing the particle-mesh Ewald method.[29, 30] To calculate the mixed Lennard-Jones potential parameters, standard Lorentz-Berthelot mixing rules were used. All MD simulations were performed using the molecular simulation software GROMACS.[31–34] The pressure was set at 1 atm and was controlled employing the Martyna-Tuckerman-Tobias-Klein (MTTK) barostat.[35] The temperature was fixed using the Nose-Hoover thermostat.[36, 37]

The system was initially generated by placing the molecules at random positions over a 3.5 nm length sides. A total of 75 ion pairs of RTIL $[C_4PYR]^+$ $[Tf_2N]^-$, plus 5, 15, and 25 ion pairs of $[Na/Li]^+[Tf_2N]^-$ were considered for modelling systems with 0.2 M, 0.5 M, and 1.0 M concentrations, respectively. For the initial set of calculations, we first carried out an energy minimization by using a steepest descent algorithm. After that, we performed MD simulations in the NPT ensemble, with a time step of 0.5 fs. Using this procedure, we allow the sys-

tems to relax to their equilibrium density at any given temperature. We considered the system at equilibrium when the volume of the unit cell, and the energy of the system, oscillate over time around a mean value. After equilibration, we carried out MD simulations in the NVT ensemble, to obtain the rest of structural and dynamical properties of the electrolytes. First, we run an equilibration simulation for 5 ns, with a time step of 1 fs, followed by a production run of 50 ns, using a time step of 2 fs. In each of the simulations, we extracted self-diffusion coefficients from the slope of the mean square displacement between 10 and 30 ns by using Einstein's relationship:

$$D_s = \lim_{t \to \infty} \frac{\langle \sum_i^n \| r(t) - r(0) \|^2 \rangle}{6t} \qquad (1)$$

Self-diffusion in this kind of system is slow and the time interval for which the diffusion regime is valid should be carefully selected. For the most unfavorable case of diffusion of sodium ions at the lowest temperature studied (298 K) and highest salt concentration (1.0 M), ion motion comprises between two and three ionic radii (see figure A5.1 in the Appendix 5) in the time span of the simulation. However, it is illustrative to compare this time with the time required for the system to reach thermodynamic equilibrium (relaxation time), which is when the diffusion regime is reached.[38] This time is given by $\tau_{relax} = mD_s/k_BT$, where m is the molecular mass and k_B and T are

the Boltzmann constant and the absolute temperature, respectively. It is easy to show that for the diffusion coefficients measured, this relaxation time is several orders of magnitude lower than the actual simulation times in all cases. In fact, it has been reported [39] that over 5 ns is sufficient to reach the diffusive regime at room temperature ILs. We have confirmed the realization of the diffusion regime (see figure A5.1 in the Appendix 5) and confirm that the mean squared displacements are purely diffusive in a time interval of 5-30 ns. To gain further assurance, we have carried out 3 additional simulations, two simulations for 50 ns and one with a time interval of 100 ns for the most unfavorable case (lowest temperature and higher salt concentration). The diffusion coefficients for the different set of simulations fluctuate around similar values (see table A5.1), hence confirming the validity of the diffusion coefficients reported.

The partial ionic conductivity of each component was obtained using the relationship between the self-diffusion coefficient and conductivity, that is, Nernst-Einstein equation:[40]

$$\sigma_i = D_{S_i} \frac{N_i}{q} \frac{q_i^2 e^2}{k_B T} \qquad (2)$$

where σ_i and D_{S_i} are the ionic conductivity and self-diffusion coefficient of species i respectively, N_i is the number of charge carriers, V is the volume of the unit cell, and $q_i e$ is the net charge of the molecule. The ionic conductivity of the system is the sum of partial conductivities of each component. As transport properties are highly density-dependent it is also important to obtain the equilibrium density given by the previous NPT simulation to obtain the partial conductivity. This simulation provides the equilibrium density controlling the volume (V) of the unit cell. In eq. 2 all parameters are fixed except D_{S_i} and V, which are calculated through NVT and NPT simulations, respectively.

RESULTS AND DISCUSSION

Structure

In Figure 2, the radial distribution functions between Li$^+$ or Na$^+$ ions and [Tf$_2$N]$^-$ anions, as obtained by both AIMD and classical MD, are presented. Good agreement is found between both kinds of calculations, showing that Lennard-Jones plus Coulombic potentials are accurate enough to describe correctly the short-range microscopic structure of these systems. Only the height of the first coordination peak is underestimated for the case of Li, which suggests that polarizable force fields would provide a further improvement in this case.[19]

In contrast, the prediction for the less polarizing ion Na$^+$ is excellent. This provides a crucial practical advantage to reduce the computational load of the MD studies, in especial for transport properties. The less intense interaction for the case of Na$^+$ is also evident from the height and position of the peak, as expected from
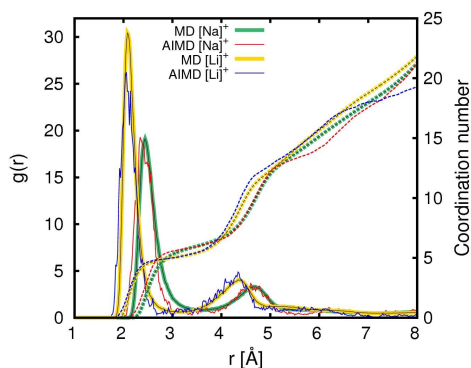
Figure 2. Radial distribution function between Na$^+$/Li$^+$ and [Tf$_2$N]$^-$ (O atom), from ab initio molecular dynamics and classical molecular dynamics with static force fields for a concentration of 1.0 M. Dashed lines stand for the spherical integration of the $g(r)$ (coordination number).
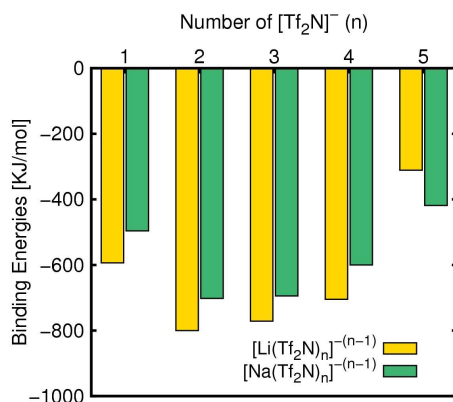
Figure 3. Binding energies (calculated with B97D/6-311++G** energy minimizations) of the systems composed by n[Tf$_2$N]$^-$ anions and one isolated Na$^+$ or Li$^+$ cation.

its lower charge/size ratio.

To gain further insight into the interaction of Na$^+$ and [Tf$_2$N]$^-$ or Li$^+$ and [Tf$_2$N]$^-$ we carried out DFT calculations. Furthermore, an interesting point to address is what is the coordination of Na/Li cations with respect to the [Tf$_2$N]$^-$ anions. Figure 3 shows the binding energies for complexes [Na(Tf$_2$N)$_n$]$^{(n-1)-}$ and [Li(Tf$_2$N)$_n$]$^{(n-1-)}$ for up to five ligands. Complexes containing two and three anions are the most stable. This is in line with data previously reported in the literature.[14, 19, 41, 42] However, this energetic trend towards forming clusters with two or three anions is not so high as to preclude the formation of clusters with four anions, as the inclusion of more solvent molecules could easily change the differences in energy

by that amount. As expected from its lower size, lithium cations in combination with the anion show a higher binding energy (more negative) than the corresponding aggregate with sodium cations. We also computed the binding energies between [Tf$_2$N]$^-$ anion and [C$_4$PYR]$^+$ cation for a single complex (n=1) showing a value of -340 kJ/mol. This value is almost half the value corresponding to lithium or sodium cations. This implies a lower interaction between ions of IL than between ions of the ionic salt.

AIMD simulations include a larger number of solvent molecules than those used in the DFT calculations for the binding energies, and make it possible to look at different concentrations of Na$^+$[Tf$_2$N]$^-$. The most stable configuration is [Na(Tf$_2$N)$_3$]$^{2-}$ with two of the four oxygen atoms of the anion pointing to the

cation.[14] With this in mind we can esti-
mate the most probable coordination num-
ber from the trajectory obtained with MD
and AIMD simulations by computing the
RDFs between sodium or lithium cation
and the oxygen atoms of the anion, and
consequently the coordination number. As
two of the four oxygen atoms of each an-
ion are closer to the Na^+ or Li^+ cations
we estimate the coordination number up
to the first minimum of the RDF. This
value is twice the coordination number,
n, of the complexes $[Na(Tf_2N)_n]^{(n-1)-}$ and
$[Li(Tf_2N)_n]^{(n-1-)}$ respectively. Results in
Figure 2 indicate that this number is be-
tween 5 and 6, in agreement with the bind-
ing energies. As expected, we obtain the
same coordination number from MD and
AIMD.

Figure 4 (top) shows the RDF between
sodium cations and $[C_4PYR]^+$ cations, as
well as between sodium cations and
$[Tf_2N]^-$ anions. As it is evident from the
height of the first coordination peak,
sodium cations interact more strongly
with the anions than with the other
cations, owing to Coulombic repulsions.
The height of the first peak of the RDF
between the sodium cation and anion de-
creases slightly with increasing salt con-
centration, although the position of the
peak remains fixed at 3.75 Å. The Na^+-
Na^+ correlation is analyzed in Figure 4
(bottom). For concentrations of 0.5 M and
1.0 M, Na^+ cations tend to pair at dis-
tances between 4 and 6 Å. Hence, sodium
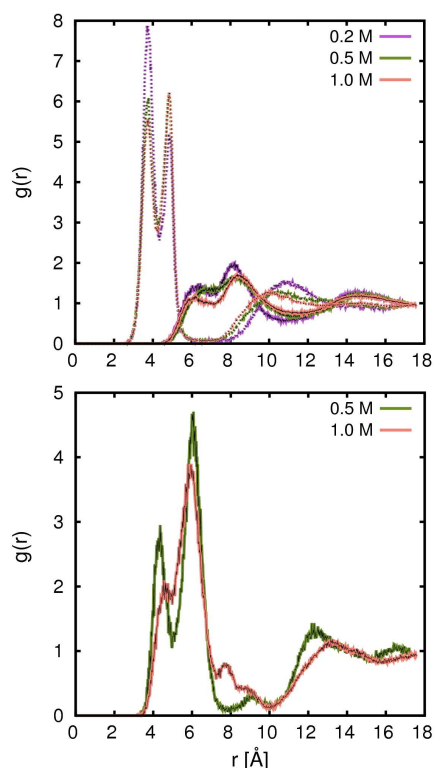
Figure 4. Radial distribution function
between Na^+-$[Tf_2N]^-$ (dashed line) and
Na^+-$[C_4PYR]^+$ (solid line)(top) and Na^+-Na^+
(bottom) at different salt concentrations
at 313 K. The reference atom for the
$[C_4PYR]^+$ cation is the nitrogen atom
of the pyrrolidinium ring and for the
$[Tf_2N]^-$ anion it is the central nitrogen atom.

cations tend to interact strongly with
$[Tf_2N]^-$ anions, as discussed before, and,
more strikingly, with other sodium cations.
These compositional effects and their im-
pact on conductivity are discussed further
below.

Denstity

The temperature and concentration
dependence of the density were obtained

from MD simulations in the NPT ensemble. Figure A5.2 in the Appendix 5 shows a comparison between the calculated density and the available experimental data by Noor et al.[12] and Tokuda et al.[43] We can see that the simulated values are in good agreement with the experimental data for electrolytes containing $Na^+[Tf_2N]^-$ with differences no larger than 2% with respect to the experiments in the whole range of temperatures studied. The density increases linearly with the amount of salt dissolved in the ILs and decreases linearly with temperature. The same applies for electrolytes including $Li^+[Tf_2N]^-$ depicted in Figure A5.2 in the Appendix 5. For the same concentration of salt the mass densities are quite similar for both sodium and lithium, with a certain prominence of sodium, on account of

its larger atomic mass.

Self-diffusion Coefficients

Figure 5 shows the diffusion coefficients of IL cations and anions, as well as sodium and lithium cations for electrolytes with a concentration of 0.5 M of salt dissolved in the IL. In the case of lithium, the results are compared with available experimental data reported by Solano et al.[19] The diffusion coefficients of $[C_4PYR]^+$ and $[Tf_2N]^-$ reproduce very well the experiments although the values for Li^+ are underestimated. This is probably due to the limitations of the simple force field used to model the Li and Na cation. Although this force field proves to be accurate enough to describe correctly the local structure (see comparison with AIMD), it can fail to reproduce their dynamics correctly. How-
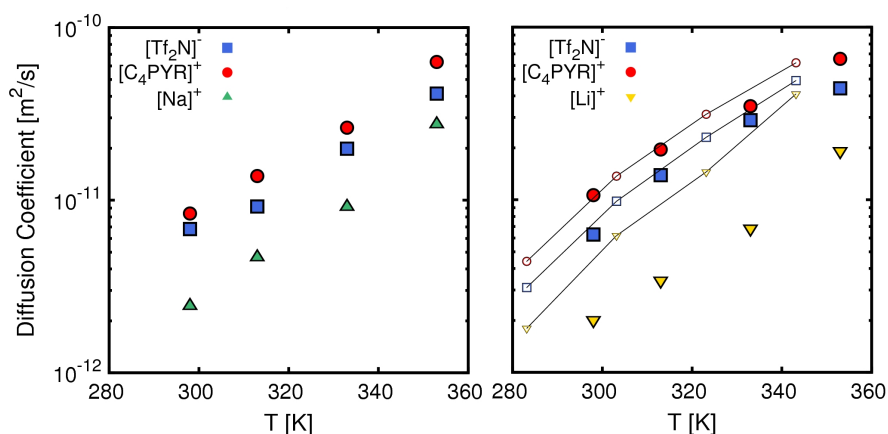
Figure 5. Self-diffusion coefficients as a function of temperature for individual species constituents of electrolytes with a fixed concentration (0.5 M) of Na+[Tf₂N]⁻ (left) and Li+[Tf₂N]⁻ (right). Simulation and experimental data [19] correspond with closed and open symbols with lines respectively.

ever, as explained below, the diffusion co-
efficient of the added salt cations does not
contribute significantly to the total conduc-
tivity of the electrolyte. However, the trend
is followed and the simulated values are
lower than those obtained for cations and
anions of IL, as found in the experiment.
For sodium-based electrolytes, the same
behavior is observed. In both cases, the
$[C_4PYR]^+$ cation shows a slightly higher
diffusivity, followed by the $[Tf_2N]^-$ anion.
Figure A5.3 in the Appendix 5 shows simi-
lar trends for concentrations of 0.2 M and
1.0 M of $Na^+[Tf_2N]^-$. Although we obtain
significantly different values for the dif-
fusion coefficients, in all situations we ob-
serve the same behavior.

To study the impact of adding Li^+ or
Na^+ salt, in Figure 6 the temperature
dependence of the self-diffusion coefficient
of sodium in electrolytes containing dif-
ferent concentrations of $Na^+[Tf_2N]^-$ is
presented. The simulations clearly show
that an increment in the salt concentra-
tion leads to lower values of diffusion
coefficient. As the added species is also
conductive, this effect points to some spe-
cific interaction taking place between the
ions, which hinders transport. This effect
will be discussed later in the light of the
structural information provided by MD
simulations. The inset in Figure 6 shows
the diffusion coefficient of sodium and
lithium for the same concentration. The
values are almost the same for sodium
and lithium, proving that the effect
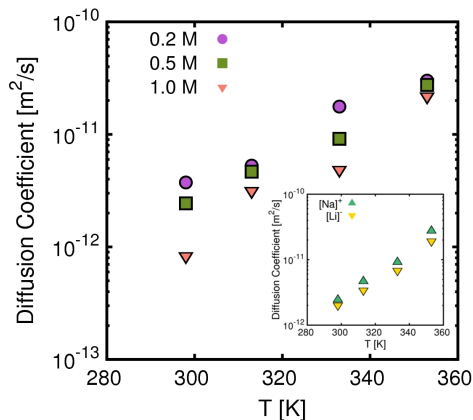
Figure 6. Self-diffusion coefficients of
sodium as a function of temperature for
different concentrations of $Na^+[Tf_2N]^-$. The
inset represents the self-diffusion coefficient
of Li^+ and Na^+ for a concentration of 0.5
M of $Na^+[Tf_2N]^-$ and $Li^+[Tf_2N]^-$, respectively.

mentioned above occurs independently of
the nature of the added cation.

Conductivity

To relate a microscopic quantity such
as the self-diffusion coefficient with a
macroscopic property such as the total
electrolyte conductivity (which is the
practical magnitude for interest in bat-
teries), we have used Nernst-Einstein
equation (eq. 2). This relationship pro-
vides partial conductivities for each ionic
compound. The total conductivity is the
sum of the partial conductivities. The tem-
perature dependence of the total conduc-
tivity for electrolytes containing sodium
or lithium salt is depicted in Figure 7.
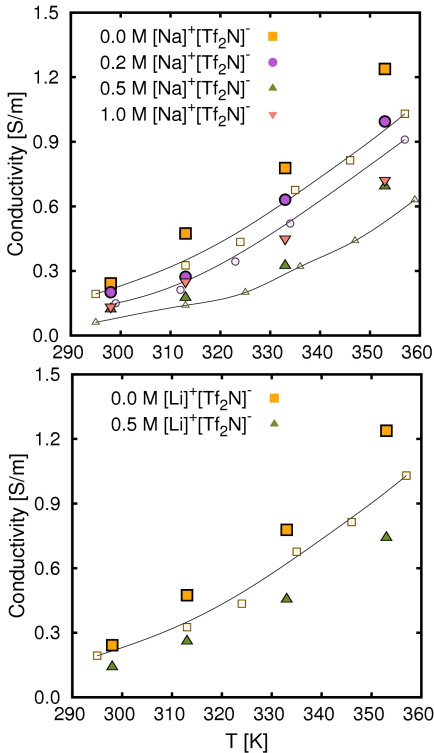
Figure 7. Conductivity as a function of temperature for electrolytes containing $Na^+[Tf_2N]^-$ (top) and $Li^+[Tf_2N]^-$ (bottom). Closed symbols represent simulation data and open symbols with lines the experimental values reported by Serra Moreno et al.[15]

In analogy to the diffusion coefficient, the conductivity increases exponentially with temperature (note that Figure 5 and 6 are in logarithmic scale). This is somehow expected, as this property obeys the Vogel-Fulcher-Tamman's equation (VFT).[15, 43] Note that experimental conductivities reported by Serra Moreno et al.[15] are in agreement with results obtained in this work and those by Tokuda et al.[43] in the case of pure IL as shown in Fig-

ure A5.4 in the Appendix 5. Furthermore, Serra Moreno et al.[15] provided ionic conductivities for electrolytes containing different ratios of $(1-x)[C_4PYR]^+ [Tf_2N]^-$ - $(x)Na^+[Tf_2N]^-$ and compared them with those containing $Li^+[Tf_2N]^-$. They found that ionic conductivity becomes progressively reduced as the salt concentration is increased (in analogy with the diffusion data). Our simulations exhibit the same behavior (see Figure 5). On the other hand, no significant differences are found between electrolytes containing sodium and lithium salts. It is worth stressing that the lowering in conductivity from pure IL electrolyte to the electrolyte with $Na^+[Tf_2N]^-$ at 0.2 M is less significant than when the concentration changes from 0.2 M to 0.5 M. In addition for salt concentration of 0.5 M and 1.0 M, we obtain similar values for the ionic conductivity. This finding could also be related to specific interactions between lithium/sodium and $[Tf_2N]^-$ anion which have been analyzed before.

It is important to note that the procedure followed to obtain the conductivity, that is, Nernst-Einstein equation to obtain the partial conductivities from the self-diffusion coefficients plus simple sum of all the partial conductivities, does in fact ignore the effect of cross-correlations between the different charged particles present in the electrolyte. These correlations could be important in a dense system. The most important correlation, based on their relative concentration, must be

between the anion and the cation components of the ionic liquid. In this respect, Every et al.[40] also analyzed the total conductivity as obtained from the Nernst-Einstein equation for pure imidazolium halide salts. Interestingly, they observed that this equation reproduced very well the experimental conductivity both at high temperatures (where both anions and cations were assumed mobile) and at low temperatures (where only the cations move). This must be considered as a strong indication that the correlations are not critical or that there is a compensation of errors that minimizes their impact on the total conductivity. The effect of correlations has also been discussed in detail by Haskins et al.[8] and Solano et al.[19] Tokuda et al.[43] who compared the conductivity obtained from the Nernst-Einstein equation and NMR diffusion coefficients (which are individual properties) and the total conductivity, as derived from impedance measurements. They observed that the NMR conductivity overestimated the impedance value by a factor of approximately 30%. This could be considered as an upper limit of the effect that correlations have in these systems. This finding can explain why Nernst-Einstein equation leads to conductivity values that systematically overestimate the experimental data in Figure 7. However, the theory still shows a reasonably degree of accuracy. This can be explained by the fact that ionic correlation leads, in fact, to a reduction of the effective charge with which ions

move.[43] The force field used in this work, for which ions have a charge of $\pm$ 0.8 e$^-$ seems then sufficient to include in an effective way the impact of correlations, hence leading to a good description of the total conductivity.

Molecular dynamics simulations provide a means for a better understanding of the behavior of IL electrolytes, based on the microscopic structure and organization of the species involved. To study this in further detail, the contribution of each component to the total conductivity is shown in Table 1.

Table 1. Partial Conductivities [Sm^{-1}] for several temperatures [K] and concentrations for Na$^+$[Tf$_2$N]$^-$.

c	T	[Tf$_2$N]$^-$	[C$_4$PYR]$^+$	Na$^+$
0.0 M	298	0.125	0.177	-
	313	0.205	0.269	-
	333	0.459	0.319	-
	353	0.666	0.572	-
0.2 M	298	0.101	0.098	0.002
	313	0.131	0.140	0.003
	333	0.308	0.315	0.008
	353	0.466	0.516	0.012
0.5 M	298	0.059	0.060	0.003
	313	0.075	0.094	0.006
	333	0.150	0.166	0.008
	353	0.291	0.371	0.032
1.0 M	298	0.057	0.073	0.005
	313	0.118	0.125	0.007
	333	0.229	0.208	0.013
	353	0.325	0.362	0.035

First of all, the contribution of sodium cation to the total ionic conductivity is almost negligible compared with the contribution of the $[C_4PYR]^+$ cation and $[Tf_2N]^-$ anion. In this respect, it is important to bear in mind that the partial conductivity includes the concentration dependence (see eq. 2), in contrast to the self-diffusion coefficient, which is an individual property. Hence, the charge-transport properties of the electrolyte conductivity are mainly due to the mobility of the IL ions, basically because they are more concentrated. On top of that, they diffuse faster (see figure 5).

The $[C_4PYR]^+$ cation and $[Tf_2N]^-$ anion exhibit similar values of partial conductivity for electrolytes containing raw IL and different concentrations of sodium salt. Increasing the concentration of $Na^+[Tf_2N]^-$ increases both the amount of sodium cations and the amount of anions. In spite of that, the contribution to the total conductivity of the $[C_4PYR]^+$ cation tends to be similar to that of the $[Tf_2N]^-$ anion as more sodium cations are added. Owing to the fact that according to eq. 2 the partial conductivity increases with the number of carriers, this is sufficient to offset the effect of decreased diffusion of $[Tf_2N]^-$ anions (see Figure 5 and A5.3 in the Appendix 5).

It is worth pointing out, that the partial conductivity of sodium remains almost constant as its concentration increases, in spite of diffusing more slowly (Figure 6). This is because, as mentioned above, ac-

cording to eq. 2, the partial conductivity scales linearly with the number of carriers, so that both effects are compensated. Hence, the observed depletion of total conductivity when sodium is added is not a direct contribution of the sodium ions themselves, but an indirect effect, a consequence of a specific interaction between them and the more concentrated IL ions, which drags their diffusivity to lower values. This hindrance of the diffusion of the IL components is what causes the overall decrease in the total conductivity. The origin of this indirect effect is what is discussed in the next section, where structural properties are analyzed.

Relationship between conductivity and microscopic structure

Knowing that the main contribution to the total conductivity arises from the IL components, we have analyzed the anion-anion and cation-cation RDFs as a function of Li/Na concentration. These results are presented in Figure 8. It is observed that the $[C_4PYR]^+$ cation RDF is unaffected by the presence of salt. However, in Figure 8 (left), an additional first peak in the RDF appears at high sodium/lithium concentrations. The emergence of this new peak at shorter distances is a consequence of the progressive formation of the clusters mentioned above. A similar effect has been discussed recently by Aguilera and co-workers [44] in terms of an increase of the correlation lengths upon lithium addition to IL electrolytes, which shows up in the form of an additional peak in the
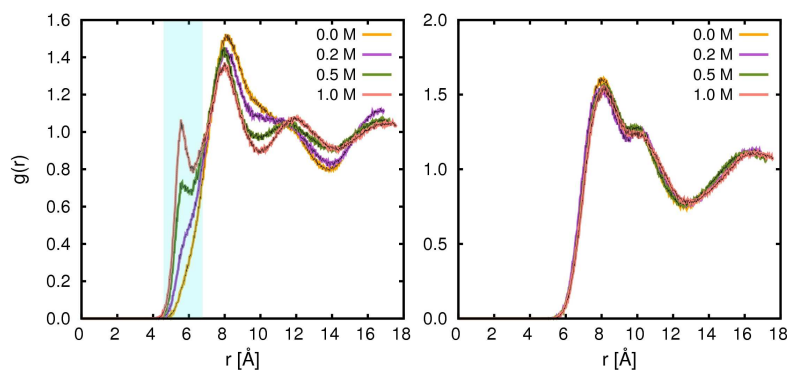
Figure 8. Radial distribution function between $[Tf_2N]^-$-$[Tf_2N]^-$ (left) and $[C_4PYR]^+$-$[C_4PYR]^+$ (right) for various concentrations of $Na^+[Tf_2N]^-$. The reference atom for the $[C_4PYR]^+$ cation is the nitrogen atom of the pyrrolidinium ring and for the $[Tf_2N]^-$ anion it is the central nitrogen atom.

small angle X-ray scattering structure factor. This finding indicates that the presence of the small Li cations causes a critical restructuring of the microscopic organization of the ionic liquid molecules, which tends to correlate the ionic movement to longer distances, that is, larger clusters are formed.

In this work, we demonstrate that this increase of the ionic correlation or clustering is crucial, as it explains the overall decrease in the diffusivity of all species in the system when more sodium/lithium is added to the electrolyte. As clusters become bulkier, their diffusion coefficients become lower, and this also drags the diffusivity of the rest of the species to lower values. Furthermore, larger salt concentrations result in more dense electrolytes (Figure A5.2 in the Appendix 5), which also leads to lower diffusivities. All these factors taken together make it possible to

understand the depletion of the total conductivity upon salt addition observed both experimentally and in the atomistic simulations.

CONCLUSIONS

Fully atomistic molecular dynamics simulations of pyrrolidinium-based room temperature ionic liquid electrolytes, with high potential for use in sodium or lithium-based batteries, provide a fairly accurate description of their density and charge transport properties. The force fields utilized, based on Lennard-Jones potentials and point charges, reproduce correctly the temperature and concentration dependence of density, diffusion coefficients and total conductivity observed in a number of experiments and they are accurate enough to reproduce the depletion of the conductivity upon addition of lithium and

sodium salt. This demonstrates that non-polarizable force fields can be accurate enough to describe correctly this kind of systems, which provides a methodological advantage for future studies. Quantum mechanics simulations show the formation of complexes $[Na(Tf_2N)_n]^{(n-1)-}$ and $[Li(Tf_2N)_n]^{(n-1)-}$ with n=2-3 and provide additional validation to our sets of force field parameters. The structural information obtained by the simulation at molecular level points to the progressive formation of Na/Li clusters as the origin of the anomalous decrease in the conductivity when more lithium or sodium salt is added.

Bibliography

[1] Plechkova, N. V.; Seddon, K. R. *Chem. Soc. Rev.* **2008**, *37*, 123–150.

[2] Pinilla, C.; Del Popolo, M. G.; Kohanoff, J.; Lynden-Bell, R. M. *J. Phys. Chem. B* **2007**, *111*, 4877–4884.

[3] Pinilla, C.; Del Popolo, M. G.; Lynden-Bell, R. M.; Kohanoff, J. *J. Phys. Chem. B* **2005**, *109*, 17922–17927.

[4] Yu, Z.; Vlachopoulos, N.; Hagfeldt, A.; Kloo, L. *Rsc Adv.* **2013**, *3*, 1896–1901.

[5] Armand, M.; Endres, F.; MacFarlane, D. R.; Ohno, H.; Scrosati, B. *Nat. Mater.* **2009**, *8*, 621–9.

[6] Appetecchi, G. B.; Montanino, M.; Balducci, A.; Lux, S. F.; Winterb, M.; Passerini, S. *J. Power Sources* **2009**, *192*, 599–605.

[7] Castiglione, F.; Ragg, E.; Mele, A.; Appetecchi, G. B.; Montanino, M.; Passerini, S. *J. Phys. Chem. Lett.* **2011**, *2*, 153–157.

[8] Haskins, J. B.; Bennett, W. R.; Wu, J. J.; Hernández, D. M.; Borodin, O.; Monk, J. D.; Bauschlicher, C. W.; Lawson, J. W. *J. Phys. Chem. B* **2014**, *118*, 11295–11309.

[9] Borgel, V.; Markevich, E.; Aurbach, D.; Semrau, G.; Schmidt, M. *J. Power Sources* **2009**, *189*, 331–336.

[10] Allen, C. J.; Mukerjee, S.; Plichta, E. J.; Hendrickson, M. A.; Abraham, K. M. *J. Phys. Chem. Lett.* **2011**, *2*, 2420–2424.

[11] Slater, M. D.; Kim, D.; Lee, E.; Johnson, C. S. *Adv. Funct. Mater.* **2013**, *23*, 947–958.

[12] Mohd Noor, S. A.; Howlett, P. C.; Macfarlane, D. R.; Forsyth, M. *Electrochim. Acta* **2013**, *114*, 766–771.

[13] Hartmann, P.; Bender, C. L.; Vračar, M.; Dürr, A. K.; Garsuch, A.; Janek, J.; Adelhelm, P. *Nat. Mater.* **2013**, *12*, 228–32.

[14] Monti, D.; Jónsson, E.; Palacín, M. R.; Johansson, P. *J. Power Sources* **2014**, *245*, 630–636.

[15] Serra Moreno, J.; Maresca, G.; Panero, S.; Scrosati, B.; Appetecchi, G. B. *Electrochem. commun.* **2014**, *43*, 1–4.

[16] Matsumoto, K.; Okamoto, Y.; Nohira, T.; Hagiwara, R. *J. Phys. Chem. C* **2015**, *119*, 7648–7655.

[17] Borodin, O.; Smith, G. D.; Henderson, W. *J. Phys. Chem. B* **2006**, *110*, 16879–16886.

[18] Li, S.; Banuelos, J. L.; Guo, J.; Anovitz, L.; Rother, G.; Shaw, R. W.; Hillesheim, P. C.; Dai, S.; Baker, G. A.; Cummings, P. T. *J. Phys. Chem. Lett.* **2012**, *3*, 125–130.

[19] Solano, C. J. F.; Jeremias, S.; Paillard, E.; Beljonne, D.; Lazzaroni, R. *J. Chem. Phys.* **2013**, *139*, 34502.

[20] Grimme, S. *J. Comput. Chem.* **2006**, *27*, 1787–99.

[21] Frisch, M. J. et al. Gaussian 09, Revision A.01. 2009.

[22] Kresse, G.; Furthmüller, J. *Phys. Rev. B* **1996**, *54*, 169.

[23] Vicent-Luna, J. M.; Idígoras, J.; Hamad, S.; Calero, S.; Anta, J. A. *J. Phys. Chem. C* **2014**, *118*, 28448–28455.

[24] Jorgensen, W. L.; Maxwell, D. S.; Tirado-Rives, J. *J. Am. Chem. Soc.* **1996**, *118*, 11225–11236.

[25] Jorgensen, W. L.; McDonald, N. A. *J. Mol. Struct. THEOCHEM* **1998**, *424*, 145–155.

[26] McDonald, N. A.; Jorgensen, W. L. *J. Phys. Chem. B* **1998**, *102*, 8049–8059.

[27] Rizzo, R. C.; Jorgensen, W. L. *J. Am. Chem. Soc.* **1999**, *121*, 4827–4836.

[28] Aqvist, J. *J. Phys. Chem.* **1990**, *94*, 8021–8024.

[29] Darden, T.; York, D.; Pedersen, L. *J. Chem. Phys.* **1993**, *98*, 10089–10092.

[30] Essmann, U.; Perera, L.; Berkowitz, M. L.; Darden, T.; Lee, H.; Pedersen, L. G. *J. Chem. Phys.* **1995**, *103*, 8577–8593.

[31] Berendsen, H. J. C.; Vanderspoel, D.; Vandrunen, R. *Comput. Phys. Commun.* **1995**, *91*, 43–56.

[32] Hess, B.; Kutzner, C.; van der Spoel, D.; Lindahl, E. *J. Chem. Theory Comput.* **2008**, *4*, 435–447.

[33] Pronk, S.; Pall, S.; Schulz, R.; Larsson, P.; Bjelkmar, P.; Apostolov, R.; Shirts, M. R.; Smith, J. C.; Kasson, P. M.; van der Spoel, D.; Hess, B.; Lindahl, E. *Bioinformatics* **2013**, *29*, 845–854.

[34] Van der Spoel, D.; Lindahl, E.; Hess, B.; Groenhof, G.; Mark, A. E.; Berendsen, H. J. C. *J. Comput. Chem.* **2005**, *26*, 1701–1718.

[35] Martyna, G. J.; Tuckerman, M. E.; Tobias, D. J.; Klein, M. L. *Mol. Phys.* **1996**, *87*, 1117–1157.

[36] Nose, S. *Mol. Phys.* **2002**, *100*, 191–198.

[37] Hoover, W. G. *Phys. Rev. A* **1985**, *31*, 1695–1697.

[38] Chandler, D. *Introduction to Modern Statistical Mechanics*; Oxford university Press: New York, 1987.

[39] Habasaki, J.; Ngai, K. L. *J. Chem. Phys.* **2008**, *129*,

194501.

[40] Every, H. a.; Bishop, A. G.; MacFarlane, D. R.; Orädd, G.; Forsyth, M. *J. Mater. Chem.* **2001**, *11*, 3031–3036.

[41] Andriola, A.; Singh, K.; Lewis, J.; Yu, L. *J. Phys. Chem. B* **2010**, *114*, 11709–11714.

[42] Kunze, M.; Jeong, S.; Paillard, E.; Schönhoff, M.; Winter, M.; Passerini, S. *Adv. Energy Mater.* **2011**, *1*, 274–281.

[43] Tokuda, H.; Ishii, K.; Susan, M.; Tsuzuki, S.; Hayamizu, K.; Watanabe, M. *J. Phys. Chem. B* **2006**, *110*, 2833–2839.

[44] Aguilera, L.; Volkner, J.; Labrador, A.; Matic, A. *Phys. Chem. Chem. Phys.* **2015**, *17*, 27082–27087.

CHAPTER

7

Molecular Dynamics Analysis of Charge Transport in Ionic Liquid Electrolytes containing added salt with Mono, Di, and Trivalent Metal Cations

José Manuel Vicent-Luna, Eneko Azaceta, Said Hamad, José Manuel Ortiz-Roldán, Ramón Tena-Zaera, Sofía Calero, and Juan Antonio Anta

Among many other applications, room temperature ionic liquids (ILs) are used as electrolytes for storage and energy conversion devices. In this work, we investigate at microscopic level the structural and dynamical properties of 1-methyl-1-butyl-pyrrolidinium bis(trifluoromethane-

sulfonyl) imide $[C_4PYR]^+$ $[Tf_2N]^-$ IL-based electrolytes for metal-ion batteries. We carried out molecular dynamics simulations of electrolytes mainly composed of $[C_4PYR]^+$ $[Tf_2N]^-$ IL with the addition of M^{n+}-$[Tf_2N]^-$ metal salt (M = Li^+, Na^+, Ni^{2+}, Zn^{2+}, Co^{2+}, Cd^{2+}, and Al^{3+}, n = 1, 2, and 3) dissolved in the IL. The addition of low salt concentration lowers the charge transport and conductivity of the electrolytes. This effect is due to the strong interaction of the metal cations with the $[Tf_2N]^-$ anions, which allows for molecular aggregation between them. We analyze how the conformation of the $[Tf_2N]^-$ anions surrounding the metal cations determine the charge transport properties of the electrolyte. We found two main conformations based on the size and charge of the metal cation: monodentate and bidentate (number of oxygen atoms of the anion pointing to the metal atoms). The microscopic local structure of the M^{n+}-$[Tf_2N]^-$ aggregates influences the microscopic charge transport as well as the macroscopic conductivity of the total electrolyte.
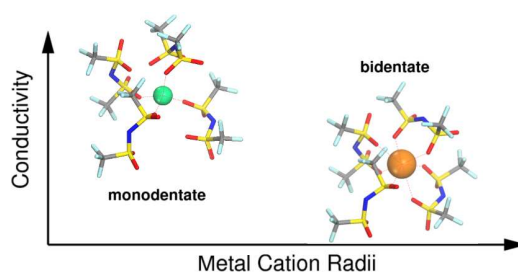
INTRODUCTION

One of the most common applications of room temperature ionic liquids (RTILs or simply ILs) is as electrolytes in electrochemical devices for energy storage.[1] In this context, rechargeable batteries are extended and useful devices to store energy. Since their discovery in 1970s,[2] Li-ion batteries have become popular energy storage solutions and nowadays represent a promising alternative to conventional devices.[3, 4] Ionic liquid-based electrolytes for Li-ion batteries have been widely investigated [5–19] by means of experiments and molecular simulations. The increasing requirements and power of this batteries and disadvantages such as degradation or high flammability, make essential the search of alternative materials.[20] For being a highly abundant raw material, Na-ion batteries have attracted intense attention as potential candidates for the replacement of Li-ion batteries.[21–31] Unfortunately, Na-ion batteries exhibit poor cycle stability and face a trade-off between power density and energy. These limitations make necessary the development of novel strategies to improve the charge storage of advanced Na-ion systems.[32] Other alternatives to Li-ion batteries based on multivalent metal cations are emerging in recent years.[20, 33–41] The ability of these metal species to transfer more than one electron can be useful to obtain faster charge rates. However, a key challenge has

been finding materials capable of producing sufficient voltage after repeated cycles of charging and discharging. Ideally, the resulting devices should be safe, flexible, low cost, and long cycle life. For an efficient search of alternatives, it is crucial to understand the molecular mechanisms that govern the behavior of the electrolytes and the interplay between their performance-determining properties. The latter can be extended not only to energy storage systems as ionic liquid-based electrolytes including multivalent cations have also been recently proposed as advanced electrolytes for the electrodeposition of metals (e.g. Co, Zn, and Al)[42–44] and semiconductors (e.g. ZnO, NiO, and CeO_2)[45–48] films with unique properties for different applications such as photovoltaics.[49] In this regard, molecular simulation is useful and has been proved to describe efficiently microscopic nature of liquid electrolytes and help in understanding the practical electrochemical behavior as a function of ionic liquid-metal cation combination.[36]

The structural and dynamical properties of N-methyl-N-alkyl-pyrrolidinium bis(trifluoromethanesulfonyl) imide $[C_n PYR]^+ [Tf_2N]^-$ IL-based electrolytes for Li-ion batteries have been investigated by molecular dynamic simulations.[6, 7, 12–15, 18] In these works, the Li^+ cation solvation structure is highlighted as the key property that governs the mobility of the ions. The $Li^+[Tf_2N]^-$ first coordination shell exhibits monodentate and bidentate configuration, with one or two

oxygen atoms of the anion pointing to the metal cation, respectively. The strong interaction between Li^+ metal cation and $[Tf_2N]^-$ anions affects the microscopic structure of the electrolytes as well as their macroscopic transport properties.

Despite the above-mentioned works, the microscopic structure and the transport properties of electrolytes for alternative metal-ion batteries are still poorly understood. In our previous work,[27] we used molecular dynamics simulations (MD) to study the microscopic behavior of $[C_4PYR]^+$ $[Tf_2N]^-$ IL-based electrolytes for Li-ion and Na-ion batteries. We identified the progressive formation of Li^+/Na^+ complexes as the origin of the anomalous depletion of the conductivity upon salt addition. The aim of this work is to expand the analysis to electrolytes containing salts of multivalent cations. We analyze transport properties (self-diffusion coefficients and conductivity) of $[C_4PYR]^+$ $[Tf_2N]^-$ IL-based electrolytes including metal salt of monovalent (Li^+ and Na^+), divalent (Ni^{2+}, Zn^{2+}, Co^{2+}, and Cd^{2+}), and trivalent (Al^{3+}) cations. We also consider the pure IL system as a reference scheme for comparison. We use experimental data reported in the literature for validation. At the same working conditions (fixed salt concentration and temperature), we found different behavior based on the nature of the metal cation. In the result section we will show that these differences are due to the microscopic arrangement of the $[Tf_2N]^-$ anions around of the

metal cations.

SIMULATION DETAILS

We carried out molecular dynamics simulations (MD) for $[C_4PYR]^+$ $[Tf_2N]^-$ IL-based electrolytes. The system consists of a cubic box of side circa 35 Å, with 76 IL ion pairs $[C_4PYR]^+$ $[Tf_2N]^-$ and 15 metal cations with the corresponding number of $[Tf_2N]^-$ as counter anions. This is 15, 30, and 45 anions for monovalent, divalent, and trivalent cations, respectively. These systems represent electrolytes with a concentration of 0.5 M of salt dissolved in the IL. Working conditions were fixed at 1 atm and 313 K. Pressure was set employing the Martyna-Tuckerman-Tobias-Klein (MTTK) barostat,[50] and temperature was controlled using the Nose-Hoover thermostat.[51, 52] All simulations were performed using the GROMACS molecular simulation software.[53–56] The initial configurations were created by randomly locating the ion pairs of the salt in an empty cubic simulation box, refilling with IL ion pairs using the Packmol package.[57] The systems were firstly equilibrated using an energy minimization method based on a steepest descent algorithm.[58] After this procedure, we run MD simulations in the NPT ensemble to obtain the equilibrium density of the electrolytes, i.e. energies and volume fluctuating over time around mean values. Starting from these configurations, we run MD simulations in the NVT en-

semble for 50 ns with time step of 2 fs. The process is repeated four times for each system in order to obtain average properties from the resulting independent trajectories. We calculated the diffusion coefficients from the slope of the mean squared displacement using the Einstein equation in the 10-40 ns time interval. We estimated the ionic conductivity through the Nernst-Einstein equation which links the conductivity with the density and diffusion properties.[59] Additional details involving the calculation of the transport properties of the electrolytes can be found in our previous works.[27, 60] We calculated the binding energies of complexes formed by a single metal cation and different number of anions. We performed consecutive energy minimization simulations combining a steepest descent and conjugate gradient algorithms [58] to obtain the less energetic configurations. The potential energy is calculated with the classical potentials used for the MD simulations. Molecular interactions were evaluated by means of effective classical potentials including Lennard-Jones and Coulombic terms. We used the molecular model of $[C_4PYR]^+$ $[Tf_2N]^-$ proposed in our previous work,[61] which was fitted to reproduce experimental values of density and diffusion coefficients. This full flexible model takes into account bonds, bending angles, and dihedral angles. This force field performs well for the ionic conductivity of electrolytes for lithium and sodium batteries.[27] Nonbonded inter-

actions were calculated for a cutoff of 12 Å and electrostatic interactions were computed with the Particle-Mesh Ewald (PME) method.[62, 63] We employed standard Lorentz-Berthelot mixing rules to calculate the cross Lennard-Jones parameters between different atoms. Potential parameters of monovalent, divalent, and trivalent cations were taken from I. S. Joung and T. Cheatham III,[64] P. Li et al.,[65] and T. Faro et al.,[66] respectively. These potentials were developed to reproduce the physical behavior of the metal cations dissolved in a solvent.

RESULTS AND DISCUSSION

Figures 1-3 show the density and transport properties of the electrolytes containing the salt with the different metal cations and compared with the pure IL system. We found good agreement between available experimental data and the values calculated for the pure IL and for the electrolytes containing Na^+ and Li^+ cations. Our simulations show that the properties of the electrolytes vary with the metal cation. In principle, these differences can be attributed to the intrinsic properties of the metal, i.e. ionic radius, charge, and molar mass. For a better understanding of these differences we analyze in depth the effect exerted by the metal cations in the global properties of the electrolytes. Figure 1 shows the average density of the electrolytes at working conditions (0.5 M of salt concentration,
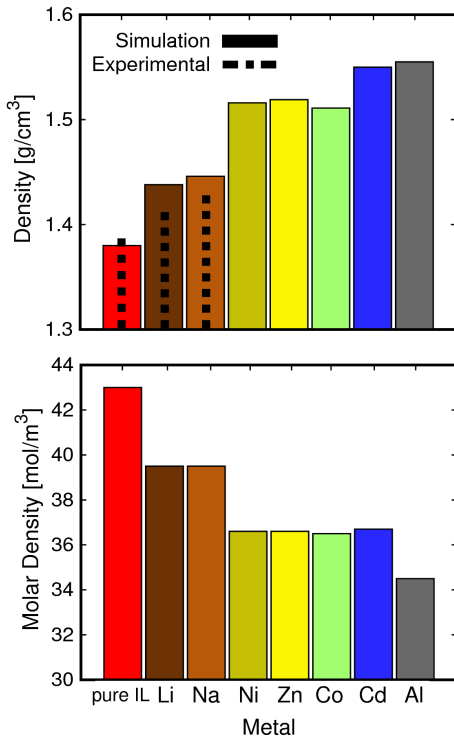
Figure 1. Calculated density (top) and molar density (bottom) of pure IL and 0.5 M electrolytes containing different metal cations. Experimental data for pure IL system are taken from Tokuda et al.[67] and electrolytes containing Li^+ and Na^+ cations are taken from Noor et al.[31]

systems. The increase of the charge of the metal cation, leads to the increase of the number of anions in the electrolyte, thus decreasing the molar density. The molar density of electrolytes containing metal cations equally charged is similar. Hence the variations observed in Figure 1 (top) are due to the different molar mass of the metal cations.

Figure 2 shows the mean squared displacement (MSD) and self-diffusion coefficients for the $[C_4PYR]^+$ cations and $[Tf_2N]^-$ anions. There are three regimes in the logarithmic representation of the MSD. However, the inset clearly shows a linear behavior in the time interval where the diffusion coefficients are extracted. Our results exhibit excellent agreement with the experimental data reported by Tokuda et al.,[67] Castiglione et al.,[10, 17] and Solano et al.[6] in the case of pure IL system and electrolytes containing Li^+ cations. The addition of salt decreases the mobility of the IL constituents, following the opposite trend to the density calculation. $[C_4PYR]^+$ cations diffuse slightly faster than $[Tf_2N]^-$ anions in each electrolyte which also agree with the experimental observations.[6, 67]

The ionic conductivity of the electrolytes is calculated with the Nernst-Einstein equation from the values depicted in figures 1-2:

$$\sigma_i = D_{S_i} \frac{N_i}{q} \frac{q_i^2 e^2}{k_B T} \qquad (2)$$

1 bar, and 313 K). The density of the pure IL system is included for comparison. The values obtained for the pure IL system and electrolytes containing Li^+ and Na^+ salts are in agreement with the experimental values reported by Tokuda et al.,[67] Haskins et al.,[7] and Noor et al.[31] On the one hand, the systems become more dense with the addition of salt to the IL. Figure 1 (bottom) shows the molar density for these

Figure 2. Mean squared displacement as a function of the simulation time for pure IL system and electrolytes containing metal cations (left) and self-diffusion coefficients of the IL constituents as a function of the metal cations (right). $[C_4PYR]^+$ cation (top) and $[Tf_2N]^-$ anion (bottom). Inset figures are the linear representation of the corresponding mean squared displacement. Experimental data for pure IL system are taken from Tokuda et al.[67] and electrolytes containing Li^+ cations are taken from Solano et al.[6]

where σ_i and D_{S_i} are the ionic conductivity and self-diffusion coefficient of species i respectively, N_i is the number of charge carriers, V is the volume of the unit cell, and $q_i e$ is the net charge of the molecule. The total ionic conductivity of the system is the summation of the partial conductivities for each component. The data are collected in Figure 3, where the ionic conductivity is represented as a function of the metal cation and compared with the reference conductivity of the pure IL system. The obtained results are compared with available experimental data for pure

IL system and electrolytes containing monovalent cations reported by Tokuda et al.,[67] Solano et al.,[6] Castiglione et al.,[10, 17] Noor et al.,[31] and Serra Moreno et al.[25] The experimental ionic conductivity of electrolytes containing lithium used for comparison were estimated using the Nernst-Einstein equation with the measurements of self-diffusion coefficients and density reported by Solano et al.[6] Conductivity and self-diffusion coefficients follow similar trends. The calculation of conductivity involves multiplying self-diffusion coefficients and charge
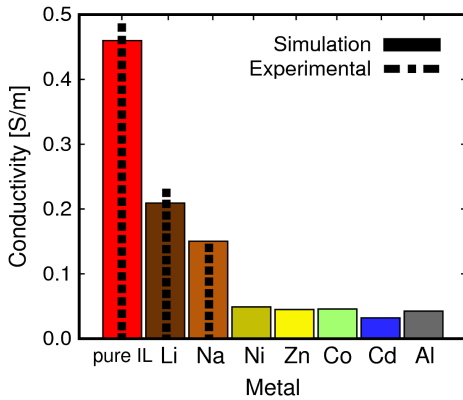
Figure 3. Conductivity of the pure IL system and electrolytes containing metal cations. Experimental data for pure IL system are taken from Tokuda et al.,[67] electrolytes containing Li^+ and Na^+ cations are taken from Noor et al.,[31] and Serra Moreno et al.[25]

carriers density (Eq 1). Then, the similarity with the self-diffusion coefficients plot means that the conductivity is governed mostly by the diffusion of the ions. As the variation of the conductivity is not contolled by density, the cause of these differences may depend mainly of a combination of cation size and charge.

In previous works [27] we demonstrated that the depletion of the conductivity upon the addition of salt is caused by the formation of aggregates or clusters composed by the metal cations and $[Tf_2N]^-$ anions. These clusters induce significant changes in the microscopic structure of the electrolytes, hindering the mobility of ions and consequently reducing the conductivity. Here, we find that the decrease in the diffusivity and the conductivity not only depends on the salt concentra-

tion, but also on the nature of metal cation. This suggests that the behavior of the aggregates varies with the metal cation. This makes essential the understanding of the role of the metal cation in the nature of the clusters. With this intention, we analyze the binding energies of complexes containing one isolated metal cation and a variety of $[Tf_2N]^-$ anions (ranging between 1 and 6). These binding energies are calculated performing consecutive energy minimization simulations to obtain the configurations with the lowest energy. Figure 4 shows the relation between the metal cation and the binding energies. The increase of the charge of the metal atom leads to the increase of the absolute value of the binding energies forming groups of monovalent, divalent and trivalent cations. The most stable configuration for the monovalent cations contains two, three, and four $[Tf_2N]^-$ anions. For the divalent cations, the most stable configuration contains four and five $[Tf_2N]^-$ anions. Following this tendency, Al^{3+} is more stable when surrounded by five anions.

The binding energies shown in Figure 4 correspond to the interaction energies of isolated complexes defined as $M^{m+}[Tf_2N]_n^{(n-m)-}$. However, the electrolyte is a fully interacting system where different kinds of aggregates coexist, all of them interacting between them and the rest of species. For this reason, we analyze the trajectories obtained from MD simulations to describe these aggregates in a full bulk simulation.
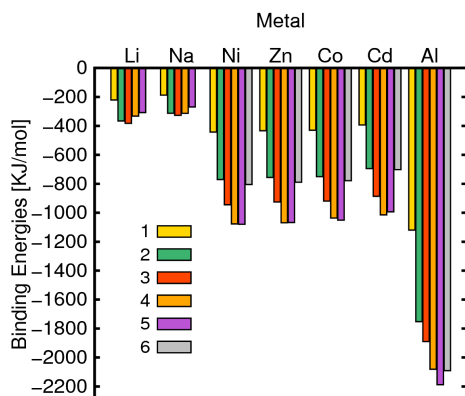
Figure 4. Binding energies of the systems composed by $n[Tf_2N]^-$ anions (n = 1-6) and one isolated metal cation.

Figure 5. Example of aggregates found in the bulk during MD simulations. The aggregates are formed by one isolated metal cation surrounded by $n[Tf_2N]^-$ anions.

Table A5-1. Percentage of aggregates containing $n[Tf_2N]^-$ anions.

M^{n+}	3	4	5	6
Li^+	0.9	68.0	31.1	0.0
Na^+	5.2	82.3	12.5	0.0
Ni^{2+}	0.0	0.0	59.5	4.05
Zn^{2+}	0.0	0.0	51.4	48.6
Co^{2+}	0.0	0.0	44.3	55.7
Cd^{2+}	0.0	0.0	45.5	54.7
Al^{3+}	0.0	0.2	38.1	61.7

Figure 5 represents a schematic example of the possible clusters found in the simulations. In addition, Table 1 collects the percentage of these aggregates which contain three, four, five, and six anions, respectively. Complexes including one or two anions are not found, even when the combination of one monovalent cation and two $[Tf_2N]^-$ anions is energetically favorable (see Figure 4). This is due to the influence of the surrounding species that alter the "ideal"situation represented in Figure 4. Then, monovalent cations are mostly solvated by four $[Tf_2N]^-$ anions and, in a smaller proportion, by five anions. For the same reason the divalent and trivalent cations only form complexes with at least five or six $[Tf_2N]^-$ anions in a similar proportion. Because the size and geometry of the anion, steric effects play an important role in the solvation of the metal cation, which cannot be solvated by more than six $[Tf_2N]^-$ anions. Based on these results, metal cations with higher charge are coordinated by more anions, as a consequence of a more intense ionic correlation. This explains the overall decrease in the diffusivity of all species of the electrolytes containing divalent and trivalent metal cations. However, the differences between

metal cations with the same charge are
not explained yet.

We found that metal cations with the
same charge are surrounded by a simi-
lar number of anions. However, the micro-
scopic organization of each $[Tf_2N]^-$ anion
around a metal cation can be classified
based on one or two oxygen atoms per an-
ion pointing to the metal cation, i.e mon-
odentate or bidentate coordination (see
Figure 5-6). Considering this, we com-
puted the coordination number between
the metal cations and $[Tf_2N]^-$ anions and
between the metal cations and the oxy-
gen atoms of $[Tf_2N]^-$ anions. The reference
atoms for the M-$[Tf_2N]^-$ coordination and
M-$O_{[Tf_2N]^-}$ coordination were the two oxy-
gen atoms binding the central nitrogen
atom, and the nitrogen atom itself. The co-
ordination numbers were calculated in the
first coordination shell between the metal
atoms and the anions, averaging over all
configurations and simulation time. The
cutoff distances of the coordination shell
is given by the RDF (Figure 6) of the
reference atoms, 5.5 Å for M-$[Tf_2N]^-$ and
3.5 Å for M-$O_{[Tf_2N]^-}$ coordination. To de-
scribe the microscopic assembly of the clus-
ters we computed the RDF between the
metal cations and the anion at short dis-
tances. This represents the first coordina-
tion sphere of the cations, i.e. the local
structure of the clusters. Figure 6 (top)
shows the RDF between the metal cation
and the nitrogen atom of the anion (M-
$[Tf_2N]^-$). The RDFs of monovalent and
divalent cations exhibit two main peaks in
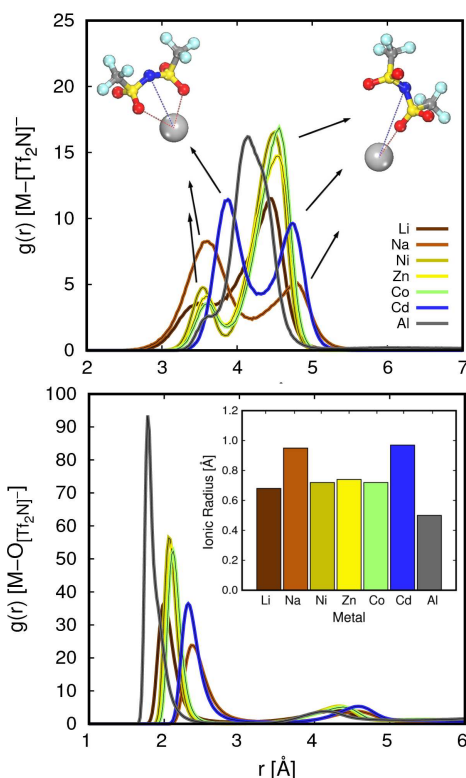
Figure 6. Short-range radial distribu-
tion function between metal cations and
nitrogen atoms of $[Tf_2N]^-$ anions (top)
and between metal cations and oxygen
atoms of $[Tf_2N]^-$ anions (bottom). Inset figure
represents the ionic radius of each metal cation.

the range of 3-4 Å and 4-5 Å, respectively.
These peaks correspond to bidentate and
monodentate coordination, respectively. In
this context, Li^+, Ni^{2+}, Zn^{2+} and Co^{2+}
cations mainly show monodentate coordi-
nation, while for Na^+ and Cd^{2+} cations
we found higher contribution of bidentate
coordination. The RDF corresponding to
Al^{3+} cations has a single peak in the mid-
dle of the two ranges, which indicates that
the two coordinations coexist. These differ-

ences can be explained taking into account
the ionic radius of the metal ions (see inset
of Figure 6). On the one hand, the ionic ra-
dius of Li^+, Ni^{2+}, Zn^{2+}, and Co^{2+} cations
is about 0.7 Å which favors monodentate
coordination. On the other hand, Na^+ and
Cd^{2+}, with an ionic radius about 1 Å, can
accommodate more oxygen atoms close to
their surface. This leads to bidentate co-
ordination for the bulkiest metal cation
studied. Finally, Al^{3+} metal cations have
the smallest ionic radius (about 0.5 Å), but
also the highest charge. This fact makes
they interact strongly with the oxygen
atoms of the $[Tf_2N]^-$ anions due to their
opposite charge. Figure 6 (bottom) depicts
the RDF between the metal cations and
the oxygen atoms of $[Tf_2N]^-$ anions. The
results confirm the strong interaction be-
tween the metal cations and oxygen atoms
of the anions since they are located at very
close distances (lower than 2.5 Å). Further-
more, the position of the first peak of the
M-$O_{[Tf_2N]^-}$ RDF follows the same trend
that the ionic radius of the cations (see
inset of Figure 6).

Figure 7 (top) represents the average
coordination number of M-$[Tf_2N]^-$ and M-
$O_{[Tf_2N]^-}$ calculated following the criterion
described above. These results summarize
the relations between size and charge of
metal cations and the conformation of the
complexes. The increase of the charge of
the cation increases the number of coor-
dinated anions per metal cation (Li^+ and
Na^+, vs Ni^{2+}, Zn^{2+}, Co^{2+}, Cd^{2+}, and Al^{3+}).
This is due to the strong electrostatic
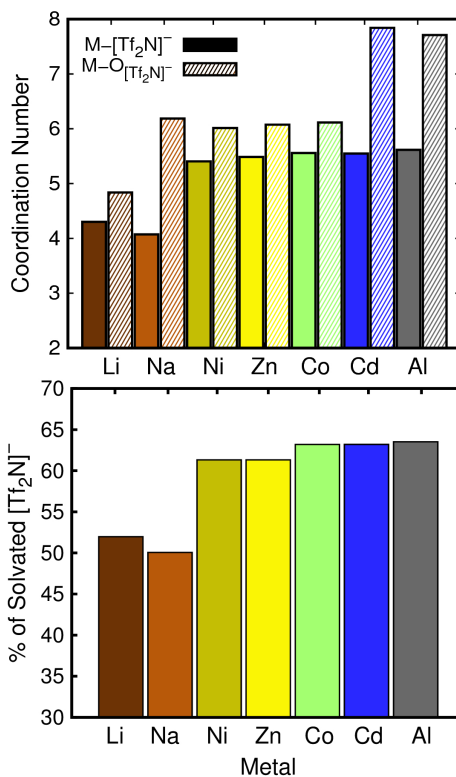
Figure 7. Number of $[Tf_2N]^-$ anions and
number of oxygen atoms of $[Tf_2N]^-$ anions
coordinated with each metal cation (top).
Percentage of $[Tf_2N]^-$ anions in the electrolyte
coordinated with metal cations (bottom).

interaction of metal cations with high
charge. Moreover, the increase in the
ionic radius favors bidentate coordination
(Li^+, Ni^{2+}, Zn^{2+}, and Co^{2+} vs Na^+ and
Cd^{2+}). The large differences between M-
$[Tf_2N]^-$ and M-$O_{[Tf_2N]^-}$ coordination num-
bers are due to major contribution of biden-
tate conformations. The bulkier cations
can accommodate more atoms of oxygen
close to their surface. This effect leads to
a higher correlation of the clusters and ex-

plains the decrease in the diffusivity of the species of the electrolytes containing Na^+ and Cd^{2+} compared with those containing Li^+, Ni^{2+}, Zn^{2+}, and Co^{2+} (see Figure 2). Finally, Al^{3+} coordinates mainly with bidentate conformation, which suggests that the high charge of the metal cation compensates the effect of the low size.

Our results describe the behavior of the local structure of the clusters. However, these complexes influence the behavior of the whole electrolyte. Figure 7 (bottom) shows the percentage of $[Tf_2N]^-$ anions existing in the electrolyte, that are coordinated with metal cations. The concentration of salt added to the IL is 0.5 M which corresponds to a molar fraction of about 0.15 of metal salt and 0.85 of IL. Although this concentration is low, the metal cations are solvated by approximately 50 % or 60-65 % of the total number of anions depending on the charge of the metal cations. This solvation determines the total structure of the electrolyte. The $[Tf_2N]^-$ -$[Tf_2N]^-$ and $[C_4PYR]^+$ -$[C_4PYR]^+$ RDFs are depicted in Figure 8. The addition of salt of different nature does not affect significantly to the overall structure of $[C_4PYR]^+$ cations. However, the $[Tf_2N]^-$ -$[Tf_2N]^-$ can be classified in three groups depending on the behavior of the pure IL system. The $[Tf_2N]^-$ -$[Tf_2N]^-$ RDF of the pure IL system behaves as simple liquid system with a smooth first peak at 8 Å. With the addition

of salt of monovalent cations, we found a small first peak at shorter distances (5 Å). This additional peak stands for the interaction of the $[Tf_2N]^-$ anions inside the clusters, while the main peak becomes from the "bulk"interaction of $[Tf_2N]^-$ anions. The small first peak emerged for electrolytes containing sodium is slightly higher than the corresponding to lithium-based electrolytes. This agrees with previous analysis of the size of the metal cation and its effect on the conformation of the clusters. For electrolytes containing Ni^{2+}, Zn^{2+}, and Co^{2+} we found a disorganized $[Tf_2N]^-$ -$[Tf_2N]^-$ RDF with a variety of peaks that reflect more complex organization. This fact is in line with the decrease of the mobility of the IL constituents as the added metal cations are more charged. Electrolytes containing Cd^{2+} and Al^{3+} exhibit a $[Tf_2N]^-$ -$[Tf_2N]^-$ RDF with a more pronounced first peak at 5 Å. This strong correlation at short distances leads to the decrease of the mobility of the species of the system. It is for this reason that the systems with high contribution of bidentate conformation of the clusters show lower mobility.

We compute the average occupation profiles of the geometric center of the anions to support previous findings (Figure 9). The spatial distribution of the anions in the pure IL system points to a homogeneous system.
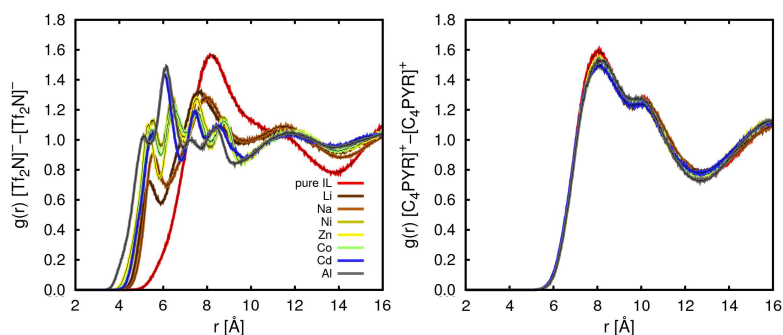
Figure 8. Anion-anion (left) and cation-cation (right) radial distribution function. The atom of nitrogen is the reference atom.
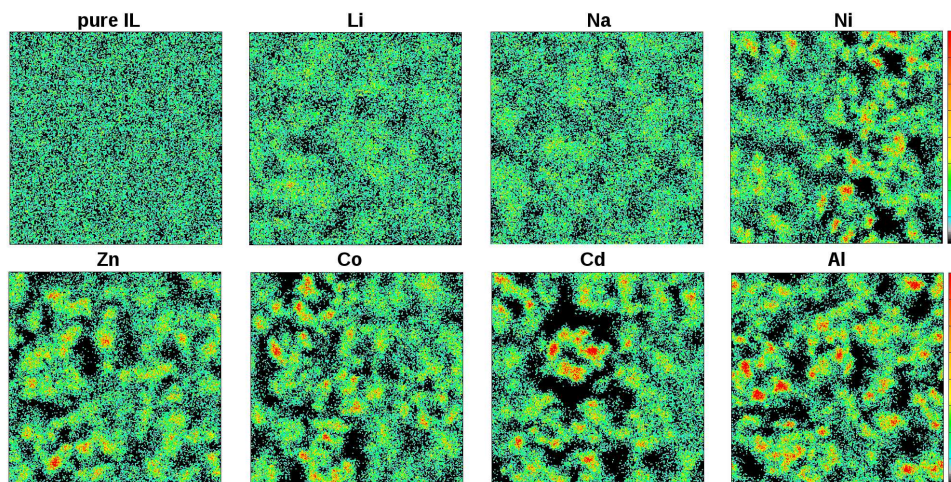
Figure 9. Average occupation profiles of the geometric center in XY plane of the $[Tf_2N]^-$ anions in the pure IL system and electrolytes containing metal cations.

The addition of salt of monovalent cations modifies the organization of the anions of the electrolyte due to the cluster formation. The arrangement of the cluster increases in electrolytes containing divalent cations with monodentate coordination (Ni^{2+}, Zn^{2+}, and Co^{2+}) making the system more heterogeneous. This heterogeneity is enhanced in electrolytes with Cd^{2+} and Al^{3+} which contains clusters of bidentate conformation. The different spatial reorganization of the microscopic structure of the anions influences the behavior of the microscopic and macroscopic properties of the entire electrolyte.

Conclusions

We investigated by means of MD simulations the role of the metal cation in the behavior of IL-based electrolytes when a fixed salt concentration is added. We analyzed metal salts containing monovalent, divalent, and trivalent cations dissolved in $[C_4PYR]^+$ $[Tf_2N]^-$ IL. We found remarkable distinct behavior in the microscopic and macroscopic properties of the electrolytes, such as density, self-diffusion coefficients, and conductivity, as the nature of the metal salt added is changed. We attributed these differences to a combination of size and charge effects of the metal cations. To do so, we analyzed thoroughly the microscopic assembly of complexes formed by the metal cation and the $[Tf_2N]^-$ anions. We found monodentate and bidentate conformations depending on the number of oxygen atoms of the anion pointing to the metal cation. These conformations and the number of $[Tf_2N]^-$ anions coordinated with the metal cations govern the structural organization of the complexes as well as the performance of the electrolyte.

Bibliography

[1]   Armand, M.; Endres, F.; MacFarlane, D. R.; Ohno, H.; Scrosati, B. *Nat. Mater.* **2009**, *8*, 621–9.

[2]   Whittingham, M. S. *Science (80-.).* **1976**, *192*, 1126.

[3]   Basile, A.; Bhatt, A. I.; O'Mullane, A. P. **2016**, *7*, ncomms11794.

[4]   Bhatt, M. D.; O'Dwyer, C. *Phys. Chem. Chem. Phys.* **2015**, *17*, 4799–4844.

[5]   Fujii, K.; Hamano, H.; Doi, H.; Song, X.; Tsuzuki, S.; Hayamizu, K.; Seki, S.; Kameda, Y.; Dokko, K.; Watan-abe, M.; Umebayashi, Y. *J. Phys. Chem. C* **2013**, *117*, 19314–19324.

[6]   Solano, C. J. F.; Jeremias, S.; Paillard, E.; Beljonne, D.; Lazzaroni, R. *J. Chem. Phys.* **2013**, *139*, 34502.

[7]   Haskins, J. B.; Bennett, W. R.; Wu, J. J.; Hernández, D. M.; Borodin, O.; Monk, J. D.; Bauschlicher, C. W.; Lawson, J. W. *J. Phys. Chem. B* **2014**, *118*, 11295–11309.

[8]   Kunze, M.; Jeong, S.; Paillard, E.; Schönhoff, M.; Winter, M.; Passerini, S. *Adv. Energy Mater.* **2011**, *1*, 274–281.

[9]   Lassègues, J.-C.; Grondin, J.; Talaga, D.; Lassegues, J. C.; Grondin, J.; Talaga, D. *Phys. Chem. Chem. Phys.* **2006**, *8*, 5629–5632.

[10]   Castiglione, F.; Ragg, E.; Mele, A.; Appetecchi, G. B.; Montanino, M.; Passerini, S. *J. Phys. Chem. Lett.* **2011**, *2*, 153–157.

[11]   Wilken, S.; Xiong, S.; Scheers, J.; Jacobsson, P.; Johansson, P. *J. Power Sources* **2015**, *275*, 935–942.

[12]   Diddens, D.; Heuer, A. *J. Phys. Chem. B* **2013**, *c*, 1–20.

[13]   Borodin, O.; Smith, G. D.; Henderson, W. *J. Phys. Chem. B* **2006**, *110*, 16879–16886.

[14]   Li, Z.; Borodin, O.; Smith, G. D.; Bedrov, D. *J. Phys. Chem. B* **2015**, *119*, 3085–3096.

[15]   Li, S.; Banuelos, J. L.; Guo, J.; Anovitz, L.; Rother, G.; Shaw, R. W.; Hillesheim, P. C.; Dai, S.; Baker, G. A.; Cummings, P. T. *J. Phys. Chem. Lett.* **2012**, *3*, 125–130.

[16]   Lassègues, J.-C.; Grondin, J.; Aupetit, C.; Johansson, P. *J. Phys. Chem. A* **2009**, *113*, 305–314.

[17]   Castiglione, F.; Famulari, A.; Raos, G.; Meille, S. V.; Mele, A.; Appetecchi, G. B.; Passerini, S. *J. Phys. Chem. B* **2014**, *118*, 13679–13688.

[18]   Lesch, V.; Li, Z.; Bedrov, D.; Borodin, O.; Heuer, A. *Phys. Chem. Chem. Phys.* **2016**, *18*, 382–392.

[19]   Menne, S.; Vogl, T.; Balducci, A. *Phys. Chem. Chem. Phys.* **2014**, *16*, 5485–5489.

[20]   Liang, J.; Li, F.; Cheng, H.-M. *Energy Storage Mater.* **2017**, *7*, A1–A3.

[21]   Monti, D.; Jónsson, E.; Palacín, M. R.; Johansson, P. *J. Power Sources* **2014**, *245*, 630–636.

[22]   Ding, C.; Nohira, T.; Hagiwara, R.; Matsumoto, K.; Okamoto, Y.; Fukunaga, A.; Sakai, S.; Nitta, K.; Inazawa, S. *J. Power Sources* **2014**, *269*, 124–128.

[23]   Yoon, H.; Zhu, H.; Hervault, A.; Armand, M.; MacFarlane, D. R.; Forsyth, M. *Phys. Chem. Chem. Phys.* **2014**, *16*, 12350–12355.

[24]   Andriola, A.; Singh, K.; Lewis, J.; Yu, L. *J. Phys. Chem. B* **2010**, *114*, 11709–11714.

[25]   Serra Moreno, J.; Maresca, G.; Panero, S.; Scrosati, B.; Appetecchi, G. B. *Electrochem. commun.* **2014**, *43*, 1–4.

[26]   Nayak, P. K.; Yang, L.; Brehm, W.; Adelhelm, P. *Angew. Chemie Int. Ed.* **2017**, n/a–n/a.

[27]   Vicent-Luna, J. M.; Ortiz-Roldan, J. M.; Hamad, S.; Tena-Zaera, R.; Calero, S.; Anta, J. A. *Chemphyschem* **2016**, *17*, 2473–2481.

[28]   Hartmann, P.; Bender, C. L.; Vračar, M.; Dürr, A. K.; Garsuch, A.; Janek, J.; Adelhelm, P. *Nat. Mater.* **2013**, *12*,

228–32.

[29] Forsyth, M.; Yoon, H.; Chen, F.; Zhu, H.; MacFarlane, D. R.; Armand, M.; Howlett, P. C. *J. Phys. Chem. C* **2016**, *120*, 4276–4286.

[30] Wongittharom, N.; Wang, C.-H.; Wang, Y.-C.; Yang, C.-H.; Chang, J.-K. *ACS Appl. Mater. Interfaces* **2014**, *6*, 17564–17570.

[31] Mohd Noor, S. A.; Howlett, P. C.; Macfarlane, D. R.; Forsyth, M. *Electrochim. Acta* **2013**, *114*, 766–771.

[32] Wang, X.; Kajiyama, S.; Iinuma, H.; Hosono, E.; Oro, S.; Moriguchi, I.; Okubo, M.; Yamada, A. **2015**, *6*, 6544.

[33] Guduru, R.; Icaza, J. *Nanomaterials* **2016**, *6*, 41.

[34] Lapidus, S. H.; Rajput, N. N.; Qu, X.; Chapman, K. W.; Persson, K. a.; Chupas, P. J. *Phys. Chem. Chem. Phys.* **2014**, *16*, 21941–21945.

[35] Xu, C.; Chen, Y.; Shi, S.; Li, J.; Kang, F.; Su, D. **2015**, *5*, 14120.

[36] Azaceta, E.; Lutz, L.; Grimaud, A.; Vicent-Luna, J. M.; Hamad, S.; Yate, L.; Cabanero, G.; Grande, H. J.; Anta, J. A.; Tarascon, J. M.; Tena-Zaera, R. *ChemSusChem* **2017**, *10*, 1616–1623.

[37] Lin, M.-C.; Gong, M.; Lu, B.; Wu, Y.; Wang, D.-Y.; Guan, M.; Angell, M.; Chen, C.; Yang, J.; Hwang, B.-J.; Dai, H. *Nature* **2015**, *520*, 324–328.

[38] Jankowski, P.; Wieczorek, W.; Johansson, P. *Phys. Chem. Chem. Phys.* **2016**, *18*, 16274–16280.

[39] Yoo, H. D. et al. *Nat. Commun.* **2017**, *8*.

[40] Jian, Z.; Luo, W.; Ji, X. *J. Am. Chem. Soc.* **2015**, *137*, 11566–11569.

[41] Parker, J. F.; Chervin, C. N.; Pala, I. R.; Machler, M.; Burz, M. F.; Long, J. W.; Rolison, D. R. *Science (80-.).* **2017**, *356*, 414–417.

[42] Tułodziecki, M.; Tarascon, J.-M.; Taberna, P.; Guery, C. *Electrochimica Acta* **2014**, *134*, 55 – 66.

[43] Endres, F.; Bukowski, M.; Hempelmann, R.; Natter, H. *Angew. Chemie Int. Ed.* **2003**, *42*, 3428–3430.

[44] Endres, F.; MacFarlane, D.; Abbott, A. *Electrodeposition from Ionic Liquids*; 2008.

[45] Azaceta, E.; Chavhan, S.; Rossi, P.; Paderi, M.; Fantini, S.; Ungureanu, M.; Miguel, O.; Grande, H.-J.; Tena-Zaera, R. *Electrochim. Acta* **2012**, *71*, 39–43.

[46] Azaceta, E.; Tena-Zaera, R.; Marcilla, R.; Fantini, S.; Echeberria, J.; Pomposo, J. A.; Grande, H.; Mecerreyes, D. *Electrochem. commun.* **2009**, *11*, 2184–2186.

[47] Tulodziecki, M.; Tarascon, J. M.; Taberna, P. L.; Guery, C. *J. Electrochem. Soc.* **2012**, *159*, D691–D698.

[48] Lair, V.; Sirieix-Plenet, J.; Gaillon, L.; Rizzi, C.; Ringuedé, A. *Electrochim. Acta* **2010**, *56*, 784–789.

[49] Azaceta, E.; Idigoras, J.; Echeberria, J.; Zukal, A.; Kavan, L.; Miguel, O.; Grande, H.-J.; Anta, J. A.; Tena-Zaera, R. *J. Mater. Chem. A* **2013**, *1*, 10173–10183.

[50] Martyna, G. J.; Tuckerman, M. E.; Tobias, D. J.; Klein, M. L. *Mol. Phys.* **1996**, *87*, 1117–1157.

[51] Nose, S. *Mol. Phys.* **2002**, *100*, 191–198.

[52] Hoover, W. G. *Phys. Rev. A* **1985**, *31*, 1695–1697.

[53] Berendsen, H. J. C.; Vanderspoel, D.; Vandrunen, R. *Comput. Phys. Commun.* **1995**, *91*, 43–56.

[54] Hess, B.; Kutzner, C.; van der Spoel, D.; Lindahl, E. *J. Chem. Theory Comput.* **2008**, *4*, 435–447.

[55] Pronk, S.; Pall, S.; Schulz, R.; Larsson, P.; Bjelkmar, P.; Apostolov, R.; Shirts, M. R.; Smith, J. C.; Kasson, P. M.; van der Spoel, D.; Hess, B.; Lindahl, E. *Bioinformatics* **2013**, *29*, 845–854.

[56] Van der Spoel, D.; Lindahl, E.; Hess, B.; Groenhof, G.; Mark, A. E.; Berendsen, H. J. C. *J. Comput. Chem.* **2005**, *26*, 1701–1718.

[57] Martinez, L.; Andrade, R.; Birgin, E. G.; Martinez, J. M. *J. Comput. Chem.* **2009**, *30*, 2157–2164.

[58] Payne, M. C.; Teter, M. P.; Allan, D. C.; Arias, T. A.; Joannopoulos, J. D. *Rev. Mod. Phys.* **1992**, *64*, 1045–1097.

[59] Every, H. a.; Bishop, A. G.; MacFarlane, D. R.; Orädd, G.; Forsyth, M. *J. Mater. Chem.* **2001**, *11*, 3031–3036.

[60] Vicent-Luna, J. M.; Romero-Enrique, J. M.; Calero, S.; Anta, J. A. *J. Phys. Chem. B* **2017**, *121*, 8348–8358.

[61] Vicent-Luna, J. M.; Idígoras, J.; Hamad, S.; Calero, S.; Anta, J. A. *J. Phys. Chem. C* **2014**, *118*, 28448–28455.

[62] Darden, T.; York, D.; Pedersen, L. *J. Chem. Phys.* **1993**, *98*, 10089–10092.

[63] Essmann, U.; Perera, L.; Berkowitz, M. L.; Darden, T.; Lee, H.; Pedersen, L. G. *J. Chem. Phys.* **1995**, *103*, 8577–8593.

[64] Joung, I. S.; Cheatham, T. E. *J. Phys. Chem. B* **2008**, *112*, 9020–9041.

[65] Li, H.; Imai, Y.; Takiue, T.; Matsubara, H.; Aratono, M. *Colloids Surfaces a-Physicochemical Eng. Asp.* **2013**, *427*, 26–32.

[66] Faro, T. M. C.; Thim, G. P.; Skaf, M. S. *J. Chem. Phys.* **2010**, *132*.

[67] Tokuda, H.; Ishii, K.; Susan, M.; Tsuzuki, S.; Hayamizu, K.; Watanabe, M. *J. Phys. Chem. B* **2006**, *110*, 2833–2839.
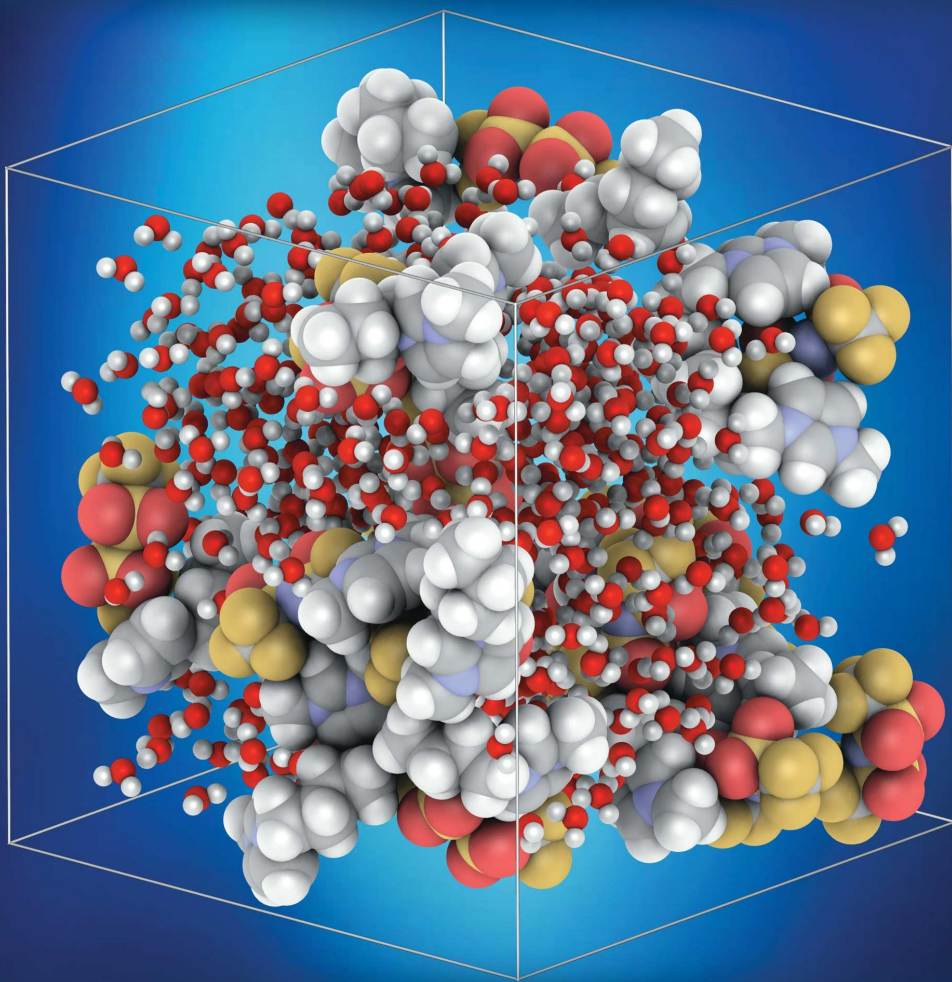
Cover Picture:
P. Gómez-Álvarez, S. Calero et al.
Aqueous Solutions of Ionic Liquids:
Microscopic Assembly

Aqueous Solutions of Ionic Liquids: Microscopic Assembly

José Manuel Vicent-Luna, David Dubbeldam, Paula Gómez-Álvarez, and Sofía Calero

Aqueous solutions of ionic liquids are of special interest, due to the distinctive properties of ionic liquids, in particular, their amphiphilic character. A better understanding of the structure-property relationships of such systems is hence desirable. One of the crucial molecular-level interactions that influences the macroscopic behavior is hydrogen bonding. In this work, we conduct molecular dynamics simulations to investigate the effects of ionic liquids on the hydrogen-bond network of water in dilute aqueous solutions of ionic liquids with various combinations of cations and anions. Calculations are performed for imidazolium-based cations with alkyl chains of different lengths and for a variety of anions, namely, $[Br]^-$, $[NO_3]^-$, $[SCN]^-$, $[BF_4]^-$, $[PF_6]^-$, and $[Tf_2N]^-$. The structure of water and the water-ionic liquid interactions involved in the formation of a heterogeneous network are analyzed by using radial distribution functions and hydrogen-bond statistics. To this end, we employ the geometric criterion of the hydrogen-bond definition and it is shown that the structure of water is sensitive to the amount of ionic liquid and to the anion type. In particular, $[SCN]^-$ and $[Tf_2N]^-$ were found to be the most hydrophilic and hydrophobic anions, respectively. Conversely, the cation chain length did not influence the results.
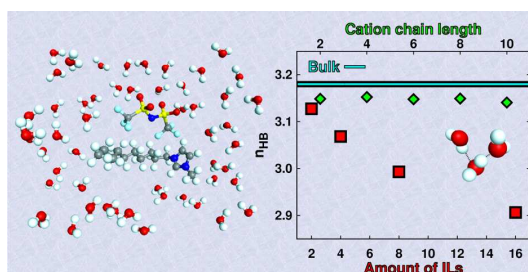
INTRODUCTION

Room-temperature ionic liquids (RTILs or only ILs) are molten salts composed of large organic cations and smaller organic or inorganic anions. Their inherent attractive physical and chemical properties make them potentially useful for a wide range of chemical and industrial applications.[1, 2] Among others, melting point, viscosity, and density, can be adjusted by varying the chemical structures of the ions comprised. This designer character is claimed to be an advantage to suit the requirements of a particular process.[3, 4] Another important property of ILs changing with structure is their miscibility. In addition to the interactions existing in conventional organic solvents (hydrogen bonding, dipole-dipole and van der Waals interactions), ILs have ionic interactions that make them very miscible with polar substances. Overall, the anion controls their water solubility, but the length of the alkyl chains in the cations also matters because of their hydrophobic nature. At the same time the presence of the alkyl chain determines their solubility in less polar fluids.

The behavior of ILs when mixed with polar solvents is of great interest from both a fundamental and industrial viewpoint due to their amphiphilic character. Especially intriguing are aqueous solutions of ILs, whose thermodynamic properties and microscopic assembly have been considerably studied.[5–26] Miscibility is another important property of ILs that changes with their structure. Despite these efforts, a deeper and more quantitative understanding of the molecular-level structure is still needed. Indeed, there is even controversy with similar simpler systems: Although it is generally assumed that ions dissolved in liquid water have a strong effect on its hydrogen-bond structure,[27, 28] a negligible effect was found by Omta et al.[29] In this context, molecular simulation (MS) techniques represent a useful alternative to experiments as MS allows the detailed exploration of the molecular arrangements inside the fluids. Here we present a comprehensive computational study of the influence of low concentrations of ILs on the H-bond network of water, and of their cross interactions. In particular, we performed molecular dynamics (MD) simulations of dilute water/ILs systems for a variety of anion types and of lengths of the alkyl chain of imidazolium-based cations. The role of these factors was thus examined. The set of considered IL ion pairs is depicted in Figure 1. We used previously validated atomistic descriptions and intermolecular interactions. The H-bond formation of water and the cross water-IL interactions were analyzed via radial distribution functions (RDFs) and H-bond statistics, which were determined by employing a geometric criterion[30] of the H-bond definition.
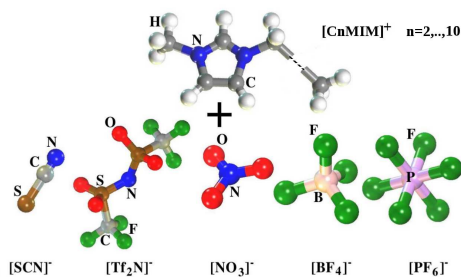
Figure 1. Set of IL ion pairs used in this work.

SIMULATION DETAILS

We considered from 1 to 16 IL ion pairs mixed with 500 water molecules, with imidazolium-based cations of alkyl chains having from 2 to 10 carbon atoms and the following set of anions: bis[(trifluoromethyl)-sulfonyl]imide ($[Tf_2N]^-$), thiocyanate ($[SCN]^-$), nitrate ($[NO_3]^-$), hexafluorophosphate ($[PF_6]^-$), tetrafluoroborate ($[BF_4]^-$), and bromide ($[Br]^-$). For these systems, we conducted MD simulations using the RASPA code.[31] The initial configurations for the systems were generated by randomly placing the ILs and water molecules in a cubic box of 30 Å length. We used a time step of 1 fs. First, we performed NPT simulations for 1 ns to relax the system close to their equilibrium density. We fixed the temperature T and pressure P using Nose-Hoover thermostat [32, 33] and Martyna-Tuckerman-Tobias-Klein barostat,[34] respectively. These simulations are equilibrated when over time, the total energy and cell volume fluctuates around a mean

value. Then, we executed the production runs for 1 million of steps (1 ns) in the NVT ensemble.

We evaluated the interactions using a classical force field including Lennard-Jones and Coulombic terms for water and ILs. Water was assumed to be rigid, while the intramolecular interactions of the ILs were described by harmonic bonds, bends, and dihedrals according to equation 1. The force field parameters for the cations were taken from Canongia Lopes et al.,[35] ($[C_nMIM]^+$), Kelkar and Maginn,[36] ($[Tf_2N]^-$), Yan et al.,[37] ($[NO_3]^-$), Cadena et al.,[38] ($[PF_6]^-$), Liu et al.,[39] ($[BF_4]^-$), Chaumont and Wipff,[40] ($[SCN]^-$), and Markovich et al.[41] ($[Br]^-$). Water was defined using the five-site TIP5P/Ew model.[42] Standard Lorentz-Berthelot combining rules were used to calculate the cross Lennard-Jones potential parameters. Lennard-Jones cut-off radius was set to 12 Å. Periodic boundary conditions were employed in the three dimensions. Electrostatic interactions were computed using the Ewald summation technique [43, 44] while no tail corrections were applied for van der Waals interactions.

$$\Phi_{int} = \sum_{bonds} k_b(r - r_0)^2 + \sum_{angles} k_\theta(\theta - \theta_0)^2$$
$$+ \frac{1}{2} \sum_{n=1}^{3} k_n[1 + \cos(n\phi)]$$
$$(1)$$

For the computation of the RDFs, we used the following criterion regarding the

atom selection: We considered the oxygen atom for water, the central atom of each anion, and the nitrogen atom of the imidazolium ring linked to the alkyl chain for the cation. The central atom coincides with the center of mass (and with the centroid of charge) due to symmetry for all the anions except for $[SCN]^-$, for which the latter is slightly shifted to the sulphur atom. We assumed the central carbon atom for these calculations as a good approximation.

The definition of H-bond formation between water molecules involves the application of a rigorous criterion. Here, the H-bond network of water in each system has been analysed in terms of the relative configuration of two water molecules, that is, using the geometric criterion of H-bond formation. Specifically, the interaction between two water molecules is defined as a hydrogen bond when their interatomic separations r_{OO} and r_{OH} are lower than certain cut-off values, which are given by the respective average distances of the first minimum location in the $g_{OO}(r)$ and $g_{OH}(r)$ RDFs, and limitation to the angle α between intermolecular $O---O$ and covalent $O-H$ vectors, where H forms the hydrogen bond, is fulfilled.

RESULTS AND DISCUSSION

The analysis of the RDFs aids to understanding the microscopic behavior of the water/ILs mixtures by providing information on the average intermolecular distances and the presence of hydrogen bonds. The selected atoms for the RDF calculations are specified in the Simulation details section. Figures 2 and 3 display the RDFs corresponding to the anion-cation, anion-water, cation-water and water-water pairs for different systems. These functions have been smoothed for clarity; see Figure A6.1 of the Appendix 6 for the raw data. Figure 2 shows the effect of the anion type on the previously mentioned pairwise interactions for water/ILs mixtures containing 16 IL ion pairs and 500 water molecules (aqueous solution of about 1 M) with $[C_{10}MIM]^+$ as cation. The position of the peak of the cation-anion RDF (Figure 2a) is clearly dependent on the type of anion. In general, it is present at about 5 Å, but the first peak for $[SCN]^-$ is located at distances larger than 6 Å, thus indicating a weak cation-anion interaction. As apparent from Figure 2b, the influence of the anion type is even more prominent when it interacts with water. $[SCN]^-$ anion is found to be the most hydrophilic anion by far. The corresponding RDF exhibits a narrow peak at distances lower than 3 Å, suggesting strong ordering of water around this anion. This result is consistent with anion-cation interactions. These functions show noticeable first peaks followed by one or two more maxima of diminishing amplitude. According to the first hydration shells, we can predict the following order of increasing hydrophobicity of the selected anions: $[SCN]^- < [NO_3]^- < [BF_4]^- < [PF_6]^- < [Tf_2N]^-$.
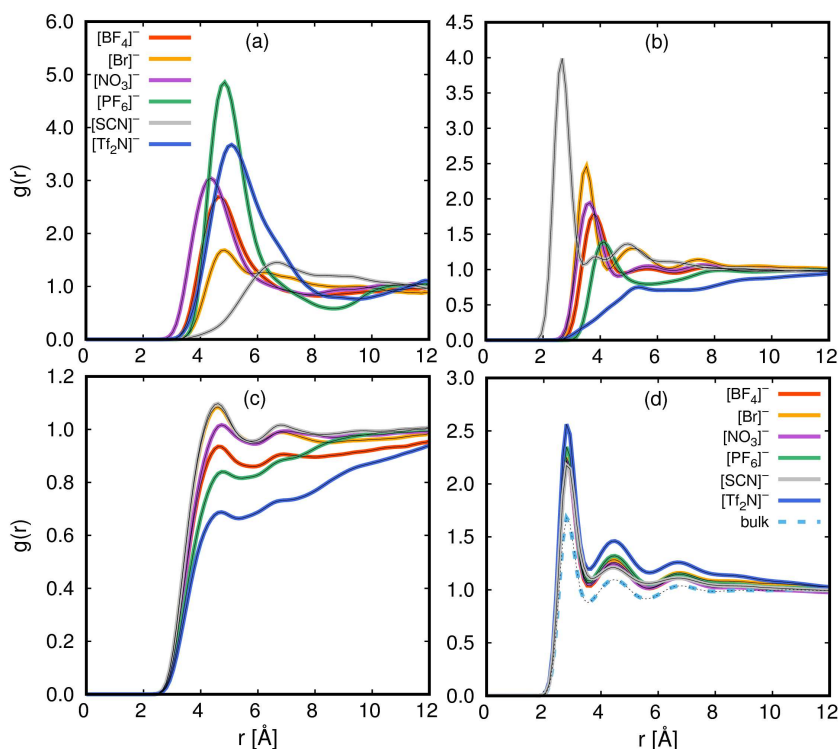
Figure 2. RDFs for a) cation-anion, b) anion-water, c) cation-water, and d) water-water pairs for mixtures of 16 IL ion pairs mixed with 500 water molecules (about 1 M) with $[C_{10}MIM]^+$ as the cation and a range of different anion types to investigate the effect of the anion type. The reference atoms for these RDFs are described in the Computational Details.

We do not include $[Br]^-$ anion in the sequence, as the size can be a misleading factor; we will discuss this issue below. On the other hand, water ordering has also been observed around the cation imidazolium rings (Figure 2c), but to a less extent. As can be seen, water-cation interaction is hardly influenced by the type of anion, the position of the first peak is similar in all cases. To obtain a deeper understanding of water-cation interactions, Figure 4 shows the RDFs between oxygen atom of water and the

hydrogen (H) atoms of the cation head for the specific case of $[Br]^-$ anion. Water interacts strongest with the H atoms linked to the carbon atom located between the nitrogen atoms (H1), with a first peak of RDF located below 2.6 Å. This is well-understood as the proton on the carbon between the two nitrogen atoms is known to have more positive charge, and is in agreement with the literature.[45] The interaction with the H atoms of the methyl group and others H atoms of

Figure 4. Radial distribution functions between H atoms of the cation head and water O atoms for a mixture of 500 water molecules with 16 IL ion pairs (about 1 M) comprised of $[C_{10}MIM]^+$ cations and $[Br]^-$ anions.

Figure 3. RDFs for cation-anion, anion-water, cation-water, and water-water pairs for mixtures of 500 water molecules with one IL ion pair (about 0.1 M) comprised of $[C_{10}MIM]^+$ cations and $[Tf_2N]^-$ anions (top), with 16 IL ion pairs (about 1 M) comprised of $[C_4MIM]^+$ cations and $[Tf_2N]^-$ anions (center), and with 16 IL ion pairs (about 1 M) comprised of $[C_{10}MIM]^+$ cations and $[Tf_2N]^-$ anions (bottom) to investigate the effect of the IL concentration (in the dilute regime) and of the cation alkyl-chain length. The reference atoms for these RDFs are described in the Computational Details.

the imidazolium ring are rather weaker (first peak of RDF greater than 2.8 Å), but obviously more significant than with those of the alkyl chain (hydrophobic nature), which are omitted. The characteristic extrema of water-water $g_{OO}(r)$ in Figure 2d remain virtually unchanged in relation to bulk liquid water regardless of the anion type. The same occurs for $g_{OH}(r)$ as shown in Figure A6.2 of the Appendix 6. The positions of the first peaks and following minima are found at about 2.8 Å and 3.6 Å for $g_{OO}(r)$, and at 1.8 Å and 2.4 Å for $g_{OH}(r)$. This is a clear indication of stable hydrogen bonding. Finally, RDFs corresponding to cation-cation pairs are included in Figure A6.3 of the Appendix 6, and reveal weak interactions. The RDFs in Figure 3 allow us to evaluate the effect on the pairwise interactions of the cation chain length (by comparing the center and the

bottom plots) and of the amount of IL ion pairs (by comparing the top and the bottom plots) for a fixed anion type, in particular $[Tf_2N]^-$. The large cation means that the positive charge is more dispersed and so cation-anion as well as cation-water interactions were expected to weaken. However, slight changes are observed when increasing chain length from 4 to 10 carbon atoms. The influence of the concentration is also almost negligible. Overall, at these IL concentrations water-water interactions unquestionably predominate.

As the RDFs corresponding to water-water interactions of the systems under study are almost identical to those in the bulk regardless of the type of anion, IL concentration and length of the alkyl chain of the cation, we employed here the widely used "distance-angle definition"[30] for hydrogen bonding in bulk water. A H-bond is considered to exist between a pair of molecules if 1) the respective oxygen atoms are separated by less than 3.6 Å, 2) the oxygen of the acceptor molecule and the hydrogen of the donor are separated by less than 2.4 Å, and 3) the α angle is less than a threshold value, usually 30°, to account for linear hydrogen bonds. Following this criterion, the H-bond statistics of water in the various solutions was computed. Our calculations find virtually all molecules associated: only about 1 percent of molecules are monomers. The degree of association in terms of the average number of hydrogen bonds per molecule n_{HB} is characterized in Figure 5. Figure 5a shows
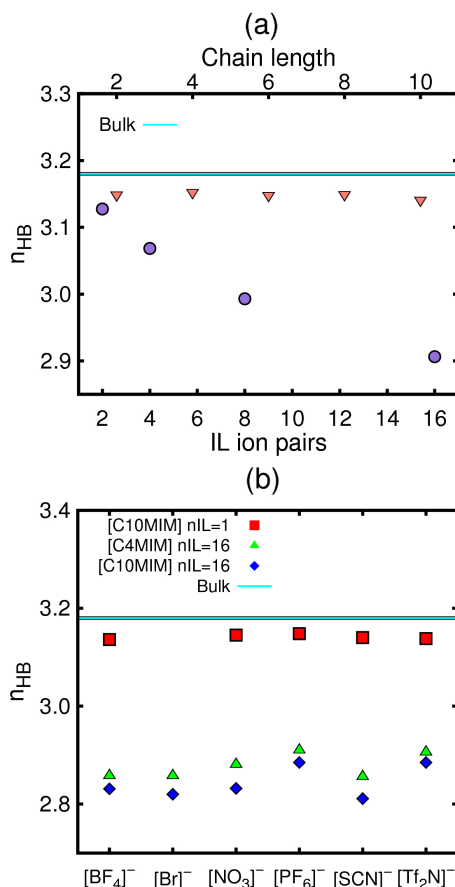
Figure 5. The average number of H bonds per molecule (n_{HB}) of water in bulk and mixed with ILs as a function of the alkyl-chain length of imidazolium-based cations for one IL ion pair (orange triangles, top x axis) and of the number of ion pairs for $[C_{10}MIM]^+$ cation (purple circles, bottom x axis) with $[Tf_2N]^-$ as anion to investigate the effect of the IL concentration (in the dilute regime) and of the cation alkyl-chain length. b) n_{HB} in the bulk and for different mixtures with ILs to study the effect of the anion type.

n_{HB} values of water in bulk and in mixtures with ILs to evaluate the behavior of this magnitude as a function of the IL

concentration (bottom x axis) and of the cation alkyl chain length (top x axis). A slight weakening of the hydrogen-bonded network of water in the dilute mixtures with ILs is observed in relation to the bulk (n_{HB} = 3.18). The results are clearly more sensitive to the amount of ILs than to the cation alkyl chain length, which suggests that interactions with anions break more hydrogen bonds than steric effects due to the presence of long cation chains. The n_{HB} value is almost the same as that of bulk water for the system with 1 IL ion pair and about 2.8 for that with 16 IL ion pairs. The average potential energy between water molecules depicted in Figure A6.4 of the Appendix 6 shows identical behavior, clearly supporting these findings. The structure-energy relationship, going hand-in-hand, shows the reliability of the procedure and results. Figure 5b allows one to observe the anion-type effect for various considered mixtures. The lowest n_{HB} values for water correspond to the solutions with [SCN]$^-$ as anion, and the highest values for those with [Tf$_2$N]$^-$ and [PF$_6$]$^-$. This is in agreement with previous comments on the degree of hydrophobicity. It is worth noting that when there are 16 IL ion pairs in the system, the effect of increasing chain length of the cations is likewise non-negligible. Finally, Figure A6.5 of the Appendix 6 shows the n_{HB} values as a function of the simulation time. The low fluctuations with respect to the mean values indicate that these are representative.

To gain insights into the H-bond network of water, we computed the H-bond populations f_i (percentages of water molecules involved in i H-bonds). The Results for various systems containing [Tf$_2$N]$^-$ anion are displayed in Figure 6. Those for the remaining targeted anions can be found in Table A6.1 in the Appendix 6. The highest percentages correspond to water molecules engaged in 3 hydrogen bonds, which represent about 40 percent regardless of the considered mixture. This value is almost the same as that for the bulk. However, the fraction of molecules with 4 hydrogen bonds considerably decreases with respect to the bulk in favor to f_1 and mainly f_2. This variation is more prominent with increasing number of ILs but not sensitive to the length of cation chain. Thus, even in low concentrations, the presence of ILs prevents the tetrahedral H-bond network of water. Likewise, we evaluated the water cluster size distribution of the aqueous solutions of ILs. Results are displayed in Figure 7. Small aggregates are the most probable, but the formation of an extended H-bond network composed by almost all water molecules is apparent from the figures. The complexity of this clustering is more affected by the amount of ILs than by the chain length or the anion type.

Next, we focus on water-anion interactions. We calculated the average minimum distances from the oxygen of water molecules to atoms of the anions more susceptible to interaction with water
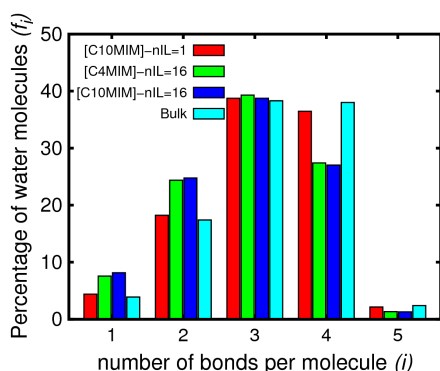
Figure 6. Percentage (f_i) of water molecules involved in i (1-5) H bonds for the bulk and for various water/IL mixtures containing $[Tf_2N]^-$ as the anion.

molecules. The results are provided in Table 1 for mixtures with the highest considered IL concentration and different ion combinations. These results prove again $[Tf_2N]^-$ and $[SCN]^-$ as the most hydrophobic and hydrophilic of the targeted anions, respectively. It is worth noting that the distances for $[SCN]^-$ anion were found to be considerably small, especially for the N atom, with values of approximately 2 Å. This suggests hydrogen bonding formation with water molecules. On the other hand, distances from the water oxygen atoms to the F atoms in $[BF_4]^-$ and $[PF_6]^-$ anions are close, as well as this to O atoms in $[NO_3]^-$. The largest distance corresponds to $[Br]^-$, which seems to be conflicting with the reported RDFs in Figure 2. This is consequence of considering the central atoms of the anions for RDF calculations. The values in Table 1 give information on the most interacting atoms of each anion with water molecules. While the reported
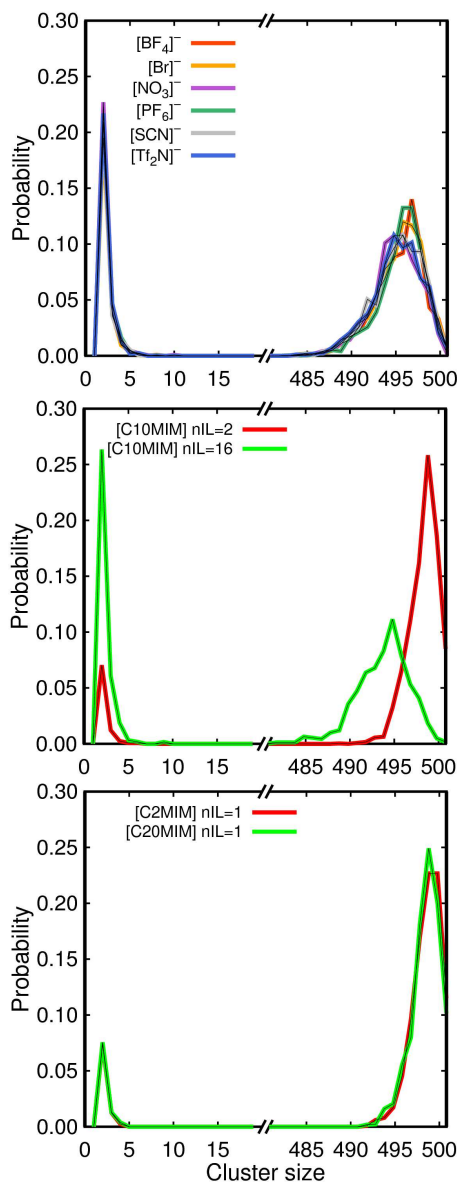
Figure 7. Water-cluster-size distributions. The influence of the anion type in mixtures with 16 IL ion pairs and $[C_{10}MIM]^+$ as the cation (top), the number of IL ion pairs in mixtures with $[C_{10}MIM]^+$ as the cation and $[Tf_2N]^-$ as the anion (center), and the cation alkyl-chain length for mixtures with one IL ion pair and $[Tf_2N]^-$ as the anion (bottom).

Table 1. Average minimum anion-water distances for different aqueous solutions of ILs concerning anion type and cation chain length (IL concentration of about 1 M: 16 IL ion pairs).

Anion	Atom	$[C_4MIM]^+$	$[C_{10}MIM]^+$
$[BF_4]^-$	F	2.56	2.56
$[Br]^-$	Br	3.15	3.14
$[NO_3]^-$	O	2.57	2.57
	N	3.02	3.01
$[PF_6]^-$	F	2.64	2.64
$[SCN]^-$	S	2.05	2.05
	N	1.96	1.96
$[Tf_2N]^-$	F	2.71	2.73
	O	2.66	2.66
	N	3.10	3.11

Figure 8. Degree of anion hydration as a function of water-anion distance for the solutions with 16 IL ion pairs (about 1 M) and $[C_4MIM]^+$ (top) and $[C_{10}MIM]^+$ (bottom), as the cation, combined with all the studied anions.

minimum distances are hardly affected by the cation alkyl chain length, considerable changes are due to the type of anion.

Figure 8 displays the degree of anion hydration as a function of the distance between the water molecules and the anion, for mixtures with 16 IL ion pairs, cations with 4 or 10-carbon chains, and all the considered anions. More specifically, it shows the average number of neighboring water molecules for distances to the anion less than 4 Å, between 4 Å and 6.5 Å and greater than 6.5 Å. The values corresponding to short distances represent the average water coordination of the anions. The lowest percentages in this range correspond to mixtures containing $[Br]^-$ as anion, and the highest to mixtures with either $[SCN]^-$ or $[Tf_2N]^-$. These results show the importance of interacting forces but also of the size of the anions for anion hydration. Most water molecules are located in the intermediate range for the different systems except for the most hydrophilic $[SCN]^-$ and hydrophobic $[Tf_2N]^-$ anions, for which the outstanding percentages of water molecules correspond to the range of shortest and furthest distances from the anion, respectively.

To illustrate and further understand the above findings, molecular graphics rendered using Materials Studio software are included. Figure 9 shows representative snapshots from the simulations of the water/IL mixtures with 16 IL ion pairs and 10 carbon atoms of alkyl chain for
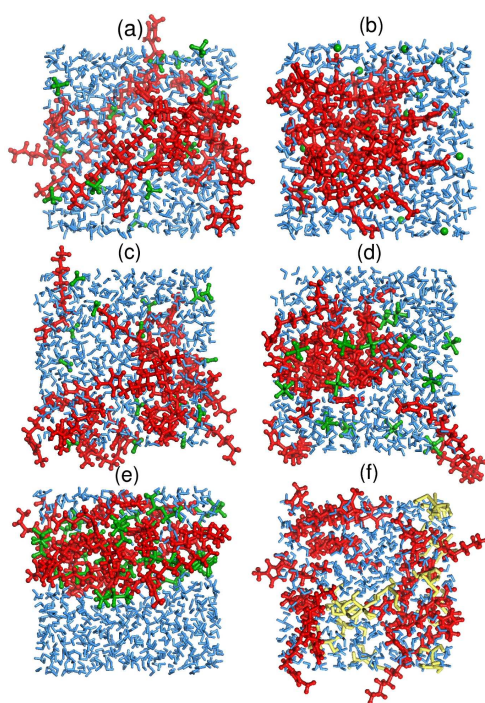
Figure 9. Representative snapshots from MD simulations at 298.15 K and 1 bar of water/IL mixtures with 16 IL ion pairs (about 1 M) containing $[C_{10}MIM]^+$ as the cation and a) $[BF_4]^-$, b) $[Br]^-$, c) $[NO_3]^-$, d) $[PF_6]^-$, e) $[Tf_2N]^-$, and f) $[SCN]^-$ anions. Water molecules, anions, and cations are plotted in blue, green and red, respectively. The yellow clusters in (f) indicate H-bond formation between water molecules and the $[SCN]^-$ anions.

the different anions. While $[Tf_2N]^-$ anions move into the cations, $[SCN]^-$ is not only embedded in the aqueous solution but also forms hydrogen bonds with water molecules, as previously commented. A snapshot of this cross hydrogen bonding formation is depicted in Figure A6.6 of the Appendix 6. The opposite occurs in the mixture with $[Tf_2N]^-$ anion. We see a clear IL clustering and IL/water

phase separation, which supports the results of Figure 8. This is confirmed by calculations of the density profile (Figure A6.7 of the Appendix 6). This behavior is in agreement with previously reported works,[18] and thus allows separation of mixtures involving water.[24] Despite not strongly interacting with water molecules (Table 1), $[Br]^-$ anions are completely dissolved in water. This makes ILs containing this type of anion useful for colloidal applications.[25, 26] The remaining considered ILs exhibit similar behaviors, which is consistent with the reported quantitative results.

CONCLUSIONS

A detailed study of the structure of water containing low concentrations of ILs, for various anion types and lengths of the cation chain has been presented using molecular dynamics simulations with validated atomistic descriptions and intermolecular interactions was presented. Overall, water molecules remain highly hydrogen-bonded, but a loss of the tetrahedral ordering typical of bulk water is observed. In particular, the fraction of molecules with four hydrogen bonds considerably decreases with respect to the bulk in favor to that of 1 and mainly two H-bonds. While the H-bond network of water weakens with increasing number of ILs, the influence of the cation chain length is hardly noticeable. This suggests that anion-water interactions destroy H-

bonding in water more prominently than steric effect caused by long alkyl chains of cations. A total or partial amount of the anions is observed to be embedded in water depending on their degree of hydrophobicity. Among the targeted anions, [SCN]$^-$ and [Tf$_2$N]$^-$ were found the most hydrophilic and hydrophobic, respectively. The former strongly interacts with water leading even to hydrogen bonding formation, whereas ion clustering and IL/water phase separation is observed for the solutions with [Tf$_2$N]$^-$ as anion.

Bibliography

[1] Plechkova, N. V.; Seddon, K. R. *Chem. Soc. Rev.* **2008**, *37*, 123–150.

[2] Smiglak, M.; Metlen, A.; Rogers, R. D. *Acc. Chem. Res.* **2007**, *40*, 1182–1192.

[3] Seddon, K. R. *J. Chem. Technol. Biotechnol.* **1997**, *68*, 351–356.

[4] Hough, W. L.; Smiglak, M.; Rodriguez, H.; Swatloski, R. P.; Spear, S. K.; Daly, D. T.; Pernak, J.; Grisel, J. E.; Carliss, R. D.; Soutullo, M. D.; Davis Jr., J. H.; Rogers, R. D. *New J. Chem.* **2007**, *31*, 1429–1436.

[5] Javadian, S.; Ruhi, V.; Heydari, A.; Shahir, A. A.; Yousefi, A.; Akbari, J. *Ind. Eng. Chem. Res.* **2013**, *52*, 4517–4526.

[6] Ridings, C.; Lockett, V.; Andersson, G. *Phys. Chem. Chem. Phys.* **2011**, *13*, 21301–21307.

[7] Li, H.; Imai, Y.; Takiue, T.; Matsubara, H.; Aratono, M. *Colloids Surfaces a-Physicochemical Eng. Asp.* **2013**, *427*, 26–32.

[8] Shi, W.; Damodaran, K.; Nulwala, H. B.; Luebke, D. R. *Phys. Chem. Chem. Phys.* **2012**, *14*, 15897–15908.

[9] Chang, H.-C.; Jiang, J.-C.; Chen, T.-Y.; Wang, H.-S.; Li, L. Y.; Hung, W.-W.; Lin, S. H. *Phys. Chem. Chem. Phys.* **2013**, *15*, 12734–12741.

[10] Freire, M. G.; Carvalho, P. J.; Gardas, R. L.; Marrucho, I. M.; Santos, L. M. N. B. F.; Coutinho, J. A. P. *J. Phys. Chem. B* **2008**, *112*, 1604–1610.

[11] Freire, M. G.; Carvalho, P. J.; Silva, A. M. S.; Santos, L. M. N. B. F.; Rebelo, L. P. N.; Marrucho, I. M.; Coutinho, J. A. P. *J. Phys. Chem. B* **2009**, *113*, 202–211.

[12] Freire, M. G.; Neves, C. M. S. S.; Carvalho, P. J.; Gardas, R. L.; Fernandes, A. M.; Marrucho, I. M.; Santos, L.

M. N. B. F.; Coutinho, J. A. P. *J. Phys. Chem. B* **2007**, *111*, 13082–13089.

[13] Kakiuchi, T. *Anal. Sci.* **2008**, *24*, 1221–1230.

[14] Tome, L. I. N.; Varanda, F. R.; Freire, M. G.; Marrucho, I. M.; Coutinho, J. A. P. *J. Phys. Chem. B* **2009**, *113*, 2815–2825.

[15] Anthony, J. L.; Maginn, E. J.; Brennecke, J. F. *J. Phys. Chem. B* **2001**, *105*, 10942–10949.

[16] Méndez-Morales, T.; Carrete, J.; Cabeza, O.; Gallego, L. J.; Varela, L. M. *J. Phys. Chem. B* **2011**, *115*, 6995–7008.

[17] Niazi, A. A.; Rabideau, B. D.; Ismail, A. E. *J. Phys. Chem. B* **2013**, *117*, 1378–1388.

[18] Sieffert, N.; Wipff, G. *J. Phys. Chem. B* **2006**, *110*, 13076–13085.

[19] Jiang, W.; Wang, Y.; Voth, G. A. *J. Phys. Chem. B* **2007**, *111*, 4812–4818.

[20] Galamba, N. *J. Phys. Chem. B* **2012**, *116*, 5242–5250.

[21] Schröder, C.; Neumayr, G.; Steinhauser, O. *J. Chem. Phys.* **2009**, *130*, 194503.

[22] Liu, W. W.; Cheng, L. Y.; Zhang, Y. M.; Wang, H. P.; Yu, M. F. *J. Mol. Liq.* **2008**, *140*, 68–72.

[23] Marsh, K.; Boxall, J.; Lichtenthaler, R. *Fluid Phase Equilib.* **2004**, *219*, 93–98.

[24] Chapeaux, A.; Simoni, L. D.; Ronan, T. S.; Stadtherr, M. a.; Brennecke, J. F. *Green Chem.* **2008**, *10*, 1301.

[25] Liu, Y.; Yang, L.; Guo, R. *Soft Matter* **2013**, *9*, 3671.

[26] He, Y.; Shang, Y.; Liu, Z.; Shao, S.; Liu, H.; Hu, Y. *Colloids Surfaces B Biointerfaces* **2013**, *101*, 398–404.

[27] Krestov, G. A. *Thermodynamics of Solvation*; Ellis Horwood: Chichester, UK, 1991.

[28] Y. Marcus, *Ion Solvation*; Wiley: Chichester, UK, 1985.

[29] Omta, A. W.; Kropman, M. F.; Woutersen, S.; Bakker, H. J. *Science* **2003**, *301*, 347–349.

[30] Luzar, A.; Chandler, D. *J. Chem. Phys.* **1993**, *98*, 8160–8173.

[31] Dubbeldam, D.; Calero, S.; Ellis, D. E.; Snurr, R. Q. *Mol. Simul.* **2016**, *42*, 81–101.

[32] Nose, S. *Mol. Phys.* **2002**, *100*, 191–198.

[33] Hoover, W. G. *Phys. Rev. A* **1985**, *31*, 1695–1697.

[34] Martyna, G. J.; Tuckerman, M. E.; Tobias, D. J.; Klein, M. L. *Mol. Phys.* **1996**, *87*, 1117–1157.

[35] Lopes, J. N. C.; Deschamps, J.; Padua, A. A. H. *J. Phys. Chem. B* **2004**, *108*, 11250.

[36] Kelkar, M. S.; Maginn, E. J. *J. Phys. Chem. B* **2007**, *111*, 4867–4876.

[37] Yan, T. Y.; Burnham, C. J.; Del Popolo, M. G.; Voth, G. A. *J. Phys. Chem. B* **2004**, *108*, 11877–11881.

[38] Cadena, C.; Anthony, J. L.; Shah, J. K.; Morrow, T. I.; Brennecke, J. F.; Maginn, E. J. *J. Am. Chem. Soc.* **2004**, *126*, 5300–5308.

[39] Liu, Z. P.; Huang, S. P.; Wang, W. C. *J. Phys. Chem. B* **2004**, *108*, 12978–12989.

[40] Chaumont, A.; Wipff, G. *Inorg. Chem.* **2009**, *48*, 4277–

4289.

[41] Markovich, G.; Perera, L.; Berkowitz, M. L.; Cheshnovsky, O. *J. Chem. Phys.* **1996**, *105*, 2675–2685.

[42] Rick, S. W. *J. Chem. Phys.* **2004**, *120*, 6085–6093.

[43] Darden, T.; York, D.; Pedersen, L. *J. Chem. Phys.* **1993**, *98*, 10089–10092.

[44] Essmann, U.; Perera, L.; Berkowitz, M. L.; Darden, T.; Lee, H.; Pedersen, L. G. *J. Chem. Phys.* **1995**, *103*, 8577–8593.

[45] Weber, C. C.; Masters, A. F.; Maschmeyer, T. *J. Phys. Chem. B* **2012**, *116*, 1858–1864.

Micelle Formation in Aqueous Solutions of Room Temperature Ionic Liquids: a Molecular Dynamics Study

José Manuel Vicent-Luna, José Manuel Romero-Enrique, Sofía Calero, and Juan Antonio Anta

1-Alkyl-3-methylimidazolium cations in the presence of water are used as a test system to study by molecular dynamics the formation of micelles in aqueous mixtures of highly anisotropic room temperature ionic liquids (IL). Structural properties, i. e., radial distribution functions (RDF) and transport parameters such as diffusion coefficients and conductivities are computed as a function of the IL/water mole fraction. The concentration plots reveal a sharp change of the slope of both the cation self-diffusion coefficient and the first peak

of the head-head RDF at approximately the same value of the concentration. This transition, considered as a measure of a critical micellar concentration, appears only for the most anisotropic systems, composed of longer alkyl chains. The formation of the micelles is confirmed from the analysis of the tail-tail and cation-water RDFs. As a general result, we found that the larger the anisotropy of the ionic liquid the lower the critical concentration and the larger the proportion of monomers forming part of the micelles. The molecular dynamics predictions are in line with the experimental evidence reported for these systems.
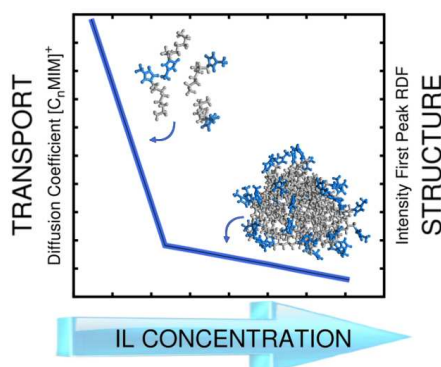
INTRODUCTION

Room temperature ionic liquids (RTILs) or simply ionic liquids (ILs) [1, 2] exhibit inherent attractive physical and chemical properties that make them of potential interest for a wide range of applications.[3, 4] ILs are salts in liquid state near room conditions composed by a combination of organic cations and organic or inorganic anions. Among other properties, they are well known for exhibiting very low vapor pressure, high thermal and electrochemical stability and relatively high ionic conductivity.[5] Another interesting characteristic of ILs is the capability of adjusting their properties such as density, viscosity, melting point or miscibility by varying the nature of the constituting ions.

Miscibility is a key property that influences the ILs behavior in water solutions. As an example, 1-Alkyl-3-methylimidazolium ($[C_n MIM]^+$) based ILs with long chains have been proposed to be used as surfactants [6–10] due to their high ability to form aggregates or micelles in the presence of water. This aggregation is a consequence of the interaction between water and the polar head or the hydrophobic tail of the cations.[11–14] Their archetypical behavior has applications for green solvents design and extraction processes. On the other hand, ILs containing shorter alkyl chain mixed with water or other organic solvents form homogeneous mixtures and can be used in catalysis and electrochemical devices.[15–20]

Therefore, from an environmental point of view, the study of the interactions between ILs and water is crucial for understanding properties that makes ILs interesting for a number of relevant and desired technological applications. Numerous studies were carried out to investigate ILs in water solutions both experimentally [6, 7, 21–25] and theoretically.[26–34] From a computational point of view, most of the studies focused on the investigation of structural and dynamical properties of ILs/water systems as well as the formation of hydrogen bonds and aggregates. Bhargava and Klein,[33] used molecular dynamics simulations (MD) to investigate the self-assembly of cations of $[C_{10}MIM]^+ [Br]^-$ for a fixed concentration of IL and water. Moreover, several MD studies[26, 30–32, 35] studied the behavior of ILs in water combining different anions and different alkyl chains of imidazolium cations. They analyzed the IL concentration dependence on the self-assembly of the hydrophobic cations covering ILs concentrations ranging from 0 % (pure water) to 100 % of molar fraction (pure IL). Jiang, W. et al,[26] studied the effect of water concentration in the nanostructural organization and dynamics of $[C_8MIM]^+ [NO_3]^-$ IL. In this work the existence of a "turnover" point that marked the formation of a more ordered micelle structure is reported. Feng, S. and Voth, G. A.[32] investigated the behavior of water/IL mixtures with the variation of the chain length of the cation (from four to

eight carbon atoms) and the nature of the anion ($[Cl]^-$ and $[BF_4]^-$). On the one hand, they stated that $[C_4MIM]^+$ cations are dissolved in water while $[C_8MIM]^+$ are able to form micelles. On the other hand, they highlighted the importance of the choice of the anion for the self-aggregation of water or others polar solvents. Méndez-Morales et al,[35] performed an extensive study of the structural and dynamical properties of water/IL mixtures varying the alkyl chain of the imidazolium cations (from two to eight carbon atoms) and the nature of the anions ($[Cl]^-$, $[Br]^-$, and $[PF_6]^-$). They investigated the clusterization of water molecules and rationalized the results based on the hydrophobicity of the cations and anions. They also described the effect of the water content in the diffusion of the systems, finding an increase in the mobility of ions at high water concentration. A related finding was reported by Niazi, A. et al,[30] who investigated the water/IL mixtures with three different ILs. They focused on the analysis of hydrogen bonds, water clustering, and diffusivity in the whole range of water/IL concentrations. They found a transition from the typical behavior of neat ILs to that of aqueous solutions at 70 % of water content. A similar observation was reported by Ramya, K. R. et al,[31] who studied the aggregation process of $[C_6MIM]^+$ $[Tf_2N]^-$ IL varying the water concentration from an energetic and structural point of view. They reported a phase separation between IL and water due to the hydrophobicity of both constituents of the IL and micelle formation at high water concentration. In our previous work,[27] we studied the self-assembly of cations in water for ILs composed by different anions and varying alkyl chain lengths of the imidazolium family focusing in how the hydrogen bond network and water structure is affected by the presence of ILs with different kind of anions. It is important to mention that in spite of the many theoretical studies where aggregates in water/IL mixtures have been identified and described, there is not yet a complete description of the cluster formation for increasing IL concentrations. This is necessary to pintpoint a critical micelle concentration (*cmc*) from the simulation. In the experiments involving micellar systems the common strategy is to investigate structural phase transitions of surfactants by increasing the concentration of ionic liquid in the mixture over several orders of magnitude while keeping water as the majority component. The variation of properties such as ionic conductivity, surface tension or enthalpy among others, with the surfactant concentration, is then used to obtain the *cmc*. Typical experimental *cmc* values of common surfactants and ILs are in the order of a few mM. Due to system size numerical limitations, atomistic molecular simulations hardly cover a high variety of concentrations without drastic changes. This complicates the link of experimental observations with computational studies further than a simple qualitative analy-

sis. Molecular simulations handle only several thousand of atoms and this restricts the range of IL concentrations that can be studied in a water solution, with water as major component of the mixture. In this report we explore the structure and dynamics of 1-Alkyl-3-methylimidazolium chloride IL with different hydrocarbon chain lengths ranging from 1-butyl- to 1-dodecyl-3-methylimidazolium cations (Figure 1) by molecular dynamics simulations. We analyze the nanostructural organization of each cation in a water media and the IL concentration dependence of several properties. By using extensive computational resources, we aim at relating the experimental observations with the results of MD simulations. The main purpose of this work is to set relations between structure and transport and between the nature of the formed aggregates and the dynamical properties that experimentally pinpoint the value of the *cmc*.
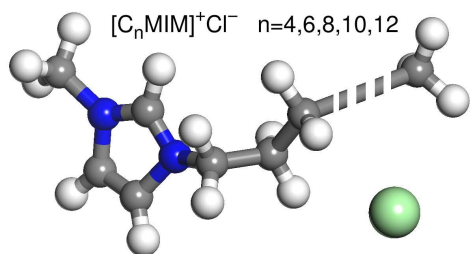
Figure 1. Atomistic representation of $[C_n MIM]^+ [Cl]^-$ ILs used in this work. The color code is as follows: N atoms in blue, C atoms in grey, H atoms in white, and Cl atom in green.

SIMULATION DETAILS

We study the structural and transport properties of 1-Alkyl-3-methylimidazolium chloride ($[C_n MIM]^+$ $[Cl]^-$) ionic liquid in the presence of water by molecular simulations. Figure 1 shows the molecular structure of the cations studied in this work. The simulation box consists of a cubic box of side approximately 60 Å containing 6000 water molecules and different amounts of $[C_n MIM]^+ [Cl]^-$ with n = 4, 6, 8, 10, and 12. The number of ion pairs ranged from 10 to 250, equivalent to concentrations between 0.1 and 1.7 M. Table 1 shows the calculated concentrations used in the simulations. Additional simulations of the pure ILs were carried out for comparison. Pure IL systems contain 75 ion pairs in a simulation box of side about 30 Å and were used to obtain the density of the neat ILs. Sonja Gabl et al,[36] state that 50 ion pairs seemed sufficient to obtain structural properties of these systems. To settle any doubt about the system size effect we have carried out a molecular dynamics simulation for 500 ion pairs in a simulation box of side length close to 50 Å. The results depicted in Figure A7.1 of the Appendix 7 show no differences for density calculation with increasing the system size. Fully flexible molecular all-atom models for ILs were based on the work of Canongia-Lopes et al.[37] The parameters of the atomistic models were taken from a our previous work,[38] where they were refined to reproduce simulta-

neously density and transport properties. For water molecules we have used the TIP5P/Ew model.[39] The cut-off of non-bonded interactions is 12 Å and cross Lennard-Jones parameters between different atom pairs were computed using standard Lorentz-Berthelot combining rules. The long-range electrostatic interactions were calculated with the particle-mesh Ewald (PME) method.[40, 41]

We performed molecular dynamics (MD) simulations in the NPT ensemble at room conditions (1 atm and 298 K) and in the NVT ensemble at room temperature (298 K). The initial configurations were created by randomly placing ion pairs in an empty cubic simulation box and refilled with water molecules using the Packmol package.[42] This way, we guarantee to start with a homogeneous distribution of molecules. For the first set of calculations we minimize the positions of the system using a steepest descent algorithm.[43] We then performed 1 ns MD simulations in the NPT ensemble to obtain a volume of the simulation box that approximately reproduces the experimental equilibrium density. Consecutive NPT simulations of 2 ns are performed to reach the equilibrated density, i.e. where the volume and energy of the systems oscillate over time around a mean value. After equilibration we carried out 5 ns production runs in the NVT ensemble. The time step employed for NPT and NVT simulations is 0.5 and 1 fs respectively. Pressure and temperature were controlled by means

of the Martyna-Tuckerman-Tobias-Klein (MTTK) barostat [44] and Nose-Hoover thermostat,[45, 46] respectively. All simulations were carried out using the GRO-MACS simulation software.[47–50] The system trajectory were recorded every 1 ps to obtain the structural and dynamical properties. Radial distribution functions (RDF) or pair distribution functions $g_{AB}(r)$ between particles of type A and B are computed via:

$$g_{AB}(r) = \frac{1}{\langle \rho_B \rangle} \frac{1}{N_A} \sum_{i=1}^{N_A} \sum_{j=1}^{N_B} \frac{\delta(r_{ij} - r)}{4\pi r^2} \quad (1)$$

where ρ_B is the B type averaged particle density. This is a key property to study the structure of liquid systems or any other systems of particles and its behavior could be different depending on the system. This work deals with systems composed by ionic liquids in water solutions, which are heterogeneous systems as it has been extensively reported in literature.[51–56] Due to the formation of local structures, as it is the case of micelles, the behavior of RDFs of homogeneous and heterogeneous systems differs.[54–57] Hence, RDFs in the present case do not reflect correlations between particles A and B as in a homogeneous system, but still provide valuable information to understand the size of the AB aggregates in a colloidal, non-homogenous system. Self-diffusion coefficients D_s were computed using Einstein's equation that relates Ds with the slope of the mean square displacement. For a 3-dimensional system this reads:

$$D_S = \lim_{t \to \infty} \frac{\langle \sum_i^n \|r(t) - r(0)\|^2 \rangle}{6t} \qquad (2)$$

For the mixture of room temperature ionic liquids and water, it has been reported by Méndez-Morales et al. [35] that the diffusive regime is reached over a simulation time of 1 ns. In these of systems, the diffusive regime is reached at shorter time scales compared with systems of neat ILs, due to the decrease of the viscosity of ILs with the addition of water.[58] Therefore, we applied Eq. (2) in the 1-3 ns time interval. We estimated the error bars by small increments in this interval. This time interval is analyzed by the first derivative of the mean squared displacement (Figure A7.2 in the Appendix 7). To ensure that the diffusive regime is attained we confirm that the first derivative of the logarithm of MSD with respect to the logarithm of time is close to the unity.[59] To analyze the validity of the chosen time scales, we have performed an additional simulation extending the simulation time. The simulation consists on 50 ns of production run for one of the most unfavorable cases to study the dynamics of the system, i.e. water/IL mixture containing the cation with the longest alkyl chain at high IL concentration. We compared the results obtained from simulations of 5 and 50 ns containing 200 $[C_{12}MIM]^+$ $[Cl]^-$ ion pairs. Additional details of the obtained results are given in the Appendix 7. The partial ionic conductivity is estimated using Nernst-Einstein equation:[60]

$$\sigma_i = D_{S_i} \frac{N_i}{V} \frac{q_i^2 e^2}{k_B T} \qquad (3)$$

where σ_i and D_{S_i} are the ionic conductivity and self-diffusion coefficient of species i, respectively, N_i is the number of charge carriers, V is the volume of the unit cell, and $q_i e$ is the net charge of the molecule. The total ionic conductivity of the system is the summation of the partial conductivities for each component.

Table 1. Number of Ion Pairs in the Simulation Box Used in This Work and Their Corresponding Molar Fraction and Molar Concentrations for ILs Containing $[C_nMIM]^+$ Cations and $[Cl]^-$ Anion.

Number of ILs	molar concentration [M]					molar fraction ILs %
	C_4MIM	C_6MIM	C_8MIM	$C_{10}MIM$	$C_{12}MIM$	
10	0.09	0.09	0.09	0.09	0.09	0.17
20	0.18	0.17	0.17	0.17	0.17	0.33
30	0.26	0.26	0.26	0.25	0.25	0.50
40	0.35	0.34	0.34	0.33	0.33	0.66
50	0.43	0.42	0.42	0.41	0.40	0.83
60	0.51	0.50	0.49	0.48	0.47	0.99
75	0.62	0.61	0.60	0.58	0.57	1.23
100	0.80	0.78	0.76	0.74	0.72	1.64
125	0.97	0.94	0.91	0.88	0.85	2.04
150	1.13	1.00	1.05	1.01	0.97	2.44
175	1.28	1.22	1.18	1.12	1.08	2.83
200	1.42	1.35	1.30	1.23	1.18	3.23
250	1.67	1.58	1.51	1.42	1.35	4.00

RESULTS AND DISCUSSION

Table 2 compares the calculated density and the available experimental data reported by Mac Dowel et al.[61] Results from MD simulations in the NPT ensemble for pure IL are in agreement with the experimental values with an error percentage about 2 % for the different alkyl chains. This error is lower for the simulations of pure water with the TIP5P/Ew model. Experimental water density is a reference value of 0.997 g/cm^3 while our computed

value is 1.002 g/cm^3 (with an error of 0.5 %). Both water and IL models reproduce the experimental liquid density of the pure components. This provides a good starting point to ensure that the force fields used for both components are realistic enough to provide accurate results.

Figure 2 represents the density of the IL/water mixtures as a function of the IL molar concentration. Increasing the IL concentration increases or decreases the density of the mixture depending on the nature of the IL. Dense systems formed by mixtures containing ILs with cations of shorter chains (n = 4 and 6) exhibit an increasing trend with the IL concentration. On the other hand, the trend of the systems with larger chains (less dense systems) decreases with the IL concentration. As expected, the density of the lowest concentrations converges to the density of the pure water system.
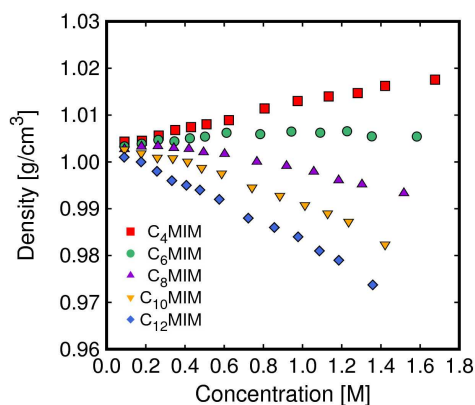
Figure 2. Calculated density as a function of the molar concentration of $[C_n\text{MIM}]^+ [\text{Cl}]^-$ in water/IL mixtures.

The ILs mole fractions used here cover up to 4 % (see Table 1). At these low concentrations, the concentration dependence on the density shows a linear behavior.

Figure 3 shows the variation of the self-diffusion coefficients of both $[C_n\text{MIM}]^+$ cations and water molecules as a function of the IL concentration. Two main observations arise. On the one hand, for a given concentration, cations with shorter chain lengths diffuse faster than these with longer chains in water media. On the other hand, the addition of more ionic liquid to the mixture, lowers the self-diffusion coefficients of the $[C_n\text{MIM}]^+$ cations in all cases. Cations with longer alkyl chains show a drastic change of the slope at intermediate IL concentrations. A behavior similar to this is found experimentally by Figueira-González et al.[6] who reported a structural transition of cationic species in

Table 2. Comparison between Experimental and Calculated Density g/cm^3 of Neat IL $[C_n\text{MIM}]^+ [\text{Cl}]^-$.^{a}

n	Exp	this work	% error
4	1.08	1.06	2.3
6	1.04	1.02	1.8
8	1.01	0.99	2.0
10		0.97	
12		0.95	

^{a}Percentage of error is also shown for comparison.
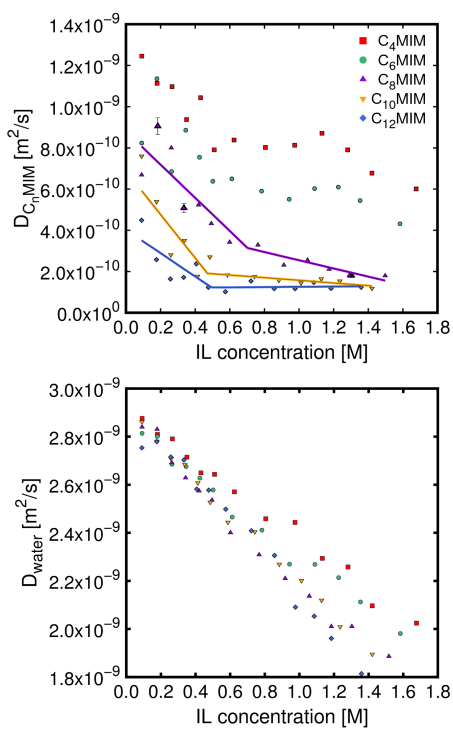
Figure 3. Self-diffusion coefficients of cations (top) and water (bottom) as a function of the $[C_n MIM]^+ [Cl]^-$ IL concentration in water/IL mixtures. Solid lines are linear fits to determine the critical concentrations. Error bars are included at selected concentrations.

water for high concentrated systems. They relate this phase transition to the change of slope in the self-diffusion coefficient of the cations. From the intersection of the fitted straight lines one can estimate a critical concentration, in principle attributable to a structural transition (see below). Results for this critical concentration laid around 0.70 M, 0.47 M, and 0.49 M for $[C_8 MIM]^+$, $[C_{10} MIM]^+$, and $[C_{12} MIM]^+$ respectively. To confirm that this transition is statistically signifi-

cant, representative error bars of the self-diffusion coefficients for some concentrations of $[C_8 MIM]^+$ cations are included in the figure. As expected, increasing the concentration decreases the error bar, since the corresponding average includes more particles.

The self-diffusion of water decreases linearly with the addition of IL. At very low concentrations, all values approximately converge to the reported value of the self-diffusion coefficient for TIP5P/Ew model of water,[39] $D_{water} = 2.8 \dot{1}0^{-9}$ m^2/s. This is close to the experimental diffusion of liquid water at room conditions,[62, 63] $D_{water} = 2.3 \dot{1}0^{-9}$ m^2/s. For fixed concentration, the diffusion of water is slightly higher in systems containing shorter cations. Figure 4 shows the concentration dependence of the ionic conductivity in the $[C_n MIM]^+ [Cl]^-$ IL/water systems. Mixtures containing $[C_4 MIM]^+$ and $[C_6 MIM]^+$ cations exhibit a substantially different behavior than mixtures containing the largest cations. In general, short chains are more conductive, especially at high concentrations. At the highest concentration studied, the conductivity of systems with $[C_4 MIM]^+$ and $[C_6 MIM]^+$ cations is almost twice the conductivity of the systems with larger cations. This is actually one of the reasons for using ILs containing small cations in electrochemical devices.[18**?** **?**]
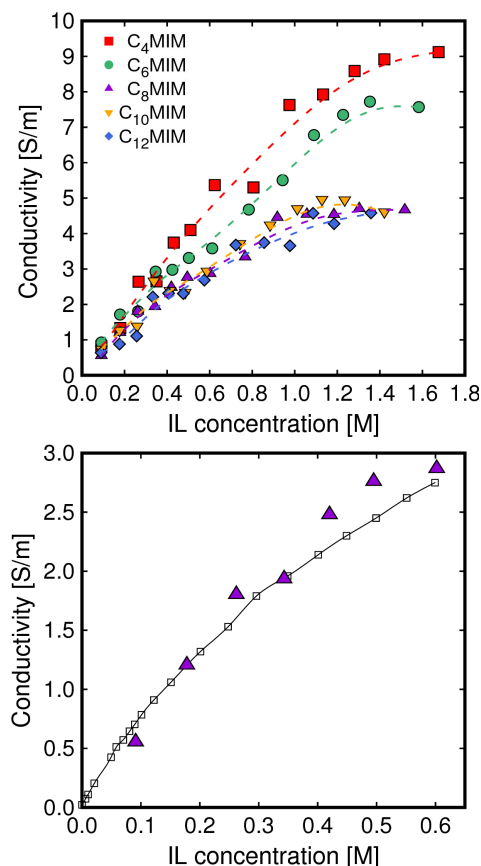
Figure 4. Conductivity as a function of the $[C_n\text{MIM}]^+[\text{Cl}]^-$ IL concentration in water/IL mixtures (top) and conductivity comparing experimental (empty black squares) and simulation data (solid triangles) for $[C_8\text{MIM}]^+[\text{Cl}]^-$ IL in water (bottom). Lines are eye guidelines.

We compared the experimental conductivity of the $[C_8\text{MIM}]^+[\text{Cl}]^-$ IL/water system [23] with our calculated values (Figure 4, bottom), and very good agreement is found in the range of concentrations measured. This, and the afore-mentioned results for the density of pure water and ILs and the diffusion of pure water confirm that the force fields used can correctly describe the behavior of mixtures of water and $[C_n\text{MIM}]^+[\text{Cl}]^-$ IL over a wide range of concentrations and molecular structures. In addition Jungnickel et al.[23] reported the conductivity corresponding to larger cations for concentrations lower than 0.1 M, i.e. out of the range studied here. In particular, they worked with critical micellar concentrations of $[C_n\text{MIM}]^+[\text{Cl}]^-$ IL in water at room conditions for cations with alkyl chain lengths ranging between 4 and 18 carbon atoms. For shorter cations, i.e. $[C_4\text{MIM}]^+$ and $[C_6\text{MIM}]^+$ there is no experimental evidence of micelle formation. These results are in line with our findings, assuming that the change of slope in the diffusion coefficient is a measure of a critical micellar concentration. In any case the behavior of the mixtures containing these two short cations differs clearly from the rest. For mixtures including $[C_8\text{MIM}]^+$ cations it has been reported a critical micelle concentration of 0.23 M, while our results for diffusion indicate a phase transition around 0.70 M. In the case of $[C_{10}\text{MIM}]^+$ and $[C_{12}\text{MIM}]^+$ cations, the critical micelle concentrations reported are 0.06 M and 0.015 M, respectively. These concentrations are lower than the accessible range to our simulations. In fact, our calculations predict a critical concentration of 0.5 M, which is one order of magnitude higher. Figueira-González et al.[6] demonstrated that the critical concentration is not unique. They

identified a second critical concentration, about one order of magnitude higher than the critical micelle concentration, related to a change in the size and shape of the aggregates formed by the cations. Our study seems to be in the range of concentrations of this second critical concentration for mixtures involving $[C_{10}MIM]^+$ and $[C_{12}MIM]^+$ cations. To clarify this hypothesis we set relations between below the transport properties with the structural properties of each mixture. At the critical micelle concentration, $[C_nMIM]^+$ cations aggregate in presence of water forming micelles where the hydrophobic tail of the cations gather together in the middle of a sphere, while the hydrophilic head is pointing to the water molecules. Figure 5 shows a schematic representation of the distribution of some cations in aqueous medium forming homogeneous and heterogeneous systems (micelles). Bearing this geometry in mind we study, via RDFs, the head-head distribution of the cations and the cation tail and water interaction. The RDFs were computed via Eq. (1). Results are presented in Figure 6 for mixtures containing $[C_nMIM]^+$ and IL ion pairs for low (molar fraction = 0.66), intermediate (molar fractions = [1.23-2.04]) and high concentrations (molar fraction = 3.23). The molar concentrations are summarized in Table 1. $[C_4MIM]^+$ and $[C_6MIM]^+$ cation distributions are unaffected when increasing the IL concentration in the mixture. However, for longest cations we observe a lowering of the first peak of the RDF with
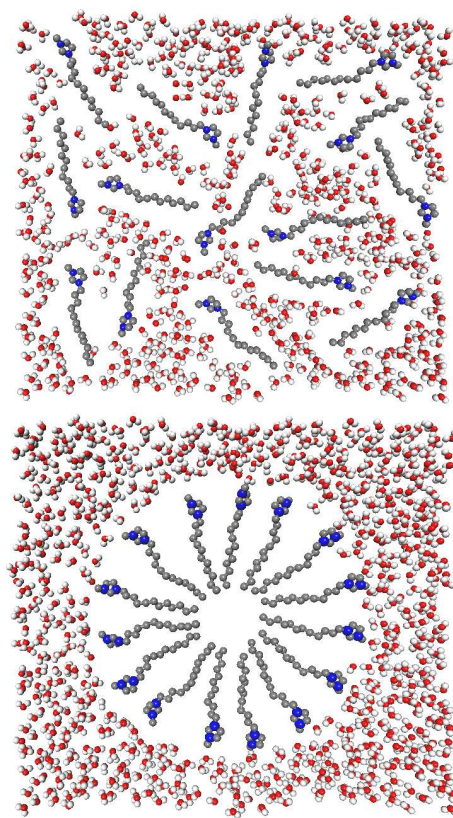
Figure 5. Two dimensional scheme of systems formed by $[C_{12}MIM]^+$ cations surrounded by water molecules. Homogeneous system (top) and heterogeneous system (bottom). The hydrogen atoms of the cations are omitted for clarity.

concentration. This effect, which increases with the length of the alkyl chain, suggests that the addition of ILs induces structural changes and leads to more homogeneous systems at microscopic level.

The aforementioned effect is also observed from the distribution of tail ends around water molecules. The RDFs between the last carbon atom of the hydrophobic alkyl chain and the oxygen atom
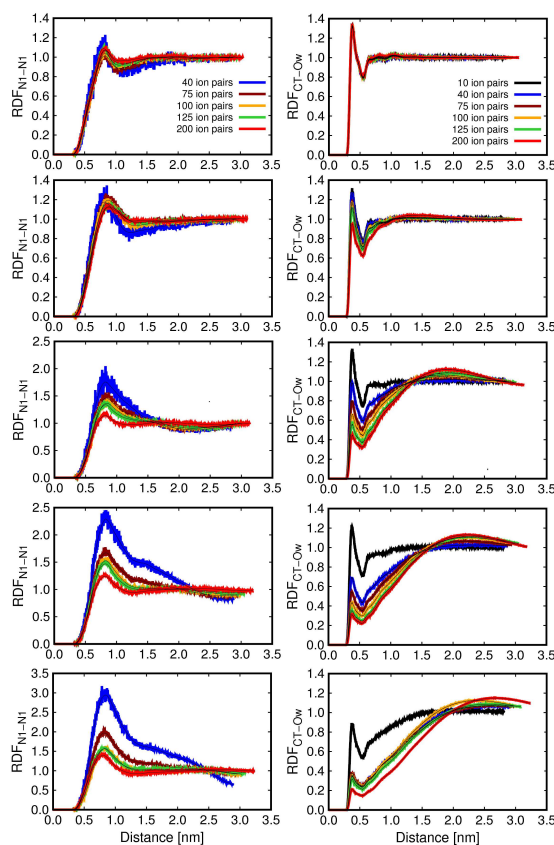
Figure 6. Left: Cation-cation RDFs. The distribution is computed using the nitrogen atoms of the imidazolium ring attached to the alkyl chain as reference atoms. **Right:** Cation-water RDFs using as reference the last carbon atom of the alkyl chain and the oxygen atom of water. From top to bottom systems containing $[C_n MIM]^+ [Cl]^-$ IL in water with n = 4, 6, 8, 10, and 12 carbon atoms respectively are shown for the indicated concentrations.

of water molecules are plotted in Figure 6 (right). In a well-formed micelle, the water molecules are far from the ends of the alkyl chains (Figure 5 bottom). The water-chain peak intensifies as the system becomes homogenous, since the probability of finding water molecules close to the carbon atoms is larger. This effect is evidenced in Figure 6, confirming the structural transition upon IL addition. To link structural changes and transport properties we study the concentration dependence on the intensity of the first peak of the RDF corresponding to the head-head interaction (Figure 6, left). Figure 7 depicts these variations for all the studied systems. The RDFs were obtained from two reference atoms of the imidazolium
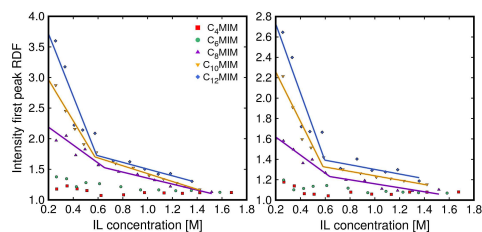
Figure 7. Intensity of the first peak of cation-cation RDFs (Figure 6 left) for varying $[C_n MIM]^+ [Cl]^-$ IL concentration. The reference atoms are nitrogen atoms of the imidazolium ring, attached to the alkyl chain (left) and attached to the methyl chain (right). Solid lines are linear fits to determine the critical concentrations.

ring. The resemblance between this plot and the change of slope in the IL diffusion coefficient already discussed in Figure 3 suggests a correlation between the variation of the transport of the cations in aqueous media and their structural conformation with respect to IL concentration. The critical concentrations extracted from RDF peak variation are 0.64 M for $[C_8 MIM]^+$, 0.58 M for $[C_{10} MIM]^+$, and 0.59 M for $[C_{12} MIM]^+$. The fact that these values are very similar to the values extracted from the self-diffusion coefficient data. This finding is very interesting because it demonstrates that structural conformations govern the mobility of the cations in the mixture. In regard to the chloride anions, they can diffuse faster than cations since they are homogeneously distributed in aqueous media. However they are still correlated with the cations head at distances around 5 Å to maintain the local electroneutrality of the system. Further-

more, the structure of the aggregates is unafected by chloride anions once water is added to the mixture. For this reason ILs used as surfactants contain these counterparts.

Figure 8 (left) shows the local density (one-body distribution function) of $[C_4 MIM]^+$, $[C_8 MIM]^+$, and $[C_{12} MIM]^+$ cations for several concentrations. $[C_4 MIM]^+$ cations are homogeneously distributed along the simulation box as evidenced by the almost constant local density. However, the local density of $[C_8 MIM]^+$ and $[C_{12} MIM]^+$ cations fluctuates strongly indicating their ability to form organized clusters that remain in time in the simulation. Differences between homogeneous and heterogeneous systems are also evidenced from the average occupation profiles depicted in Figure 8 (right). These profiles were obtained at low and high concentration of the geometric center of the $[C_n MIM]^+$ cations in the XY plane. RDF and density are magnitudes that correspond to time averages of particle positions. For a deep understanding of the behavior of the clustered cations we looked at the cation assembling.

Figure 9 (top) shows the average percentage of aggregated $[C_n MIM]^+$ cations in water media for all the concentrations studied. These aggregates are calculated based on a geometric criterion. We consider that a cluster (micelle-like shape) is formed if: i) the distance between the extreme carbon atoms of the alkyl chain is lower than 7.5 Å, ii) there is no water
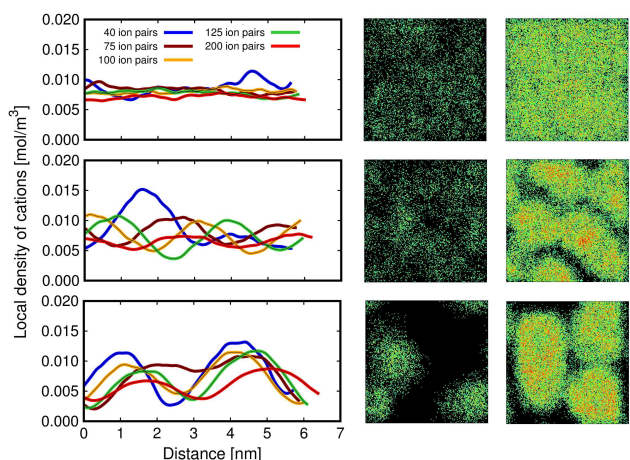
Figure 8. Local density of cations across the x direction (left) and average occupation profiles at low and high concentration of the geometric center of cations in the XY plane (right). Results shown correspond to systems containing [C$_4$MIM]$^+$ (top), [C$_8$MIM]$^+$ (center), and [C$_{12}$MIM]$^+$ (bottom) cations.

molecules at a distance closer than 5 Å from the cation tail, and iii) the cluster is formed by at least 12 cations. Since the choice of the distances is arbitrary, we selected these values based on the position of the first minimum of the tail-tail RDF (Figure 9, bottom) and cation tail-water RDF (Figure 6, right), respectively. Using this criterion, the results depicted in Figure 9 (top) reveal that [C$_4$MIM]$^+$ cations are unable to form clusters while [C$_6$MIM]$^+$ cations show a partial aggregation (lower than 25 %) at very high concentrations. However cations with longer alkyl chains aggregate easily. The [C$_8$MIM]$^+$ cations are dissolved in water as monomers at low concentrations.

An increase in the concentration of ILs leads cations to aggregate partially (lower than 25 %) up to concentration of 0.6 M. At concentrations over 0.9 M, the average percentage of aggregates [C$_8$MIM]$^+$ cations overcome 75 % reaching to 90 % at high concentrations. For [C$_{10}$MIM]$^+$ and [C$_{12}$MIM]$^+$ cations, the aggregation process starts in the low concentration regime. These results are in line with our previous analysis of the transport and structural properties and with all reported experimental observations.[6, 23] Using the percentage of aggregation of cations in a concentration regime with well-defined micelles, one can estimate the value of cmc with the analytic theory.[64, 65] This theory states that the cmc matches with the free monomer concentration in micellar solutions. This is:

$$cmc = \frac{n_{free}}{V_{Total} - V_{micelles}} \qquad (4)$$
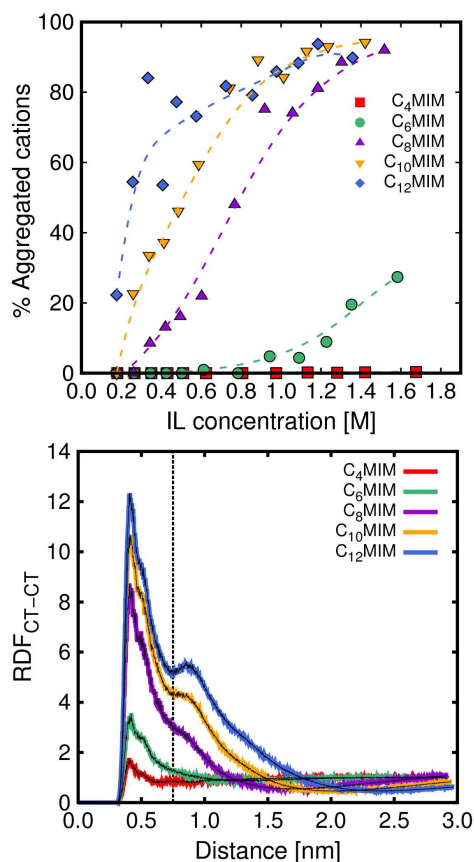
Figure 9. Average percentage of aggregated cations as a function of the IL concentration for systems containing $[C_n MIM]^+ [Cl]^-$ IL in water (top). Lines are eye guidelines. Tail-tail RDFs (bottom) of $[C_n MIM]^+$ cations for a concentration of 75 IL ion pairs.

time, the volume of a monomer is calculated from the van der Waals radius of its atoms. We averaged this approximation for the five concentrations over 1 M for systems containing $[C_8 MIM]^+$, $[C_{10} MIM]^+$, and $[C_{12} MIM]^+$ cations, which are able to form micelles. The results give a value of *cmc* of 0.22, 0.12, and 0.16 for ILs containig $[C_8 MIM]^+$, $[C_{10} MIM]^+$, and $[C_{12} MIM]^+$ cations respectively. These theoretical values are closer to the experimental data reported by Jungnickel et al.[23] which are 0.23, 0.06, and 0.015 for the same systems.

Figure 9 (bottom) shows the tail-tail RDF of each $[C_n MIM]^+$ cation (using as reference atom the last carbon atom of the tail) for high concentrations. The peak height at 4.5 Å is is less intense for the shorter cations than for the longer cations. This result confirms that for a given concentration, cations with larger alkyl chains aggregate more easily since their hydrophobic tails tend to be closer in the presence of water.

Figure 10 depicts the average cluster size distribution (number of cations per cluster) and the number of cluster distribution for the three longest cations (that can form micelles) and for different amount of IL ion pairs (corresponding to low, intermediate and high concentrations). The systems containing $[C_8 MIM]^+$ cations form micelles with 15 and 25 cations. These cations are distributed in different number of micelles, from 1 to 9 as increasing the concentration. The systems containing

where n_{free} is the number of free monomers in the solution, and V_{Total} and $V_{micelles}$ are the volume of the simulation box and the volume occupied by micelles, respectively. The volume occupied by micelles is estimated multiplying the volume of a monomer by the number of cations forming the micelles. At the same
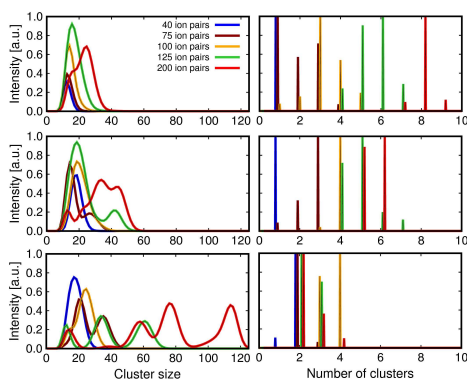
Figure 10. Cluster size distribution (number of cations per cluster) (left) and number of cluster distribution (right) for systems containing $[C_8MIM]^+$ (top), $[C_{10}MIM]^+$ (center), and $[C_{12}MIM]^+$ (bottom) cations.

$[C_{10}MIM]^+$ cations exhibit similar behavior, but they can form micelles with a high number of cations (up to micelles with 50 cations) and therefore the number of clusters is lower. Finally, $[C_{12}MIM]^+$ cations show an increasing number of cations per cluster when the IL concentration is increased but they are distributed among a maximum of 4 clusters. We found big aggregates of $[C_{12}MIM]^+$ cations containing more than 100 molecules at high concentrations. Although at high concentrations $[C_8MIM]^+$, $[C_{10}MIM]^+$, and $[C_{12}MIM]^+$ cations aggregate with a percentage higher than 90 % (Figure 9), the size and distribution of these aggregates is totally different (Figure 10). Increasing the chain length simplifies the aggregation process and enlarges the size of the the aggregates.

Figure 11 illustrates previous analy-sis with representative snapshots from MD simulations of low and high concentration of $[C_nMIM]^+ [Cl]^-$ (n = 4, 8, and 12) in water/IL mixtures. As shown in the figure, $[C_4MIM]^+$ cations for the low and high concentrations, are homogeneously distributed in aqueous media.

In the case of $[C_8MIM]^+$ cations, they are dissolved as monomers at low concentrations, but at high concentrations they aggregate forming a heterogeneous system with micelles that have on average less than 30 cations (Figure 10). $[C_{12}MIM]^+$ cations are able to aggregate even at low concentrations. At high concentrations, they form micelles of around 100 cations.

The representative conformations of cation aggregates are shown in Figure 11b. These are monomers, spherical micelles of different sizes, and cylindrical micelles. As discussed above, the sizes and the shapes of the aggregates depend on both the nature of the cation and their concentration in the water/IL systems.

CONCLUSIONS

The formation of micelles and the prediction of a critical micellar concentration was investigated using molecular dynamics simulations. In line with experimental observations, sufficiently long alkyl chains produce a sharp change of the slope in the diffussion-concentration plot. The critical concentration appears at similar values when the height of the first peak of
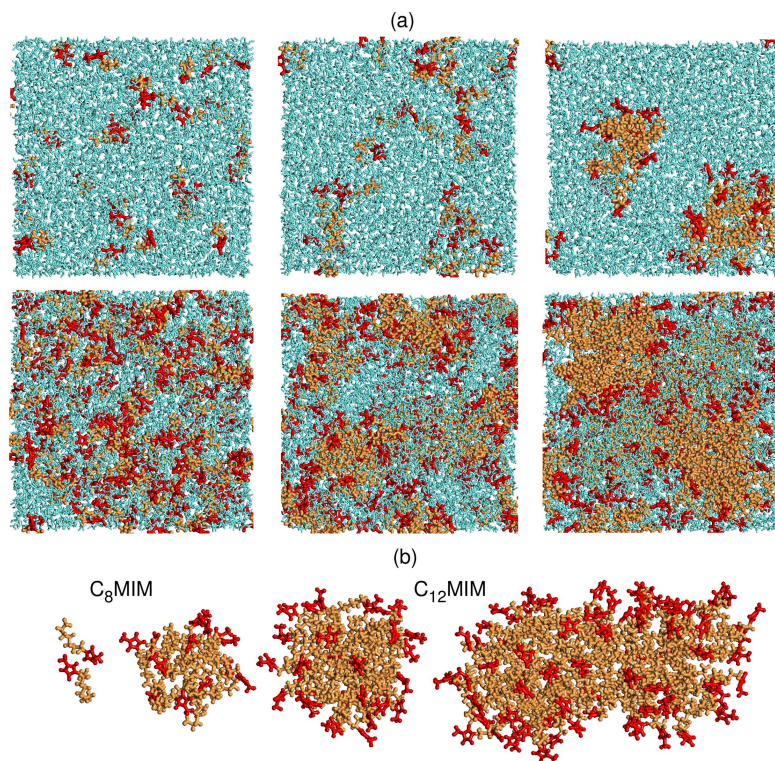
Figure 11. (a) Snapshots from MD simulations corresponding to water/IL mixtures for a concentration of 30 IL ion pairs (top) and 200 IL ion pairs (bottom). From left to right systems containing $[C_4MIM]^+$, $[C_8MIM]^+$, and $[C_{12}MIM]^+$ cations, respectively. (b) Snapshots of aggregated $[C_8MIM]^+$ and $[C_{12}MIM]^+$ cations. The color code is as follows: tail of the cations in orange, head of the cations in red and water molecules in blue. For clarity, chloride anions are omitted in the snapshots.

the head-head RDF is plotted as a function of concentration. This is an indication of structural changes associated to the formation of micelles, as evidenced by the analysis of the tail-tail and tail-water RDFs. We also observed that the fraction of monomers forming part of the micelles increases with the length of the alkyl chain, hence confirming the molecular correlation between anisotropy and critical micelar concentrations. We there-fore conclude that molecular dynamics simulations prove useful to detect formation of micelles as well as to predict critical micelle concentrations in room temperature ionic liquid/water mixtures.

Bibliography

[1]   Hallett, J. P.; Welton, T. *Chem. Rev.* **2011**, *111*, 3508–3576.

[2]   Welton, T. *Chem. Rev.* **1999**, *99*, 2071–2083.

[3] Plechkova, N. V.; Seddon, K. R. *Chem. Soc. Rev.* **2008**, *37*, 123–150.

[4] Seddon, K. R. *J. Chem. Technol. Biotechnol.* **1997**, *68*, 351–356.

[5] Zhang, S. J.; Sun, N.; He, X. Z.; Lu, X. M.; Zhang, X. P. *J. Phys. Chem. Ref. Data* **2006**, *35*, 1475–1517.

[6] Figueira-González, M.; Francisco, V.; García-Río, L.; Marques, E. F.; Parajó, M.; Rodríguez-Dafonte, P. *J. Phys. Chem. B* **2013**, *117*, 2926–2937.

[7] Javadian, S.; Ruhi, V.; Heydari, A.; Shahir, A. A.; Yousefi, A.; Akbari, J. *Ind. Eng. Chem. Res.* **2013**, *52*, 4517–4526.

[8] He, Y.; Shang, Y.; Liu, Z.; Shao, S.; Liu, H.; Hu, Y. *Colloids Surfaces B Biointerfaces* **2013**, *101*, 398–404.

[9] Liu, Y.; Yang, L.; Guo, R. *Soft Matter* **2013**, *9*, 3671.

[10] Tourne-Peteilh, C.; Coasne, B.; In, M.; Brevet, D.; Devoisselle, J. M.; Vioux, A.; Viau, L. *Langmuir* **2014**, *30*, 1229–1238.

[11] Tome, L. I. N.; Varanda, F. R.; Freire, M. G.; Marrucho, I. M.; Coutinho, J. A. P. *J. Phys. Chem. B* **2009**, *113*, 2815–2825.

[12] Freire, M. G.; Carvalho, P. J.; Silva, A. M. S.; Santos, L. M. N. B. F.; Rebelo, L. P. N.; Marrucho, I. M.; Coutinho, J. A. P. *J. Phys. Chem. B* **2009**, *113*, 202–211.

[13] Freire, M. G.; Carvalho, P. J.; Gardas, R. L.; Marrucho, I. M.; Santos, L. M. N. B. F.; Coutinho, J. A. P. *J. Phys. Chem. B* **2008**, *112*, 1604–1610.

[14] Freire, M. G.; Neves, C. M. S. S.; Carvalho, P. J.; Gardas, R. L.; Fernandes, A. M.; Marrucho, I. M.; Santos, L. M. N. B. F.; Coutinho, J. A. P. *J. Phys. Chem. B* **2007**, *111*, 13082–13089.

[15] Vicent-Luna, J. M.; Ortiz-Roldan, J. M.; Hamad, S.; Tena-Zaera, R.; Calero, S.; Anta, J. A. *Chemphyschem* **2016**, *17*, 2473–2481.

[16] Palm, R.; Kurig, H.; Tonurist, K.; Jaenes, A.; Lust, E. *Electrochim. Acta* **2012**, *85*, 139–144.

[17] Palm, R.; Kurig, H.; Tonurist, K.; Jaenes, A.; Lust, E. *Electrochem. commun.* **2012**, *22*, 203–206.

[18] Tonurist, K.; Thomberg, T.; Jaenes, A.; Kink, I.; Lust, E. *Electrochem. commun.* **2012**, *22*, 77–80.

[19] Kuang, D.; Klein, C.; Zhang, Z.; Ito, S.; Moser, J.-E.; Zakeeruddin, S. M.; Graetzel, M. *Small* **2007**, *3*, 2094–2102.

[20] Guillén, E.; Fernández-Lorenzo, C.; Alcántara, R.; Martín-Calleja, J.; Anta, J. A. *Sol. Energy Mater. Sol. Cells* **2009**, *93*, 1846–1852.

[21] Wei, Y.; Wang, F.; Zhang, Z. Q.; Ren, C. C.; Lin, Y. *J. Chem. Eng. Data* **2014**, *59*, 1120–1129.

[22] Smirnova, N. A.; Safonova, E. A. *Colloid J.* **2012**, *74*, 254–265.

[23] Jungnickel, C.; Luczak, J.; Ranke, J.; Fernandez, J. F.; Muller, A.; Thoming, J. *Colloids Surfaces a-Physicochemical Eng. Asp.* **2008**, *316*, 278–284.

[24] Blesic, M.; Marques, M. H.; Plechkova, N. V.; Seddon, K. R.; Rebelo, L. P. N.; Lopes, A. *Green Chem.* **2007**, *9*, 481–490.

[25] Geng, F.; Liu, J.; Zheng, L.; Yu, L.; Li, Z.; Li, G.; Tung, C. *J. Chem. Eng. Data* **2010**, *55*, 147–151.

[26] Jiang, W.; Wang, Y.; Voth, G. A. *J. Phys. Chem. B* **2007**, *111*, 4812–4818.

[27] Vicent-Luna, J. M.; Dubbeldam, D.; Gomez-Alvarez, P.; Calero, S. *Chemphyschem* **2016**, *17*, 380–386.

[28] Zolghadr, A. R.; Ghatee, M. H.; Zolghadr, A. *J. Phys. Chem. C* **2014**, *118*, 19889–19903.

[29] Brodskaya, E. N. *Colloid J.* **2012**, *74*, 154–171.

[30] Niazi, A. A.; Rabideau, B. D.; Ismail, A. E. *J. Phys. Chem. B* **2013**, *117*, 1378–1388.

[31] Ramya, K. R.; Kumar, P.; Kumar, A.; Venkatnathan, A. *J. Phys. Chem. B* **2014**, *118*, 8839–8847.

[32] Feng, S.; Voth, G. A. *Fluid Phase Equilib.* **2010**, *294*, 148–156.

[33] Bhargava, B. L.; Klein, M. L. *J. Phys. Chem. A* **2009**, *113*, 1898–1904.

[34] Chaban, V. V.; Verspeek, B.; Khandelia, H. *J. Phys. Chem. Lett.* **2013**, *4*, 1216–1220.

[35] Méndez-Morales, T.; Carrete, J.; Cabeza, O.; Gallego, L. J.; Varela, L. M. *J. Phys. Chem. B* **2011**, *115*, 6995–7008.

[36] Gabl, S.; Schroder, C.; Steinhauser, O. *J. Chem. Phys.* **2012**, *137*.

[37] Lopes, J. N. C.; Padua, A. A. H. *J. Phys. Chem. B* **2006**, *110*, 19586–19592.

[38] Vicent-Luna, J. M.; Idígoras, J.; Hamad, S.; Calero, S.; Anta, J. A. *J. Phys. Chem. C* **2014**, *118*, 28448–28455.

[39] Rick, S. W. *J. Chem. Phys.* **2004**, *120*, 6085–6093.

[40] Darden, T.; York, D.; Pedersen, L. *J. Chem. Phys.* **1993**, *98*, 10089–10092.

[41] Essmann, U.; Perera, L.; Berkowitz, M. L.; Darden, T.; Lee, H.; Pedersen, L. G. *J. Chem. Phys.* **1995**, *103*, 8577–8593.

[42] Martinez, L.; Andrade, R.; Birgin, E. G.; Martinez, J. M. *J. Comput. Chem.* **2009**, *30*, 2157–2164.

[43] Payne, M. C.; Teter, M. P.; Allan, D. C.; Arias, T. A.; Joannopoulos, J. D. *Rev. Mod. Phys.* **1992**, *64*, 1045–1097.

[44] Martyna, G. J.; Tuckerman, M. E.; Tobias, D. J.; Klein, M. L. *Mol. Phys.* **1996**, *87*, 1117–1157.

[45] Nose, S. *Mol. Phys.* **2002**, *100*, 191–198.

[46] Hoover, W. G. *Phys. Rev. A* **1985**, *31*, 1695–1697.

[47] Berendsen, H. J. C.; Vanderspoel, D.; Vandrunen, R. *Comput. Phys. Commun.* **1995**, *91*, 43–56.

[48] Hess, B.; Kutzner, C.; van der Spoel, D.; Lindahl, E. *J. Chem. Theory Comput.* **2008**, *4*, 435–447.

[49] Pronk, S.; Pall, S.; Schulz, R.; Larsson, P.; Bjelkmar, P.; Apostolov, R.; Shirts, M. R.; Smith, J. C.; Kasson, P. M.; van der Spoel, D.; Hess, B.; Lindahl, E. *Bioinformatics* **2013**, *29*, 845–854.

[50] Van der Spoel, D.; Lindahl, E.; Hess, B.; Groenhof, G.; Mark, A. E.; Berendsen, H. J. C. *J. Comput. Chem.* **2005**, *26*, 1701–1718.

[51] Zhu, X.; Zhang, H.; Xu, Y. J. *J. Solution Chem.* **2016**, *45*, 359–370.

[52] Svensson, A.; Piculell, L.; Karlsson, L.; Cabane, B.; Jonsson, B. *J. Phys. Chem. B* **2003**, *107*, 8119–8130.

[53] Aerov, A. A.; Khokhlov, A. R.; Potemkin II, *J. Chem. Phys.* **2012**, *136*.

[54] Wang, J. M.; Wolf, R. M.; Caldwell, J. W.; Kollman, P. A.; Case, D. A. *J. Comput. Chem.* **2005**, *26*, 114.

[55] Wong, A. C. T.; Yu, K. W. *Phys. a-Statistical Mech. Its Appl.* **2002**, *312*, 50–58.

[56] Indra, S.; Guchhait, B.; Biswas, R. *J. Chem. Phys.* **2016**, *144*.

[57] Hansen, J.-P.; McDonald, I. R. *Theory Simple Liq. (Fourth Ed.*; Academic Press: Oxford, 2013; pp 105–147.

[58] Rilo, E.; Vila, J.; Pico, J.; García-Garabal, S.; Segade, L.; Varela, L. M.; Cabeza, O. *J. Chem. Eng. Data* **2010**, *55*, 639–644.

[59] Ramya, K. R.; Kumar, P.; Venkatnathan, A. *J. Phys. Chem. B* **2015**, *119*, 14800–14806.

[60] Every, H. a.; Bishop, A. G.; MacFarlane, D. R.; Orädd, G.; Forsyth, M. *J. Mater. Chem.* **2001**, *11*, 3031–3036.

[61] Mac Dowell, N.; Llovell, F.; Sun, N.; Hallett, J. P.; George, A.; Hunt, P. A.; Welton, T.; Simmons, B. A.; Vega, L. F. *J. Phys. Chem. B* **2014**, *118*, 6206–6221.

[62] Krynicki, K.; Green, C. D.; Sawyer, D. W. *Faraday Discuss.* **1978**, *66*, 199–208.

[63] Jones, J. R.; Rowlands, D. L. G.; Monk, C. B. *Trans. Faraday Soc.* **1965**, *61*, 1384–1388.

[64] Israelachvili, J. N. *Intermolecular and Surface Forces*; Academic Press: Waltham. MA, 2011.

[65] McCutchen, M.; Chen, L. G.; Bermudez, H.; Matysiak, S. *J. Phys. Chem. B* **2015**, *119*, 9925–9932.

Conclusions

The main conclusions of combining ionic liquids with porous materials for gas capture and separation are: (Chapters 2, 3, and 4)

1.- Ionic liquids embedded within the pores of metal organic frameworks and covalent organic frameworks increase the adsorption of carbon dioxide up to a certain pressure. This pressure depends on the pore size of the structure. The enhancement in the adsorption of carbon dioxide is due to the strong interaction between carbon dioxide and ILs ion pairs (particularly with the anion) which is a consequence of the polar nature of both compounds. However, the effect of ILs in the nitrogen and methane adsorption only matters in the high pressure range, where the the amount of adsorbed gas is reduced by steric effects of the IL ion pairs.

2.- The adsorption selectivity of CO_2/CH_4 and CO_2/N_2 equimolar mixtures increases in favor of carbon dioxide with increasing the IL concentration in the entire pressure range studied in this thesis. This is a consecuence of the affinity of carbon dioxide towards the IL ion pairs.

3.- At high values of pressure, the addition of water instead of ionic liquids to covalent organic frameworks also increases the adsorption selectivity in favor of carbon dioxide for the CO_2/CH_4 equimolar mixtures. However, to avhieve this effect we need more water than IL.

4.- The selectivity enhacement is especially remarkable for structures with large interconnected cavities, where the behavior of the IL is similar as in liquid phase. This is attributed to the improved solubility of carbon dioxide in the IL.

5.- The separation capabilities of the structures with narrow pores can be improved using ILs to control the pore size. This could lead to the exclusion of the less adsorbed

component of the mixture, thus purifying the mixture in the preferred component. This strategy can be used to improve the separation of methane and nitrogen and it can be applicable to other mixtures containing gases of low solubility in the IL.

6.- The presence of ILs in the pores reduces the mobility of the adsorbates but still allows diffusion through the cavities even for the highest concentration of IL studied.

The conclusions concerning the use of ionic liquids as electrolytes for energy conversion and storage are: (Chapters 5, 6, and 7)

7.- Molecular dynamics simulations with fully atomistic models based on effective potentials (Lennard-Jones interatomic potential with point charges) provide a quite complete description of the behavior of ionic liquid-based electrolytes.

8.- The models used reproduce accurately the temperature and alkyl chain dependence of the density and self diffusion coefficients of $[C_n MIM]^+$ $[Tf_2N]^-$ and $[C_n PYR]^+$ $[Tf_2N]^-$ ILs, as well as their mixtures with acetonitrile. These force fields also describe correctly the density, self-diffusion coefficients, and conductivity as a function of the temperature and concentration of metal salt added to $[C_4PYR]^+$ $[Tf_2N]^-$ IL-based electrolytes.

9.- The self-diffusion coefficients of iodide, acting as redox mediator in the dye-sensitized solar cells, increase significantly upon the addition of a low amount of organic solvent to the pure ionic liquid system. This is key for a compromise between stability and efficiency of the dye-sensitized solar cells.

10.- The addition of metal salt to $[C_4PYR]^+$ $[Tf_2N]^-$ IL-based electrolytes produces a depletion in the conductivity of the system. This increases with the amount of salt added. The origin of the anomalous decrease in the conductivity is the cluster formation between the metal cations and the $[Tf_2N]^-$ anions. The local microscopic structure of these complexes has an impact on the total structure of the system, which affects to the macroscopic charge-transport in these electrolytes.

11.- For a fixed concentration of metal salt added to $[C_4PYR]^+$ $[Tf_2N]^-$ IL-based electrolytes, our results predict different behavior of the properties of the systems depending on the nature of the metal cation. This is the case for mono-, di-, and trivalent cations of different ionic radii. These differences are due to the microscopic arrangement of the $[Tf_2N]^-$ anions around of the metal cations.

12.- Two main conformations can be distinguished in the simulations (monodentate and bidentate) depending on the number of oxygen atoms of the anion pointing to the cation. These conformations and the coordination number of $[Tf_2N]^-$ anions surrounding the metal atoms are determined by the size and charge of the metal cation.

Related to the study of the behavior of ionic liquids in water solutions, the most relevant conclusions are: (Chapters 8 and 9)

13.- The presence of $[C_nMIM]^+$ -based ionic liquid in water media modifies the typical tetrahedral ordering of water molecules in liquid phase. The fraction of water molecules with four H-bonds considerably decreases with respect to the pure water system in favor of molecules with one or two H-bonds.

14.- The H-bond network of water weakens with increasing number of IL ion pairs, while the influence of the cation alkyl-chain length is negligible.

15.- Among the studied anions, $[SCN]^-$ is the most hydrophilic and $[Tf_2N]^-$ is the most hydrophobic. $[SCN]^-$ anions can form H-bond with water molecules, whereas systems containing $[Tf_2N]^-$ anions show IL/water phase separation.

16.- $[C_nMIM]^+$ cations with sufficiently long alkyl chains form micelles in presence of water. This is evidenced by a drastic change of the slope in the representation of the self-diffusion coefficients of the cations as a function of the IL concentration. The same behavior is observed in the representation corresponding to the height of the first peak of the head-head radial distribution function against the IL concentration. This suggests that the mobility of the cations in water media is governed by their self-assembly.

17.- In line with experimental observations $[C_nMIM]^+$ cations with shorter alkyn chains ($[C_4MIM]^+$ and $[C_6MIM]^+$) are unable to aggregate in the studied conditions. However, $[C_8MIM]^+$, $[C_{10}MIM]^+$, and $[C_{12}MIM]^+$ cations show structural phase transition with increasing the IL concentration. The size, shape, and fraction of monomers forming part of the resulting micelles vary with the length of the alkyl chain of the cations.

18.- Molecular dynamics simulations are useful to detect formation of micelles as well as to predict critical micelle concentrations in $[C_nMIM]^+$ -based room temperature ionic liquid/water mixtures.

Resumen y conclusiones (Summary and conclusions in spanish)

En esta tesis se estudian sistemas basados en líquidos iónicos para su uso en aplicaciones energéticas. Se denomina líquidos iónicos a temperatura ambiente (RTILs o simplemente ILs, por sus siglas en inglés) a sales compuestas por un catión orgánico y un anión inorgánico u orgánico que se presentan en estado líquido en un amplio intervalo de temperatura (generalmente por debajo de los 100 °C). La combinación de diferentes aniones y cationes da lugar a una enorme variación de ILs con propiedades físico-químicas muy diferentes y de gran interés. Debido al gran número de compuestos que se pueden generar, es complicado estudiar el comportamiento de todos ellos experimentalmente. En este contexto, la simulación molecular es de gran utilidad para aumentar nuestro conocimiento sobre los ILs. Usando técnicas de simulación molecular es posible investigar y comprender el comportamiento de un sistema desde un punto de vista molecular, para una aplicación dada. En este trabajo, se han usado técnicas de simulación molecular (Monte Carlo y dinámica molecular) para tratar diversas aplicaciones con un enfoque medioambiental. En concreto, se han estudiado tres tipos de aplicaciones: 1) ILs confinados en materiales nanoporosos para la captura y separación de gases, 2) electrolitos compuestos por ILs para el almacenamiento y conversión de energía y 3) ILs disueltos en medio acuoso.

Líquidos iónicos confinados en materiales nanoporosos para la captura y separación de dióxido de carbono (Capítulos 2, 3 y 4).

En el capítulo 2 se estudia el efecto que ejercen los ILs dentro de las cavidades de la estructura metal-orgánica Cu-BTC en la captura y separación de dióxido de carbono. Se analizan diferentes cantidades de ILs compuestos por un catión (1-etil-3-metil-imidazolio [EMIM]$^+$) y seis aniones de diferente tamaño y composición.

En el capítulo 3 se compara el uso del IL (Tiocianato de 1-etil-3-metil-imidazolio

[EMIM]$^+$ [SCN]$^-$) y el uso de agua en la hidratación de estructuras covalentes orgánicas para la separación de dióxido de carbono y metano.

El capítulo 4 se centra en el estudio del efecto del IL (Tiocianato de 1-etil-3-metil-imidazolio [EMIM]$^+$ [SCN]$^-$) dentro de varias estructuras metal-orgánicas para la separación de dióxido de carbono y purificación de gas natural. Se estudian cuatro estructuras con diferente topología y tamaño de poro. Además de la adsorción de gases, se analiza la difusión de moléculas confinadas en los poros con y sin la presencia de ILs.

Las principales conclusiones que se extraen de este bloque de resultados, son:
La presencia de ILs dentro de los poros de estructuras nanoporosas, favorece la adsorción de dióxido de carbono hasta cierta presión, debido a la interacción de éste con el IL. Ésta presión dependerá del tamaño de poro de cada estructura. Por otra parte, el IL no modifica el comportamiento de la isoterma de adsorción de metano o nitrógeno debido a que estos gases interaccionan debilmente con el IL. Por consiguiente, el uso de ILs incrementa el factor de separación (selectividad de adsorción) en mezclas CO_2/CH_4 y CO_2/N_2 en favor del dióxido de carbono.
El uso de agua compo disolvente, en lugar de ILs, es una alternativa en estructuras estables con agua, para la separación de dióxido de carbono en el rango de altas presiones.
La separación de gases se puede llevar a cabo por medio de dos estrategias en la selección de la estructura adecuada: 1) elegir estructuras con gran tamaño de poro, donde el IL se comporte como en estado líquido y sea éste el que aumente la adsorción de gases que interaccionen fuertemente con el. 2) Elegir estructuras con poros estrechos, en los que el IL controlará el tamaño de poro, excluyendo el componente minoritario de una mezcla de gases y así aumentar la pureza del componente mayoritario. Por último se observa que el IL hace que disminuya la mobilidad de los gases dentro de los poros de las estructuras, aunque sigue permitiendo la difusión a través de las mismas.

Electrolitos para células solares de colorante y baterías de iones metálicos basados en líquidos iónicos (Capítulos 5, 6 y 7).

En el capítulo 5 se desarrollan modelos de potenciales de interacción para ILs compuestos por el anión (bis-trifluorometano sulfonilimida [Tf$_2$N]$^-$) y dos cationes (1-etil-3-alquil-imidazolio, [C$_n$MIM]$^+$ y N-alquil-N-metil-pirrolidinio, [C$_n$PYR]$^+$) de diferente longitud de cadena hidrocarbonada. Una vez validados los modelos se estudia el transporte de ión yoduro como mediador redox de un electrolito de célula solar de colorante y se compara con resultados experimentales. Por último se realizan simulaciones en las

que se combina el IL con un disolvente orgánico (acetonitrilo). El propósito de esta mezcla es aumentar la eficiencia de la célula solar con un mínimo de pérdida de estabilidad.

Usando los modelos desarrollados anteriormente, en el capítulo 6 se analiza el comportamiento de electrolitos basados en IL ([C_4PYR]$^+$ [Tf_2N]$^-$) para su uso en baterías de ión litio y sodio. Para ello se investiga el efecto de aumentar la temperatura y la concentración de sal de sodio o litio, en las propiedades de transporte del electrolito. Se estudian propiedades como la difusión y la conductividad y su relación con los cambios estructurales a nivel molecular debidos a la presencia de sal metálica.

En el capítulo 7 se extiende el estudio de los electrolitos de IL para baterías variando el catión metálico de la sal añadida. Se investigan cationes de distinto tamaño iónico y distinta carga. Se analiza su influencia en la estructura molecular del electrolito y sus consecuencias en el transporte de carga.

Las principales conclusiones que se obtienen en este bloque son:
Los modelos desarrollados en este estudio basado en potenciales clásicos reproducen el comportamiento de los electrolitos basados en IL. Los coeficientes de difusión del ión yoduro aumentan considerablemente cuando se añade una pequeña cantidad de acetonitrilo al IL. Con ello se puede diseñar un electrolito con un buen balance entre eficiencia y estabilidad.

La adición de sal metálica al IL produce un descenso en la conductividad del electrolito debido a la fuerte interacción del anión [Tf_2N]$^-$ con el catión metálico que causa la formación de agregados moleculares. Éstos agregados afectan a la estructura molecular del electrolito y consecuentemente a su transporte de carga y dependen de las propiedades de los cationes metálicos que componen la sal. La estructura molecular de los agregados varían con la carga y el radio iónico del catión, presentando dos conformaciones principales (monodentada o bidentada, dependiendo del número de átomos de oxígeno que apuntan al catión).

Soluciones acuosas de líquidos iónicos (Capítulos 8 y 9).

En el capítulo 8 se estudia el efecto de cierta cantidad de ILs en la red de enlaces de hidrógeno del agua en estado líquido. Se combinan cationes de la familia 1-etil-3-alquil-imidazolio ([C_nMIM]$^+$) de diferente longitud de cadena hidrocarbonada con diversos aniones para estudiar su grado de hidrofobicidad.

En el capítulo 9 se analizan mezclas de IL y agua en los que ésta es el componente mayoritario. Se investiga el efecto de la longitud de la cadena a medida que se varía la concentración de IL ($[C_n MIM]^+ [Cl]^-$) en una cantidad fija de agua. Se relacionan las propiedades de transporte de los cationes en la disolución acuosa con las propiedades estructurales y se estudia la agregación de los cationes o formación de micelas.

Las principales conclusiones que se obtienen en este bloque son:

La presencia de ILs en agua modifica la estructura tetrahédrica típica del agua en estado líquido. Aumentando la concentración de IL, disminuye la cantidad de enlaces de hidrógeno por molecula de agua en la mezcla. Sin embargo el efecto de incrementar la longitud de la cadena del catión es insignificante en el número medio de enlaces de hidrógeno. El anión $[SCN]^-$ demuestra ser el más hidrofílico de este estudio con una gran interacción con el agua. Por otra parte, el anión $[Tf_2N]^-$ es el más hidrofóbico.

Los cationes $[C_n MIM]^+$ con una longitud de cadena suficientemente larga, son capaces de formar micelas en presencia de agua a partir de una concentración crítica. Ésta concentración micelar crítica está relacionada con el cambio de pendiente de los coeficientes de difusión frente a la concentración de IL. Las propiedades estructurales muestran un comportamiento similar, lo que sugiere que existe una relación estrecha entre estructura molecular y transporte. La longitud de la cadena del catión es un factor importante en su proceso de agregación. A mayor longitud de cadena, más facilidad de agregación y las micelas que se observan difieren tanto en tamaño como en forma dependiendo también de la concentración de IL.

Appendix 1

Associated content of:

Effect of Room Temperature Ionic Liquids on CO_2 Separation by Cu-BTC Metal-Organic Framework

Figure A1-1 shows the cation-anion radial distribution function for RTILs containing $[Tf_2N]^-$ and $[PF_6]^-$ anions for a variety of RTILs concentrations inside Cu-BTC. We observe a first peak around 4 Å. This peak is at a similar distance than the peak obtained in the bulk[S1,S2]. Figure A1-2 depicts the radial distribution function for RTILs containing $[SCN]^-$, $[BF_4]^-$, and $[NO_3]^-$ anions. All anions have the first peak at a similar distance, except thiocyanate anion for which it appears at 2 Å. This result indicates that $[SCN]^-$ is closer to the cation than the rest, attributing this behaviour to the small size of the anion. RTILs are not adsorbed in the structure but introduced ad hoc within the pores. Figure A1-3 shows the radial distribution function of the Cu metal center and the cation and anion, respectively. This illustrates the position of RTILs molecules inside the MOF for different concentrations of ionic liquids. As shown in the figure the anions are near the copper atoms and the cations are distributed homogeneously.
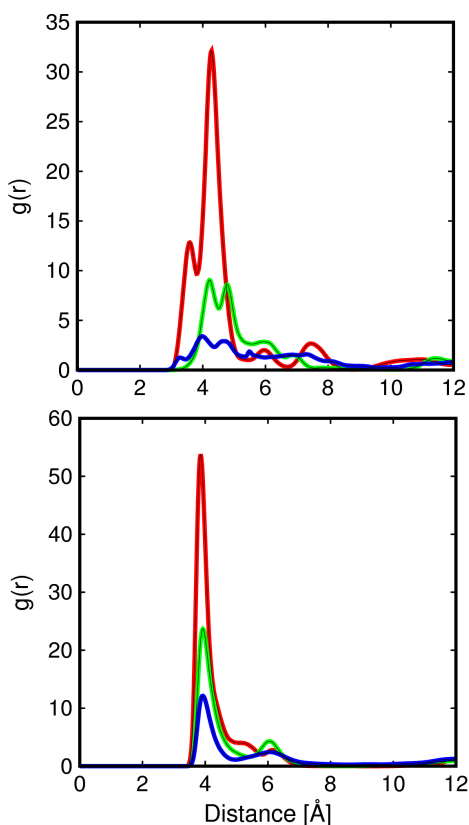
Figure A1.1. Cation-anion radial distribution function for $[Tf_2N]^-$ (top) and $[PF_6]^-$ (bottom) with 4 (red), 8 (green), and 16 (blue) molecules of RTILs per unit cell confined inside the pores of Cu-BTC.
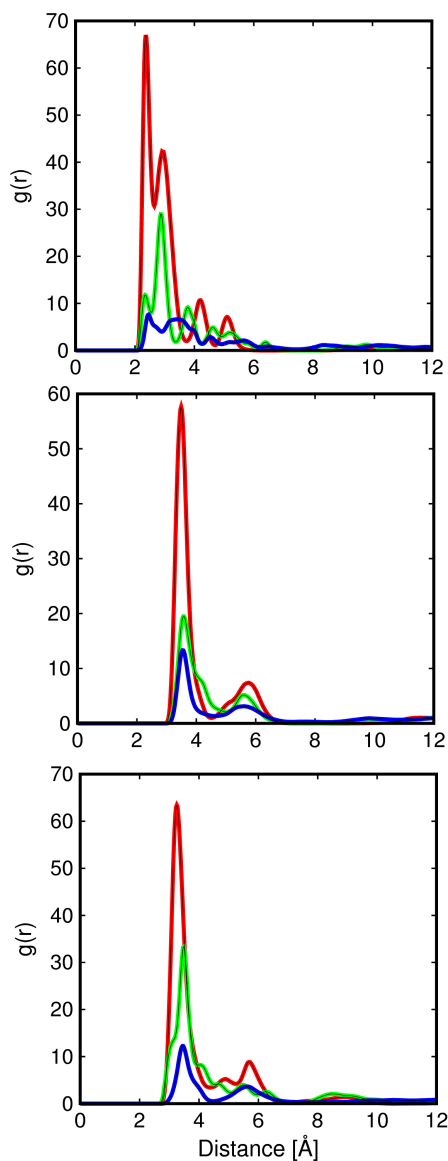
Figure A1.2. Cation-anion radial distribution function for [SCN]$^-$ (a), [BF$_4$]$^-$ (b), and [NO$_3$]$^-$ (c) with 4 (red), 8 (green), and 16 (blue) molecules of RTILs per unit cell confined inside the pores of Cu-BTC.
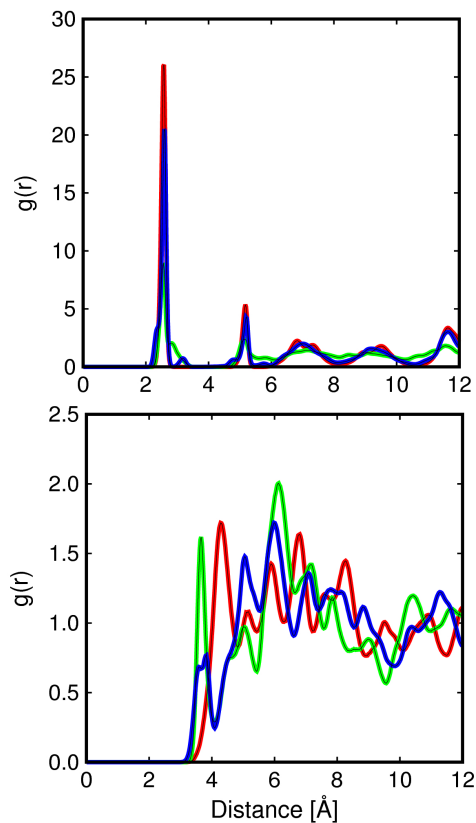
Figure A1.3. Radial distribution function between Cu atoms and [SCN]$^-$ (top) and [EMIM]$^+$ (bottom) with 4 (red), 8 (green), and 16 (blue) molecules of RTILs per unit cell confined inside the pores of Cu-BTC.
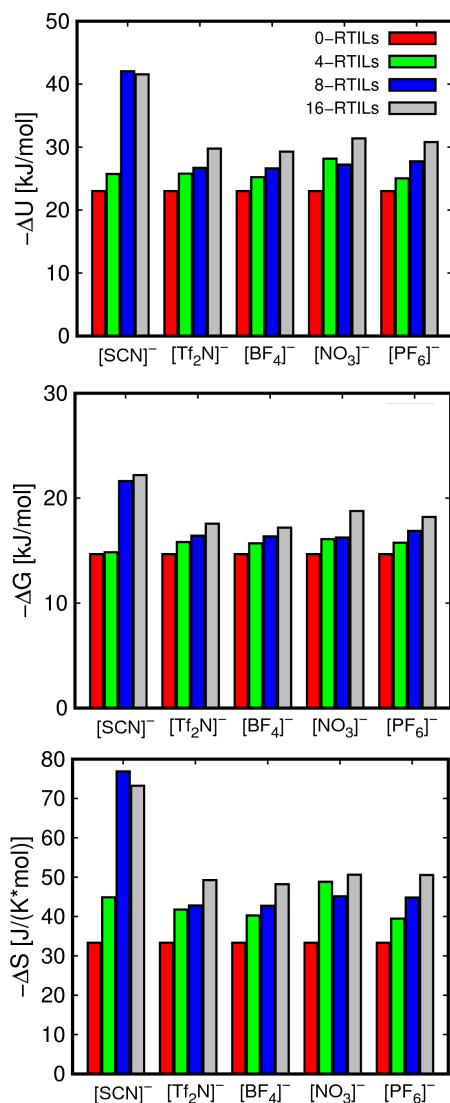
Figure A1.4. Energies and entropies of adsorption computed for carbon dioxide in Cu-BTC. (a) Internal energy, (b) Gibbs free energy, and (c) adsorption entropy.
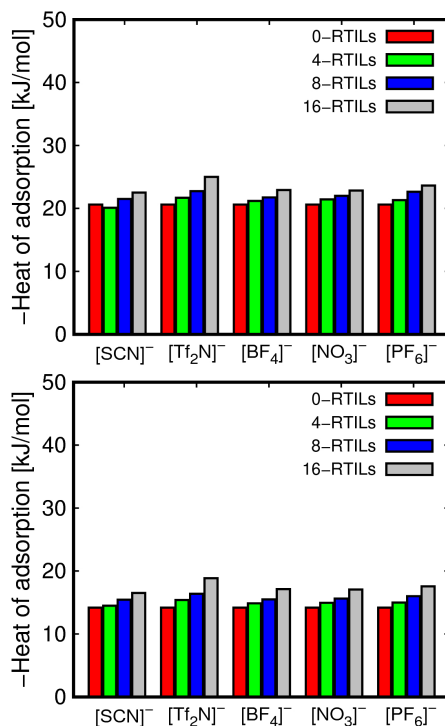
Figure A1.5. Computed isosteric heats of adsorption for methane (top) and nitrogen (bottom) in Cu-BTC.
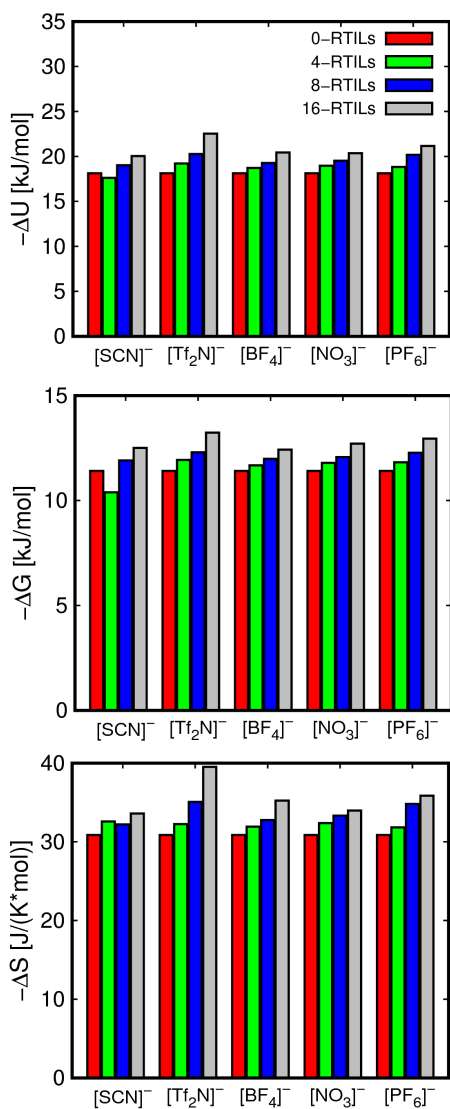
Figure A1.6. Energies and entropies of adsorption computed for methane in Cu-BTC. (a) Internal energy, (b) Gibbs free energy, and (c) adsorption entropy.
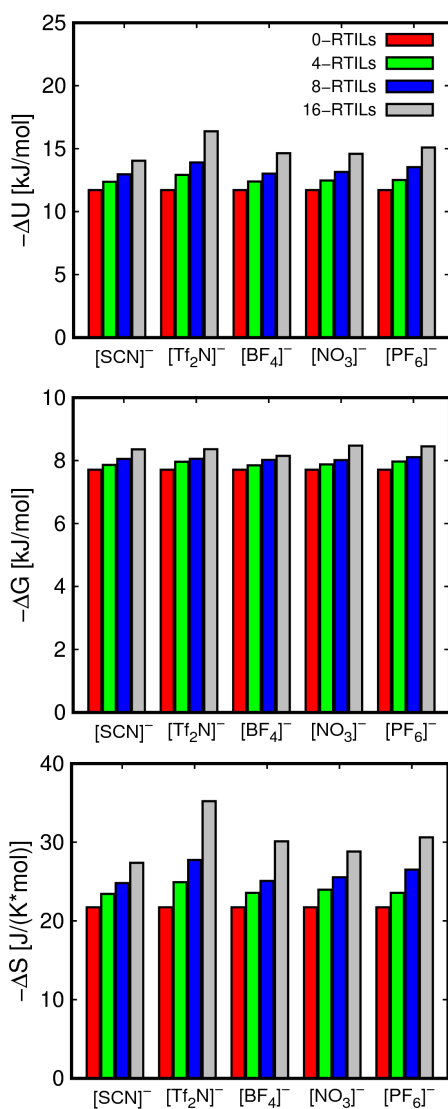
Figure A1.7. Energies and entropies of adsorption computed for nitrogen in Cu-BTC. (a) Internal energy, (b) Gibbs free energy, and (c) adsorption entropy.
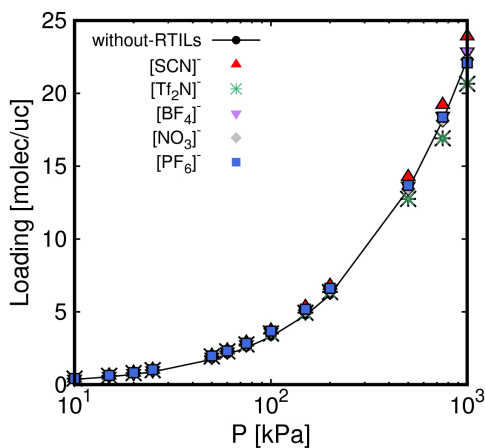
Figure A1.8. Adsorption isotherms obtained for nitrogen in the bare Cu-BTC and in the structure with 8 molecules of RTILs per unit cell.
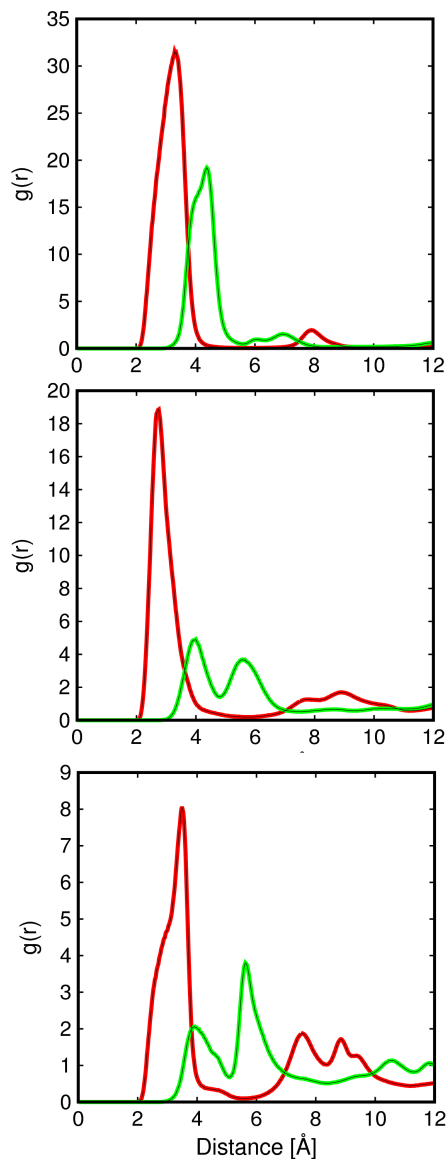
Figure A1.9. Radial distribution function between carbon dioxide and [EMIM]$^+$ (green) and [SCN]$^-$ (red) respectively, with 4 (a), 8, (b), and 16 (c) molecules of RTILs per unit cell inside the pores of Cu-BTC.
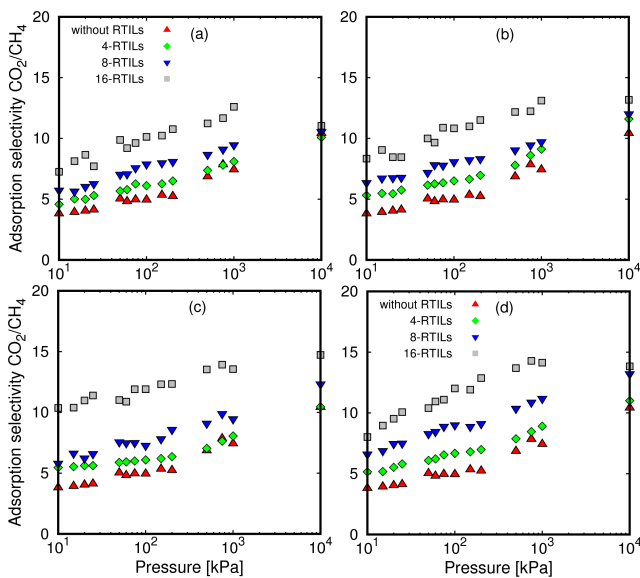
Figure A1.10. CO_2/CH_4 adsorption selectivity in Cu-BTC for systems containing (a) $[Tf_2N]^-$, (b) $[BF_4]^-$, (c) $[NO_3]^-$, (d) and $[PF_6]^-$ anions.
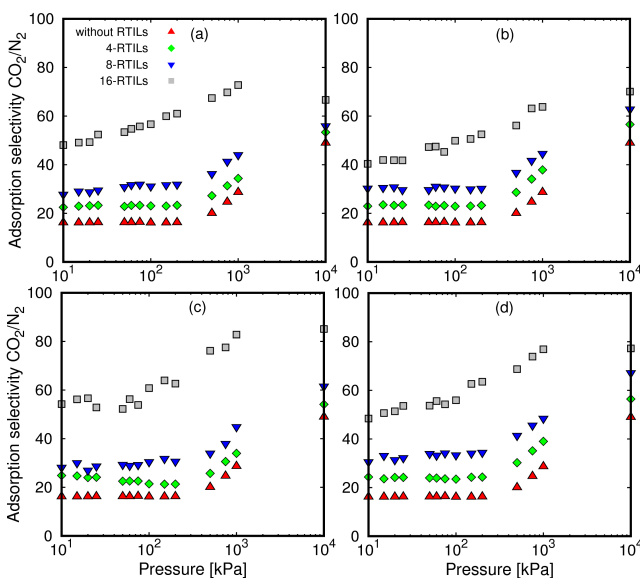
Figure A1.11. CO_2/N_2 adsorption selectivity in Cu-BTC for systems containing (a) $[Tf_2N]^-$, (b) $[BF_4]^-$, (c) $[NO_3]^-$, (d) and $[PF_6]^-$ anions.
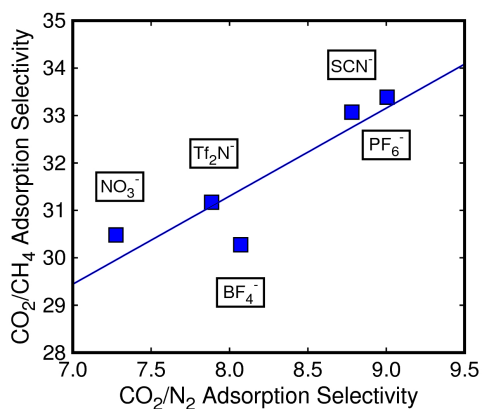
Figure A1.12. Adsorption selectivity of CO_2/CH_4 mixture as a function of the adsorption selectivity of CO_2/N_2 mixture for different anions at room conditions.

REFERENCES:

[S1] Rajput, N., et al., On the Influence of Pore Size and Pore Loading on Structural and Dynamical Heterogeneities of an Ionic Liquid Confined in a Slit Nanopore. *J. Phys. Chem. C*, **2012**, 116, 5170-5182.

[S2] Alavi, S. and D.L. Thompson, Molecular Dynamics Studies of Melting and Some Liquid-State Properties of 1-ethyl-3-methylimidazolium hexafluorophosphate emim PF6. *J. Chem. Phys.*, **2005**. 122, 154704-154710.

Appendix 2

Associated content of:

Storage and Separation of Carbon Dioxide and Methane in Hydrated Covalent Organic Frameworks
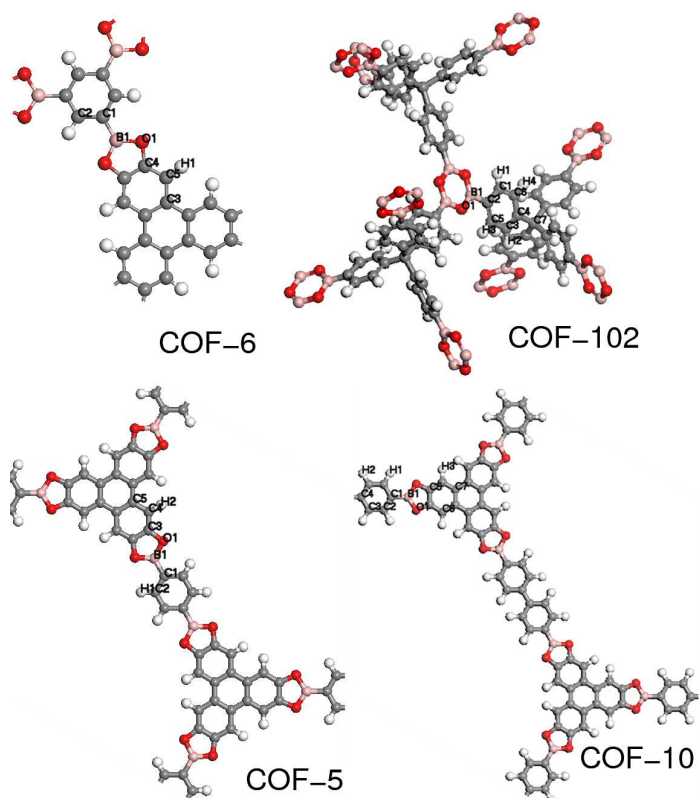
Figure A2.1. Schematic representation and atom labelling for COF-5, COF-6, COF-10, and COF-102. Hydrogen atoms in white, Boron atoms in pink, Oxygen atoms in red and Carbon atoms in grey.
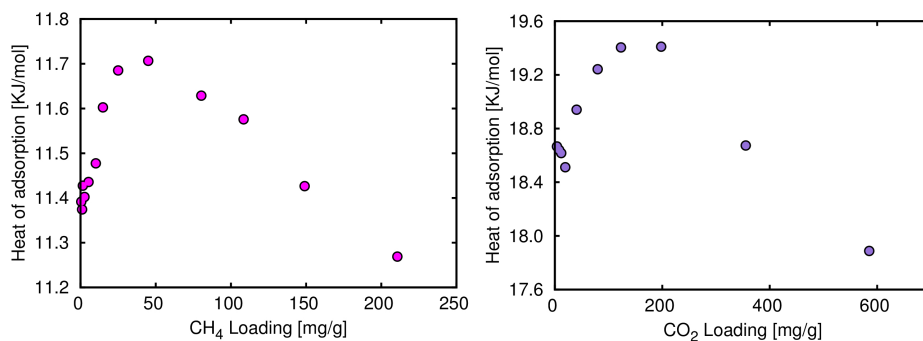
Figure A2.2. Heats of adsorption as a function of loading calculated for CH_4 (left) and CO_2 (right) in COF-5 at 298 K.
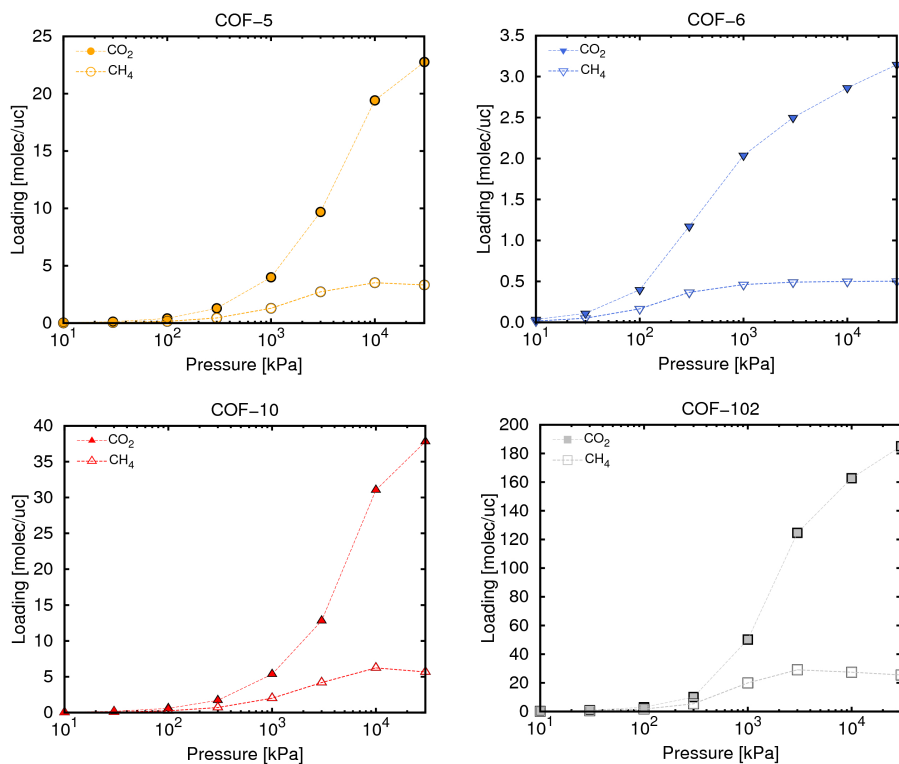
Figure A2.3. Adsorption isotherms calculated for the CO_2/CH_4 equimolar mixture at 298 K in COF-5, COF-6, COF-10, and COF-102.
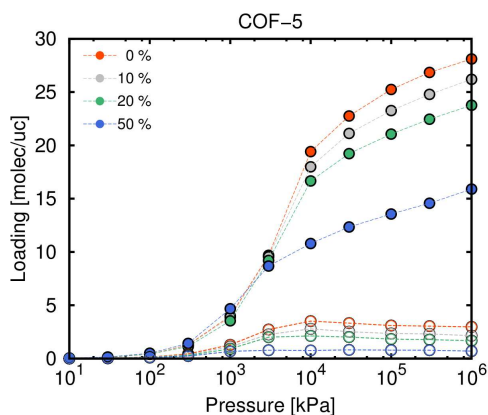
Figure A2.4. Adsorption isotherms calculated for the CO_2/CH_4 equimolar mixture in the dehydrated (0 %) and the hydrated (10%, 20% and 50%) COF-5 at 298 K. CO_2 (full symbols) and CH_4 (empty symbols).
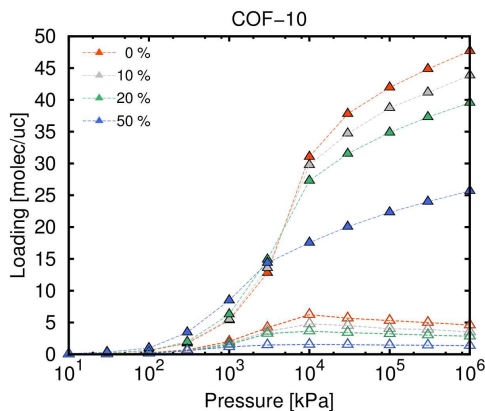
Figure A2.6. Adsorption isotherms calculated for the CO_2/CH_4 equimolar mixture in the dehydrated (0 %) and the hydrated (10%, 20% and 50%) COF-10 at 298 K. CO_2 (full symbols) and CH_4 (empty symbols).
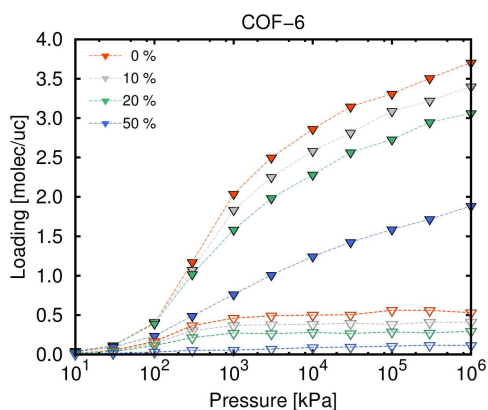
Figure A2.5. Adsorption isotherms calculated for the CO_2/CH_4 equimolar mixture in the dehydrated (0 %) and the hydrated (10%, 20% and 50%) COF-6 at 298 K. CO_2 (full symbols) and CH_4 (empty symbols).
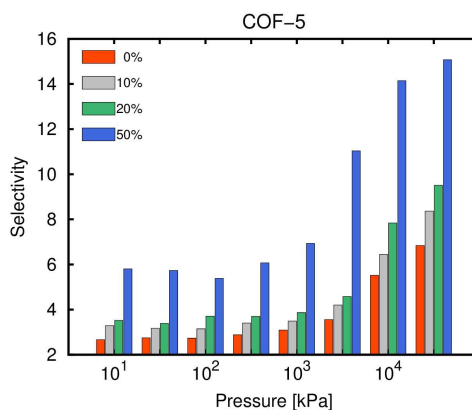
Figure A2.7. CO_2/CH_4 adsorption selectivity obtained from the adsorption isotherms of the equimolar mixture at 298 K in the dehydrated (0%) and the hydrated (10%, 20% and 50%) COF-5.
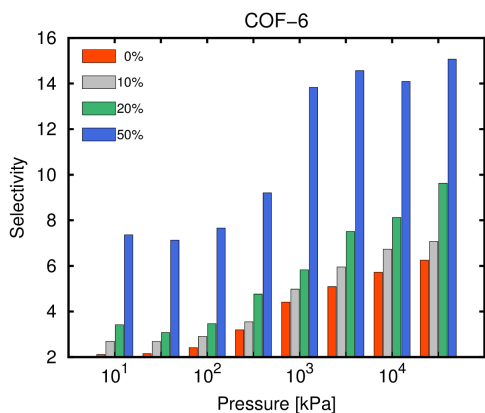
Figure A2.8. CO_2/CH_4 adsorption selectivity obtained from the adsorption isotherms of the equimolar mixture at 298 K in the dehydrated (0%) and the hydrated (10%, 20% and 50%) COF-6.
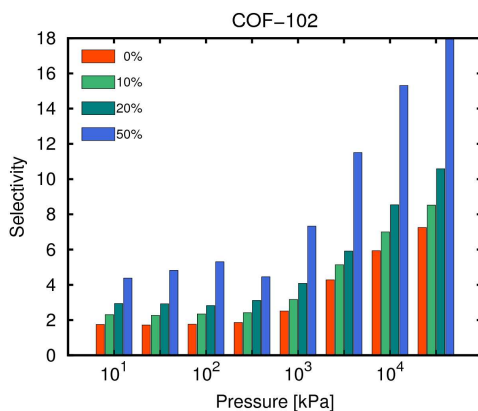
Figure A2.10. CO_2/CH_4 adsorption selectivity obtained from the adsorption isotherms of the equimolar mixture at 298 K in the dehydrated (0%) and the hydrated (10%, 20% and 50%) COF-102.
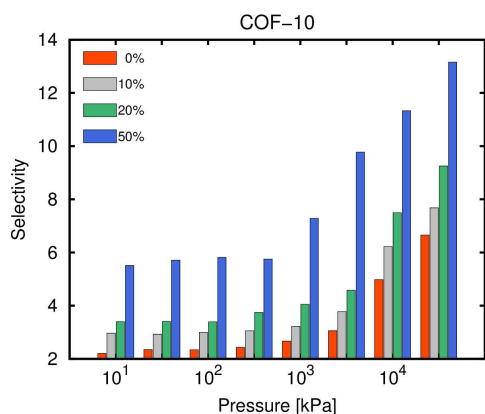
Figure A2.9. CO_2/CH_4 adsorption selectivity obtained from the adsorption isotherms of the equimolar mixture at 298 K in the dehydrated (0%) and the hydrated (10%, 20% and 50%) COF-10.
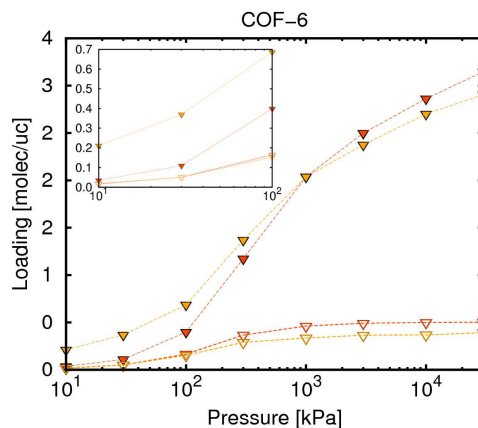
Figure A2.11. Adsorption isotherms calculated for the CO_2/CH_4 equimolar mixture at 298 K in COF-6 containing 10% of IL (yellow) and without IL (red). CO_2 (full symbols) and CH_4 (empty symbols).
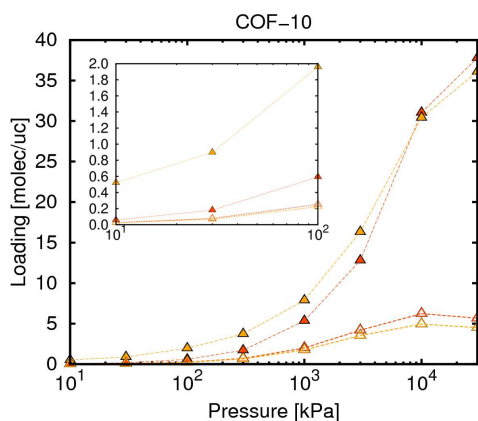
Figure A2.12. Adsorption isotherms calculated for the CO_2/CH_4 equimolar mixture at 298 K in COF-10 containing 10% of IL (yellow) and without IL (red). CO_2 (full symbols) and CH_4 (empty symbols).
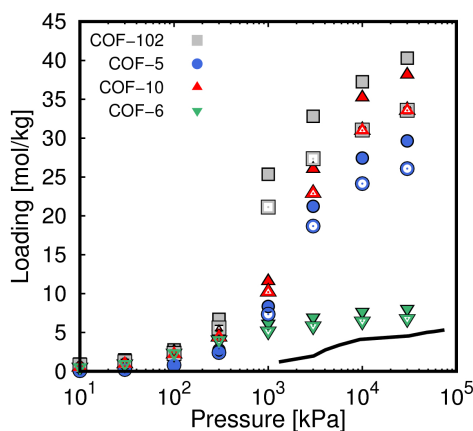
Figure A2.14. Adsorption isotherm of carbon dioxide in COF-5 (yellow circles), COF-6 (blue down triangles), COF-10 (red up triangles), and COF-102 (grey squares) containing 10% of IL. Open symbols represent data that do not take into account the weight of the solvent, closed symbols represent data that take into account the weight of the solvent. The black line is the experimental absorption isotherm of carbon dioxide in neat $[EMIM]^+ [SCN]^-$ IL (Taken from the solubility given in ref. 1).
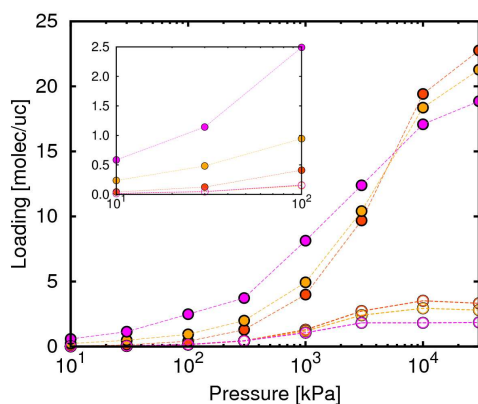
Figure A2.13. Adsorption isotherms calculated for the CO_2/CH_4 equimolar mixture at 298 K in COF-5 containing 10% of IL (yellow) and without IL (red). CO_2 (full symbols) and CH_4 (empty symbols).
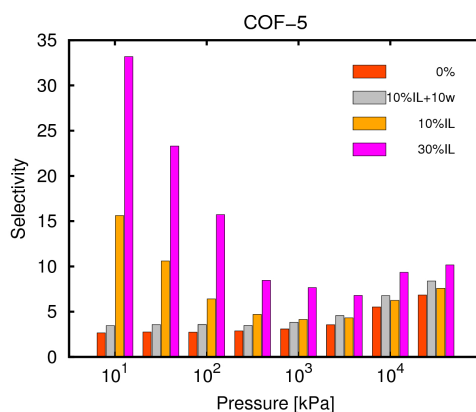
Figure A2.15. CO_2/CH_4 adsorption selectivity calculated from the adsorption isotherm of the equimolar mixture in COF-5 (0%), COF-5 with IL (10%-30%), and COF-5 with 10% IL and 10% water.
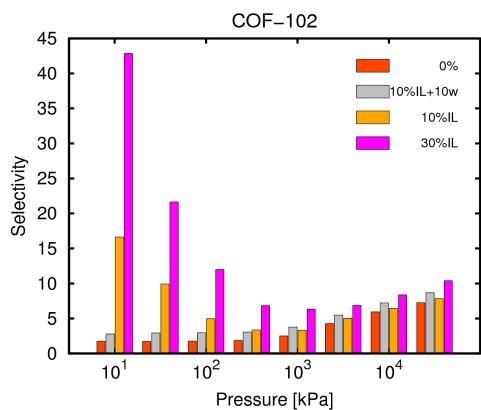
Figure A2.16. CO_2/CH_4 adsorption selectivity calculated from the adsorption isotherm of the equimolar mixture in COF-102 (0%), COF-102 with IL (10%-30%), and in COF-102 with 10% IL and 10% water.
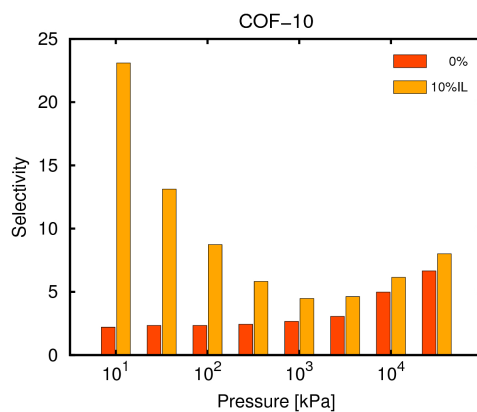
Figure A2.18. CO_2/CH_4 adsorption selectivity calculated from the adsorption isotherm of the equimolar mixture in COF-10 (0%) and COF-10 with 10% of IL.
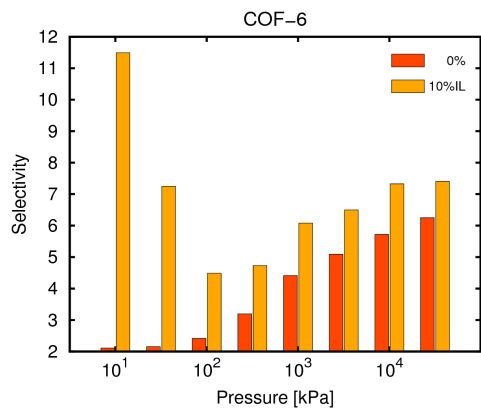
Figure A2.17. CO_2/CH_4 adsorption selectivity calculated from the adsorption isotherm of the equimolar mixture in COF-6 (0%) and COF-6 with 10% of IL.

Associated content of:

Role of Ionic Liquid [EMIM]$^+$ [[SCN]$^-$ In the Adsorption and Diffusion of Gasses in Metal-Organic Frameworks
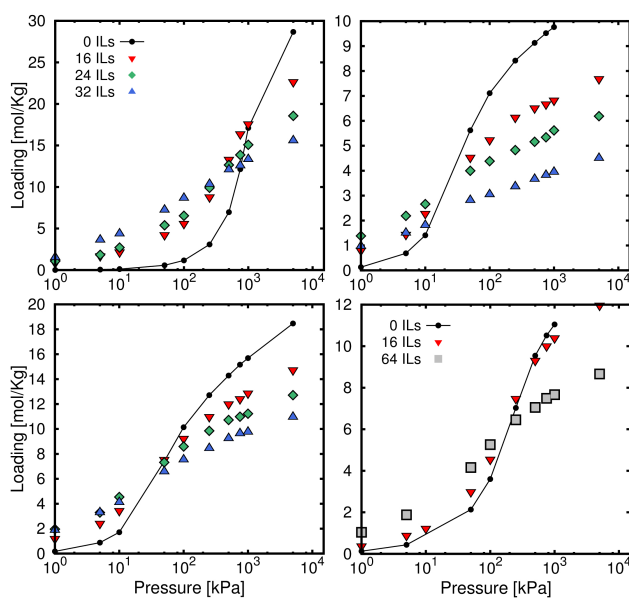
Figure A3.1. Calculated adsorption isotherms of single component carbon dioxide in IRMOF-1 (top-left), MIL-47 (top right), MOF-1 (bottom left), and HMOF-1 (bottom right) with different amount of IL (molecules per simulation box) loaded within the pores.
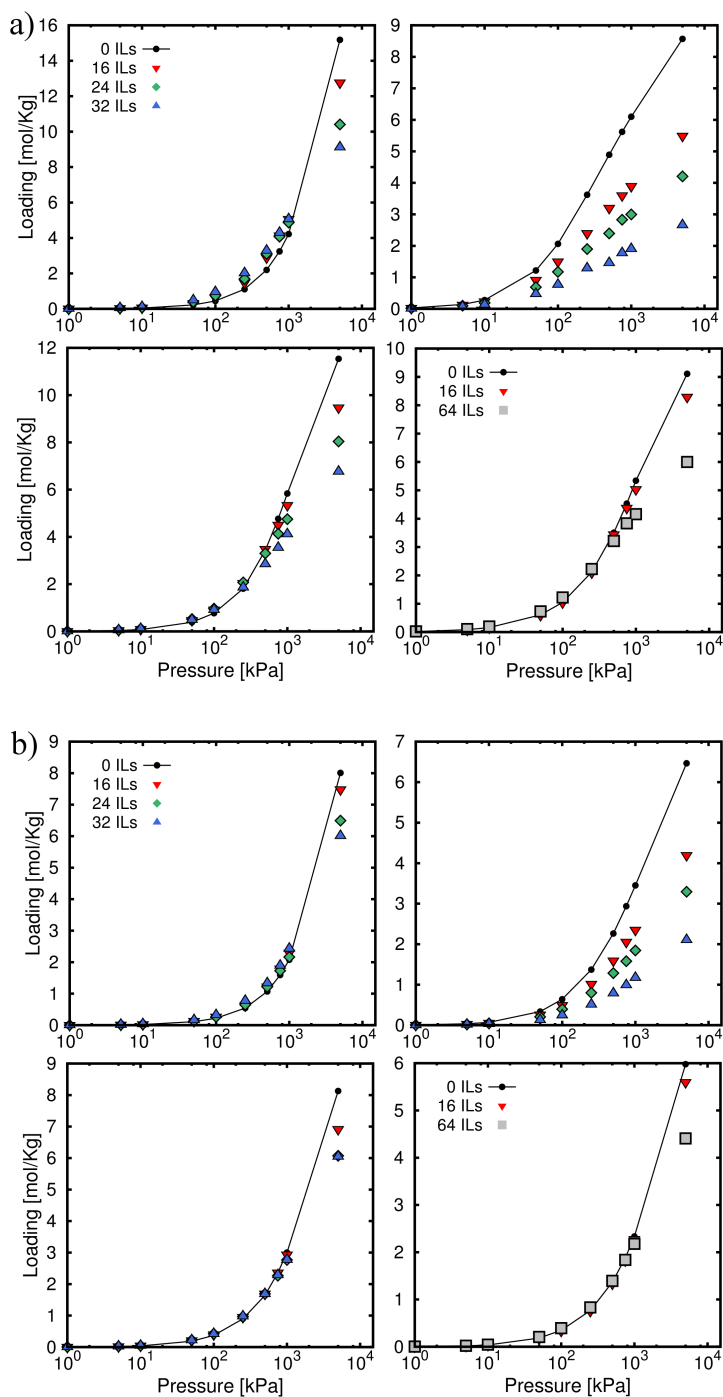
Figure A3.2. Calculated adsorption isotherm of single component (a) methane and (b) nitrogen in IRMOF-1 (top-left), MIL-47 (top right), MOF-1 (bottom left), and HMOF-1 (bottom right) with different amount of IL (molecules per simulation box) loaded within the pores.
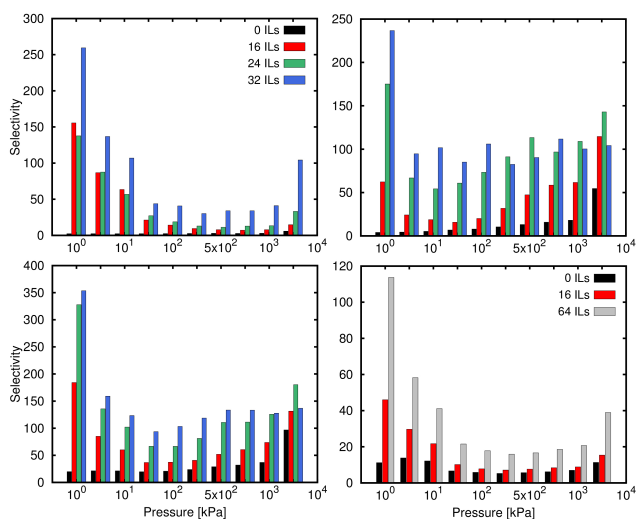
Figure A3.3. Calculated adsorption selectivity for the adsorption of the equimolar mixture CO_2/CH_4 in IRMOF-1 (top-left), MIL-47 (top right), MOF-1 (bottom left), and HMOF-1 (bottom right) with ILs loaded within the MOF pores.
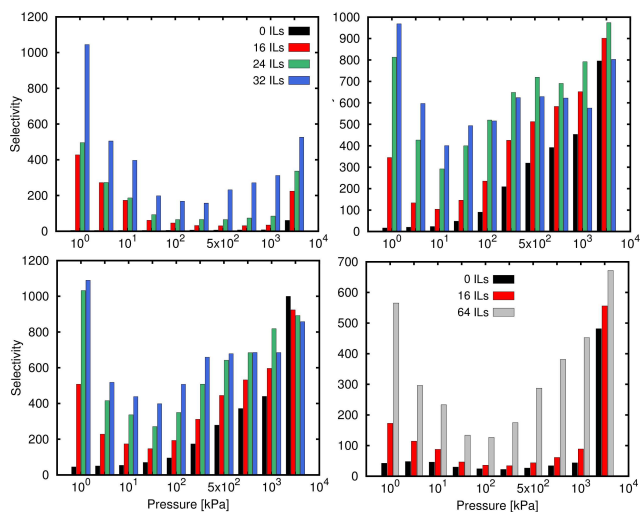
Figure A3.4. Calculated adsorption selectivity for the adsorption of the equimolar mixture CO_2/N_2 in IRMOF-1 (top-left), MIL-47 (top right), MOF-1 (bottom left), and HMOF-1 (bottom right) with ILs loaded within the MOF pores.
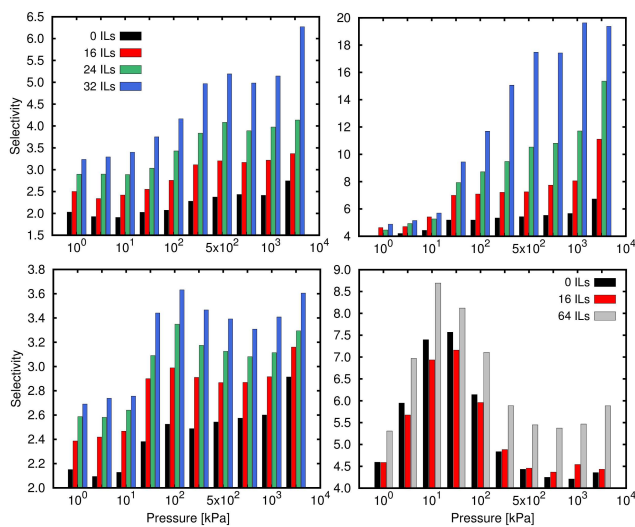
Figure A3.5. Calculated adsorption selectivity for the adsorption of the equimolar mixture N_2/CH_4 in IRMOF-1 (top-left), MIL-47 (top right), MOF-1 (bottom left), and HMOF-1 (bottom right) with ILs loaded within the MOF pores.
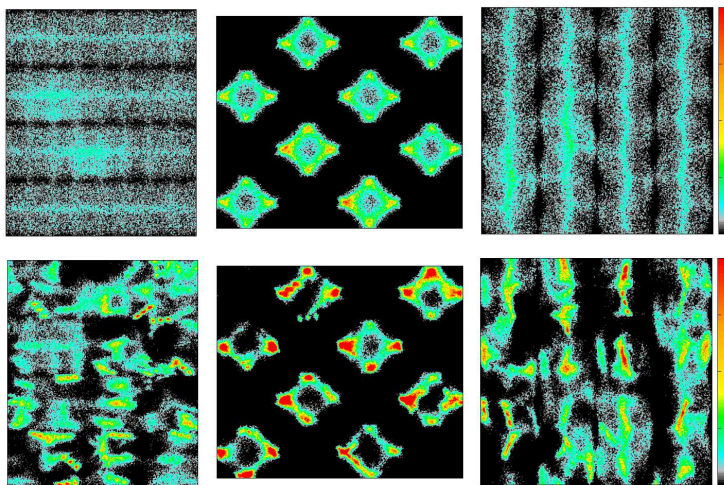
Figure A3.6. Average occupation profiles of carbon dioxide in the bare MIL-47 (top) and loaded with 32 IL ion pairs (bottom).
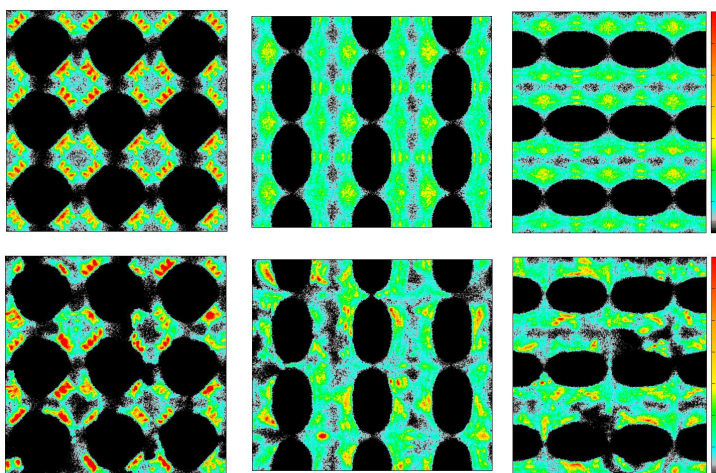
Figure   A3.7.   Average   occupation   profiles   of   carbon   dioxide   in the   bare   MOF-1   (top)   and   loaded   with   32   IL   ion   pairs   (bottom).
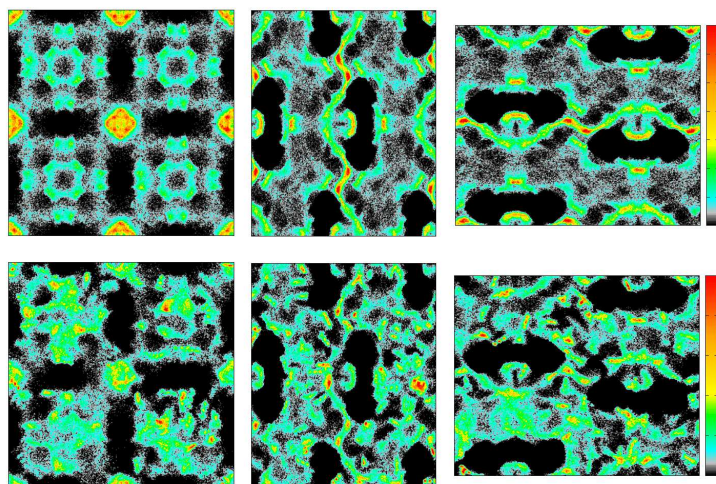
Figure   A3.8.   Average   occupation   profiles   of   carbon   dioxide   in the   bare   HMOF-1   (top)   and   loaded   with   64   IL   ion   pairs   (bottom).
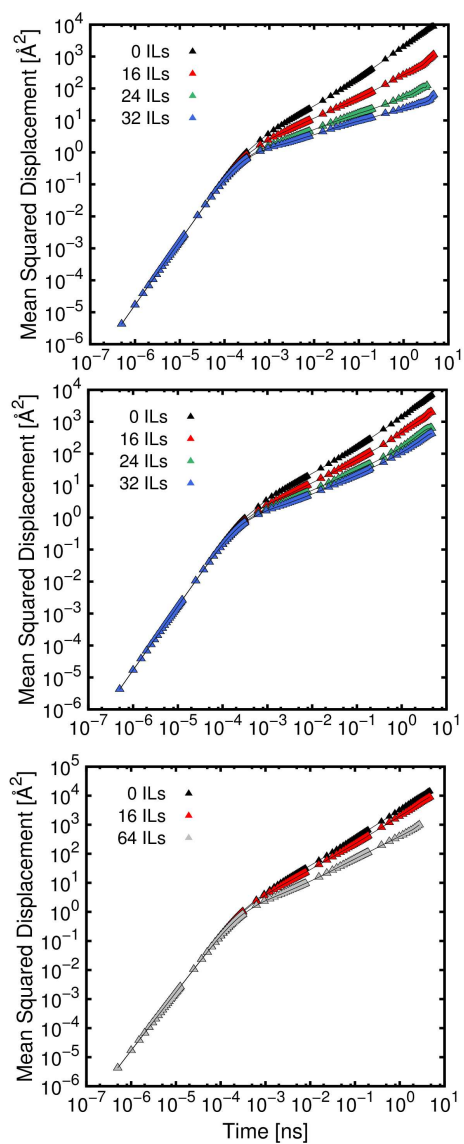
Figure A3.9. Mean squared displacement of carbon dioxide in MIL-47 (top), MOF-1 (center), and HMOF-1 (bottom) loaded with ILs.

Appendix 4

Associated content of:

Ion Transport in Electrolytes for Dye-Sensitized Solar Cells: A Combined Experimental and Theoretical Study

Table A4-1. Atomic point charges, Lennard-Jones, and intramolecular parameters for $[C_nPYR]^+$ (Nomenclature is shown in figure A4.1).

Atom types	ε [kJ/mol]	σ [nm]	Charge [e]
H_A	0.1255	0.242	0.20
H_C	0.1255	0.250	0.18
H_1	0.1255	0.242	0.20
N_A	0.7113	0.325	-0.26
C_{CN}	0.2929	0.355	-0.12
C_{CC}	0.2929	0.355	-0.35
C_{1T}	0.2761	0.350	-0.30
C_1	0.2761	0.350	-0.10
C_2	0.2761	0.350	-0.36
C_S	0.2761	0.350	-0.36
C_T	0.2761	0.350	-0.54

Bonds	K_r [kJ/mol/nm^2]	r_0 [nm]
$C*-C*$	112100	0.1529
$C*-H*$	259000	0.1090
N_A-C_1/C_{1T}	141000	0.1466
N_A-C_{CN}	178700	0.1529
$C_{CC}-C_{CC}$	217600	0.1510
$C_{CC}-C_{CN}$	217600	0.1440

Bends	K_ϕ [kJ/mol/rad^2]	ϕ_0 [deg]
$H*-C*-H*$	276.1	107.8
$N_A/C*-C*-C*$	418.4	112.7
$N_A/C*-C*-H*$	313.2	110.7
$C_1/C_{1T}-N_A-C_{CN}/C_{1T}$	292.6	110.0
$C_{CN}-N_A-C_{CN}$	292.6	102.6
$N_A-C_{CN}-C_{CC}$	292.6	107.0
$C_{CN}-C_{CC}-C_{CC}$	292.6	107.0
$N_A-C_{CN}-H_A$	146.3	110.0
$C_{CN}-C_{CC}-H_A$	146.3	110.0
$C_{CC}-C_{CC}-H_A$	146.3	110.0

Torsions	δ [deg]	K_χ [kJ/mol]	n
$H_C-C_T-C_S-H_C$	0	0.670	3
$H_C-C_T-C_2-H_C$	0	0.670	3
$H_C-C_T-C_S-C_S$	0	0.670	3
$H_C-C_T-C_S-C_2$	0	0.670	3
$H_C-C_S-C_S-C_2$	0	0.670	3
$H_C-C_S-C_2-C_1$	0	0.670	3
$H_C-C_S-C_2-H_C$	0	0.670	3
$H_C-C_S-C_S-H_C$	0	0.670	3
$H_C-C_S-C_2-C_1$	0	0.670	3
$C_T-C_S-C_2-C_1$	0	0.628	1
$C_T-C_S-C_S-C_2$	0	0.628	1
$C_T-C_S-C_S-C_S$	0	0.628	1
$C_S-C_S-C_2-C_1$	0	0.628	1
$C_S-C_S-C_S-C_2$	0	0.628	1
$C_S-C_S-C_S-C_S$	0	0.628	1
$H_C-C_2-C_1-H_1$	0	0.816	3
$H_C-C_2-C_1-N_A$	0	0.000	0
$C_T-C_2-C_1-N_A$	180	0.419	3
$C_S-C_2-C_1-N_A$	180	0.419	3
$C_{CN}-N_A-C_1-H_1$	180	0.816	2
$C_{CN}-N_A-C_1-C_2$	180	0.000	3
$C_{CN}-N_A-C_{1T}-H_1$	180	0.816	2
$H_A-C_{CN}-C_{CC}-H_A$	180	8.374	2
$H_A-C_{CC}-C_{CC}-H_A$	180	8.374	2
$C_T-C_S-C_2-H_C$	0	0.816	3
$C_S-C_S-C_2-H_C$	0	0.816	3
$C_T-C_S-C_S-H_C$	0	0.816	3
$C_T-C_2-C_1-H_1$	0	0.816	3
$C_S-C_2-C_1-H_1$	0	0.816	3
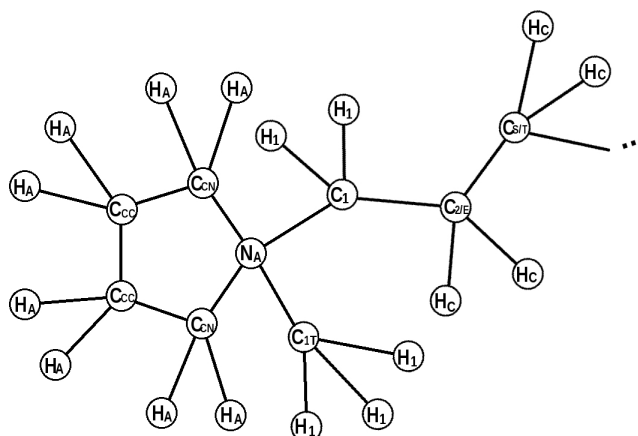
Figure A4.1. Two dimensional schematic representation and nomenclature of the $[C_n PYR]^+$ cation used in this work.
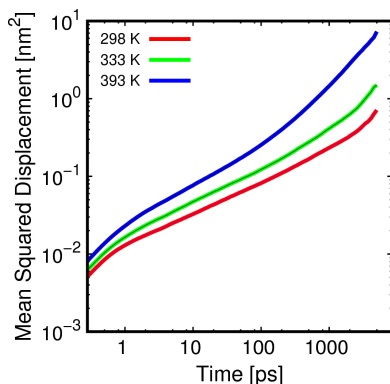

Figure A4.2. Mean squared displacement (MSD) of a $[C_4 PYR]^+$ cation as a function of time, for three different temperatures.

Simulated values of the self-diffusion coefficients (D_s) are determined by using Einstein's relation:

$$D_S = \lim_{t \to \infty} \frac{\langle \sum_i^n ||r(t) - r(0)||^2 \rangle}{6t}$$

The end of the ballistic regime occurs for times below 2 ps. There is a subdiffusive regime at short times (between 2 ps and 500 ps), and finally the self-diffusion coefficient is obtained from the slope of MSD between 1 ns and 3 ns.
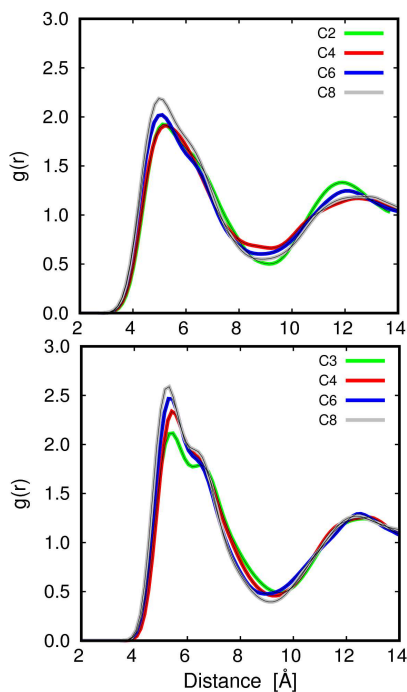
Figure A4.3. Cation-anion Radial Distribution Functions (RDFs) at room temperature for $[C_2 MIM]^+ [Tf_2 N]^-$ (top) and $[C_4 PYR]^+ [Tf_2 N]^-$ (bottom) as a function of the chain length. The RDF is computed between nitrogen atom of the anion and nitrogen (N_A) attached to alkyl chain of the cations.
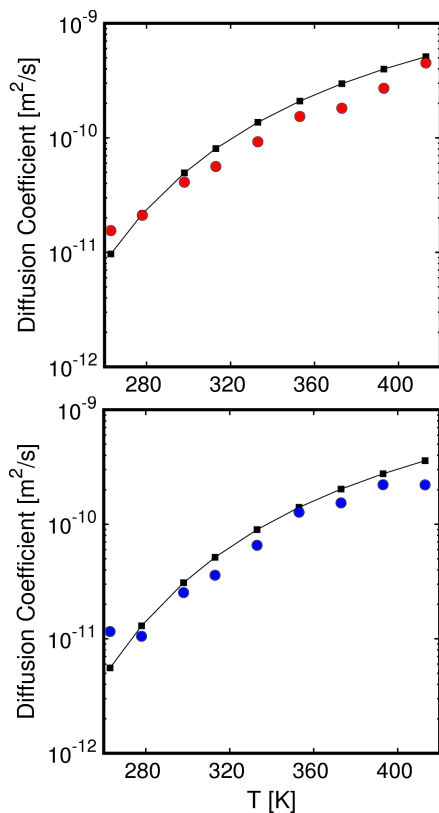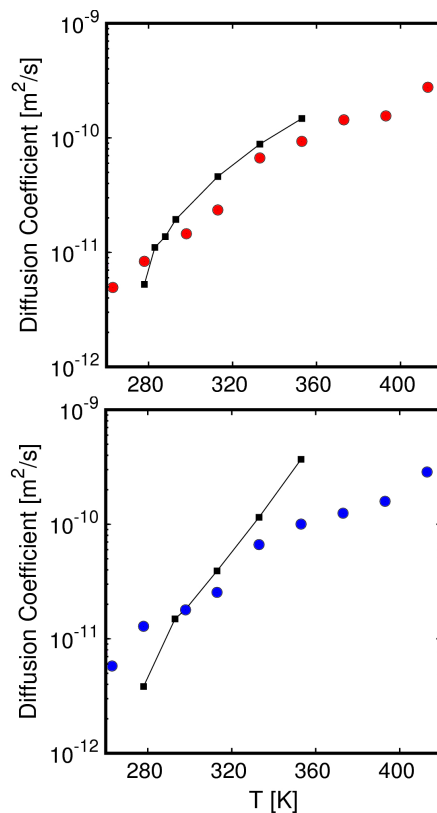
Figure A4.4. Self-diffusion coefficients of [C$_2$MIM]$^+$ cation (top) and [Tf$_2$N]$^-$ anion (bottom) as a function of temperature. Black symbols with solid lines correspond to experimental data and color symbols correspond to simulation data.
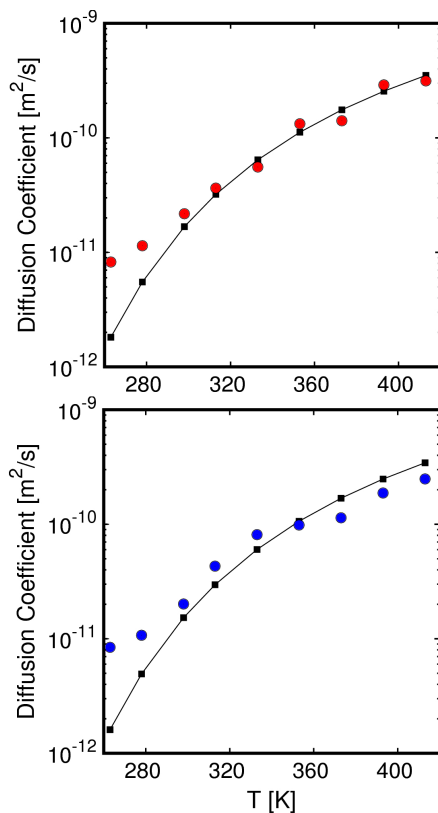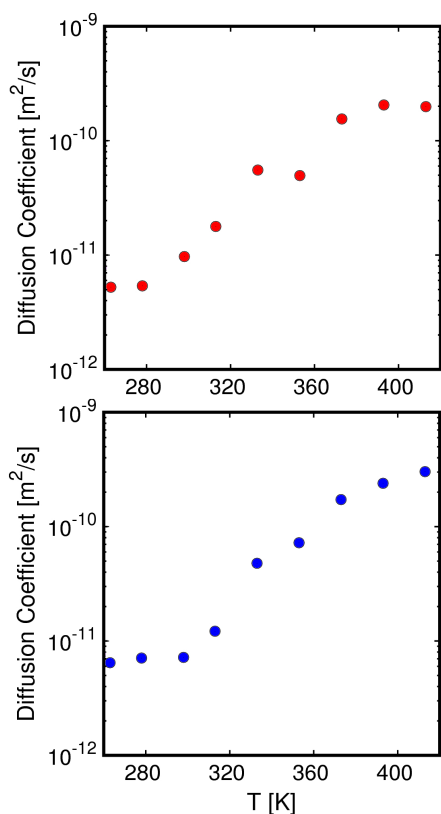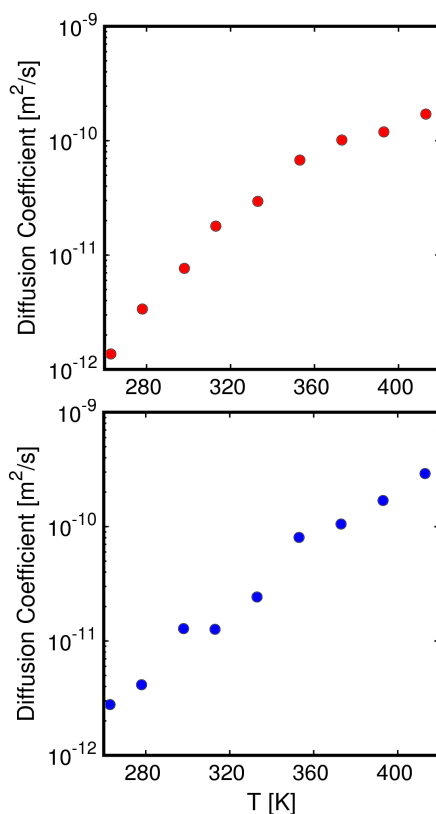
Figure A4.5. Self-diffusion coefficients of [C$_6$MIM]$^+$ cation (top) and [Tf$_2$N]$^-$ anion (bottom) as a function of temperature. Black symbols with solid lines correspond to experimental data and color symbols correspond to simulation data.
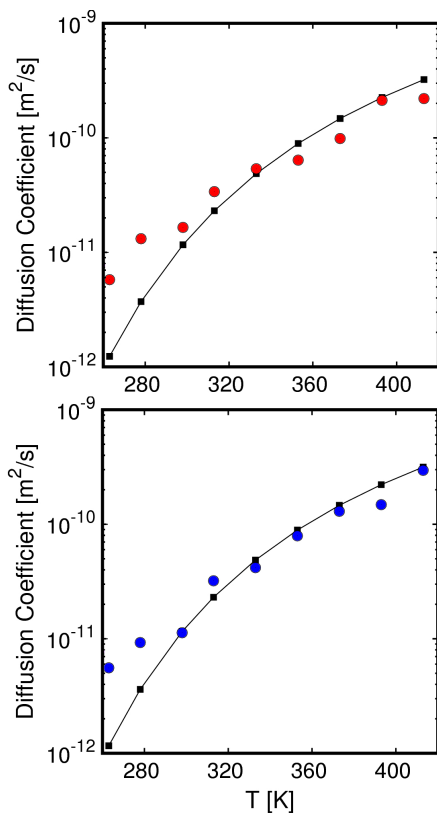
Figure A4.6. Self-diffusion coefficients of $[C_8MIM]^+$ cation (top) and $[Tf_2N]^-$ anion (bottom) as a function of temperature. Black symbols with solid lines correspond to experimental data and color symbols correspond to simulation data.

Figure A4.7. Self-diffusion coefficients of $[C_3PYR]^+$ cation (top) and $[Tf_2N]^-$ anion (bottom) as a function of temperature. Black symbols with solid lines correspond to experimental data and color symbols correspond to simulation data.

Figure A4.8. Self-diffusion coefficients of $[C_6PYR]^+$ cation (top) and $[Tf_2N]^-$ anion (bottom) as a function of temperature.

Figure A4.9. Self-diffusion coefficients of $[C_8PYR]^+$ cation (top) and $[Tf_2N]^-$ anion (bottom) as a function of temperature.
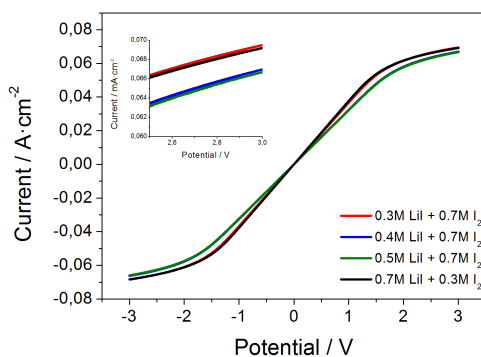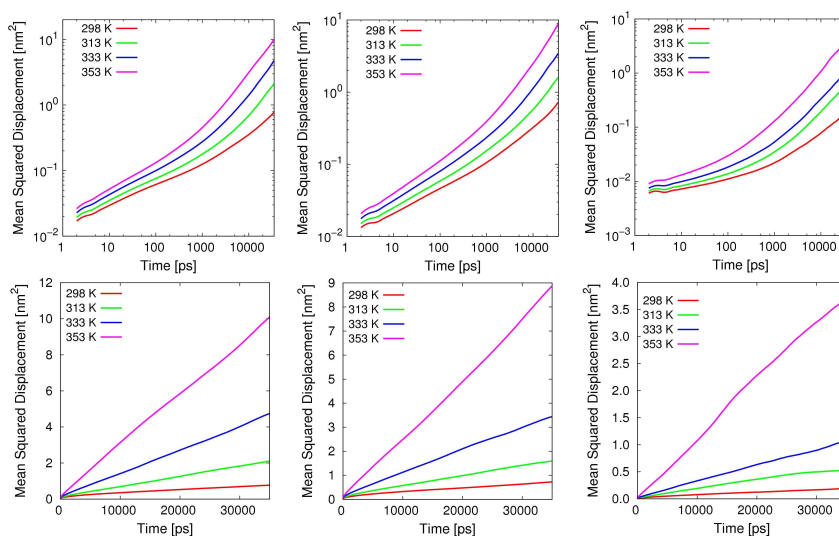

Figure A4.10. . Current as a function of applied voltage for electrochemical sandwich cells, for different concentrations of redox mediator.
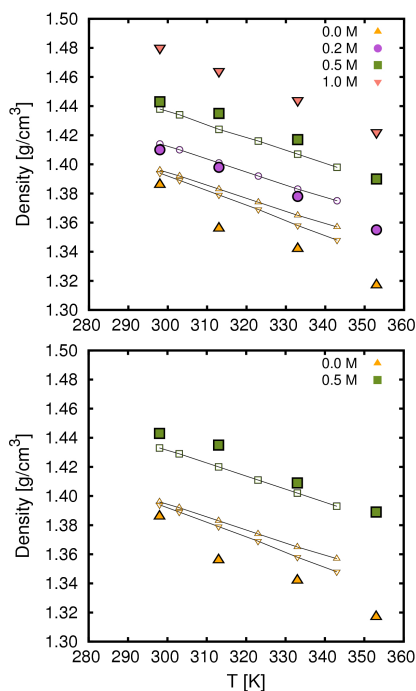
Appendix 5

Associated content of:

Quantum and Classical Molecular Dynamics of Ionic Liquids Electrolytes for Na/Li-based Batteries: Molecular Origins of the Conductivity Behavior
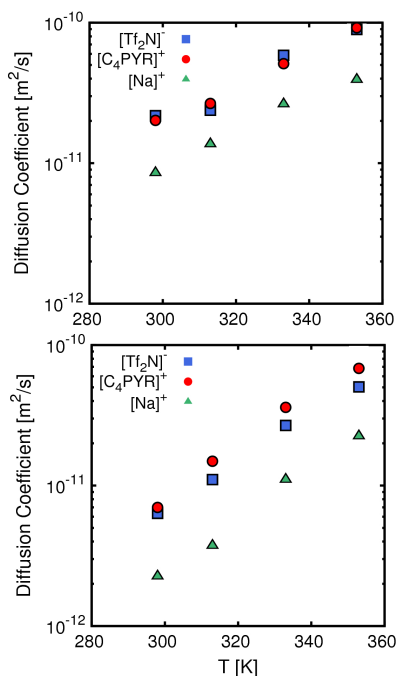

Figure A5.1. Logarithmic representation (top) and linear representation (bottom) of the mean squared displacement as a function of the simulation time for electrolytes with a fixed concentration of 1.0 M of $Na^+[Tf_2N]^-$. From left to right, $[C_4PYR]^+$, $[Tf_2N]^-$ and Na^+ respectively. Results shown correspond to the time interval for which the diffusion coefficients were extracted.

Table A5-1. Diffusion coefficients [x 10^{-11} m^2/s] for individual species of electrolytes with a fixed concentration of 1.0 M of Na$^+$[Tf$_2$N]$^-$ at 298 K. Results are for a comparison between 3 different simulations of 50 ns and 1 simulation of 200 ns, with diffusion coefficients extracted from Eq. (1) in time intervals of 30, 30, 30 and 100 ns, respectively.

	Sim. 1 [30 ns]	Sim. 2 [30 ns]	Sim. 3 [30 ns]	Sim. 4 [100 ns]
[C$_4$PYR]$^+$	0.59	0.42	0.51	0.58
[Tf$_2$N]$^-$	0.44	0.32	0.35	0.45
Na$^+$	0.16	0.15	0.15	0.18

Figure A5.3. Self-diffusion coefficients as a function of temperature for individual species constituents of electrolytes with a fixed concentration of 0.2 M of Na$^+$[Tf$_2$N]$^-$ (top) and 1.0 M of Na$^+$[Tf$_2$N]$^-$ (bottom).

Figure A5.2. Density of the electrolytes versus temperature for different concentrations of Na$^+$[Tf$_2$N]$^-$ (top) and Li$^+$[Tf$_2$N]$^-$ (bottom). Simulated values and experimental data correspond with closed and open symbols with lines respectively.
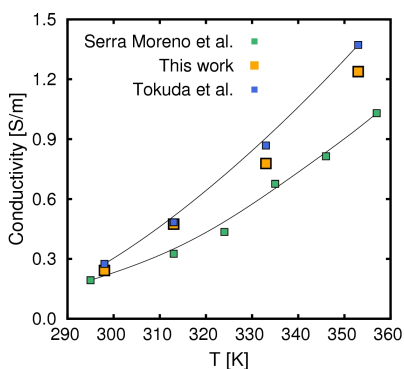
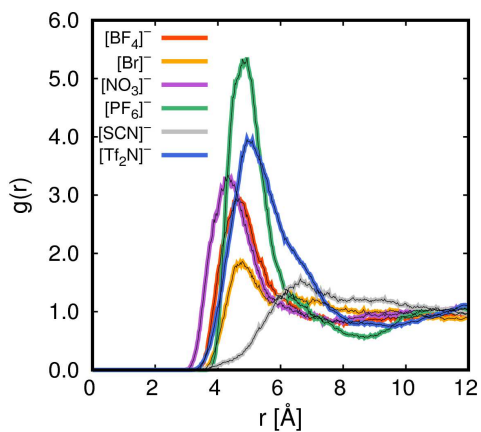**Figure A5.4.** Conductivity as a function of the temperature for electrolytes containing raw IL [C$_4$PYR]$^+$ [Tf$_2$N]$^-$.
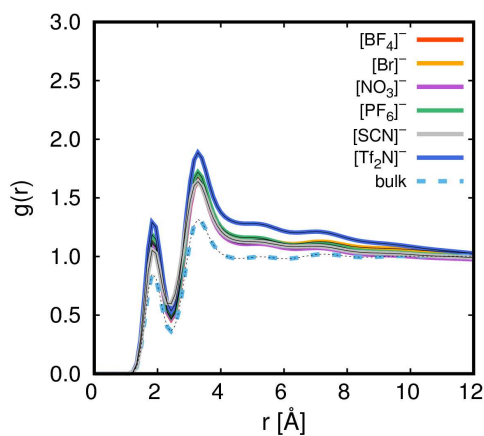
Appendix 6

Associated content of:

Aqueous Solutions of Ionic Liquids: Microscopic Assembly


Figure A6.1. Raw data (no smoothing applied) corresponding to cation-anion radial distribution functions for water/IL mixtures with 16 IL ion pairs with $[C_{10}MIM]^+$ as cation and different anion types.


Figure A6.2. Water-water $g_{OH}(r)$ radial distribution function in the bulk and mixed with 16 IL ion pairs containing $[C_{10}MIM]^+$ as cation and different anion types.
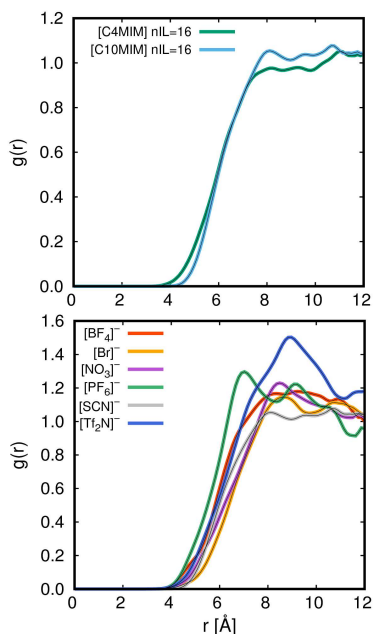
Figure A6.3. Cation-cation radial distribution functions corresponding to water/IL mixtures with 16 IL ion pairs: different cation chain lengths with $[Tf_2N]^-$ as anion (top), and different anion types with $[C_{10}MIM]^+$ as cation (bottom).
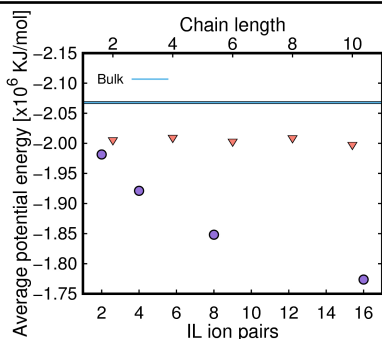
Figure A6.4. Average potential energy between water molecules in the bulk, and with low concentrations of ILs as a function of the chain length of imidazolium-based cations for 16 IL (down triangles in top x axis) and of the number of ion pairs for $[C_{10}MIM]^+$ (circles in bottom x axis) with $[Tf_2N]^-$ as anion.
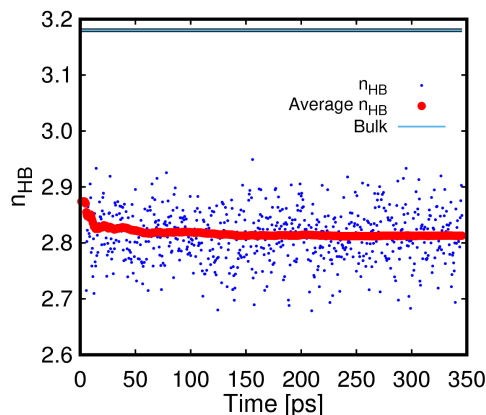
Figure A6.5. Average number of hydrogen bonds per molecule $n_H B$ as a function of the simulation time for water molecules mixed with 16 IL ion pairs for $[C_{10}MIM]^+$ as cation and $[BF_4]^-$ as anion. The data are obtained from NVT simulations. The running average decreases in time and converged around 175-200 ps to its converged value. The initial configurations were taken from previous equilibrium NPT calculations.
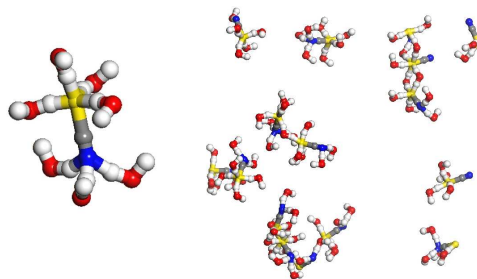
Figure A6.6. Snapshot of schematic representation of hydrogen bonding formation between water molecules and $[SCN]^-$-type anion (for the aqueous solutions with $[C_{10}MIM]^+$ as cation and 16 IL ion pairs).
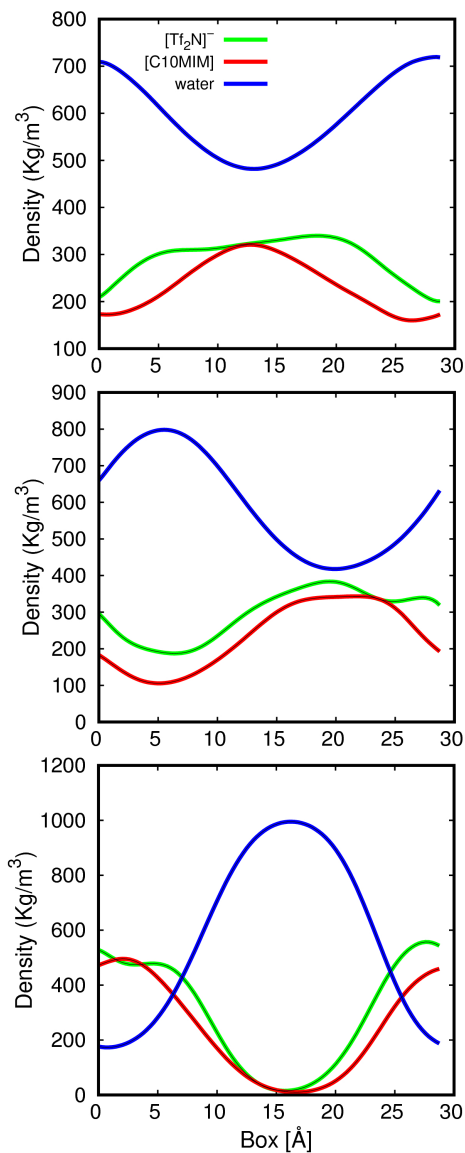
Figure A6.7. Density profiles at 298.15 K and 1 bar of the water/IL mixture with 16 IL ion pairs containing $[C_{10}MIM]^+$ cation and $[Tf_2N]^-$ anion. From left to right: x, y, and z directions.

Table A6-1. HB populations f_i (percentages of molecules involved in i hydrogen bonds) of water mixed with 16 ILs (about 1 M) for various combinations of cations and anions, and in the bulk.

$[C_{10}MIM]^+$	f_1	f_2	f_3	f_4	f_5	f_6
$[BF_4]^-$	8.8	26.3	39.1	24.6	1.2	0.0
$[Br]^-$	8.7	26.8	39.5	23.9	1.1	0.0
$[NO_3]^-$	8.6	26.4	39.4	24.5	1.2	0.0
$[PF_6]^-$	7.7	25.1	39.5	26.5	1.3	0.0
$[SCN]^-$	8.9	26.9	39.6	23.3	1.2	0.0
$[Tf_2N]^-$	8.2	24.8	38.7	27.0	1.3	0.0

$[C_4MIM]^+$	f_1	f_2	f_3	f_4	f_5	f_6
$[BF_4]^-$	7.9	25.7	40.0	25.2	1.1	0.0
$[Br]^-$	7.8	25.7	40.2	25.1	1.1	0.0
$[NO_3]^-$	7.8	25.1	39.4	26.5	1.2	0.0
$[PF_6]^-$	7.7	25.1	39.5	26.5	1.3	0.0
$[SCN]^-$	7.9	25.7	40.4	24.6	1.3	0.0
$[Tf_2N]^-$	7.6	24.4	39.3	27.4	1.3	0.0

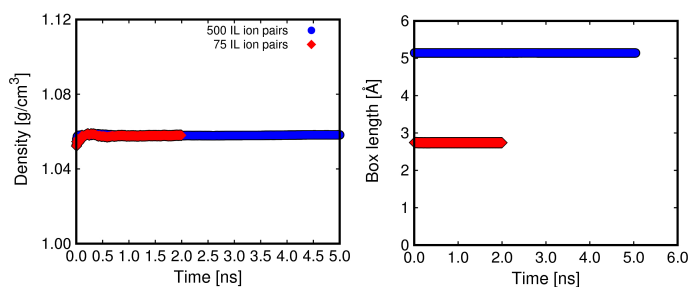| **Bulk**	f_1	f_2	f_3	f_4	f_5	f_6
	3.9	17.4	38.3	38.0	2.4	0.0

Appendix 7

Associated content of:

Micelle Formation in Aqueous Solutions of Room Temperature Ionic Liquids: a Molecular Dynamics Study

■ System size effect

Figure A7.1.   Time   evolution   of   the   average   density   and   average   cell   length   of   water/IL   mixtures   containing   75   and   500 $[C_4MIM]^+$ $[Cl]^-$ IL   ion   pairs.

■ Simulation time effect

Figures A7.2-7.3 compare the resulting data from two independent simulations with different time scales for a system containing 200 $[C_{12}MIM]^+$ $[Cl]^-$ ion pairs and 6000 molecules of water. MSD of cations and water depicted in Figure A7.2 show similar trend for the simulations of 5 and 50 ns respectively. The obtained self-diffusion coefficients of cations in both simulations are $1.18 \cdot 10^{-10}$ and $1.49 \cdot 10^{-10}$ m²/s, respectively. These values are in line with the values obtained for systems containing $[C_{12}MIM]^+$ cations in the range of 0.51-1.35 M, which fluctuates between $1.02 \cdot 10^{-10}$ and $1.54 \cdot 10^{-10}$ m²/s. The deviation of the self-diffusion coefficients of water varying the simulation time

scale is insignificant. In addition, the diffusive regime can be examined computing the time-dependent parameter: $\beta(t) = \frac{dLn(MSD(t))}{DLn(t)}$. When $\beta(t)$ is close to the unity, the system is in a linear diffusive regime. These values are shown in the bottom graph of Figure A7.2. According to this approximation, the systems are in the diffusive regime in the time scales used to extract the self-diffusion coefficients (between 1 and 3 ns and 10 and 30 ns for simulations of 5 and 50 ns respectively), as can be seen in the figure. Water describes a more linear behavior, since it has a larger diffusion constant and better statistics due to the high number of molecules considered in the simulations. Figure A7.3 shows no dependence with the time scale of the structural properties analyzed in Figures 6, 8, 9, and 10 of the main text.
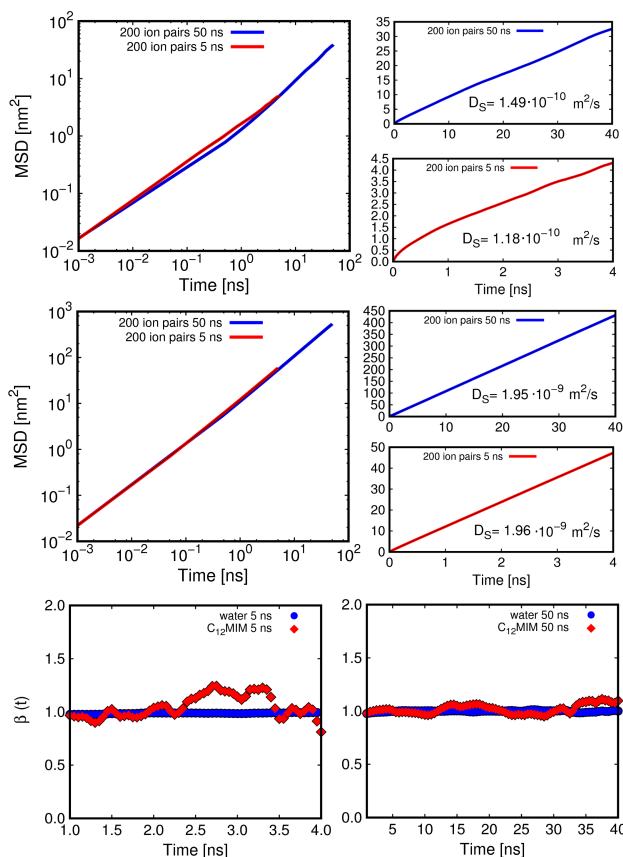
Figure A7.2. Log-log and linear representations of the mean squared displacement of $[C_{12}MIM]^+$ (top) and water (center) at different simulation timescales and their corresponding first derivatives (bottom) as a function of time.
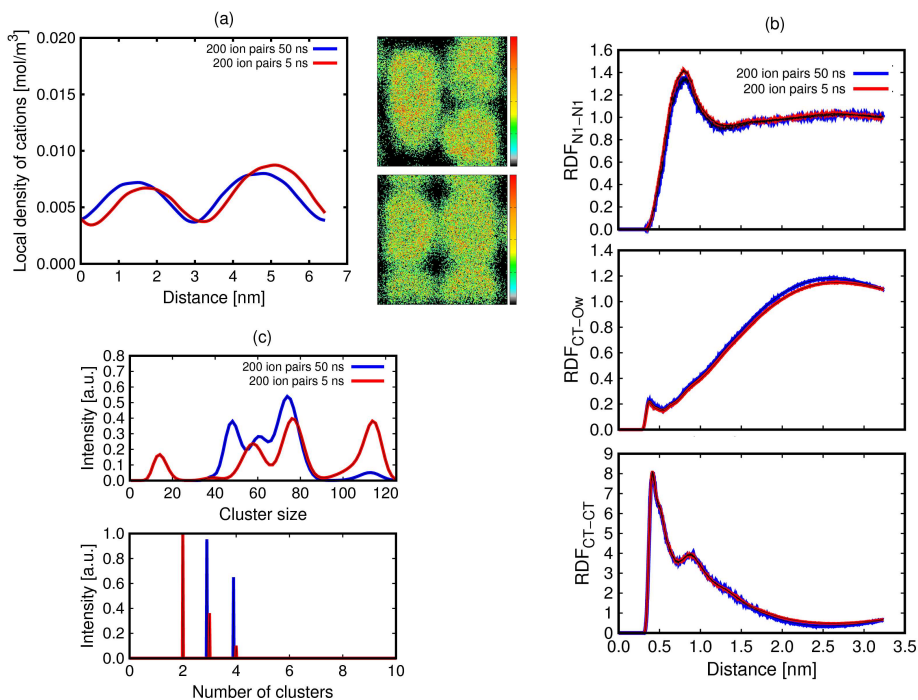
Figure A7.3. Comparison of the results obtained in this work for a system with concentration corresponding to 200 ion pairs of $[C_{12}MIM]^+$ $[Cl]^-$ at different simulation time scales. (a) Local density of cations across the X direction (left) and average occupation profiles at low and high concentration of the geometric center of cations in the XY plane (right). (b) Head-head of cations, tail of cations-water, and tail-tail of cations RDFs. (c) Cluster size distribution (number of cations per cluster) and number of cluster distribution.

List of publications

Publications included in this thesis

- **Chapter 2**

  Vicent-Luna, J. M.; Gutiérrez-Sevillano, J. J.; Anta, J. A.; Calero, S. "Effect of Room-Temperature Ionic Liquids on CO_2 Separation by a Cu-BTC Metal-Organic Framework" *J. Phys. Chem. C*, 117 (20762-20768), **2013**.

- **Chapter 3**

  Vicent-Luna, J. M.; Luna-Triguero, A.; Calero, S. "Storage and Separation of Carbon Dioxide and Methane in Hydrated Covalent Organic Frameworks" *J. Phys. Chem. C*, 120 (23756-23762), **2016**.

- **Chapter 4**

  Vicent-Luna, J. M.; Gutiérrez-Sevillano, J. J.; Anta, J. A.; Calero, S. "Role of Ionic Liquid [EMIM]$^+$ [SCN]$^-$ in the Adsorption and Diffusion of Gasses in Metal-Organic Frameworks" *Submitted*, **2017**.

- **Chapter 5**

  Vicent-Luna, J. M.; Idígoras, J.; Hamad, S.; Calero, S.; Anta, J. A. "Ion Transport in Electrolytes for Dye-Sensitized Solar Cells: A Combined Experimental and Theoretical Study" *J. Phys. Chem. C*, 118 (18448-18455), **2014**.

- **Chapter 6**

  Vicent-Luna, J. M.; Ortiz-Roldán, J. M.; Hamad, S.; Tena-Zaera, R.; Calero, S.; Anta, J. A. "Quantum and Classical Molecular Dynamics of Ionic Liquid Electrolytes for Na/Li-Based Batteries: Molecular Origins of the Conductivity Behavior" *ChemPhysChem*, 17 (2473-2481), **2016**.

- **Chapter 7**

  Vicent-Luna, J. M.; Azaceta, E. Ortiz-Roldán, J. M.; Hamad, S.; Tena-Zaera, R.; Calero, S.; Anta, J. A. "Molecular Dynamics Analysis of Charge Transport in Ionic Liquid Electrolytes Containing Added Salt with Mono, Di, and Trivalent Metal Cations" *Submitted*, **2017**.

- **Chapter 8**

  Vicent-Luna, J. M.; Dubbeldam, D.; Gómez-Álvarez, P.; Calero, S. "Aqueous Solutions of Ionic Liquids: Microscopic Assembly" *ChemPhysChem*, 17 (380-386), **2016**.

- **Chapter 9**

  Vicent-Luna, J. M.; Romero-Enrique, J. M.; Calero, S.; Anta, J. A. "Micelle Formation in Aqueous Solutions of Room Temperature Ionic Liquids: A Molecular Dynamics Study" *J. Phys. Chem. B*, 121 (8348-8358), **2017**.

Publications not included in this thesis

- Luna-Triguero, A.; Vicent-Luna, J. M.; Calero, S. "Phase Transition induced by Gas Adsorption in ZJU-198 Metal-Organic Framework" *Submitted*, **2017**.

- Min, J. G.; Luna-Triguero, A.; Byun, Y.; Balestra, S. R. G.; Vicent-Luna, J. M.; Calero, S.; Camblor, M.; Hong, S.B. "Stepped propane adsorption in pure-silica ITW zeolite " *Submitted*, **2017**.

- Luna-Triguero, A.; Vicent-Luna, J. M.; Gómez-Álvarez, P.; Calero, S. "Improving Olefin Purification using Metal Organic Frameworks with Open Metal Sites" *Submitted*, **2017**.

- Sławek, A.; Vicent-Luna, J. M.; Marszałek, B.; Makowski, W.; Calero, S. "Ordering of n-Alkanes Adsorbed in the Micropores of AlPO$_4$-5: a Combined Molecular Simulations and Quasi-Equilibrated Thermodesorption Study" *J. Phys. Chem. C*, **2017**. (DOI: 10.1021/acs.jpcc.7b08927).

- Sławek, A.; Vicent-Luna, J. M.; Marszałek, B.; Makowski, W.; Calero, S. "Quasi-Equilibrated Thermodesorption Combined with Molecular simulation for Adsorption and Separation of Hexane Isomers in Zeolites MFI and MEL" *J. Phys. Chem. C*, 121 (19226-19238), **2017**.

■ Azaceta, E.; Lutz, L.; Grimaud, A.; Vicent-Luna, J. M.; Hamad, S.; Yate, L.; Cabañero, G.; Grande, H. G.; Anta, J. A.; Tarascon, J. M.; Tena-Zaera, R. "Electrochemical reduction of oxygen in aprotic ionic liquids containing metal cations: Na-O_2 system case study" *ChemSusChem*, (1616-1623), **2017**.

■ Luna-Triguero, A.; Vicent-Luna, J. M.; Becker, T.;Vlugt, T.; Dubbeldam, D.;Gómez-Álvarez, P.; Calero, S. "Effective Model for Olefin/Paraffin Separation using (Co, Fe, Mn, Ni)-MOF-74" *ChemistrySelect*, 2 (665-672), **2017**.

■ Luna-Triguero, A.; Vicent-Luna, J. M.; Gómez-Álvarez, P.; Calero, S. "Olefin/Paraffin Separation in Open Metal Site Cu-BTC Metal-Organic Framework" *J. Phys. Chem. C*, 121 (3126-3132), **2017**.

■ Sławek, A.; Vicent-Luna, J. M.; Marszałek, B.; Balestra, S. R. G.; Makowski, W.; Calero, S. "Adsorption of N-Alkanes in MFI and MEL: Quasi-Equilibrated Thermodesorption Combined with Molecular Simulations" *J. Phys. Chem. C*, 120 (25338-25350), **2016**.

■ Vicent-Luna, J. M.; Ortiz-Roldán, J. M.; Hamad, S.; Tena-Zaera, R.; Calero, S.; Anta, J. A. "**Inside-Cover:** Quantum and Classical Molecular Dynamics of Ionic Liquid Electrolytes for Na/Li-Based Batteries: Molecular Origins of the Conductivity Behavior" *ChemPhysChem*, 17 (2449-2449), **2016**.

■ Vicent-Luna, J. M.; Dubbeldam, D.; Gómez-Álvarez, P.; Calero, S. "**Inside-Cover:** Aqueous Solutions of Ionic Liquids: Microscopic Assembly" *ChemPhysChem*, 17 (329-329), **2016**.

■ Bermúdez-García, J. M.; Vicent-Luna, J. M.; Yanez-Vilar, S.; Hamad, S.; Sánchez-Andújar, M.; Castro-García, S.; Calero, S.; Senaris-Rodriguez, M. A. "Liquid Self-Diffusion of H_2O and DMF Molecules in Co-MOF-74: Molecular Dynamics Simulations and Dielectric Spectroscopy Studies" *Phys. Chem. Chem. Phys.*, 18 (19605-19612), **2016**.

■ Ramdin, M.; Chen, Q.; Balaji, S. P.; Vicent-Luna, J. M.; Torres-Knoop, A.; Dubbeldam, D.; Calero, S.; de Loos, T. W.; Vlugt, T. J. H. "Solubilities of CO_2, CH_4, C_2H_6, and SO_2 in Ionic Liquids and Selexol from Monte Carlo Simulations" *J. Comput. Sci.*, 15 (74-80), **2016**.

■ Ramdin, M.; Balaji, S. P.; Vicent-Luna, J. M.; Torres-Knoop, A.; Chen, Q.; Dubbeldam, D.; Calero, S.; de Loos, T. W.; Vlugt, T. J. H. "Computing Bubble-Points of

CO$_2$/CH$_4$ Gas Mixtures in Ionic Liquids from Monte Carlo Simulations" *Fluid Phase Equilib.*, 418 (100-107), **2016**.

■ Luna-Triguero, A.; Vicent-Luna, J. M.; Dubbeldam, D.; Gómez-Álvarez, P.; Calero, S. "Understanding and Exploiting Window Effects for Adsorption and Separations of Hydrocarbons" *J. Phys. Chem. C*, 119 (19236-19243), **2015**.

■ Ramdin, M.; Balaji, S. P.; Vicent-Luna, J. M.; Gutiérrez-Sevillano, J. J.; Calero, S.; de Loos, T. W.; Vlugt, T. J. H. "Solubility of the Precombustion Gases CO$_2$, CH$_4$, CO, H$_2$, N$_2$, and H$_2$S in the Ionic Liquid [BMIM][Tf2N] from Monte Carlo Simulations" *J. Phys. Chem. C*, 118 (23599-23604), **2014**.

■ Gutiérrez-Sevillano, J. J.; Vicent-Luna, J. M.; Dubbeldam, D.; Calero, S. "Molecular Mechanisms for Adsorption in Cu-BTC Metal Organic Framework" *J. Phys. Chem. C*, 117 (11357-11366), **2013**.

Non-peer reviewed journals

■ Vicent-Luna, J. M. "Effect of Na/Li concentration in ionic liquid electrolytes for ion batteries" *Layman's Summary for the Atlas Of Science*, **2016**.

■ Vicent-Luna, J. M. "Estudio de las Propiedades Dinámicas y Estructurales del Argon Líquido" *MoleQla*, ISSN 2173-0903, 11 (9.1) **2013**.

■ Vicent-Luna, J. M. "Líquidos Iónicos: Propiedades y Aplicaciones" *MoleQla*, ISSN 2173-0903, 10 (3.1) **2013**.

■ Vicent-Luna, J. M. "Comment on: Unconventional, Highly Selective CO$_2$ Adsorption in Zeolite SSZ-13" *Revista Materiales en Adsorción y Catálisis*, ISSN 2173-0253, 3, **2012**.

Acknowledgements/Agradecimientos

Después de todo este paseo acompañado de coeficientes de difusión, densidades, funciones de distribución radial, isotermas de adsorción, colorines y demás "*movidas*", toca ponerse serio y acordarse de todos los que me han acompañado y ayudado a culminar esta etapa.

En primer lugar quiero agradecer todo el apoyo recibido por parte de mis directores Sofía C. y Juan A. A. Gracias por la confianza que habeis depositado en mi, por ser un gran ejemplo, por toda la dedicación y el esfuerzo que habeis hecho para enseñarme. Por que no sólo sois responsables de que haya realizado este trabajo, si no que durante este tiempo también me habeis motivado para quiera seguir avanzando con ganas en el mundo de la ciencia, gracias.

Gracias a Juanjo G. por guiarme cuando empecé en este trabajo, por todos los consejos y por todos los ratos que hemos pasado dentro y fuera del laboratorio, ya sea en Montequinto, Sevilla, Bornos, Holanda, Bélgica o donde sea. Sin tu apoyo este paseo hubiese sido más complicado. A Ana M., siempre dispuesta a echar un cable ya sea en persona, por facebook, whatsapp, hangouts o e-mail. Has sido un ejemplo de organización, ya sea trabajando, realizando trámites burocráticos o planificando viajes.

Gracias a todos con lo que he compartido laboratorio estos años, primeramente a los doctorandos, Ismael M., Paco L., Rocío B., Salva R., Julio P., José M. O. y como no, también a los doctores, Patrick M., Paula G. y Rabdel R. con vuestra ayuda, consejos e historias. Gracias a Said H. por todos los atajos que me has enseñado en forma de *script* y *alias*, por mostrarme la forma de como ser eficiente y por la ayuda en todas las colaboraciones que hemos sacado adelante. En general al grupo RASPA, por que cuando tienes una duda, te das la vuelta y haces alguna pregunta, todos se vuelven para ayudarte. Por estos detalles y otros muchos, ese es el ambiente de un lugar donde

gusta trabajar. Por todas las risas que nos hemos echado y todas las veces que hemos arreglado el mundo durante la hora de comer. A katie D. por ese añito que pasaste con nosotros, en el que viniste para aprender, pero acabaste enseñando hasta a jugar a juegos de mesa. A José L. L. por la ayuda con los "papeleos".

Thanks to Thijs V. for welcoming me in your group, for the nice discusions about science, and the motivation of teaching me. To Mahinder R. for the useful talks and e-mails and their resulting good collaborations. To Tim B. for sharing the last moments of this stage with nice discusions. I am especially grateful to David D. for all the support during this time. Always having a quick response which solve any doubt. Thanks to Andrzej S. for all the moments during your stays in the group. You came to learn some simulation stuffs from me and you left being a friend.

Gracias al resto de colaboradores de los artículos de esta tesis, Jesús I., Ramón T., Eneko A., y José M. R. por vuestro esfuerzo. Gracias a Chema O. por todos los ratos que hemos pasado y por hacer que aquel máster que hicimos fuese mucho menos aburrido. También me gustaría acordarme de J. B. Parra por ser la voz de la experiencia y por sus historias y explicaciones a través del telófono o e-mail y junto con Conchi A. por los buenos momentos en las veces que hemos coincidido y vuestro apoyo experimental.

Gracias al resto de personas que han hecho posible que llegase aquí. A mis profesores de la UCO por proporcionarme los conocimientos y herramientas necesarias para desarrollar este trabajo. No quiero olvidarme de aquellos que me dieron su apoyo incluso antes de empezar la carrera. Aquellos profesores que me motivaron para seguir estudiando, Antonio D., Natalia M. y Miguel A. C. Especialmente a Miguel A. C. por ser el único culpable de que me interesase por la física, la cual me ha traido hasta aquí.

Gracias a todos mis amigos con los que he pasado muy buenos ratos durante este tiempo. A Blas D. por hablar, por escuchar, por compartir, por aconsejar, por debatir, por las cervezas en la barra del bar, por los paseos en cualquier momento y por miles de cosas más que no caben en un párrafo. A Mayte R. que también ha estado siempre dispuesta y con una sonrisa para recorrernos las montañas o salir de fiesta tantos fines de semana. A Manuel P. por haber estado ahí desde que teníamos siete u ocho años y seguir sumando.

A Azahara L. por que tengo motivos para mencionarte en todos los párrafos de esta sección, compañera, colaboradora, amiga, familia, etc. Simplemente gracias por todo y por estar a mi lado y por supuesto ser la mejor "mami" que Ali pueda tener. A Ali

porque es el bebé más adorable del mundo, que desde que llegaste todo se ve de otra manera.

Gracias a mis padres por todo el apoyo que me han dado constantemente, no sólo durante el desarrollo de ésta tesis, si no desde que me alcanza la memoria (y un poquillo más). Gracias por haber creido en mí todo el tiempo. A mi hermano, que ha crecido casi sin darme cuenta. A mis tios Manolo L. y Maribel T. por darme un segundo hogar lejos de casa. A la "madrinita" Ana. L. entre otras millones de cosas por hacer que los teletienda de madrugada sean superdivertidos. A mi primo R. C. Vicent por todo lo que hemos vivido juntos y por que siempre hay algo que aprender de ti y de tu filosofía. También acordarme del resto de mi familia, por que con ellos ahí si da gusto ir al pueblo de visita. A mis abuelos, que aunque se fueron, grabaron en mí grandes recuerdos para que perduren siempre.

Vive de tal manera que quienes
reían cuando tu al nacer llorabas,
lloren cuando tu al morir sonrías.

UNIVERSIDAD
PABLO D**E**
OLAVIDE
S E V I L L A

GRUPO
DE MATERIALES
NANOESTRUCTURADOS
CON APLICACIONES
TECNOLÓGICAS

NANO STRUCTURED SOLAR CELLS GROUP